The Structures and Properties of Layered Pnictides and Oxychalcogenides

Michael J. Pitcher

A thesis submitted in part fulfilment of the requirements for the degree of Doctor of Philosophy at the University of Oxford

Balliol College
University of Oxford
March 2011



The work described in this thesis was carried out in the Inorganic Chemistry Laboratory, South Parks Road, Oxford from October 2007 to March 2011 under the supervision of Dr Simon J. Clarke. All the work described is my own unless stated to the contrary, and has not been submitted for any degree at this or any other university.

Michael J. Pitcher

March 2011

Abstract

The Structures and Properties of Layered Pnictides and Oxychalcogenides

Michael Pitcher Balliol College

D.Phil Thesis Hilary 2011

This work focuses principally on two compounds, $CeCu_{1-x}OS$ and LiFeAs, which have related layered structures but exhibit radically different physical properties. The nature of the air-sensitivity of the ZrCuSiAs-type oxysulfide $CeCu_{1-x}OS$ has been investigated by neutron diffraction and magnetometry. It was found that this compound can be made fully stoichiometric, with structural and magnetic properties that are consistent with other *Ln*CuOS compounds, indicating that this is a bona-fide Ce^{3+} compound. Upon air exposure, Cu ions are extruded from the sulfide layer to leave a Cu-deficient phase with contracted unit cell parameters and a diminished paramagnetic moment consistent with mixed-valence $Ce^{3+/4+}$. The extruded Cu forms CuO and can be re-inserted into the sulfide layer by heating under a reducing atmosphere. This explains the anomalous behaviour of CeCuOS reported throughout the literature and has implications for the behaviour of other layered Cu-sulfides with oxidisable cations. At low temperatures Cu-deficient $CeCu_{0.8}OS$ was found to exhibit structural ordering of Cu^{+} ions and vacancies, resulting in a $\sqrt{5}a \times \sqrt{5}a$ basal expansion of the high-temperature unit cell.

The layered iron arsenide LiFeAs was synthesised and found to be superconducting below 17 K. Joint XRD/NPD measurements showed unambiguously that the compound adopts the anti-PbFCl structure with Li ions in a square-pyramidal $LiAs_5$ environment. No evidence was found for an orthorhombic structural distortion at low temperatures. Further diffraction experiments showed that the compound can be made with non-stoichiometric compositions $Li_{1-y}Fe_{1+y}As$ for small values of y (< 0.05), as Fe can be accommodated on the Li site. This type of non-stoichiometry was found to strongly inhibit superconductivity (which was quenched entirely when $y > 0.02$).

Three series of compounds of type $LiFe_{1-x}M_xAs$ (M =Mn, Co, Ni) were synthesised and characterised structurally by high-resolution XRD and/or NPD. Substitution by Co and Ni was found to cause a monotonic decrease in T_c, and Ni was found to be twice as effective at suppressing T_c as Co. MuSR measurements showed the penetration depth increasing with Co and Ni substitution, consistent with the superconducting state becoming less robust. Substitution by Mn was found to strongly inhibit superconductivity, and this behaviour is reminiscent of the non-stoichiometric $Li_{1-y}Fe_{1+y}As$ materials.

The structures and superconducting properties of LiFeAs and NaFeAs were studied under high pressures. Equations of state were obtained for each compound. Hydrostatic pressure was found to distort of the $FeAs_4$ away from ideal tetrahedral geometry in both compounds. These changes caused a monotonic decrease in T_c in LiFeAs, but had a smaller and more complex effect on the T_c of NaFeAs. Furthermore, NaFeAs was found to undergo a structural transition above $P = 22$ GPa, but the high-pressure structure could not be solved and this will become target for future work.

Acknowledgements

The work presented in this thesis would not have been possible without assistance and guidance from several people. First and foremost, Dr. Simon Clarke has provided patient supervision throughout my time in the group, and his encouragement, ideas and enthusiasm have been invaluable. I am also grateful to Dr. Masaki Mito for conducting the high-pressure magnetometry experiments; to Dr. Peter Baker and the group of Prof. S. Blundell for conducting μSR measurements and providing analysis; and to Dr. Joke Hadermann for electron diffraction measurements.

Thanks also go to past and present members of the Clarke group. In particular, a lot of hard work by Dr. Dinah Parker has been crucial to the work on LiFeAs and NaFeAs; the consistently helpful advice from Dr. Paul Adamson has saved me from countless frustrating afternoons with GSAS; and Mr. Jack Wright has been responsible for educating me in the ways of μSR. Dr. Catherine Smura, Dr. Sebastian Herkelrath, Dr. Raquel Cortes-Gil, Mr. Alex Corkett and Ms. Alice Taylor have all provided help, advice and company on beamlines and all deserve my gratitude.

A number of instrument scientists have provided assistance with neutron and X-ray diffractometers: Dr. R. Smith (Polaris), Dr. R. Ibberson, Dr. K. Knight and Dr. A. Daoud-Aladine (HRPD) from ISIS; Dr. E. Suard (D2B) from the ILL; Dr. C. Tang, Dr. J. Parker and Dr. S. Thompson (I11) from Diamond; Dr. M. Brunelli, Dr. G. Garbarino, Dr. W. Crichton (ID27), Dr. M. Hanfland (ID09a), Dr. A. Fitch and Dr. I. Margiolakis (ID31) from the ESRF. I am also grateful to Mr. C. Goodway, Mr. M. Kibble and Mr. C. Barry at ISIS for their assistance with the He-gas cell and the Paris-Edinburgh cell. Thanks also go to Dr. P. Wiseman for maintainance the X-ray diffractometers and SQUID magnetometers in the ICL.

Finally, I wish to thank Nicole and my family and friends for their support and good company throughout my time here in Oxford.

Contents

1 Introduction **1**

1.1 Solid State Chemistry 1
1.2 Layered Oxychalcogenides and Oxypnictides 3
1.2.1 Common crystal structures 3
1.2.2 Ion-vacancy ordering 6
1.3 Layered Pnictides 8
1.3.1 Compounds with the $ThCr_2Si_2$ structure type 9
1.3.2 Compounds with the PbFCl (or Cu_2Sb) structure type 9
1.4 Superconducting Materials 10
1.4.1 Discovery and early research 10
1.4.2 Bardeen-Cooper-Schrieffer theory and conventional superconductivity 11
1.4.3 High temperature superconductivity 12
1.5 Common Magnetic Phenomena 18
1.5.1 Diamagnetism and Paramagnetism 18
1.5.2 Ferromagnetism and Antiferromagnetism 21
1.6 Aims of this work 24

2 Experimental Techniques **27**

2.1 Synthetic Methods 27
2.1.1 Solid-state synthesis 27
2.1.2 Argon-filled dry box 28
2.1.3 Synthesis of starting materials 29
2.2 Analytical Methods 30
2.2.1 Crystal Symmetry and Diffraction 30
2.2.2 Diffraction of X-rays 31
2.2.3 Diffraction of Neutrons 37
2.2.4 Powder Diffraction 38
2.2.5 The Rietveld Method 39
2.2.6 Laboratory X-ray Sources 43
2.2.7 Synchrotron X-ray Sources 45
2.2.8 Neutron Sources and Time-of-Flight Diffraction 48
2.2.9 D.C. SQUID Magnetometry 56
2.2.10 SQUID Magnetometry at High Pressures 61
2.2.11 Muon-spin Rotation (μSR) Spectroscopy 62

3 Copper Deficiency and Structural Ordering in $CeCu_{1-x}OS$ 65
3.1 Introduction . . . 65
3.2 Investigating the compositional differences between "green" and "black" CeCuOS . . . 70
3.2.1 Synthesis of "Green" and "Black" CeCuOS . . . 70
3.2.2 Neutron powder diffraction . . . 71
3.2.3 SQUID Magnetometry . . . 75
3.3 Reaction of $CeCu_{(1-x)}OS$ with x.CuO under a reducing atmosphere . 78
3.3.1 Laboratory XRD . . . 78
3.3.2 SQUID Magnetometry . . . 80
3.4 Structural ordering in $CeCu_{(1-x)}OS$ . . . 80
3.4.1 Sample preparation . . . 84
3.4.2 High resolution XRPD . . . 85
3.4.3 Neutron diffraction . . . 94
3.4.4 Comparison with a family of iron selenides $K_xFe_{2-y}Se_2$ . . . 96
3.5 Summary and conclusions . . . 98

4 Structure and Superconductivity of LiFeAs and $Li_{1-y}Fe_{1+y}As$ 101
4.1 Introduction . . . 101
4.2 Initial synthesis of two samples of LiFeAs . . . 104
4.3 Magnetometry studies of two samples of LiFeAs . . . 106
4.4 Diffraction studies of two samples of LiFeAs . . . 109
4.5 Synthesis of an Fe-rich series $Li_{1-y}Fe_{1+y}As$ . . . 114
4.6 Magnetometry studies of an Fe-rich series $Li_{1-y}Fe_{1+y}As$ . . . 123
4.7 Summary and Conclusions . . . 125

5 The Effect of Doping in $LiFe_{1-x}M_xAs$ (M =Mn, Co, Ni) 127
5.1 Introduction . . . 127
5.2 The synthesis of $LiFe_{1-x}M_xAs$ (M =Mn, Co, Ni) . . . 130
5.3 Structural Characterisation of $LiFe_{1-x}Co_xAs$ . . . 132
5.3.1 High-resolution X-ray powder diffraction . . . 132
5.4 Structural characterisation of $LiFe_{1-x}Ni_xAs$ . . . 139
5.4.1 Laboratory X-Ray Powder Diffraction . . . 139
5.4.2 High Resolution XRPD . . . 141
5.4.3 Neutron powder diffraction . . . 142
5.5 Structural characterisation of $LiFe_{1-x}Mn_xAs$ . . . 147
5.6 Structural comparisons between M = Mn, Co, Ni and $Li_{1-y}Fe_{1+y}As$. 148
5.7 Magnetic characterisation of $LiFe_{1-x}M_xAs$ . . . 151
5.7.1 dc-SQUID Magnetometry . . . 151
5.7.2 Muon Spin Rotation . . . 161
5.8 Summary and Conclusions . . . 164

6 Effect of Pressure on the Structure and Superconductivity of LiFeAs and NaFeAs 166
6.1 Introduction . . . 166
6.2 Response of the Structure and Superconductivity of LiFeAs to High Pressures . . . 170

6.2.1 High pressure XRD from **0 – 17** GPa 170
6.2.2 High pressure NPD from **0 – 10** GPa 177
6.2.3 High pressure magnetometry from **0 – 4.3** GPa 187
6.3 Response of the Structure and Superconductivity of NaFeAs to High Pressures 195
6.3.1 High-pressure XRD from **0 – 24** GPa 195
6.3.2 High pressure magnetometry from **0 – 1.6** GPa 206
6.4 Summary and conclusions 207

7 Summary **212**

References **218**

Appendix A **I**

Appendix B **IV**

Appendix C **VII**

Appendix D **X**

Appendix E **XVII**

Appendix F **XXVII**

Chapter 1

Introduction

1.1 Solid State Chemistry

The solid state is comprised of a huge and diverse range of materials, including many which have chemical or physical properties that make them technologically useful and commercially important, and countless others that have interesting properties with potential for future utility. The synthesis and investigation of new solid materials (and the modification and optimisation of known materials) has significantly extended this world of useful, functional and interesting materials by both design and serendipity.

There are many classes of solid with useful physical properties. Magnetically ordered materials such as $\gamma-Fe_2O_3$ are used to store data in computer hard-drives; ferroelectric and piezoelectric materials (such as the perovskites $PbZr_{1-x}Ti_xO_3$ and $BaTiO_3$) are used in a wide variety of electronic devices, along with multitudes of different semiconducting materials (such as GaAs and other "III-V" semiconductors); while materials with favourable optical properties can be used in applications as simple as pigmentation (e.g. white TiO_2, with a large refractive index arising from a band gap just outide the visible region, is used in a highly diverse range of products including white paint and toothpaste). There are compounds with other dramatic physical properties, such as colossal magnetoresistance in perovskite-type manganites,[1] which are yet to find a technological use.

Solids can also be useful for their chemical properties. One important example is the rechargeable battery anode material $LiCoO_2$,[2] which is used to power millions of the world's portable electronic devices by the reversible intercalation of Li. The highly porous zeolites and aluminophosphates are widely used for their adsorption properties and as high surface area supports for various industrial catalysts. Zeolites and other porous materials such as metal-organic frameworks (MOFs) have also been investigated for their potential as hydrogen or CO_2 storage materials.[3, 4] The search for materials with favourable hydrogen storage properties has also covered a number of other types of solid such as metal hydrides[5] and amidoboranes.[6]

The properties of complex new solid materials are often difficult to predict accurately, and this occasionally leads to unexpected discoveries. One of the most famous examples of this is the discovery of high-temperature superconductivity in layered perovskite-based cuprates,[7] which earned its researchers the Nobel Prize in Physics in 1987. Much more recently, high-T_c superconductivity was reported in the layered oxy-arsenide $LaFeAsO_{1-x}F_x$ by a group who were originally researching optically transparent p-type semiconductors. Superconducting materials such as the cuprates, with $T_c > 77$ K and high critical fields, could potentially be used in place of conventional superconducting alloys for the generation of large magnetic fields in scientific and medical instruments, or conceivably for long-range power transmission,[8] as cooling by liquid nitrogen would be significantly cheaper than liquid helium. The technological application of these materials is currently inhibited by their mechanical properties, but if these problems can be overcome (e.g. by the development of superconducting tapes or wires)[9] they may become commercially important.

Most of the materials mentioned so far are oxides, which represent perhaps the most explored class of solid-state compound. Oxides are often synthesised successfully at high temperatures under normal (oxidising) atmospheric conditions, and exhibit a vast array of different structures and compositions. Almost all elements are able to form compounds with oxygen, and many are known to form a number

of different oxides. Non-oxide and mixed-anion solids are less abundant and are often more complicated to synthesise, as common anions such as sulfide, nitride and phosphide are readily oxidised, and care must be taken to exclude atmospheric oxygen and moisture during synthesis to avoid oxidation and/or hydrolysis of the target compound. As for oxides, the properties of non-oxide and mixed-anion compounds are diverse, but they are less extensively studied. Much current research is focused on these types of materials, with the aim of developing and discovering new compounds with novel crystal structures and properties to complement those found in oxides.

1.2 Layered Oxychalcogenides and Oxypnictides

1.2.1 Common crystal structures

In mixed-anion systems, layered crystal structures are commonly adopted as a result of a mis-match in size between the different anions. In the case of oxysulfides, the O^{2-} and S^{2-}anions have the same number of valence electrons but their ionic radii are very different at 1.40 Å and 1.84 Å respectively.[10] It is therefore strongly unfavourable for these anions to share the same crystallographic site, and thermodynamically stable phases form with long-range ordering of the anions, which often results in layered structures. This type of layered anion ordering is also particularly common in oxypnictides, and is adopted by some non-oxide systems such as silicopnictides (e.g. ZrCuSiAs)[11] or fluorochalcogenides (e.g. SrCuSF).[12] There are several examples of oxyhalides and oxynitrides with crystallographically ordered anions (e.g. Ba_2InO_3F and Ba_3ZnN_2O) [13, 14] but these systems are often found to have anions that are disordered over a long range due to the similar ionic radii of nitride and fluoride to oxide.

Many layered mixed-anion compounds also contain more than one type of cation. In these systems it is very common to observe ordering of the cations into the different layers according to the particular bonding preferences of the ordered anions. Oxide

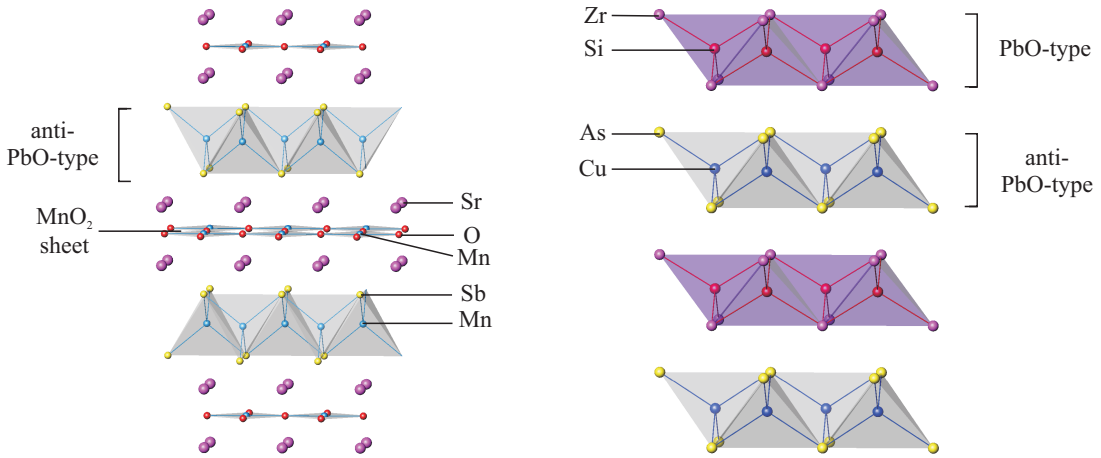


Figure 1.1: The layered $Sr_2Mn_3Sb_2O_2$ (LHS) and ZrCuSiAs (RHS) structures commonly adopted by oxychalcogenides and oxypnictides.

is strongly electronegative and bonds preferentially to correspondingly "hard" cations such as group 1 and 2 metals, lanthanides and early transition metals. In contrast, sulfide bonds preferentially to "soft" cations with low-energy *d*-orbitals (typically late transition metals in low oxidation states). This results in the partitioning of the crystal structure into distinct oxide-like and chalcogenide-like portions, which is a feature of several common oxychalcogenide/oxypnictide crystal structures discussed below.

The crystal structures of the quaternary and quinary oxysulfides and oxypnictides are heavily represented by two common types, which are illustrated in figure 1.1. The ZrSiCuAs structure (sometimes referred to as the LaAgOS or $HfCuSi_2$ structure) is a very common structure type for quaternary mixed-anion compounds, and exhibits a great amount of compositional flexibility.[15] The structure consists of alternating anti-PbO-type metal-chalcogenide layers and PbO-type lanthanide-oxide layers. Several extensive families of compounds take this structure, including LaCuSeO ($LnM^{I}Ch$O) and LaFeAsO ($LnM^{II}Pn$O), while alkaline-earth compounds (e.g. SrFeAsF)[16] and actinide-containing compounds (e.g. UCuPO[17] and ThCuAsO)[18] are also known. The ubiquity of this structure type makes it perhaps inevitable that several member compounds have interesting or unusual electronic and structural properties. One example is two-dimensional fast-ion conductivity in the silver sulfide LaAgOS;[19] another is LaFePO, which in 2006 was reported to be superconducting at low

temperatures.[20] This ultimately lead to the realisation of high-T_c superconductivity in an entire class of layered iron-arsenide compounds,[21] and those with the highest T_c (of up to 55 K) adopt this crystal structure. These compounds will be discussed in more detail in section 1.4.

The $Sr_2Mn_3Sb_2O_2$ structure contains anti-PbO-type chalcogenide/pnictide layers like those in many representatives of the ZrCuSiAs structure, but these are alternately stacked with a more complex perovskite-related oxide layer. This layer consists of MO_2 sheets with M in a square-planar site, which are separated from the chalcogenide layer by Sr^{2+} ions. The majority of compounds with this structure contain two different transition metals, with the more oxo-philic occupying the square-planar site in the MO_2 sheets. Like ZrSiCuAs this structure shows a great deal of compositional flexibility, and is well represented by wide range of quinary oxyantimonides and oxyarsenides,[22] as well as a number of oxyphosphides, oxysulfides (e.g. $Sr_2ZnO_2Cu_2S_2$)[23] and some less common oxybismuthides.[24] Compounds with this structure type often show 2D antiferromagnetic order within the MO_2 sheets with weaker magnetic interactions between layers,[25] which can lead to complex magnetic behaviour such as metamagnetism.[26] In such compounds, the spacing between layers (and hence the strength of the inter-layer magnetic coupling) can be conveniently controlled by substituting Sr^{2+} by Ba^{2+} or Ca^{2+}.

In common with certain classes of layered oxide such as the Ruddlesden-Popper phases ($A_{n+1}M_nO_{3n+1}$), the crystal structures of layered mixed-anion compounds can be members of much broader structural families. For example, the oxysulfide $Sr_2MnO_2Cu_{2-x}S_2$ (with the $Sr_2Mn_3Sb_2O_2$ structure) forms the most basic member of two homologous series, which are illustrated in figure 1.2. The first, of general formula $Sr_2MnO_2Cu_{2m-x}S_{m+1}$ ($m = 1, 2, 3$), has members with double- or triple-thickness sulfide layers which are still closely related to the anti-PbO-type single layer but now have a structure recognisable as that of α-Cu_2S (i.e. they are fragments of the anti-fluorite structure).[27, 26] The second series has oxide layers of variable thickness, of general formula $Sr_{n+1}M_nO_{3n-1}Cu_{2-x}S_2$ where $n = 1, 2, 3$ and $M = Fe^{3+}$

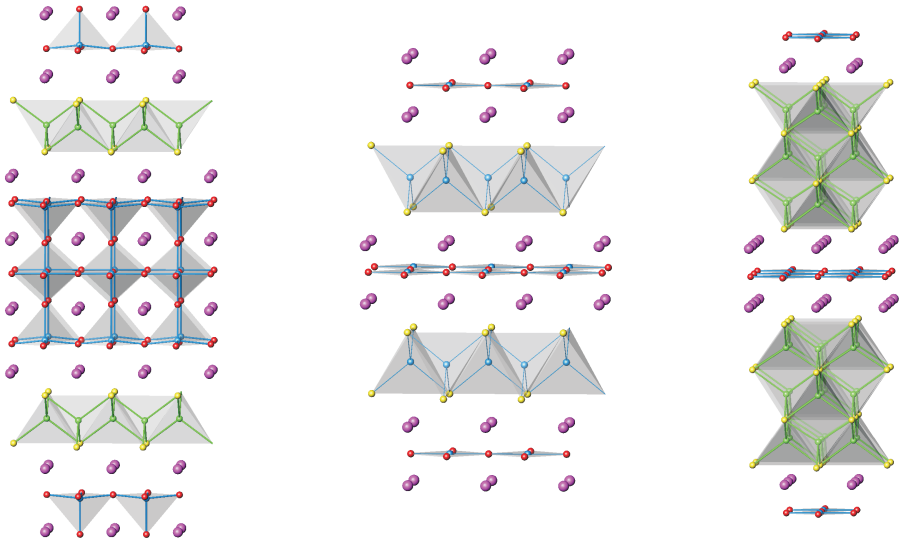


Figure 1.2: The homologous series $A_{n+1}M_nO_{3n-1}Cu_{2m}S_{m+1}$ with thick oxide layers ($m = 1$, $n = 3$, LHS); thick sulfide layers ($m = 3$, $n = 1$, RHS); and the common $Sr_2Mn_3Sb_2O_2$ structure ($m = 1$, $n = 1$, centre).

or Sc^{3+}.[23, 28] The thick oxide layers in these compounds now clearly represent fragments of the cubic perovskite structure. These types of series are not limited to oxychalcogenides, as recent research into superconductivity in similar layered oxyarsenides has uncovered other similar homologous series with thick perovskite-type oxide layers.[29, 30]

1.2.2 Ion-vacancy ordering

As mentioned above, layered oxysulfides contain anti-PbO-type sulfide layers that can be considered as fragments of the anti-fluorite structure. The anti-fluorite structure is adopted by α-Cu_2S, which is one of several binary chalcogenides known to contain highly mobile cations at ambient temperatures (other examples include the analogous Ag-containing compounds α-Ag_2S and α-Ag_2Se). These chalcogenides show some similarities to fast-ion conductors such as α-AgI and Na β-alumina, but exhibit a much higher electronic conductivity.[31] It is apparent that the property of high cation mobility can be preserved even when these chalcogenides are incorporated into layered structures. For example, a neutron diffraction study of ZrCuSiAs-type

The material originally presented here is not currently available in ORA

Figure 1.3: The low-temperature ordering of the $Cu_{1.5}S_2$ layer in $Sr_2MnO_2Cu_{1.5}S_2$. Figure is from reference [35]

LaAgOS[19] showed a significant degree of delocalisation of the Ag^+ cations within the 2-dimensional AgS layers. Neutron diffraction measurements have also suggested that the Cu-mobility is high in $Sr_2MnO_2Cu_{5.5}S_4$,[26] and this is supported by the ability of these compounds to undergo a Li intercalation/Cu extrusion reaction with *n*-BuLi in solution[32] or in an electrochemical cell.[33]

Several layered Cu-oxysulfides, including all three members of the homologous series $Sr_2MnO_2Cu_{2m-x}S_{m+1}$[26] and ZrCuSiAs-type $CeCu_{1-x}OS$,[34] are known to form with an intrinsic deficiency of Cu in the anti-fluorite-type layer. In these materials up to 25 % of the Cu sites may be vacant.[35] High cation mobility has implications for the low temperature structures of these materials, as the cations and vacancies may order crystallographically to produce a superstructure, which is typically a basal expansion of the high-temperature unit cell. This ordering tends to occur at moderately low temperatures, such as 240 K in $Sr_2MnO_2Cu_{1.5}S_2$.[35, 36] The superstructure adopted by this compound, illustrated in figure 1.3, is a $2\sqrt{2}a \times \sqrt{2}a \times c$ basal expansion of the high-T unit cell, and is isostructural with both the ordered anti-type $O_{1.5}Y_2$ layer in $SrY_2CuFeO_{6.5}$,[37] and the ordering in $TlFe_{1.5}S_2$.[38]

There are currently no reports of this type of transition in ZrCuSiAs-type compounds (although $La_2O_2CdSe_2$ - an extreme example of a ZrCuSiAs-type compound with a cation deficient chalcogenide layer - crystallises as a superstructure of ZrCuSiAs where $CdSe_4$ tetrahedra do not share edges).[39] However, $CeCu_{1-x}OS$ appears to be a good candidate for low-T structural ordering and has been shown

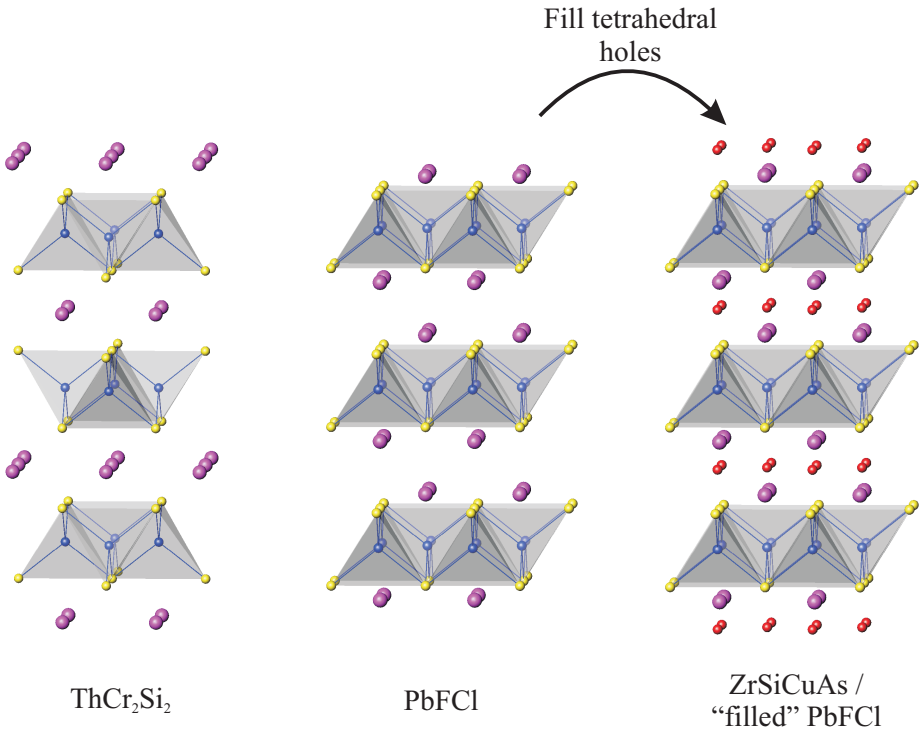


Figure 1.4: The $ThCr_2Si_2$ and PbFCl structures (LHS and centre, respectively), and their relation to the ZrCuSiAs "filled-PbFCl" structure (RHS).

to form stable phases over a wide compositional range ($0 \leq x \leq 0.25$).[40, 41] It is therefore conceivable that this compound could adopt more than one low-temperature superstructure, depending on composition. The low-T structural behaviour of this compound will be investigated in Chapter 3.

1.3 Layered Pnictides

Layered crystal structures are common throughout solid state chemistry and are not confined to mixed-anion systems, as is demonstrated by the existence of many layered binary compounds (e.g. CdI_2 and SnO). Much of the work presented in this thesis is focused on the structural and physical properties of layered ternary iron pnictide compounds. Two common layered crystal structures adopted by ternary pnictides are outlined below, and are illustrated in figure 1.4.

1.3.1 Compounds with the $ThCr_2Si_2$ structure type

The $ThCr_2Si_2$ structure is perhaps the most common structure adopted by ternary pnictide compounds and is well represented by compounds of other anions (especially silicides and germanides); there are currently over 600 known compounds of this structure type.[42] Compounds with this structure typically contain two types of cation: a large group 1, group 2 or rare-earth cation and a smaller transition metal cation. The transition metal cations form anti-PbO-type layers with the pnictide anions, and these layers are spaced apart by the the alkali metal cations which occupy cubic 8-coordinate inter-layer sites. The unit cell is body-centred tetragonal. There are few known compounds with the anti-type structure; Nd_2O_2Te is one rare example.[43]

There are many examples of compounds with this structure exhibiting ferromagnetic or antiferromagnetic order (e.g. $EuCo_2P_2$[44] and $CaCo_2P_2$[45] show FM and AFM order, respectively), and it was recently discovered that this structure is adopted by an important class of high-T_c superconductor,[46] exemplified by the solid solution $Ba_{1-x}K_xFe_2As_2$. Consequently, the majority of current research on $ThCr_2Si_2$-type compounds is focused on this area, and has very recently expanded to include the cation-deficient members $K_{1-x}Fe_{2-2x}Se_2$ which adopt a superstructure at ambient temperatures due to long-range ordering of Fe cations and vacancies within the anti-PbO-type layers.[47, 48]

1.3.2 Compounds with the PbFCl (or Cu_2Sb) structure type

The PbFCl structure is adopted by a diverse range of compounds which range from the highly ionic (such as BaFCl) to the predominantly covalent (such as Cu_2As), and is represented by both binary and ternary compounds. The anti-type structure is equally common. In all there are over 200 known compounds with this crystal structure.[49] The structure is related to that of $ThCr_2Si_2$, as it consists of (anti-) PbO-type layers separated by large inter-layer anions (or cations). However, in the PbFCl structure these inter-layer ions occupy a 5-coordinate square-pyramidal site, and as a result the

alignment of the PbO-type layers is different (by a translation $x + 1/2$, $y + 1/2$) to that in $ThCr_2Si_2$. The resulting tetragonal unit cell is primitive, rather than *I*-centred.

Alternatively, PbFCl may be thought of as an FCC-type array of Pb, with F occupying alternate layers of tetrahedral holes and Cl occupying all of the octahedral holes. The Cl ions are displaced from the centre of the octahedra due to repulsion of the ions in the tetrahedral sites, and this gives rise to their square-pyramidal coordination.

The PbFCl structure is also related to the ZrCuSiAs structure, which is obtained if the remaining tetrahedral holes are occupied (as illustrated in figure 1.4). Hence, the ZrCuSiAs structure is sometimes referred to as the "filled" PbFCl structure. The ternary iron arsenides LiFeAs and NaFeAs (which exhibit high temperature superconductivity) both take the anti-PbFCl structure, and much of the work presented in this thesis will focus on these two compounds.

1.4 Superconducting Materials

1.4.1 Discovery and early research

The phenomenon of low temperature superconductivity, whereby a material conducts electrical current with zero resistance and exhibits perfect diamagnetism, was first observed 100 years ago in 1911 by Heike Kamerlingh Onnes, three years after his successful condensation of helium. In a series of experiments designed to test contemporary theories of metals, Kamerlingh Onnes used liquid helium to conduct resistivity measurements on a sample of mercury, and found that the resistivity of this metal fell abruptly to zero below a critical temperature of 4.2 K.[50, 51] Furthermore, it was later shown to be possible to construct a superconducting circuit from tin or lead in which current continued to flow even after the external power supply had been removed.

Two decades later in 1933, Meissner and Ochsenfeld showed that the superconducting transition coincides with the complete expulsion of external magnetic

flux from the volume of the superconductor. Like the exhibition of zero resistivity, this onset of perfect diamagnetism (subsequently known as the Meissner effect) was found to be an intrinsic property of superconductors. These observations could not be explained by any of the contemporary theories of resistivity and magnetism in metals, and the phenomenon remained largely unexplained until the mid-1950s.

1.4.2 Bardeen-Cooper-Schrieffer theory and conventional superconductivity

By this time, a theory developed by the brothers F. and H. London had attempted to explain the Meissner effect in terms of superconducting electrons that are condensed into a single macroscopic quantum state; while the effect of isotopic enrichment on the superconducting transition temperature had suggested that lattice vibrations play a crucial rôle. These ideas formed the foundations of Bardeen-Cooper-Schrieffer (BCS) theory, which was published in 1957[52] (and awarded the Nobel Prize in Physics in 1972) and was found to explain all of the essential properties of the known superconductors: zero resistivity, the Meissner-Ochsenfeld effect and the isotope effect.

According to BCS theory, vibrations of the crystal lattice ("phonons") facilitate a small attractive interaction between conduction electrons near the Fermi level. Below the superconducting transition temperature, this attraction causes these electrons to condense into "Cooper pairs" with a corresponding energy gap opening at the Fermi level (which is equivalent to the energy required to break a Cooper pair). The formation of this gap stabilises the superconducting state relative to the normal state. The equation for this energy gap is used to derive an expression for the transition temperature:

$$k_B T_c = 1.13\hbar\omega_D \exp(-1/\lambda)$$

where $\hbar\omega_D$ is the Debye energy (the theoretical maximum phonon energy of the

crystal) and λ is the electron-phonon coupling constant. Therefore, large values of λ (i.e. strong electron-phonon coupling) and high frequency phonons are required to obtain the highest values of T_c. An important prediction of this theory is that superconductivity due to electron-phonon coupling is only feasible below temperatures of $30-40$ K.

Superconductors that obey the BCS theory (so-called "conventional" superconductors) include all of the superconducting elemental metals and alloys, and a few examples of more complex superconducting compounds discovered more recently, such as MgB_2 (which has a very high BCS T_c of 39 K). However, since the publication of this theory, several classes of superconducting compound have been discovered with very high transition temperatures and other properties that cannot be accounted for by BCS. Two of the principal families of non-BCS superconductors will be discussed in the following section.

1.4.3 High temperature superconductivity

Copper Oxides

In 1986, a report of superconductivity in a sample of composition $Ba_xLa_{5-x}Cu_5O_{5(3-y)}$[7] was remarkable not only because of the nature of the material (a perovskite-type oxide rather than a conventional metal or alloy) but due to a very high onset T_c of around 30 K, which at the time was by far the highest superconducting transition temperature ever observed. This discovery aroused a huge amount of interest, and was quickly followed by reports of superconductivity in $La_{2-x}Sr_xCuO_4$ [53] (which takes the layered K_2NiF_4 structure) and several other layered cuprate materials such as $YBa_2Cu_3O_{6+x}$ ($T_c \approx 93$ K),[54] the "2212" Bi-containing compound $Bi_2Sr_2CaCu_2O_8$ (85 K),[55] and the "2223" compounds $Bi_2Sr_2Ca_2Cu_3O_{10}$ (110 K)[56] and the Tl-containing analogue $Tl_2Ba_2Ca_2Cu_3O_{10}$ (125 K).[57] The highest known T_c currently stands at $\sim$ 133 K for the compound $HgBa_2Ca_2Cu_3O_{8+\delta}$.[58]

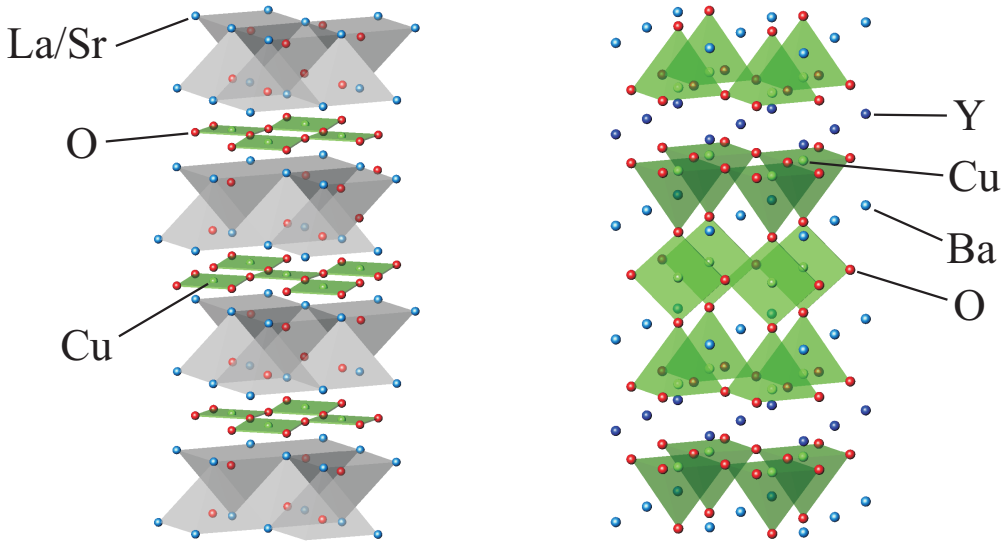


Figure 1.5: Structures of the cuprate superconductors $La_{2-x}Sr_xCuO_4$ (LHS) and orthorhombic $YBa_2Cu_3O_{6+x}$ (RHS), with their 2-dimensional CuO_2 sheets highlighted in green.

These materials all adopt layered perovskite-related crystal structures and all contain the common structural feature of 2-dimensional CuO_2 planes (formed by corner-sharing square-planar CuO_4 units) which are separated by different intermediate spacing layers. $La_{2-x}Sr_xCuO_4$ has arguably the simplest crystal structure in this class, and the copper oxide planes in this compound form 2-dimensional sheets that are widely separated by a lanthanum/strontium oxide layer. In contrast, YBCO has a more complex structure which contains 1-dimensional chains of corner-linked CuO_4 squares along the crystallographic *b*-direction, in addition to closely-spaced 2-dimensional CuO_2 sheets separated by yttrium ions. The anion vacancies between the parallel 1-D chains are able to host additional oxide ions. These two structures are illustrated in figure 1.5.

Most of the cuprates are stable over a range of oxide occupancies (e.g. in $YBa_2Cu_3O_{6+x}$ $0 \leq x \leq 1$) and others can be readily doped by aliovalent substitution (e.g. $La_{2-x}Sr_xCuO_4$). This high degree of compositional flexibility allows the superconducting and magnetic properties to be studied as a function of composition, and extensive phase diagrams have been determined for all of these compounds. A typical phase diagram is illustrated in figure 1.6. The phase diagrams of all

The material originally presented here is not currently available in ORA

Figure 1.6: Phase diagram for $YBa_2Cu_3O_{6+x}$, representing typical magnetic behaviour as a function of oxide content (i.e. on hole-doping). This figure is taken from reference [59].

of these materials have common features; all consist of a Mott-Hubbard insulating antiferromagnetically ordered region around a Cu valence of +2. These materials can be either hole-doped or electron-doped (which respectively correspond to formal oxidation or reduction of copper) to evade the Mott-Hubbard state, which yields metallic materials and ultimately leads to a non-magnetic superconducting region beyond some critical composition.

The extremely high T_cs of these materials cannot be explained within the framework of BCS theory, and the properties of the superconducting state differ in several ways from that which occurs in the conventional metals.[60] The Cooper pairing mechanism in cuprates is yet to be fully explained by theory, but is generally thought to be based on Cooper pairs formed by coupling to magnetic fluctuations, rather than BCS-type electron-phonon coupling.

Iron pnictides and chalcogenides

In 2008, a report of superconductivity below 26 K in $LaFeAsO_{1-x}F_x$[21] marked the unexpected discovery of a new family of high-T_c superconductors analogous to that

of the cuprates. Substitution of smaller lanthanides for La and tuning of the fluoride content rapidly led to the optimisation of T_c to 55 K in $SmFeAsO_{1-x}F_x$,[61] which is far above the BCS limit. $LaFeAsO_{1-x}F_x$ takes the ZrCuSiAs structure and contains anti-PbO-type FeAs layers. As discussed in section 1.2, the anti-PbO-type layer is a structural fragment common to many crystal structures, and in the wake of this exciting discovery suddenly the race was on to synthesise new (and old) materials containing FeAs layers, which could potentially exhibit extremely high T_c values.

Superconductivity was soon reported in several structure types with a variety of transition temperatures, but none exceeded 55 K. The principal members of this new superconducting family are illustrated together in figure 1.7 and include $Ba_{1-x}K_xFe_2As_2$[46] ($T_c = 38$ K) which takes the $ThCr_2Si_2$ structure; tetragonal FeSe [62] which takes the anti-PbO structure with a vacant inter-layer space; LiFeAs [63, 64] which takes the anti-PbFCl structure ($T_c = 17$ K); and some structurally more complex materials such as Sr_2VO_3FeAs ($T_c = 37$ K)[65] with perovskite-related oxide spacing layers. Several close structural relatives of Sr_2VO_3FeAs are also known but not all exhibit superconductivity.[29, 30]

The Fe-based superconductors have much in common with the cuprate superconductors. The non-doped "parent" materials with a formal oxidation state of +2 for Fe are generally poor metals[66] and take layered tetragonal crystal structures at ambient temperature. On cooling, they exhibit an orthorhombic distortion, which coincides with antiferromagnetic ordering of the small ($< 1\ \mu_B$) Fe moments. Magnetic phase diagrams for several of these compounds are shown in figure 1.8.

There are several ways to realise superconductivity in Fe-pnictides, as the compositional flexibility of their structures offers several options for modification. The parent materials may be electron-doped (e.g. $LaFeAsO_{1-x}F_x$)[21] or hole-doped (e.g. $Ba_{1-x}K_xFe_2As_2$).[46] In some cases it is also possible to induce superconductivity through the application of non-hydrostatic pressure (e.g. in $CaFe_2As_2$).[70, 71, 72] Inspection of the phase diagrams of several systems generally shows that, as the systems are doped towards the superconducting regime, the structural and

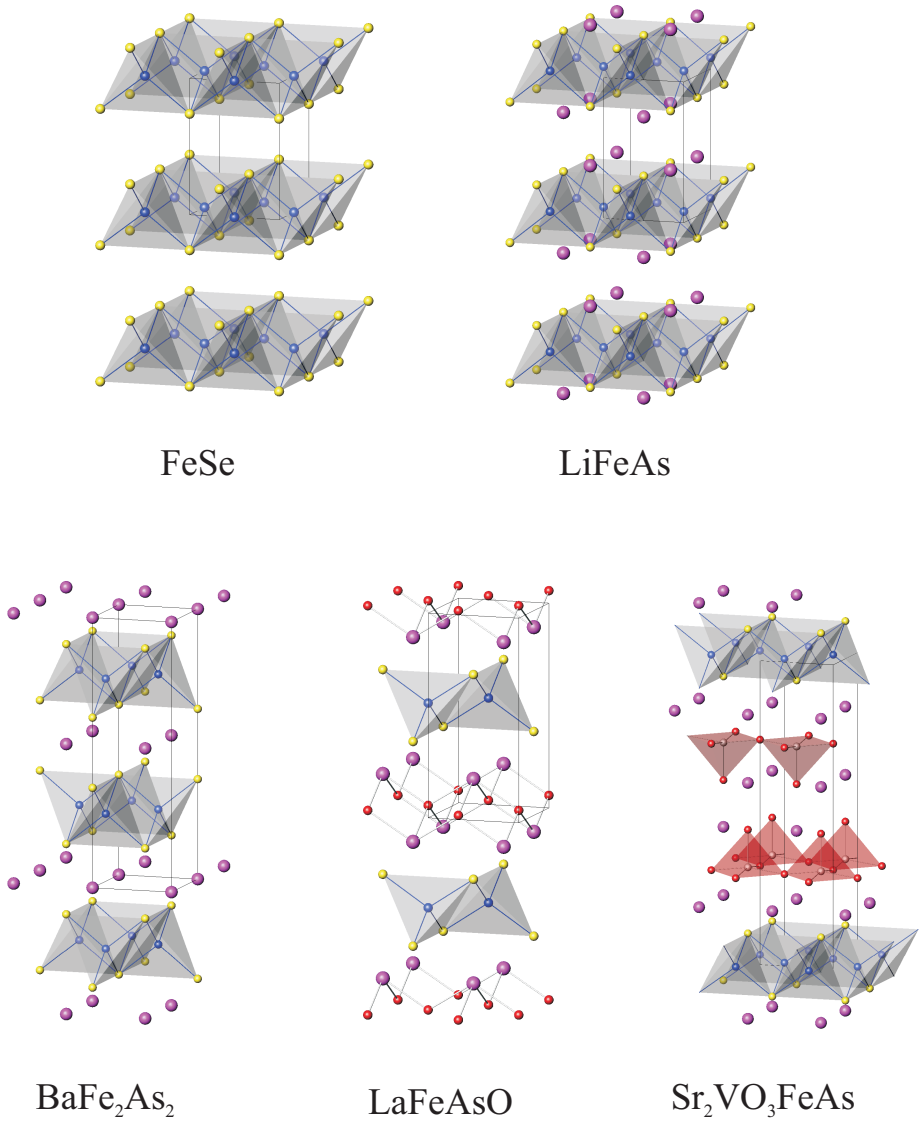
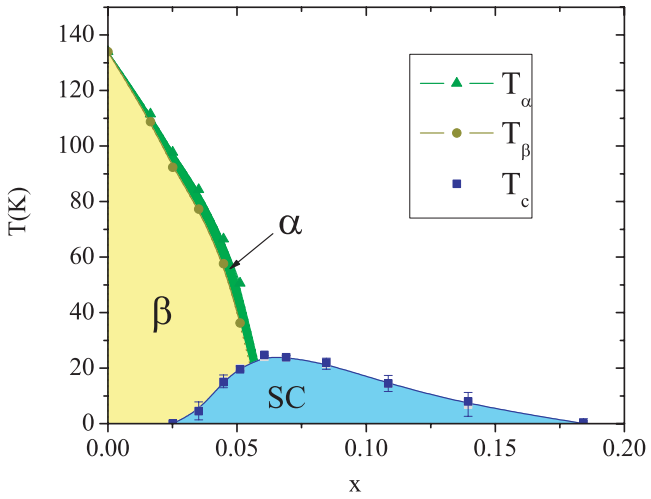
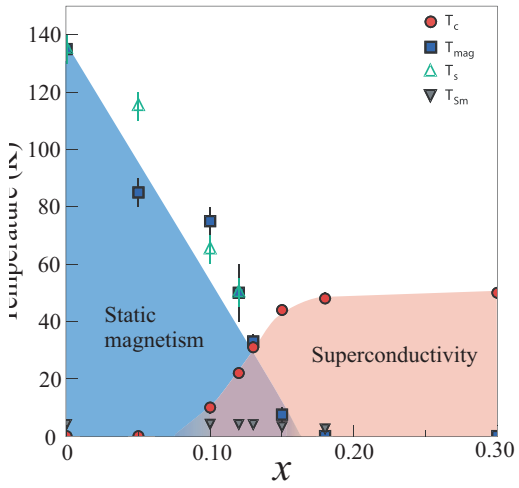


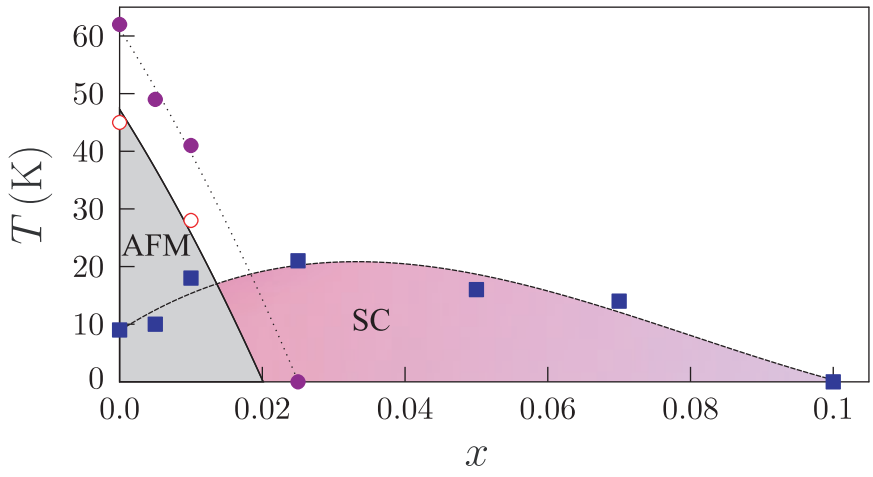
Figure 1.7: The five principal crystal structure types of the Fe-based superconductors. The grey shaded tetrahedra represent the anti-fluorite-type FeAs layers. Black outlines indicate the unit cells.



(a) $BaFe_{2-x}Co_xAs_2$[67]



(b) $SmFeAsO_{1-x}F_x$[68]



(c) $NaFe_{1-x}Co_xAs$[69]

Figure 1.8: Magnetic phase diagrams showing the effect of electron-doping on the magnetic/superconducting behaviour of three different Fe-based superconductors.

antiferromagnetic transition temperatures are reduced and become inequivalent, with T_N occurring at the slightly lower temperature. There is then a small region where antiferromagnetism and superconductivity appear to coincide, before the system enters the fully superconducting domain.

It is clear from comparison with the phase diagrams of the cuprates (figures 1.6 and 1.8) that the behaviour of the cuprates and the Fe-pnictides is qualitatively similar; in both cases magnetic order must be suppressed before superconductivity emerges. This type of behaviour has also been recognised in a wide range of other unconventional superconductors.[73] However, unlike in the cuprates, there appears to be a significant overlap between the superconducting and antiferromagnetic domains in Fe-based superconductors (see figure 1.8). The true nature of this co-existence (i.e. the question of whether this is due to intrinsic sample inhomogeneity with different domains supporting either superconductivity or AFM; or whether it is due to microscopic co-existence of superconductivity *and* AFM in the same domain) is a highly topical issue in condensed matter physics.

1.5 Common Magnetic Phenomena

1.5.1 Diamagnetism and Paramagnetism

The dimensionless magnetic susceptibility χ_{vol} is defined in terms of sample magnetisation M and applied magnetic field H:

$$\chi_{vol} = \frac{M}{H}$$

A material can be classified as diamagnetic or paramagnetic according to the response of its magnetic susceptibility to an externally applied magnetic field. A diamagnetic material has a negative magnetic susceptibility (and is therefore repelled by the source of the magnetic field) while a paramagnetic material has a positive magnetic susceptibility (and is attracted by the source of a magnetic field).

Diamagnetism can be explained classically by the action of a magnetic field on the orbital motion of an electron, which induces a small current and generates an opposing magnetic field, as described by Lenz's law. This is generally temperature independent. A diamagnetic response to an applied field is intrinsic to all materials, although it is generally several orders of magnitude weaker than Curie and Curie-Weiss type paramagnetism (described below) and is overwhelmed in these types of materials. Consequently, diamagnetism is most commonly observed in non-metallic materials with no un-paired electrons.

A material may be paramagnetic if it contains electrons with un-paired spins. The un-paired spins align parallel to an applied field, increasing the flux-density within the sample, which corresponds to a positive magnetisation. Paramagnets may be molecular materials (such as O_2 or organic radical species) or extended solids. Paramagnetic materials can be further classified according to whether the un-paired electrons are localised or itinerant.

In most molecular paramagnets and extended solids with localised un-paired electrons, magnetic susceptibility is found to obey the Curie Law, which is valid for an array of non-interacting spins:

$$\chi_{mol} = \frac{C_{mol}}{T} \tag{1.1}$$

In this situation, magnetic susceptibility is inversely proportional to temperature. The proportionality constant C_{mol}, known as the Curie constant, is given by:

$$C_{mol} = \frac{N_A \mu_{eff}^2 \mu_B^2}{3k_B} \tag{1.2}$$

Evaluation of the Curie constant from a plot of $1/\chi$ against T can be used to experimentally determine the value of the effective magnetic moment μ_{eff} for a given paramagnetic material, as it follows from equation 1.2 that $\mu_{eff} \simeq 2.84\sqrt{C}$. The effective magnetic moment is itself a function of the total angular momentum of the paramagnetic species, given by:

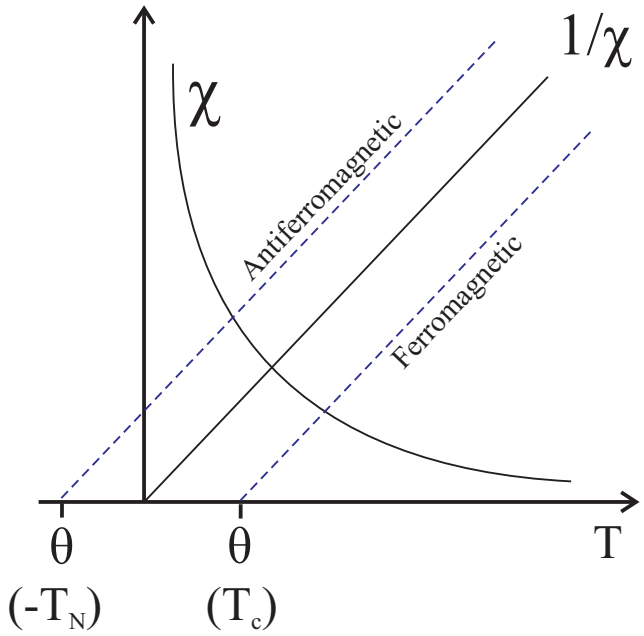


Figure 1.9: Variation of magnetic susceptibility (χ) and its reciprocal ($1/\chi$) with T for Curie paramagnets (black line) and Cure-Weiss paramagnets (blue dashed lines).

$$\mu_{eff} = g\sqrt{J(J+1)} \tag{1.3}$$

where J ($= L+S$) represents total angular momentum and g is the Landé g-factor:

$$g = 1 + \frac{J(J+1)+S(S+1)-L(L+1)}{2J(J+1)} \tag{1.4}$$

In compounds of the lanthanides, in which the $4f$ orbitals barely participate in covalent bonding, these formulae can be used directly to calculate reliable expectation values for μ_{eff}. In compounds of the transition metals, ligand field effects lift the degeneracy of the d orbitals and (to a first approximation) quench their associated orbital angular momentum. Hence, the conditions $L = 0$ and $J = S$ can be applied to equations 1.3 and 1.4 to yield the *spin-only* formula for the effective magnetic moment:

$$\mu_{s.o.} = 2\sqrt{S(S+1)} \tag{1.5}$$

For paramagnetic materials with interacting spins (which may have a tendency to exhibit ferromagnetic or antiferromagnetic order at low temperatures), the magnetic

susceptibility is better described by the Curie-Weiss law (equation 1.6 below, and illustrated in figure 1.9). Under these conditions, T is replaced by an effective temperature $(T-\theta)$, where θ is the empirical "Weiss temperature". The sign and magnitude of θ is dependent on the interaction between the spins. If $\theta > 0$, the interactions are predominantly ferromagnetic. For Curie-Weiss paramagnets that do exhibit low-T ferromagnetic order, the value of θ is expected to be close to the Curie temperature T_c. Similarly if $\theta < 0$ the interactions are predominantly antiferromagnetic, and for materials that order antiferromagnetically $\mid \theta \mid$ is expected to be close to the Néel temperature T_N. In Curie-Weiss paramagnets, the Curie constant is generally only evaluated at temperatures much greater than the Weiss temperature.

$$\chi_{mol} = \frac{C_{mol}}{T-\theta} \tag{1.6}$$

In contrast, paramagnetism in materials with itinerant electrons (i.e. metals) is not temperature dependent. These metallic materials exhibit Pauli paramagnetism, which arises in the conduction band due to the loss of degeneracy of the spin-up and spin-down electron states in an applied magnetic field. The lower-energy spin-state is preferentially occupied so that the population of spin-up and spin-down electrons is no longer equal. This leaves a positive net magnetisation which is proportional to the density of states at the Fermi level. Pauli paramagnetism is usually of similar magnitude to diamagnetism and generally several orders of magnitude weaker than Curie paramagnetism because only electrons near the Fermi energy can contribute. For example, metallic copper has a broad conduction band resulting in a relatively low density of states at the Fermi level, and therefore the Pauli paramagnetism is weaker than the intrinsic diamagnetic response, resulting in very weak net diamagnetism.

1.5.2 Ferromagnetism and Antiferromagnetism

While Curie and Curie-Weiss paramagnets consist of a dilute array of non-interacting (or weakly-interacting) spins and may be in the solid, liquid or gas phase, many solid

compounds that consist of a more concentrated array of strongly-interacting spins can exhibit long range ferromagnetic or antiferromagnetic order below some critical temperature.

In a ferromagnet, the un-paired spins spontaneously align parallel to one another below a critical temperature (known as the Curie temperature, T_c) to form a domain structure. These ordered domains may, in turn, be oriented parallel to an applied magnetic field to give an overall positive magnetisation for the material. This corresponds to a significant increase in magnetisation as the material is cooled through the Curie temperature, which then saturates as all of the domains become co-aligned (as illustrated in figure 1.10). Above the Curie temperature, the material reverts back to paramagnetism.

In contrast to Curie-Weiss paramagnets most ferromagnets are metallic, as the most common ferromagnetic-coupling interactions are double-exchange and the long-range RKKY interaction (also known as "itinerant exchange"). In double-exchange ferromagnets such as $La_{1-x}Sr_xMnO_3$, mixed-valency metal centres are aligned with parallel spins, which allows electron-hopping between them with no flipping of spins. This energetically-favourable electron-hopping is the reason for their metallic conductivity and the stability of the ferromagnetic state, and consequently the onset of double-exchange ferromagnetic ordering is sometimes associated with an insulator to metal transition (for example in $La_{0.75}Ca_{0.25}MnO_3$).[74]

The RKKY interaction is important in metallic compounds which also contain localised electrons; these localised spins can be coupled by the polarisation of conduction electrons. This interaction can be ferromagnetic or antiferromagnetic (depending on the distance between interacting moments). Perhaps the most familiar metallic ferromagnetic materials are the transition metals Fe, Co and Ni. In these metals, the electronic ground state is spin-polarised, as the narrow 3d bands (and correspondingly high density of states at the Fermi level) make it energetically favourable to accommodate un-paired electrons at higher energy levels, rather than pairing the spins.

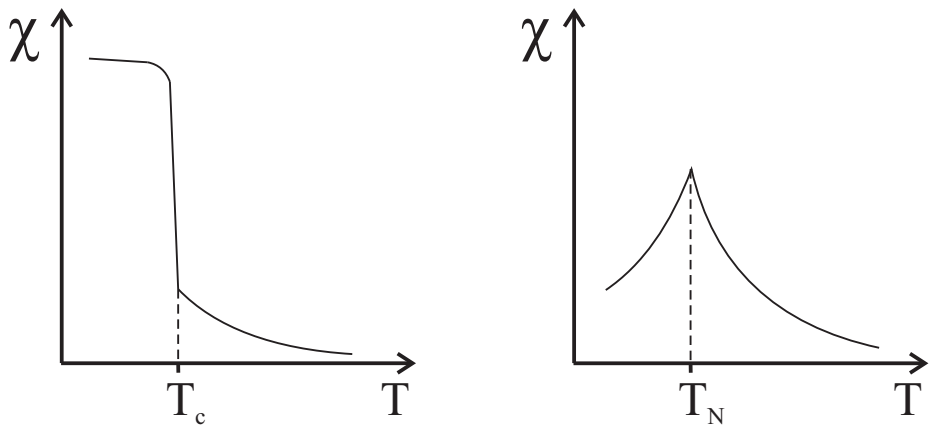


Figure 1.10: The general behaviour of magnetic susceptibility (χ) with temperature in a ferromagnetic (LHS) and antiferromagnetic material (RHS). T_c and T_N denote the Curie and Néel temperature, respectively.

Antiferromagnetism is the most common form of long-range magnetic ordering in solids. Below the critical Néel temperature T_N, neighbouring interacting spins align antiparallel to one another, resulting in a decrease in magnetic susceptibility (which becomes extremely small as $T \rightarrow 0$). Above T_N , the thermal energy overcomes the spin-spin coupling and the material reverts to paramagnetism. Antiferromagnetic interactions generally arise through the superexchange and double-exchange mechanisms. The superexchange mechanism is an interaction between two non-neighbouring magnetic ions that is mediated by a non-magnetic ion (e.g. an oxide or fluoride ion) which lies between them. Most antiferromagnets order only at low temperatures (i.e. < 298 K), but there are a few examples of very high Néel temperatures such as 953 K in hexagonal α-Fe_2O_3.[75]

An unusual form of antiferromagnetic order can occur when the magnitudes of the ordered moments are not uniform, which gives rise to a strong increase in magnetisation below T_N, which is superficially similar to ferromagnetism. This is known as ferrimagnetism, and commonly occurs in mixed-valence compounds such as Fe_3O_4.

It is also possible for antiferromagnetic and ferromagnetic interactions to be present in the same material, and certain materials may be driven from antiferromagnetic order to ferromagnetic order by the presence of an external field. This behaviour

(known as metamagnetism) has been studied most extensively in $FeCl_2$[76] (which takes the layered $CdCl_2$ structure), but is also known, for example, in a series of layered oxychalcogenides in which inter-layer antiferromagnetic interactions compete with intra-layer ferromagnetism (previously discussed in section 1.2).[26]

1.6 Aims of this work

The research described in this thesis will focus on two materials, CeCuOS and LiFeAs (and some of their derivatives), that are structurally related but have drastically different physical properties.

The oxysulfide $CeCu_{1-x}OS$, which takes the layered ZrCuSiAs structure, is a somewhat enigmatic member of the series *Ln*CuOS (*Ln* = La-Eu or Bi). This series of fully stoichiometric compounds shows generally well-behaved trends in structural parameters and physical properties, yet several reports of the properties of CeCuOS show that this compound has anomalously small unit cell parameters and an effective magnetic moment which is significantly diminished from the free-ion value for Ce^{3+}. A comprehensive early report suggested that the material might be intrinsically deficient in Cu due to partial oxidation of Ce^{3+},[40] and later work confirmed that this is the case in a sample of stoichiometry $CeCu_{0.8}OS$.[34]

However, work by C. F. Smura found that it is possible to prepare nominally stoichiometric CeCuOS which has similar characteristics to other *Ln*CuOS compounds; its lattice parameters are non-anomalous (i.e. comparable to those expected from the lanthanide contraction) and it is green/brown in colour.[77] This material was found to be strongly air-sensitive, turning black on exposure to moist air with a small contraction of the lattice parameters - a process that could be reversed by heating under a reducing atmosphere. A preliminary investigation [41] was unable to determine a compositional difference between the green and black materials. The first section of Chapter 3 presents a detailed comparison of the compositions of these two phases using neutron powder diffraction techniques and SQUID magnetometry,

and investigates an alternative synthetic route to fully stoichiometric CeCuOS based on these findings.

Several layered oxysulfides with Cu-deficient CuS layers are known to exhibit long-range ordering of Cu ions and vacancies at low temperatures. This phenomenon has not yet been observed in a ZrCuSiAs-type material, but the possibility of variable Cu occupancy in $CeCu_{1-x}OS$ means there is potential for it to occur in this system. The second section of Chapter 3 investigates the occurrence of this type of structural ordering in a sample of $CeCu_{0.8}OS$ by high-resolution powder X-ray diffraction, including the solution of the low-T superstructure.

The layered iron arsenide LiFeAs, which takes the layered anti-PbFCl structure with anti-PbO-type FeAs layers separated by Li^+ cations, is a member of the recently discovered family of high-temperature Fe-based superconductors. Although first synthesised in 1968,[78] superconductivity was only reported in this material very recently.[63, 64, 79] The first section of Chapter 4 describes an initial detailed characterisation of this material by neutron powder diffraction, with the aim of establishing the true location of the Li^+ ion in this compound (a question which could not be answered satisfactorily in the original report)[78] and establishing its basic superconducting properties. The later part of this chapter then investigates the response of superconductivity to small changes in stoichiometry of type $Li_{1-y}Fe_{1+y}As$ (where $y < 0.05$), using a combination of neutron and X-ray powder diffraction with SQUID magnetometry. This type of non-stoichiometric composition is uncommon in the Fe-based superconductors and is shared only by $Fe_{1+y}Ch$.

A significant amount of recent research concerns the effects of doping on superconductivity in compounds of type $BaFe_2As_2$ and LaFeAsO by substituting a small amount of Co or Ni for Fe, which has been shown to have strong effects on the magnetic and superconducting properties and can be used to tune materials between the superconducting or antiferromagnetic regimes. Chapter 5 extends this to the investigation $LiFe_{1-x}Co_xAs$ and $LiFe_{1-x}Ni_xAs$, with the intention of mapping out a magnetic/superconducting phase diagram for transition-metal-doped LiFeAs and

comparing this with other systems. These materials are characterised by neutron and/or X-ray powder diffraction, with SQUID magnetometry and muon-spin rotation spectroscopy to investigate superconducting properties.

Finally, the response of the structures and superconducting properties of LiFeAs and its isostructural sodium analogue NaFeAs to high pressures are investigated in Chapter 6. This follows several studies suggesting that certain structural parameters (such as the regularity of the $FeAs_4$ tetrahedron) have a significant influence on the observed superconducting transition temperature. High-pressure studies on similar systems have shown that T_c can be strongly influenced by applied pressure, and in some cases these materials undergo a phase transition (e.g. the transition to a "collapsed" tetragonal phase in $CaFe_2As_2$).[80] This work is intended to establish the effect of structural changes on the superconductivity of these materials by using high-pressure X-ray and neutron powder diffraction coupled with high-pressure SQUID magnetometry (which was conducted by Dr. Masaki Mito of the Kyushu Institute of Technology, Japan). A previously unknown high-pressure phase of NaFeAs is also investigated.

Chapter 2

Experimental Techniques

2.1 Synthetic Methods

2.1.1 Solid-state synthesis

The most common method of solid-state synthesis is the ceramic method. First, precise stoichiometric amounts of powdered starting materials are weighed out and ground together using a pestle and mortar (usually made from a very hard mineral such as agate). Grinding ensures that reagent grains are intimately mixed throughout the sample and reduces the size of the grains, maximising their surface area to substantially increase the reaction rate. The ground reaction mixture is commonly pressed to form a pellet, which maximises the surface contact between reagent grains and enhances the reaction rate. Finally, the powder or pellet is heated to very high temperatures (typically in the range 600-1500°C) for several hours or days to overcome the high kinetic barrier to reaction, allowing the thermodynamically favoured product to form.

For the synthesis of non air-stable compounds (or syntheses involving non air-stable mixtures) it is important to heat the mixture under inert conditions. This is sometimes achieved by heating under a flow of inert gas such as nitrogen or argon (especially if the mixture contains volatile components such as decomposing carbonates or nitrates), but for non-volatile mixtures it is more effective to seal the

reaction inside an evacuated silica ampoule. Such an ampoule can be heated to temperatures of up to ~1200°C. If the reaction is particularly sensitive to the presence of moisture, the silica can be pre-baked at the reaction temperature to eliminate adsorbed H_2O (e.g. the homologous series $Sr_2MnO_2Cu_{2m-\delta}S_{m+1}$ [26] requires this treatment).

For reactions involving volatile metals (such as alkali metals or the alkaline earths) an evacuated silica tube is generally not suitable, as a high internal pressure of corrosive metal vapour (which may react with the ampoule) presents an explosion hazard. For such reactions it is far safer and more effective to seal the reaction mixture inside an ampoule of suitably inert metal. The early second- and third-row transition metals niobium, tantalum, molybdenum and tungsten are well suited to this application due to their extremely high melting points. Ampoules of the ductile metals Nb and Ta may be prepared by crimping the end of the loaded tube and sealing under an argon atmosphere using arc-welding apparatus. A welded ampoule of this type can withstand internal pressures of several bar, and can provide a suitably inert environment for the reaction (although in some cases an inert alumina liner must be used). The metal ampoule must then be sealed inside an evacuated silica tube to avoid catastrophic corrosion by atmospheric oxygen, which occurs very rapidly at typical reaction temperatures.

2.1.2 Argon-filled dry box

All samples and air-sensitive reagents were stored and handled in a Glove Box Technology argon-filled dry box, with argon recirculated through a BASF copper catalyser and molecular sieve bed to remove O_2 and H_2O respectively. The O_2 concentration is monitored by an integrated O_2 sensor, and is kept below 5ppm under normal working conditions. Atmosphere quality is also checked periodically by observing the oxidation of a freshly-cut piece of sodium metal: such a piece will remain shiny for at least 30 minutes if the atmosphere is clean.

The material originally presented here is not currently available in ORA

Figure 2.1: (From reference [82]). Schematic diagram of the CS_2 gas flow apparatus used to synthesise $CeCuS_2$. Argon is bubbled through liquid CS_2 and flows over the reaction mixture, which is contained in an alumina boat inside a long silica tube. A split tube furnace is used to heat the reaction to 950 °C for 4-5 hours. The sulfur vapour produced by the reaction condenses on the cool end of the tube, and unreacted CS_2 vapour is destroyed by bubbling through bleach and potassium permanganate solution.

2.1.3 Synthesis of starting materials

The following materials are not commercially available and were synthesised as follows:

Preparation of $CeCuS_2$

The ternary sulfide $CeCuS_2$ was used as a starting reagent in the synthesis of $CeCu_{(1-x)}OS$ and its derivatives. The compound was first described by C. F. Smura [77, 81] following an attempt to synthesise CeCuOS directly by a reactive gas flow. The gas-flow apparatus are illustrated in figure 2.1. There are two ways to synthesise the compound, both utilising the same gas-flow method but with slightly different starting reagents. In the original report, stoichiometric quantities of Cu_2S and CeO_2 were ground together and heated to 900 °C under a flow of CS_2vapour. One minor drawback of this method is that it requires the prior synthesis of Cu_2S from the elements. The second method simply replaces Cu_2S with CuO as a starting reagent, and uses a slightly higher reaction temperature of 950°C. Both methods require 2-3 cycles of grinding and heating before a phase-pure product is obtained.

Preparation of FeAs

FeAs was prepared by a ceramic method using a mixture of Fe powder (Alfa, 99.998%) and pre-ground As powder (Alfa, 99.9999%). The mixture was sealed in an evacuated silica tube and heated to 500 °C at a slow rate (1 °C/min) to avoid building up a significant partial pressure of As vapour. The reaction was then kept at 500°C for 3 days and cooled radiatively to room temperature.

Preparation of Li_3As

This highly air-sensitive material was prepared from pre-ground As powder (Alfa, 99.9999%) and Li pieces (Aldrich, 99.9%), sealed in a niobium tube under flowing argon (as described in section 2.1.1), then heated to 220 °C for 16 hours to allow all of the Li metal to react. This results in a crystalline mixture of Li_3As and LiAs, which is ground and pelletised, then sealed in a fresh niobium tube and heated to 750°C for 24 hours to yield phase-pure Li_3As.

2.2 Analytical Methods

2.2.1 Crystal Symmetry and Diffraction

A crystal structure is constructed from a 3-dimensional lattice which is decorated with a repeating structural motif (a unique unit of atoms or molecules). The lattice can be classified by selecting points to form a parallelepiped, defining the *unit cell*, with edges of length *a, b, c,* and angles of α, β, γ between them. The values of these unit cell parameters define the *crystal system*. In the case where $a \neq b \neq c$ and $\alpha \neq \beta \neq \gamma$, the lattice has intrinsic translational symmetry and may have inversion symmetry, but has no rotational axes or mirror planes. Such a lattice is described as a "triclinic" system and must be defined with six unique lattice parameters. At the other extreme, the "cubic" system has the highest number of non-translational symmetry elements (i.e. rotational axes and mirror planes) and is defined by only two unique lattice parameters

$a\,(=b,c)$ and $\alpha\,(=\beta=\gamma=90^o)$. There are seven crystal systems in total.

The unit cell may contain just a single lattice point, in which case the lattice is described as *primitive*, and given the space-group symbol *P*. However, it is sometimes necessary to define a unit cell that incorporates more than one lattice point, and such a cell is described as *centred*. The second step in classifying the lattice is to identify this centring, and combine it with the crystal system to obtain the Bravais lattice type.

If the two lattice points are related by a translation of $x+1/2$, $y+1/2$, $z+1/2$, the lattice is *body centred* (space-group symbol *I*). There are two types of *face centred* lattice where lattice points are related by a $x+1/2$, $y+1/2$ translation: with a lattice point in the centre of each unit cell face *(F),* or with lattice points on only two opposing faces *(A, B, C).* These centring types are not compatible with all of the crystal systems due to symmetry constraints (e.g. only orthorhombic, tetragonal and cubic systems may be *I*-centred), so when combined with the seven possible lattice systems they present a total of 14 possible Bravais lattices. The Bravais lattice type is used in combination with the internal symmetry operators for the unit cell to define one of the 230 unique *space groups* for the crystal.

The extended translational symmetry in crystals allows diffraction methods to be used as powerful tools for structural determination, as outlined in the following sections.

2.2.2 Diffraction of X-rays

The diffraction of X-rays by a crystal is the foundation of the most common type of crystallography. When a beam of X-ray radiation propagates through a crystal, several processes occur that cause a loss of intensity. One is fluorescence, where photons are absorbed by ionising core electrons and secondary photons are emitted in random directions as the resulting ions relax to their ground state. In a diffraction experiment, fluorescence contributes to the background signal and can be minimised by using X-rays of an appropriate wavelength.

Another significant process is scattering by electrons, which occurs via the Coulombic interaction of the electron with the oscillating electric field of the X-ray. Scattering processes can be elastic or inelastic. If the scattering is elastic, the scattering electron acts as a secondary source of radiation by emitting an electromagnetic wave with the same frequency as the incident photon. This process gives rise to the Bragg scattering that is used for crystallography. Alternatively, the scattering electron may absorb a small amount of energy from the incident photon (particularly if the electron is "free" or loosely bound to its atom, as in a metal), and the scattering process is then inelastic. This process is not useful for diffraction experiments but is always observed as a component of the background signal.

The first theory of the diffraction of X-rays by crystals was developed by von Laue in the early 20th century. He considered the crystal as a three dimensional lattice with rows of regularly spaced atoms, but the theory can be illustrated by a one dimensional lattice (see figure 2.2). Here, a parallel monochromatic beam of X-rays is incident upon a row of regularly-spaced atoms. Each atom in the row acts as a point scatterer - a secondary source of monochromatic X-rays with a spherical wavefront. Interference then occurs between these scattered beams, and maximum constructive interference will occur when the path lengths differ by an integer number (n) of wavelengths (λ) such that:

$$AB - CD = a(\cos\theta_i - \cos\theta_d) = n\lambda \tag{2.1}$$

This is the first Laue equation and is valid for a one-dimensional system. A real crystal is a three-dimensional system with three Laue equations, corresponding to each orthogonal *x, y, z* axis, which must be satisfied simultaneously for constructive interference to occur.

Although the Laue equations provide a rigorous description of X-ray diffraction, their solution involves the determination of up to 12 variables. This complexity limits their usage in practical crystallography. An alternative formulation, proposed by W. L.

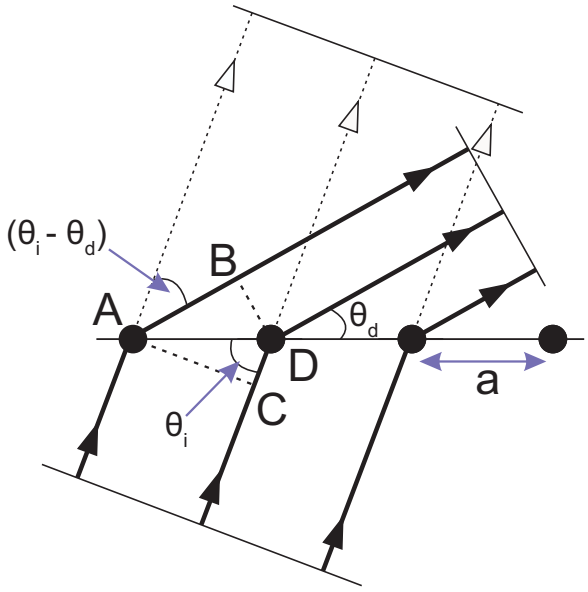


Figure 2.2: Schematic diagram illustrating Laue scattering of monochromatic radiation from a single source by a one-dimensional lattice. The labelled distances and points are used to construct the first Laue equation (equation 2.1).

Bragg, considers diffraction arising from "reflection" of X-rays from planes within a crystal, known as Miller planes. These planes are defined by three indices h, k and l, which intersect the unit cell axes at $\frac{a}{h}$, $\frac{b}{k}$ and $\frac{c}{l}$ respectively.

According to this picture (illustrated in figure 2.3), constructive interference will occur when the difference in path lengths $(B'C - BC)$ is equal to an integer number of wavelengths, $n\lambda$. From the figure it can be seen that:

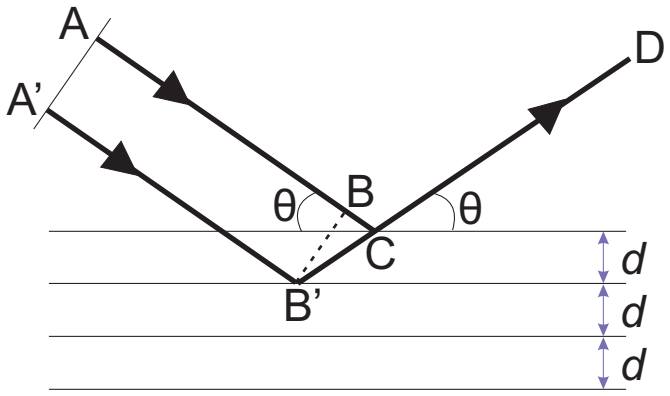


Figure 2.3: Bragg reflection of monochromatic incident radiation (from a single source) from regularly-spaced planes of atoms. The labelled distances and points are used to construct the Bragg equation (equation 2.5).

$$B'C = \frac{d_{hkl}}{\sin\theta} \tag{2.2}$$

and

$$BC = (B'C)\cos 2\theta \tag{2.3}$$

therefore for maximum constructive interference we must have:

$$\frac{d_{hkl}}{\sin\theta} - \frac{d_{hkl}\cos 2\theta}{\sin\theta} = n\lambda \tag{2.4}$$

which simplifies to

$$2d_{hkl}\sin\theta = n\lambda \tag{2.5}$$

Equation 2.5 is the *Bragg equation*. This neatly relates d-spacing to the diffracted angle for a beam of given wavelength. Therefore, if a monochromatic beam of X-rays is incident upon a crystal, and the diffracted intensity is monitored using θ as a variable, a diffracted beam is only observed at discrete values of θ that are dependent on d_{hkl}, the spacing of the diffracting planes (which is determined by the lattice parameters of the crystal). Alternatively, θ may be fixed and λ used as the variable to obtain the same information. By assigning Miller indices to each observed reflection (a process known as *indexing* the pattern) it is possible to identify the crystal system, while systematic absences (caused by translational symmetry within the unit cell) indicate the presence of lattice centring, thus the Bravais lattice type may be deduced.

The information derived from a diffraction experiment using Bragg's Law is of fundamental importance, but it falls short of describing the actual arrangement of atoms in a real crystal. To complete the picture, the intensity of each reflection must be considered. For a perfect crystal, intensity I_{hkl} depends on the following equation:

$$I_{hkl} = sLp \mid F_{hkl} \mid^2 \tag{2.6}$$

where s is a scale factor (accounting for factors such as data acquisition time); L is the Lorentz factor (dependent on instrument geometry); p is the polarisation correction. F_{hkl} is the "structure factor", and is dependent on the structure of the crystal. This factor dominates the equation so it can be considered that:

$$I_{hkl} \propto | F_{hkl} |^2$$

The structure factor describes the effects of a number of crystal characteristics, and is defined by the complex expression:

$$F_{hkl} = \sum_{n=1}^{N} f_n(\theta) \exp\left[2\pi i(hx_n + ky_n + lz_n)\right] .q \tag{2.7}$$

Equation 2.7 is valid for a crystal of general symmetry. Here, $f_n(\theta)$ is the *atomic form factor*, which is the θ-dependent scattering amplitude of atom n. The co-ordinates of atom n are given by x_n, y_n, z_n; and q is the temperature-dependent *Debye-Waller factor*. If the crystal is centrosymmetric with identical atoms at (x,y,z) and $-(x,y,z)$, the expression can be simplified by separating the real and imaginary components to give:

$$F_{hkl} = \sum_{n=1}^{N} f_n(\theta) \left[\cos 2\pi(hx_n + ky_n + lz_n)\right] .q + \sum_{n=1}^{N} f_n(\theta) \left[\sin 2\pi(hx_n + ky_n + lz_n)\right] .q \tag{2.8}$$

Using the identity $\sin(-x) = -\sin(x)$ then leaves F_{hkl} as a real number:

$$F_{hkl} = \sum_{n=1}^{N} f_n(\theta) \left[\cos 2\pi(hx_n + ky_n + lz_n)\right] .q \tag{2.9}$$

In principle, if the scattering amplitudes of the constituent atoms are known, the intensity of the observed Bragg reflections can be used to derive the co-ordinates of atoms within the unit cell, to give a full description of the crystal structure.

X-rays are scattered by electrons, and therefore the atomic form factor, $f_n(\theta)$, is proportional to the electron count (Z) of the scattering atom. Consequently, heavy

elements are the strongest scatterers of X-rays. The θ-dependence arises from the finite separation of electrons within the scattering atom: the atomic radius is of the order of 1 Å, so two photons scattered from different regions of the same atom will emerge with slightly different path lengths, introducing a small degree of destructive interference which increases with θ. More precisely, the form factor is the Fourier transform of the spatial distribution of the scattering object, and therefore $f_n(\theta)$ follows a Gaussian for X-rays and a flat line for neutrons (which are scattered from points).

The Debye-Waller factor, q, models the temperature-dependent vibrations of the atoms about their equilibrium positions. As temperature increases, atoms exist at a greater average distance from their equilibrium positions. This can be considered as an increase in the effective sizes of the atoms, and causes observed intensities to decrease more rapidly with increasing θ. For simple isotropic thermal motion of this kind, q_{iso} is given by equation 2.10, where $B_{iso} = 8\pi^2 U_{iso}$[83] (and both B_{iso} and U_{iso} are experimentally-determined isotropic temperature factors).

$$q_{iso} = \exp\left(\frac{-B_{iso}\sin^2\theta}{\lambda^2}\right) \tag{2.10}$$

Evaluation of the structure factor is the key to solving a crystal structure by diffraction methods, but because the observed intensity of a reflection is proportional to F_{hkl}^2, only the amplitude of F_{hkl} can be observed and its phase remains unknown. This is a fundamental problem and is generally overcome with computational power (e.g. the "Patterson methods", "direct methods" or charge-flipping methods that are commonly used in single-crystal diffraction experiments).[84] In a powder diffraction experiment, the problem is generally side-stepped by using the Rietveld refinement technique (see section 2.2.5 on page 39), but this requires an accurate starting model and is not considered to be a structural solution technique.

2.2.3 Diffraction of Neutrons

Particles possess wave-like characteristics as described by the de Broglie relationship ($\lambda = h/p$, where p is momentum and h the Planck constant). Consequently, neutrons can be diffracted by a crystal if they have an appropriate energy. This type of diffraction is described by the same equations that govern X-ray diffraction (see section 2.2) but the scattering mechanism is quite different, as neutrons are scattered by atomic nuclei via the nuclear force. The nuclear force acts at a range of 10^{-15}m, compared to a typical incident wavelength of 10^{-10}m, so the scattering objects for neutron diffraction are extremely small and the atomic form factors are essentially independent of the incident angle (θ) of the beam (although θ-dependence of diffracted intensity does still arise from the Debye-Waller factor).

Neutron scattering amplitudes are not related to electron count: instead every isotope possesses a unique *coherent scattering length* (the effective size of the nucleus), that is not related to chemical properties and may take a negative value. Typical scattering lengths range from ~ -5 fm to ~ 16 fm. This makes neutron diffraction an excellent tool for detecting light elements in the presence of heavy ones, and also allows elements with similar X-ray scattering factors to be distinguished. The existence of negative scattering lengths has interesting implications for the study of compounds where a crystallographic site is shared by isotopes with positive and negative values, and for the construction of "null scattering" alloys as containers. Vanadium has a very small coherent scattering length (~ -0.38 fm) and is commonly used to make sample containers.

Another significant property of the neutron is its magnetic moment - it is a spin-$1/2$ particle. This means that neutrons can also be diffracted by a lattice of ordered magnetic moments. A beam of neutrons incident upon a magnetically ordered crystal will yield two superimposed diffraction patterns: a *structural* pattern and a *magnetic* pattern. Neutron diffraction can therefore be used to solve a magnetic structure crystallographically, which was first demonstrated by Shull and co-workers [85] in

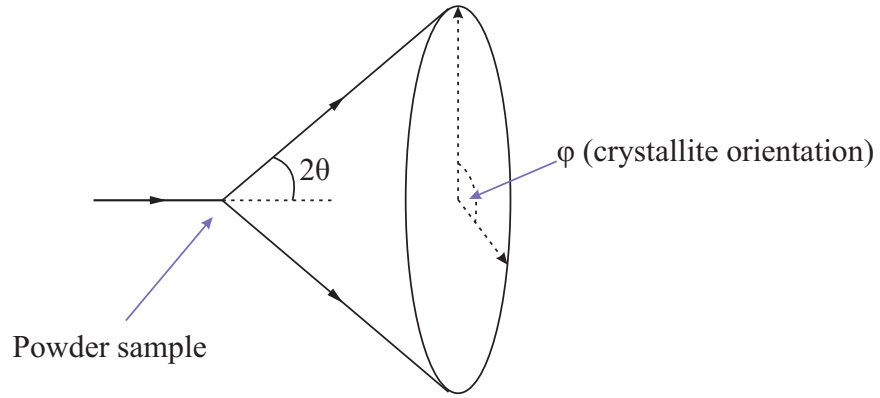


Figure 2.4: Schematic diagram of a Debye-Scherrer reflection cone arising from diffraction of an incident beam by a polycrystalline powder sample.

1951. Because magnetic scattering occurs from localised electrons in the outermost atomic orbitals, magnetic form factors are strongly θ-dependent (even more so than X-ray scattering) and magnetic Bragg peaks are generally only observed to any appreciable degree at low scattering angles.

2.2.4 Powder Diffraction

For many diffraction experiments it is not convenient (or even possible) to use a single crystal. This is especially true for single crystal neutron diffraction, which requires the growth of extremely large crystals or uses many small co-aligned crystals if any useful data are to be recorded. Instead powder diffraction can be used to obtain data from a polycrystalline sample, which should have a narrow distribution of crystallite sizes of a few microns. Ideally each crystallite in the sample should be oriented randomly at angle ϕ to the incident beam, so that each *hkl* reflection gives a cone-shaped diffracted beam (known as a Debye-Scherrer cone) with contributions from many crystallites. This situation is illustrated in figure 2.4.

In a typical powder diffraction experiment the intensity of the diffracted beam is measured as a function of 2θ, which is to effectively take a cross-section through the Debye-Scherrer cones. All of the collected information is therefore condensed into one dimension, and *hkl* peaks with identical or similar *d*-spacings become co-incident or (because of finite peak widths) overlap to some degree. The structure factor (given

by equation 2.6) can be modified by adding a multiplicity factor to account for the equivalence of certain classes of reflection. For example, in a cubic system such as NaCl, the (111) reflection is equivalent to seven other planes, each of which contributes to the observed intensity:

$$(111)\ (11\bar{1})\ (1\bar{1}1)\ (\bar{1}11)$$

$$(1\bar{1}\bar{1})\ (\bar{1}1\bar{1})\ (\bar{1}\bar{1}1)\ (\bar{1}\bar{1}\bar{1})$$

So I_{111} for NaCl must be multiplied by a factor of 8. However, overlapping peaks that are not of the same class become convoluted, and it is not possible to determine accurately their individual contributions to the overall intensity. Peak overlap tends to become more problematic as the crystal symmetry decreases, so powder methods are most often used most for high-symmetry extended solids and less often for complex molecular solids.

The problem of overlapping peaks, combined with the phase problem, makes it very difficult to use powder diffraction as a tool for direct structure solution. However, it is still an important and extensively used technique. X-ray powder diffraction (XRPD) is widely used to identify known phases by their characteristic diffraction patterns, and is extremely useful when assessing the purity of a sample or identifying the components of a mixture; and high quality powder diffraction data are especially powerful when used in combination with the Rietveld method (2.2.5), which is used to derive high-quality structural information (a technique used extensively in this work).

2.2.5 The Rietveld Method

The Rietveld method, originally developed for powder neutron diffraction by H. M. Rietveld in the late 1960s, [86, 87] is a technique applied to powder diffraction data to derive the maximum amount of useful structural information from a polycrystalline powder. It is not a structure solution technique; instead it relies on the input of a reasonably accurate starting model of the crystal in question, which is used to generate

a theoretical diffraction pattern. By refining this model to fit the observed data, the model comes to closely resemble the actual crystal structure. In this work Rietveld refinements were carried out using the GSAS package [88] with EXPGUI, [89] a graphical user interface.

As mentioned in the previous section, all but the highest symmetry crystals exhibit significant overlap between individual *hkl* reflections, making it extremely difficult (if the unit cell is unknown) to identify the true number of Bragg reflections contributing to an observed peak and to assign the correct intensity to each. Instead of trying to use the integrated intensity of each peak as the individual observables, the Rietveld method considers the intensity of each individual data point as a single observable. In a typical powder diffraction experiment there are around 2000 such data points.

The intensity of an arbitrary data point y_i may contain contributions from several Bragg reflections. The F_{hkl} values of neighbouring Bragg reflections are then generated from the structural model, and used to calculate a theoretical intensity for this point (labelled y_{ci}). There are several other factors that contribute to observed intensity and these are included in the following formula for the calculation of y_{ci}: [90]

$$y_{ci} = y_{bi} + s\sum_{hkl} L_{hkl} P_{hkl} A \mid F_{hkl} \mid^2 \phi(2\theta_i - 2\theta_{hkl}) \tag{2.11}$$

where s (scale factor), L_{hkl} (combined Lorentz, polarisation and multiplicity), P_{hkl} (preferred orientation) and A (absorption) are factors that depend mainly on experimental set-up; ϕ is a reflection *profile function* that describes the peak shapes (usually instrument-dependent to some degree); and y_{bi} is the background intensity (often generated by a separate polynomial function). F_{hkl} corresponds to the structure factor for the proposed structural model.

When the corresponding values of y_{ci} have been calculated, the difference $y_i - y_{ci}$ (by extension the difference between the subject crystal and the model) is incorporated into a "residual function" S_y, which is then minimised by a least-squares method:

$$S_y = \sum_i \frac{(y_i - y_{ci})^2}{y_i} \tag{2.12}$$

The least squares optimisation can be thought of as a feedback loop where certain user-defined parameters of the starting model are refined, and the improved model is fed into the next cycle to be further refined until a stable solution - the best fit for the observed pattern - is reached. At this point, refinement of further parameters may be allowed. When the refinement is complete, it is assessed by both statistical outputs and by graphical means. A satisfactory model generates a calculated pattern that closely corresponds to the observed pattern, and a difference plot should be almost featureless.

There are also several statistical outputs used to evaluate a refinement, known as *R-factors*. The *R*-structure factor (R_F) is based on Bragg intensities derived from the final model and not on direct observables: reflections are disregarded if they are not close in *d*-spacing to calculated reflections, and the factor is therefore biased in favour of the model being used. However, R_F can be useful because it is only sensitive to fits of Bragg reflections, rather than the full pattern, so it is a useful indicator of how good the structural model is without considering other factors (such as the presence of an impurity phase). The *R*-structure factor is given by:

$$R_F = \frac{\sum_K | (I_{K_{obs}})^{1/2} - (I_{K_{calc}})^{1/2} |}{\sum_K (I_{K_{obs}})^{1/2}} \tag{2.13}$$

where $I_{K_{obs}}$ is the intensity of an observed reflection *K,* and $I_{K_{calc}}$ is the calculated intensity of reflection *K*.

Factors that describe the quality of the full-pattern fitting are based on directly observed intensities. These include the *R*-pattern (R_p) and *R*-weighted pattern (R_{wp}) factors given by:

$$R_p = \frac{\sum_i | y_i - y_{ci} |}{\sum_i y_i} \tag{2.14}$$

$$R_{wp} = \sqrt{\frac{\sum_i w_i (y_i - y_{ci})^2}{\sum_i w_i y_i^2}} = \sqrt{\frac{S_y}{\sum_i w_i y_i}} \tag{2.15}$$

The weighted *R*-factor R_{wp} is arguably the most meaningful gauge of the least-squares refinement process, because it includes the residual function in the numerator (see equation 2.12). Unlike R_F, this *R*-factor can be strongly affected by problems with the fitting that are not related to the quality of the structural model (for example the presence of a minority phase or the incorrect modelling of the profile function).

The final important *R*-factor is the *R*-expected factor, which can be considered as a measure of data quality and is defined as:

$$R_{exp} = \sqrt{\frac{N_{obs} - N_{var}}{\sum_i w_i y_i^2}} \tag{2.16}$$

where N_{obs} and N_{var} are the number of observables and the number of refined parameters, respectively. For a typical powder experiment $N_{obs} \approx 2000$ so we expect $N_{obs} \gg N_{var}$. The expected *R*-factor represents the R_{wp} value expected if the refined model were perfect, with the only differences due to statistical fluctuations. Hence a *goodness-of-fit* parameter, χ, can be defined in terms of R_{exp} and R_{wp}:

$$\chi = \sqrt{\frac{S_y}{N_{obs} - N_{var}}} = \sqrt{\frac{R_{wp}}{R_{exp}}} \tag{2.17}$$

For an ideal powder diffraction experiment with a sufficient number of data points, sufficient counting time (such that y_{ci} is not dominated by the background intensity y_{bi} - see equation 2.11) and an appropriate number of refined variables, an excellent structural model could be expected to yield a χ value somewhere in the range $1.0 \leq \chi \leq 1.3$. However, conditions are not always ideal: large values of R_{exp} caused by insufficient counting time or the refinement of too many variables can give a misleadingly low χ (in some cases < 1). Likewise, a well-fitted high background can give values of R_{wp} that are much smaller than we might expect for a well-fitting model

alone. It is also possible to obtain anomalously high values of χ - for example, if data collection times are very long, then R_{exp} values can become very small.

In summary, when assessing the value of a structural model it is important not to rely on statistical indicators alone - a graphical representation is an excellent way to judge the quality of the fit and makes it easy to identify certain problems with the refinement (e.g. the presence of a minority phase or a poorly modelled background). A model can be considered to be satisfactory if it fits the observed data well, the statistical indicators look reasonable, and if it makes physical and chemical sense.

2.2.6 Laboratory X-ray Sources

All of the samples reported in this work were initially characterised using laboratory-based powder diffractometers. In these instruments, electrons are produced by heating a tungsten filament, then accelerated through a voltage of 40 kV to bombard a metal target. Both instruments used in the course of this work use a copper target. The incident electrons have sufficient energy to ionise core (K-shell) electrons from the Cu atoms, resulting in an excited ion. Subsequent relaxation of the ion, as the core hole is filled by a $2p$ or $3p$ electron, is accompanied by the emission of an X-ray photon of characteristic wavelength. A $2p \rightarrow 1s$ transition yields a K_α photon, while the $3p \rightarrow 1s$ transition yields a K_β photon. For XRPD a monochromatic beam is required, and usually the longer-wavelength K_α radiation is selected.

Both transitions are complicated by spin-orbit coupling: K_α is actually a doublet with two discrete frequencies arising from spin-orbit coupling in the $2p$ orbital, giving rise to $^2P_{3/2}$ and $^2P_{1/2}$ states in a 2:1 ratio. These are referred to as K_{α_1} and K_{α_2}, with wavelengths (for Cu) of 1.54051 Å and 1.54433 Å respectively.

2.2.6.1 Philips PW1710

This is a low-resolution instrument used primarily for assessing sample purity (particularly starting reagents $CeCuS_2$ and FeAs) and monitoring reaction progress. It

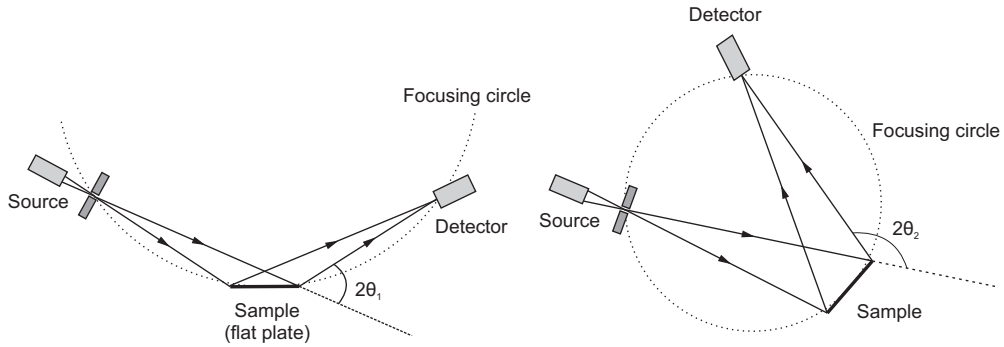


Figure 2.5: Illustration of a parafocusing arrangement in Bragg-Brentano geometry for two different Bragg reflections. The sample rotates at half the angular velocity of the detector to remain at a tangent to the focusing circle, while the detector-sample distance remains constant.

operates in Bragg-Brentano geometry with a fixed X-ray source and a moving detector on the 2θ axis. The sample is mounted on a flat plate, which rotates at half the angular velocity of the detector so as to remain at a tangent to the focusing circle (see figure 2.5). The incident beam is not monochromated so contains both K_{α_1} and K_{α_2} wavelengths.

The instrument is equipped with a secondary monochromator, which reduces background due to sample fluorescence in the diffracted beam. This is most effective for samples containing the late 1st-row transition metals Mn, Co and Fe, which are good absorbers of Cu K_α radiation. Air stable samples are mounted on an open aluminium or glass slide. These slides can be sealed inside a specially designed air-tight cell if the sample is air-sensitive, at the cost of a lower incident/diffracted intensity and higher background signal.

2.2.6.2 PANalytical XPert Pro

This high-resolution, high-intensity instrument is more sophisticated than the Philips diffractometer. The incident beam is monochromated by the (111) reflection of specially cut germanium crystals to leave only Cu K_{α_1} radiation (1.54051Å), which improves resolution and peak shape at the cost of some intensity. It operates in Bragg-Brentano geometry with a fixed source and moving detector and sample platform. The detector is position sensitive over a 2θ range of 2.112°, which improves the effective

counting time. To obtain the highest quality data, air-stable samples can be mounted on a spinning platform to improve the powder average. If the sample is not air-stable, the instrument can be used in flat-plate mode with the sample mounted on a flat aluminium or glass slide inside an air-tight cell. This instrument was used extensively throughout this work to obtain high quality data suitable for Rietveld refinement.

2.2.7 Synchrotron X-ray Sources

A synchrotron provides extremely intense beams of polarised radiation by using finely tuned bending magnets to accelerate electrons to relativistic speeds in large storage rings. Each time an electron is accelerated by a bending magnet, it emits horizontally polarised radiation at a tangent to the ring, which can be extracted to an experimental beamline. Current "third generation" storage rings (such as the Diamond Light Source and the European Synchrotron Radiation Facility) also include tunable magnetic *insertion devices* which generate a very high flux of radiation by forcing electrons through an oscillating magnetic field along otherwise straight sections of the ring. An "undulator" device imposes a gently oscillating field to enhance selected wavelengths by constructive interference; while a "multipole wiggler" device causes greater electron deflection, resulting in a more intense but incoherent beam of radiation.

Synchrotron X-ray sources have significant advantages over laboratory sources. Firstly, the beam is several orders of magnitude more intense. This not only allows for rapid collection times but more importantly it means that significant sacrifices in intensity can be made in order to maximise the resolving power of a diffractometer. As a consequence, synchrotron-based powder diffractometers offer arguably the highest available resolution for powder crystallography (rivalled only by the highest resolution time-of-flight neutron diffractometers). A second advantage is that a wide spectrum of wavelengths is available, which means that for a fixed-wavelength experiment an optimal wavelength can be selected. Alternatively it is common to find energy-dispersive powder diffractometers, which measure the diffraction of a white beam of X-

The material originally presented here is not currently available in ORA

Figure 2.6: Photograph of the I11 high-resolution X-ray diffractometer showing the sample-detector arrangement with 5 multianalyser crystal (MAC) detectors. On the right hand side is a diagram of the analyser-detector arrangement within a single MAC detector arm. (Both images are taken from references [91, 92]).

rays through a fixed scattering angle. This mode is often used for extreme-environment applications such as high-pressure diffraction.

2.2.7.1 I11 High-Resolution Diffractometer (Diamond Light Source, U.K.)

This beamline (described in detail by Thompson *et al.*)[91] uses photons from an undulator source which provides the highest beam flux at energies of 11-20 keV (approx. 0.6-1.1Å). The white beam is monochromated by two silicon (111) crystals and is then reflected from a pair of harmonic rejection mirrors to remove contamination by higher-energy harmonic photons.

The instrument operates in Debye-Scherrer geometry and has a highly efficient detector bank consisting of 45 individual detectors, each with a corresponding Si (111) analyser crystal, mounted on 5 separate arms at 30° (2θ) intervals. Each arm contains 9 detectors separated by 2°. Consequently, in order to obtain a full pattern with a 2θ range from 5-145°, the detector bank needs only to be scanned through an angle of 30° so that the data from each detector overlaps. This allows very rapid collection of a high-quality data set. A photograph of the instrument and a diagram of a detector arm are shown in figure 2.6.

Samples are mounted in spinning glass capillaries. For this work, air-sensitive compounds related to LiFeAs were sealed under an argon atmosphere in 0.5mm

borosilicate capillaries. Sample temperature was controlled with a nitrogen cryostream between 80-500 K, and for temperatures below 80 K a Phenix cryostat was used (with sample contained in an aluminium capillary to enhance heat exchange).

2.2.7.2 ID31 High-Resolution Diffractometer (E.S.R.F., France)

This instrument is similar in principle to I11, with a comparable resolution. It receives a white beam from an undulator source, which is monochromated by two Si (111) crystals. The detector bank is a single multianalyser stage consisting of bank of 9 detectors separated by approximately 2°, each with a corresponding Si (111) analyser crystal, which provides a scanning 2θ range of 18°. The major advantage of ID31 over I11 is that the incident beam has a high flux at shorter wavelengths than those available to I11. For this work measurements were taken using 0.4 Å radiation with samples contained in spinning borosilicate glass capillaries. Temperature control was provided by a He-cooled flow cryostat, designed to allow the sample capillary to spin, and able to cool to temperatures as low as 4 K.

2.2.7.3 ID27 High-Pressure Diffractometer (E.S.R.F., France)

This instrument is designed to be used with the sample contained in a diamond anvil pressure cell or Paris-Edinburgh pressure cell, both of which require the incident beam to have a very small diameter. Two undulators are used as the radiation source, which is designed to give a very high flux at the highest photon energies (and hence a beam capable of penetrating the sample environment equipment), allowing wavelengths as short as 0.2Å to be used here. The instrument is most commonly used in angle-dispersive (fixed λ) mode with a 2D image-plate detector, but can also be used in energy-dispersive (fixed 2θ) mode with a fixed solid-state detector.

In angle-dispersive mode the beam is monochromated by a Si (111) monochromator and two mirrors are used to focus the beam at the sample position. The sample remains in a fixed position and the diffraction pattern is collected on a 345 mm diameter disc-shaped image-plate detector. To reduce the high background signal from

the sample environment equipment (which can be overwhelming for a large P-E cell in angle-dispersive mode) two banks of Soller slits can be installed between sample and detector. The beamline is also equipped with a laser spectrometer for monitoring the sample pressure by ruby fluorescence, and a laser annealing system to enable variable pressure-temperature experiments in diamond anvil cells. Work presented in Chapter 5 used this instrument in fixed-wavelength mode at ambient temperatures.

2.2.7.4 ID09a High-Pressure Diffractometer (E.S.R.F., France)

Like ID27, the diffractometer on the ID09a beamline is designed for high-pressure diffraction with samples loaded into diamond anvil cells. The beam has a small cross-section of 30×30 μm^2 which can be further reduced for work at the very highest pressures. The beam is focused by a spherical mirror and monochromated by a Si (111) monochromator, to give a typical experimental wavelength of 0.4 Å. The diffracted beam is detected by a rectangular Mar555 image-plate detector (which has a 555 mm diagonal). The beamline is equipped with a laser spectrometer for monitoring the sample pressure by ruby fluorescence, but which may also be used for Raman scattering experiments. Sample temperature can be controlled with a He-cooled cryostat, resistive heating equipment, or laser heating (for extremely high temperatures). During the course of this work, measurements were taken at ambient temperatures only.

2.2.8 Neutron Sources and Time-of-Flight Diffraction

The generation of neutrons for diffraction is expensive and hazardous, and is therefore carried out at specialised facilities. There are two types of facility used to generate neutrons for diffraction: reactor sources and spallation sources.

The reactor source at the Institut Laue-Langevin in Grenoble, France, uses fission of ^{235}U as a source of neutrons. The reactor provides an extremely high neutron intensity of 1.5×10^{15} s^{-1}cm^{-2},[93] and neutron energies are equilibrated in a heavy-

water moderator to produce a thermal beam with a peak flux at 1.2 Å, which is extracted to experimental beamlines. Diffractometers at the ILL utilise this thermal beam, but for some applications it is further moderated to obtain a "hotter" (higher energy) or "colder" (lower energy) distribution.

Spallation sources do not produce a continuous beam. The neutrons are generated by the collision of a high-energy particle beam with a large heavy-metal target. At the ISIS facility (Rutherford Appleton Laboratory, U.K.) a synchrotron supplies a pulsed beam of protons to a tungsten target, with a frequency of 50 Hz and a proton energy of 800 MeV. This generates intense pulses of high-energy neutrons, which are extracted to experimental beamlines through an appropriate moderator to provide a useful wavelength distribution. A direct consequence of a pulsed neutron beam is that diffraction experiments are conducted in energy-dispersive mode, with detectors at fixed scattering angles. This is known as *time of flight* (T.o.F.) diffraction. Neutron velocity is related to its wavelength by the de Broglie relationship:

$$\lambda = \frac{h}{p} = \frac{h}{m_n v} \tag{2.18}$$

where h is the Planck constant, p is momentum, m_n is neutron mass and v is velocity. By considering the fixed path length of the neutron from moderator to detector, distance L, and the time t taken for a neutron to reach the detector, the relationship gives:

$$\lambda = \frac{ht}{m_n L} \tag{2.19}$$

We can substitute equation 2.19 into the Bragg equation (2.5) to relate the neutron time-of-flight to d-spacing:

$$\frac{ht}{m_n L} = 2d_{hkl} \sin\theta \tag{2.20}$$

Hence, by using detectors at fixed 2θ positions and a fixed path length L, the values

of d_{hkl} can be determined by using neutron time-of-flight as the variable.

As discussed in section 2.2.3, the intensities of neutron Bragg reflections are not strongly 2θ-dependent. Consequently, the minimum observable d-spacing is dictated by other factors. In a constant-wavelength experiment, the lower limit is reached when $2\theta = 180°$ so that $\sin\theta = 1$. Substituting this into the Bragg equation gives $d_{min} = \frac{\lambda}{2}$ as the absolute limit.

In contrast, there is no absolute limit to the d_{hkl} values that can be observed by time-of-flight diffraction. Instead, for a detector at fixed scattering angle 2θ the lower limit is dependent on the wavelength of the highest-energy neutrons in the pulse. For a hypothetical detector positioned at $2\theta = 180°$, this leaves $d_{min} = \frac{t_{min}}{2}$. At ISIS, in order to prevent pulses from overlapping, the neutron beam is not heavily moderated. This results in a relatively high population of fast neutrons with short wavelengths, allowing reflections with very short d-spacings (e.g. 0.2 Å on Polaris) to be observed. Such d-spacings observed by neutron diffraction have a much stronger signal than those observed by synchrotron XRPD.

As the d_{hkl} range observed by a fixed detector is dependent on the distribution of wavelengths in the pulse, it can also be seen from the form of equation 2.20 that the θ-position of the detector will affect the range of d-spacings that it observes. Hence, a detector bank at a low scattering angle $(\sin\theta \to 0)$ will observe the longest d-spacings for a given time-of-flight, while detectors at high scattering angles $(\sin\theta \to 1)$ will observe the smallest d-spacings. It is therefore conventional to have multiple detector banks on a time-of-flight diffractometer, each with a unique d_{hkl} range.

The position of a detector also affects its resolution in time-of-flight diffraction, as described by the resolution function given by equation 2.21.[94] Here, Δd is peak width at position d, and is dependent on the uncertainty in time-of-flight (Δt), the uncertainty in path-length (ΔL) and also on uncertainty in the diffracted angle $(\Delta\theta)$:

$$R(d) = \frac{\Delta d}{d} = \sqrt{\Delta\theta^2 \cot^2\theta + (\frac{\Delta t}{t})^2 + (\frac{\Delta L}{L})^2} \tag{2.21}$$

As $2\theta \rightarrow 180°$ the $\cot^2\theta$ term becomes vanishingly small, so resolution increases for a given t and constant path length L. It is clear that an instrument with a long path length (L) and a high-angle detector will provide the highest possible resolution. On the ToF diffractometers at the ISIS pulsed neutron source, detector banks are arranged such that $\Delta d/d$ is constant across a single detector bank,[94] with the result that Bragg peaks get narrower (Δd decreases) at smaller d-spacings.

Low-angle detector banks are primarily used to study structures with Bragg peaks at very high d-spacings, particularly magnetic peaks and those due to long-range structural ordering. High-angle banks are used to collect the highest-resolution data with good counting statistics at small d-spacings. Often an intermediate bank is used to collect data with a good resolution across an intermediate range of d-spacings.

For continuous-wave neutron diffractometers the resolution is θ-dependent and can be described by a Caglioti function [83, 95] with the form:

$$\sigma^2 = U\tan^2\theta + V\tan\theta + W \tag{2.22}$$

where σ is proportional to the FWHM of the peak, and parameters *U, V, W* are dependent on both sample and instrument. As θ increases the resolution goes through a λ-dependent minimum (as U is generally positive and V is negative) and then increases towards the highest angles. Therefore, in general, peak widths at short d-spacings are narrower when using ToF diffraction, and those at long d-spacings are narrower when CW diffraction is employed.[96]

2.2.8.1 Polaris High-Intensity Diffractometer (ISIS, UK)

Polaris is a high-intensity medium-resolution time-of-flight diffractometer. The pulsed incident neutrons are moderated by an ambient temperature H_2O moderator and arrive with a wavelength distribution of 0.1 - 6.0 Å. The instrument has four detector banks at fixed scattering 2θ angles of 14°, 35°, 90° and 135°. The bank at 135° provides the highest resolution and measures d-spacings from 0.2 - 3.2 Å. The bank at 35° has the

second-lowest resolution and measures *d*-spacings between 0.5 - 8.15 Å. The 14° bank was not used for this work, due to its very low resolution.

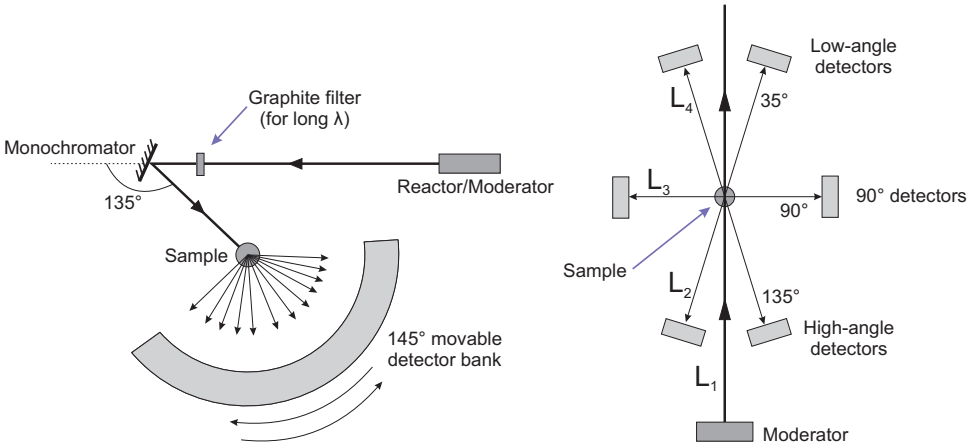
The sample is contained in a vanadium can, which only makes a very weak contribution to the diffraction pattern due to the very small coherent scattering length of vanadium (-0.38 fm). The maximum beam size at the sample is 40 x 20mm (extremely large compared to that used for X-ray diffraction), allowing very large samples to be studied. This is important, as larger samples maximise the scattering signal from the weakly-interacting neutrons. Polaris is also useful for the study of small samples and samples under non-ambient conditions, due to its very high intensity beam. In the course of this work, it was used for measurements under ambient conditions, low temperatures (with a He-cooled cryostat) and high pressures (using the equipment described in sections 2.2.8.4 and 2.2.8.5).

2.2.8.2 HRPD: High-Resolution Powder Diffractometer (ISIS, UK)

HRPD is a high-resolution time-of-flight diffractometer, with high-resolution primarily attained by maximising the path length, L, from moderator to detector (see the resolution function for time-of-flight diffraction, equation 2.21). The path length on HRPD is approximately 100 m, almost an order of magnitude greater than that of Polaris ($L_{Polaris} = 12$ m). A nickel-plated glass beam guide is used to prevent a significant loss in intensity over this distance, which would be considerably reduced by a normal inverse-square relationship ($I \propto 1/L^2$).

Neutrons reach the instrument with a distribution of wavelengths from approximately 0.5 - 10 Å, with peak flux at ~ 2 Å. This entire λ range cannot be used simultaneously, as the long path length requires that incident wavelengths are carefully controlled to eliminate "frame overlap" (where the highest-energy neutrons from one pulse catch up with the lowest-energy neutrons from the previous pulse). Two disc choppers situated close to the moderator are used to select an appropriate λ-range.

HRPD has three fixed detector banks: a high *d*-spacing low-angle detector at 30°; a 90° detector; and the highest-resolution back-scattering detector at 168°. Data from



(a) Constant-wavelength beamline D2B

(b) Polaris time-of-flight diffractometer, where total path length $L = L_1 + L_n$

Figure 2.7: Schematic diagrams of (a) D2B, a typical constant-wavelength neutron diffractometer with angle-dispersive detectors and (b) Polaris, a typical time-of-flight diffractometer with fixed-angle detectors.

the low-angle detector were not used in the course of this work.

2.2.8.3 D2B (ILL, France)

D2B is a high resolution two-axis diffractometer that uses neutrons from the high-flux reactor at the Institut Laue-Langevin. The layout of the instrument is illustrated in figure 2.7, which includes a diagram of a typical time-of-flight instrument for comparison.

The instrument operates in Debye-Scherrer geometry with a constant wavelength beam, selected from the incident thermal beam by appropriate rotation of a Ge [115] monochromator. The most commonly used wavelengths are $\lambda = 1.594$ Å, which is close to the peak in the wavelength distribution of the thermal beam and yields the highest flux; and $\lambda = 2.398$ Å, which is used for the study of higher d-spacings. For wavelengths of 2.398 Å and above, a graphite filter is inserted before the monochromator to eliminate contamination of the monochromated beam by harmonic wavelengths.

The sample is contained in a cylindrical vanadium can, and the scattered beam is detected by a two-dimensional scanning detector that consists of 128 ^{3}He counting

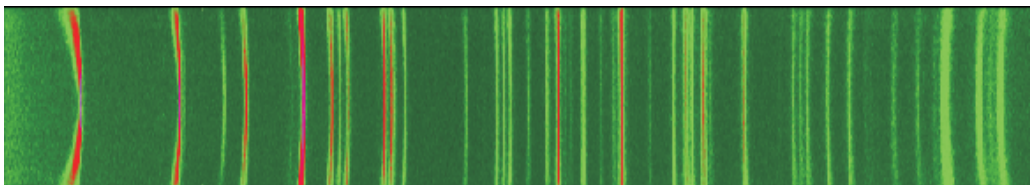


Figure 2.8: Diffraction pattern of $LiMn_{0.05}Fe_{0.95}As$ taken from D2B using the full height of the 2D detector (2θ increasing from left to right, with increasing diffracted intensity indicated by a green-yellow-red-purple colour scale), showing the curvature of the Debye-Scherrer cones.

tubes spaced at 1.25° intervals to cover an angular range of $5 \leq 2\theta \leq 165°$. The full height of the detector is 200 mm. However, when using large samples it is common to sacrifice some detected scattering by using only the mid-section of the detector (i.e. a narrow strip that lies in the same plane as the incident beam and the sample), as this avoids problems with peak asymmetry caused by the curvature of the Debye-Scherrer cones. This effect is shown clearly in figure 2.8.

2.2.8.4 High-pressure neutron diffraction: Helium gas cell

High-pressure studies were conducted using the high-intensity Polaris diffractometer with two different types of pressure cell. The first is a helium gas cell constructed from a cylinder of null-scattering titanium-zirconium alloy (illustrated in figure 2.9). The sample is loaded directly into the chamber of the cell and sealed with a Bridgman-type seal. The cell is then loaded into the instrument and gas pressure is applied by a gas intensifier system, linked by a steel capillary, which can generate pressures of up to 0.7 GPa. Pressure is monitored by a piezoelectric device, so a crystalline pressure marker is not required.

The large sample volume (6mm diameter x 30mm height) is a significant advantage for this type of cell, giving a strong scattering signal and reduced data collection times (approximately 4 hours for a highly crystalline sample). It is also compact with good thermal conductivity, so can also be readily inserted into a cryostat for variable temperature work. The pressures applied to the sample by the cell can be considered to be hydrostatic while He remains in the gas phase. At low temperatures, care must

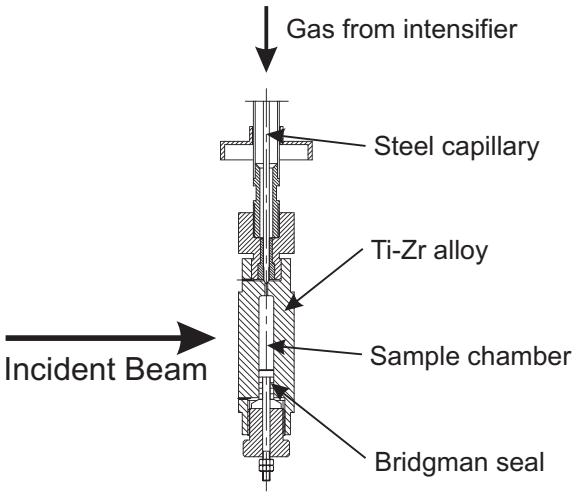


Figure 2.9: A cross-section diagram of the Ti:Zr He-gas pressure cell used for time-of-flight diffraction on the Polaris diffractometer (note that this apparatus can also be used for constant-wavelength apparatus). This figure is adapted from reference [97].

be taken to avoid the freezing of He, which causes the applied pressure to become non-hydrostatic.

2.2.8.5 High-pressure neutron diffraction: Paris-Edinburgh cell

For pressures greater than 0.7 GPa a Paris-Edinburgh pressure cell was used. In this type of cell the sample is contained in an encapsulated gasket which is mechanically compressed between two anvils by a hydraulic press, with a small amount of liquid used as the pressure transmitting medium. In this work, "Fluorinert" (a fluorocarbon, of molecular formula C_8F_{18}) was used as the medium. With Fluorinert, the P-E cell at ISIS can apply a maximum hydrostatic pressure of ~ 2 GPa.[98, 99] The sample volume is very small (approximately 5 mm^3) and becomes noticeably smaller at higher pressures. This requires the width of the incident beam to be narrowed accordingly, to reduce both the background signal from scattering by the pressure apparatus and the hazards associated with irradiating such equipment.

The sample environment is illustrated in figure 2.10. The incident beam coincides with the pressure axis of the cell and must penetrate one tungsten carbide anvil; this causes a high background and can also contribute extra Bragg reflections to the observed pattern. The diffracted beam is monitored by a detector bank at a $2\theta = 90°$, as

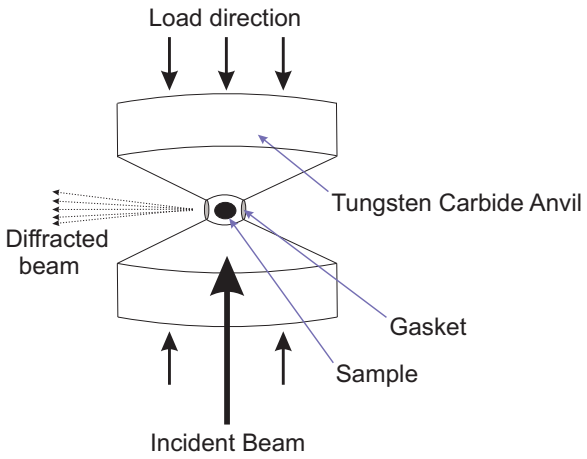


Figure 2.10: Schematic diagram of the anvil-sample arrangement and diffraction geometry in the Paris-Edinburgh cell, which was used for high-pressure measurements on the Polaris diffractometer. Note that the apparatus leaves only a small window at $2\theta = 90°$ for the detection of the diffracted beam.

the presence of the bulky equipment makes the forward-scattering and back-scattering detectors inaccessible. In order to monitor the pressure in the sample, a material with a known structural pressure-response is added as a "marker". This must have a simple structure to avoid significant overlap of sample peaks, so materials such as Pb or NaCl are commonly used.

Paris-Edinburgh cells offer the highest possible pressures for study by neutron diffraction, far exceeding those that can be attained in a gas cell. However, the above factors, combined with the small sample volume and significant beam attenuation, mean that a high-intensity instrument is essential. Even with an instrument such as Polaris, data collection times are very long and the precision of the refined parameters generally compares poorly with those obtained from a gas cell.

2.2.9 D.C. SQUID Magnetometry

Magnetic properties were characterised using a Quantum Design MPMS SQUID magnetometer. This instrument uses a superconducting quantum interference device (SQUID) as an extremely sensitive probe of the magnetic moment of a sample in an externally applied field. The device itself is a superconducting loop intersected by two Josephson junctions (thin strips of insulating material). When a small current is

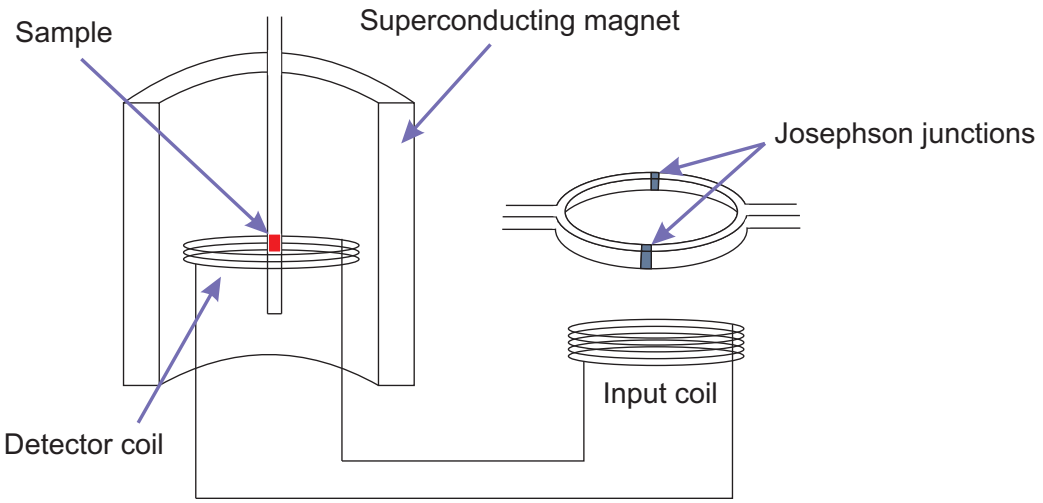


Figure 2.11: Schematic diagram of the sample-magnet-detector arrangement in the SQUID magnetometer.

applied across the device, the Cooper pair wavefunctions tunnel through the Josephson junctions, allowing the whole loop to conduct with zero resistance. When the applied current exceeds the critical current of the Josephson junctions their resistivity becomes finite, and a corresponding voltage is generated across the device. The current can be induced or modified by an external magnetic field, in which case the output voltage is related to the magnitude of the field.

In order to usefully incorporate a SQUID into a magnetometer, it must be protected from fluctuating external fields. The device is therefore housed away from the sample and protected by a superconducting shield. The sample is mounted within an induction coil and magnetised by a He-cooled superconducting magnet. Once magnetised, vertical translation of the sample induces a current in this detector coil. The detector coil is coupled to a larger input coil, which in turn is coupled to the SQUID, generating an output SQUID voltage that is proportional to the magnetic moment of the sample. This arrangement is illustrated in figure 2.11.

The sample chamber is kept under an atmosphere of helium, and can be cooled from a maximum temperature of 330 K to a minimum of 2 K. Magnetic signal from the sample environment is minimised by containing the sample within a gelatin capsule mounted inside a plastic drinking straw. The superconducting magnet can generate

fields in the range $-5\text{T} \leq B \leq 5\text{T}$, so sample magnetisation can be measured as a function of both temperature and applied field strength.

2.2.9.1 Measurement of superconducting compounds

A superconducting sample is distinguished by the onset of a strong diamagnetic signal below some critical temperature T_c. The diamagnetic signal is due to the Meissner effect: the onset of perfect diamagnetism with the result that all magnetic flux is expelled from the superconductor. The magnitude of this signal can be used to determine the superconducting fraction of a sample of known volume.

For a non-superconducting sample in an applied flux density B, the flux density inside the sample is given (in S.I. units) by:

$$B_i = \mu_0(H+M) = B + \mu_0 M \tag{2.23}$$

where B_i is internal flux density and $\mu_0 M$ is the contribution from sample magnetisation. In the superconducting state, $B_i = 0$ and equation 2.23 becomes:

$$M = \frac{-B}{\mu_0} = -H \tag{2.24}$$

therefore the dimensionless volume magnetic susceptibility, χ_{vol}, becomes:

$$\chi_{vol} = \frac{M}{H} = -1 \tag{2.25}$$

The measured magnetic susceptibility, χ_{meas}, is actually defined by the magnetic moment (μ_m) of the sample and the applied flux B (where $B = \mu_0 H$):

$$\chi_{meas} = \frac{\mu_m \mu_0}{B} \tag{2.26}$$

χ_{meas} has units of volume (m^3). Therefore χ can be obtained by dividing χ_{meas} by sample volume (calculated approximately from the sample mass and its crystallographic density):

$$\chi_{vol} = \frac{\mu_m \mu_0}{BV} = \frac{\mu_m \mu_0 \rho}{Bm} \tag{2.27}$$

where m and ρ are sample mass and density, respectively. If $\chi_{vol} = -1$ the sample is fully superconducting; while values between $-1 < \chi_{vol} < 0$ indicate some superconducting fraction (e.g. -0.5 corresponds to 50%). It should be noted that this analysis ignores several important factors, such as sample shape and grain-boundary flux-trapping effects, that can affect magnetisation. With these inaccuracies in mind, assessment of superconducting volume fraction was conducted by comparison of similar samples (with the "most superconducting" sample normalised to 1), which were assumed to have similar shapes and packing densities.

For superconducting compounds, magnetisation was measured as a function of temperature in the region $2 \leq T$ (K) ≤ 50 in an small applied field (usually 50 Oe) which is lower than the critical field of the sample. The superconducting transition temperature, T_c, was generally taken to be the temperature at which the sample becomes diamagnetic. Alternatively, T_c may be obtained by extrapolating the steepest section of the superconducting transition and finding the intersection with the extrapolated normal-state curve (as illustrated in figure 2.12), and this method is used in Chapter 5 for compounds of type $LiFe_{1-x}M_xAs$. Superconducting volume fraction was calculated from the magnetic susceptibility at 2 K. For some samples, the lower critical field H_{c1} was measured by a scan of M vs H at 2 K.

2.2.9.2 Measurement of paramagnetic compounds

For paramagnetic compounds, an initial scan of M vs H at 300 K is made to ensure the relationship is linear. A scan of M vs T in the region $2 \leq T \leq 300$K in a constant field of typically about 0.1 T is then conducted. If magnetisation has a non-linear dependence on H at low fields, measurements can be made at two higher applied fields H_2 and H_1 that lie in the linear region above the ferromagnetic saturation field. Magnetic susceptibility χ_{mol} is then calculated from molar magnetisation values using equation

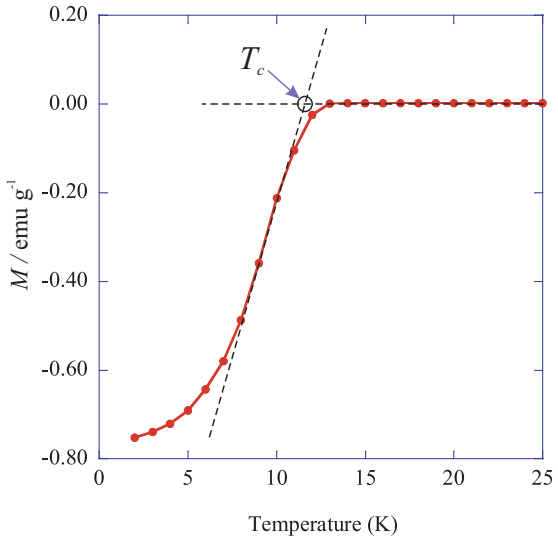


Figure 2.12: A magnetisation *vs* temperature plot for a typical superconductor, illustrating the derivation of T_c by taking the intercept of the extrapolated superconducting transition and normal-state magnetisation (black dashed lines). This intercept method was used consistently throughout this work.

2.28:

$$\chi_{mol} = \frac{M_{H_2} - M_{H_1}}{(H_2 - H_1)} \tag{2.28}$$

For a Curie paramagnet, molar magnetic susceptibility is related to the effective magnetic moment by the Curie law (in c.g.s. units):

$$\chi_{mol} = \frac{\mathrm{N_A}\mu_{eff}^2\mu_B^2}{3k_BT} = \frac{C}{T} \tag{2.29}$$

where μ_{eff} is the effective magnetic moment and C is the Curie constant. From this equation it is clear that a plot of $1/\chi_{mol}$ as a function of temperature can be used to obtain the Curie constant of a given sample, and hence derive μ_{eff}. This value, in turn, can often be used to infer the oxidation and/or spin state of a paramagnetic ion (as discussed in the previous chapter). This type of analysis can also be used for Curie-Weiss paramagnets, which order ferromagnetically or antiferromagnetically at low temperature and are subject to the Curie-Weiss law:

$$\chi_{mol} = \frac{C}{(T-\theta)} \tag{2.30}$$

where θ is the empirical Weiss temperature, obtained by extrapolating $1/\chi_{mol}$ from the paramagnetic region to find the intercept on the temperature axis. While Curie-type and Curie-Weiss-type paramagnetism results in a relatively large and positive magnetic susceptibility that is temperature dependent, paramagnetic solids with itinerant electrons (i.e. metals) usually exhibit temperature-independent Pauli paramagnetism, with a positive magnetic susceptibility that is several orders of magnitude weaker than that of a typical Curie paramagnet. The magnitude of this type of magnetic susceptibility is dependent on the density of states at the Fermi level.

2.2.10 SQUID Magnetometry at High Pressures

High-pressure magnetic measurements on several superconducting samples were conducted by Dr. Masaki Mito (Kyushu Institute of Technology, Japan, and visiting academic in the Department of Physics, Oxford) by a.c. magnetometry using a customised piston cylinder pressure cell. The samples were polycrystalline powders, which were mixed with an inert pressure-transmitting fluid (Apiezon J-oil) and loaded into a cylindrical Teflon cell with a small piece of high-purity tin added as a pressure calibrant. The Teflon cell is then housed inside the cylindrical pressure cell, illustrated in figure 2.13. Pressure is applied through two ceramic pistons by screwing in two locking nuts at opposing ends of the cylinder.

The cylinder and the locking nuts are made from a CuBe alloy, which provides a minimal magnetic signal and good thermal conductivity. These properties are essential, as the sample must be in thermal equilibrium with the external environment during the experiment, and its magnetic response must not be overwhelmed by response of the pressure cell. The pistons are constructed from zirconia: this is diamagnetic, has good thermal conductivity and high hardness. The maximum pressure generated by this cell is approximately 1.6 GPa at ambient temperatures, and 1.4 GPa at liquid helium

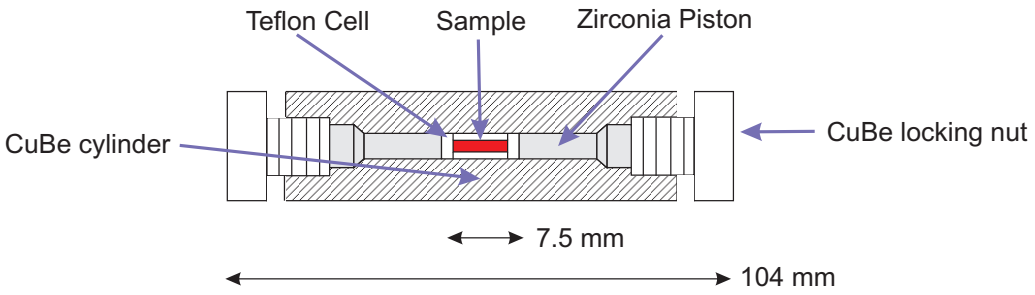


Figure 2.13: Schematic diagram of the piston-cylinder pressure cell used for high-pressure measurements (up to 1.6 GPa) in the SQUID magnetometer.

temperatures.[100] Apiezon J-oil remains in the liquid state throughout this regime, and therefore all applied pressures are considered to be hydrostatic.

2.2.11 Muon-spin Rotation (μSR) Spectroscopy

The positive muon (μ^+) is a charged spin-$^1/_2$ particle that spontaneously decays into a positron and two neutrinos with a lifetime (t_μ) of 2.2 μs. It can be used as an extremely sensitive probe of magnetism within a crystal, and is especially useful for studying small-moment magnetic ordering (i.e. moments that are too weak to give appreciable magnetic neutron scattering), short-range magnetic ordering, and various properties of superconductors (most notably the penetration depth).

In a μSR experiment, a polycrystalline sample is irradiated by a spin-polarised beam of positive muons (μ^+), and magnetic fields perpendicular or parallel to the initial muon spin may be applied. Positive muons are attracted to regions of high electron density, so some of these incident muons are trapped by particular sites within the crystal and begin to precess about the local magnetic fields there, with a Larmor frequency $\omega = \gamma_\mu B$ (where γ_μ is the gyromagnetic ratio of the muon, and B is the local flux density). When the muon decays, the positron is preferentially emitted in the direction of the parent muon spin, and ejected from the crystal towards detectors placed around the sample.

The instrument (illustrated schematically in figure 2.14) consists of a forward detector and a backward detector, and the number of positrons detected by each at

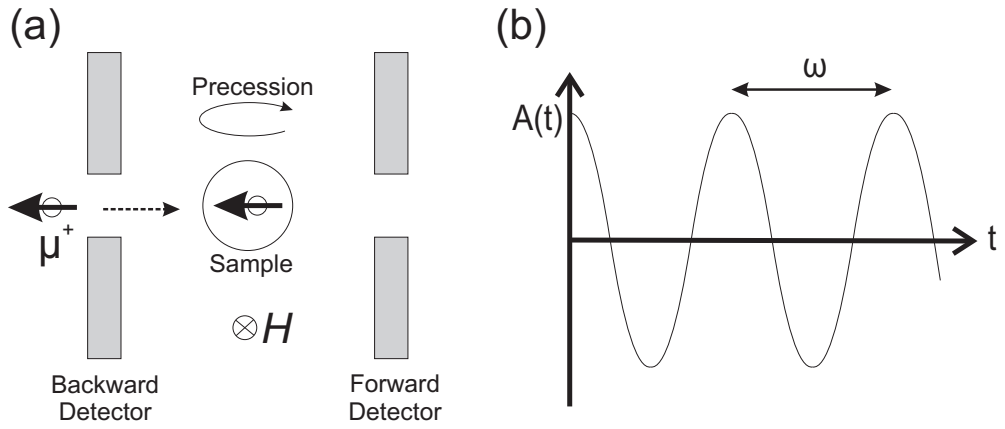


Figure 2.14: (a) Schematic diagram of a μSR experiment, whereby polarised muons implanted within the sample precess about their local fields, followed by emission/detection of a positron in the direction of the parent muon spin; (b) The asymmetry function arising from the detection of emitted positrons for an ensemble of muons in a common field, which consequently has only one frequency component.

a given time is contained in the normalised *asymmetry function* $A(t)$:

$$A(t) = \frac{N_B(t) - N_F(t)}{N_B(t) + N_F(t)} \tag{2.31}$$

where $N_{B,F}(t)$ are time-dependent functions describing the number of positrons observed at each detector, which decay as e^{-t/t_μ}. For an ensemble of muons precessing in the same field, the asymmetry function oscillates with frequency ω. Often in a magnetically ordered crystal, $A(t)$ contains more than one oscillation frequency because muons on different crystallographic sites will experience different local fields. Deconvolution of these frequencies yields information about the ordering scheme.

For the study of type-II superconductors, the sample is cooled into the superconducting regime and a transverse field (greater than the lower critical field of the sample) is applied to generate a "vortex lattice", which is an ordered array of supercurrent vortices flowing about each penetrating flux line. The properties of the vortex lattice can be probed directly by μSR. These include the London penetration depth which, in turn, is dependent on the Cooper pair density and the symmetry of the superconducting gap. Another related property measured is "superfluid stiffness" (which is proportional to $1/\lambda^2$, where λ is the penetration depth). For

type-II superconductors, the superfluid stiffness appears to be related to the transition temperature T_c by a linear scaling factor, known as Uemura scaling.[101, 102] The nature of this relationship can yield information about pairing and electromagnetic screening, and crucially it allows these properties to be readily compared to those of other materials.

In the course of this work, μSR experiments and data analysis were carried out by Dr. Peter Baker (ISIS, UK), Dr. Tom Lancaster (Department of Physics, Oxford) and Mr. Jack Wright (Departments of Physics and Chemistry, Oxford), using the MuSR instrument at ISIS, UK, and the GPS instrument at the Paul Scherrer Institut, Switzerland.

Chapter 3

Copper Deficiency and Structural Ordering in $CeCu_{1-x}OS$

3.1 Introduction

The layered oxysulfide compound CeCuOS is a member of a large family of related materials of type *Ln*CuO*Ch*. These compounds take the common tertragonal ZrSiCuAs crystal structure which consists of PbO-type lanthanide-oxide layers stacked alternately with anti-PbO-type copper chalcogenide layers (illustrated in figure 3.1). Stable compounds form with the largest lanthanide ions (La - Nd) and Bi regardless of the identity of the chalcogenide, but the selenide series *Ln*CuOSe accommodates the greatest range of lanthanides down to HoCuOSe,[103] while telluride compounds are not known beyond NdCuOTe. Sulfides show an intermediate tolerance and are stable as far as EuCuOS.

The structural and electronic properties of these materials have been widely studied and are relatively well understood. They are generally band gap insulators and have been investigated for their potential use as optically transparent semiconductors.[104, 105] The compositional flexibility of the structure means that the band gap can be readily tuned. For example, introducing a heavier chalcogenide or decreasing the size of the lanthanide is found to decrease the size of the band gap by modifying

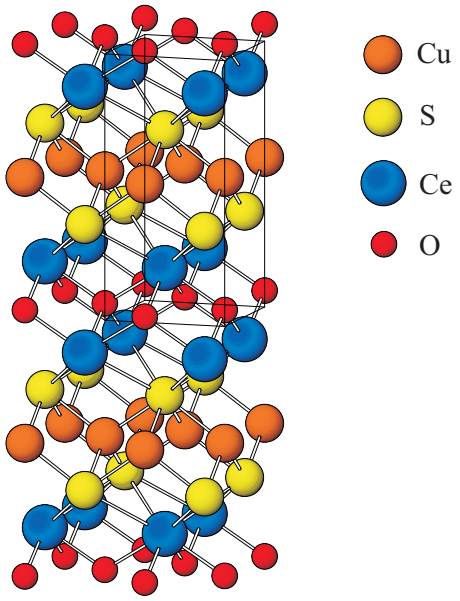


Figure 3.1: The tetragonal ZrSiCuAs crystal structure adopted by *Ln*CuOS. The unit cell is outlined in black.

the electronic structure of the chalcogenide layer. In the sulfides, band structure calculations and PES measurements show that the states at the top of the valence band are dominated by the CuS layer, consisting primarily of antibonding Cu 3d/S 3p and Cu 3d/Cu 3d states, while the lowest energy conduction band states form from antibonding *Ln* 5d/Cu 4s/S 3p states. Introducing a heavier chalcogenide (Se, Te) in place of S can therefore broaden the valence band, while a decrease in Cu-Cu distance by substituting smaller lanthanides has a similar broadening effect.

Across the *Ln*CuO*Ch* series, trends in structural parameters are predictable and consistently well behaved. For the oxyselenide and oxytelluride series *Ln*CuOSe and *Ln*CuOTe, the unit cell volume changes in accordance with the lanthanide contraction. All of the compounds also show similar magnetic properties, behaving as Curie-Weiss paramagnets with local moments on the lanthanide ions that are close to free-ion values.[106]

However, while the oxysulfide series generally observes these common trends, reports of the properties of the *Ln* = Ce member (CeCuOS) vary widely. An extensive study of these materials by Charkin *et al. [40]* found that CeCuOS has an anomalously small unit cell volume (see figure 3.2), which they ascribe to a copper-deficient

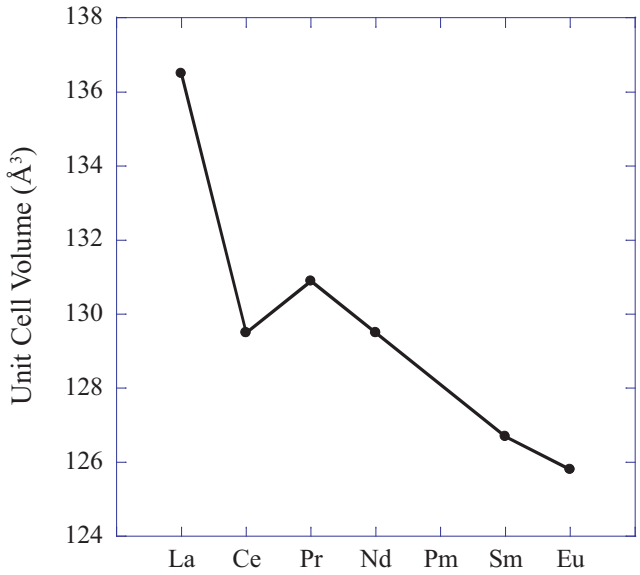


Figure 3.2: A plot of unit cell volumes for *Ln*CuOS compounds across the early lanthanide series, showing the anomalously small lattice parameters of CeCuOS. These data are taken from reference [40].

sulfide layer with concomitant partial oxidation of Ce^{3+} to Ce^{4+}. They found that stoichiometric CeCuOS could not be prepared, and their samples always contained a small amount of Cu metal. They also noted that the compound was always black in colour, rather than the green/brown colour of the rest of the series. A later study [107] found that nominally stoichiometric CeCuOS exhibits a significantly higher conductivity than other members of the series and also has very different optical properties,which is taken as evidence of a different electronic structure.

Several studies of nominally stoichiometric CeCuOS have provided further evidence of mixed-valence Ce: one study reports that the effective magnetic moment of Ce is 1.62 μ_B, [108] which is significantly diminished from the free-ion value of 2.54 μ_B and consistent with mixed-valence $Ce^{3+/4+}$. However, a separate study on a different sample [109] found the effective magnetic moment to be much higher at 2.1 μ_B and also noted that the anomalously small unit cell volume was due to an anomalous contraction of the Ce-S bond. Direct evidence for mixed-valence Ce has also been observed by X-ray photoelectron spectroscopy.[110]

Following these reports, a wide-ranging study of CeCuOS and isostructural CeAgOS by Chan *et al.* [34] found significant non-stoichiometry due to deficiencies

of Cu/Ag in both systems, which were black in colour, with single crystal XRD experiments yielding a refined composition of $CeCu_{0.809(4)}OS$ at 153 K. This sample of $CeCu_{0.809(4)}OS$ was found to have an effective magnetic moment of 2.1 μ_B per Ce ion, in agreement with a previous report.[109]

The attempts by Chan *et al.* [34] to synthesise stoichiometric CeCuOS were unsuccessful, although stoichiometric CeAgOS was obtained. This work is consistent with the observations of Charkin *et al.* and suggests that the formation of copper-deficient $CeCu_{0.809(4)}OS$ is favoured over the formation of the stoichiometric compound, regardless of the stoichiometry of the reaction mixture. Their results also imply that previous reports of property measurements on "CeCuOS"[107, 108, 110] are likely to have been conducted on samples of type $CeCu_{1-x}OS$.

In 2004 the discovery by C. F. Smura [77] of an apparently new phase of CeCuOS, which is green/brown in colour (shown in the photograph in figure 3.3), raised new questions over the composition and chemistry of CeCuOS. The lattice parameters of this phase were found to lie on a smooth trend with other *Ln*CuOS, consistent with the regular lanthanide contraction. On exposure to air this material was found to turn black rapidly, but it retained the ZrSiCuAs crystal structure with no detectable decomposition. Furthermore, it was found that the green/brown phase could be recovered from air-exposed black CeCuOS by heating under a reducing atmosphere. A subsequent investigation [41] confirmed these results, and used laboratory X-ray diffraction and neutron powder diffraction to show that the transition was accompanied by a small decrease of the lattice parameters driven by a contracting Ce-S bond. However, the neutron diffraction data were not of high enough quality to refine the compositions (e.g. Cu site or O-site occupancy).

From these reports it is clear that CeCuOS exhibits some reversible physical and/or chemical changes under atmospheric or reducing conditions while retaining its structural integrity, but the precise nature of this change is not clear. The work presented in the early part of this chapter seeks to address this problem by establishing an accurate composition for the green/brown phase for comparison with its air-exposed

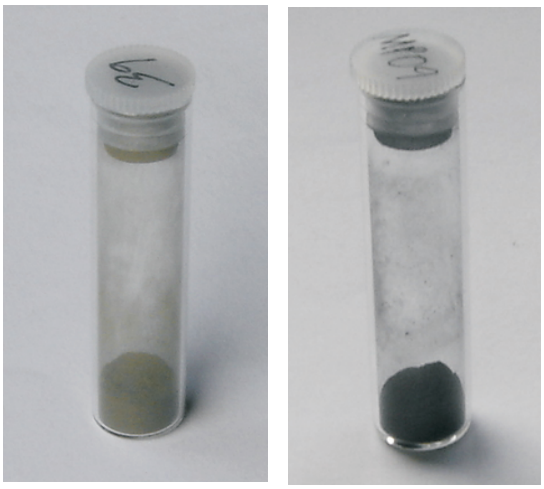


Figure 3.3: Powder samples of freshly-prepared “green” CeCuOS, and air-exposed “black” CeCuOS.

black counterpart, and investigating the changes in magnetic properties that might be expected to occur with changes in Ce oxidation state. An alternative synthetic route to stoichiometric CeCuOS is also investigated.

The later part of this chapter details the investigation of structural changes that occur at low temperatures in Cu-deficient $CeCu_{(1-x)}OS$ compounds. This investigation follows previous work in the group on an homologous series of Cu-deficient oxysulfides $Sr_2O_2MnCu_{1.5}S_2$, $Sr_2O_2MnCu_{(4-x)}S_3$ and $Sr_2O_2MnCu_{(6-x)}S_4$, which have similar anti-PbO/antifluorite-type CuS layers related to those of CeCuOS. Each of these compounds are found to exhibit superstructures due to ordering of Cu ions and vacancies at temperatures of around 100 K. However, this type of ordering has not yet been reported in oxysulfide compounds with the ZrSiCuAs structure (presumably due to a lack of intrinsically Cu-deficient materials) and it is therefore of interest to investigate the possibility of its occurrence in $CeCu_{(1-x)}OS$ and characterise any resulting low-temperature superstructures. Also, comparison will be made with the superstructures recently found in a range of superconducting iron selenides.

3.2 Investigating the compositional differences between "green" and "black" CeCuOS

3.2.1 Synthesis of "Green" and "Black" CeCuOS

A large sample of nominally stoichiometric CeCuOS, of approximate mass 6 g, was prepared by similar methods to those used in previous studies.[41, 77] All manipulations were carried out in an argon-filled dry box. Stoichiometric amounts of $CeCuS_2$ (prepared by the method described in Chapter 2), CeO_2 and Cu were thoroughly ground for 75 minutes with an agate pestle and mortar. One mole of powdered KCl (pre-dried under vacuum at 700 °C) per mole of CeCuOS was added during the final stages of grinding. The ground mixture was then loaded into an alumina crucible and sealed under vacuum in a protective silica tube. This reaction vessel was then heated to 900 °C and kept at this temperature for 10 days. This produced a dark brown powder. The KCl was removed from the product by washing with dried methanol under nitrogen using standard Schlenk line techniques. Inspection by XRPD showed that the product was single-phase CeCuOS with no visible contamination by KCl.

Approximately half of this sample (2.96 g) was taken to generate "black" CeCuOS by exposure to oxidising conditions. To do this in a controlled way, the powder was loaded into an alumina boat and sealed inside a 25mm diameter silica tube with steel end-caps (which are fitted with 3-way valves to control gas flow). This was then subjected to a flow of moist oxygen (generated by bubbling O_2 through de-ionised water) at ambient temperature for 48 hours. This caused the powder to turn from dark brown to jet-black. A cursory inspection by laboratory XRPD showed that the black powder had maintained the ZrSiCuAs structure, and there were no obvious signs of decomposition (such as peak broadening or the appearance of new Bragg reflections). It was also apparent that the lattice parameters had contracted. This sample was subsequently stored in an argon-filled dry box.

3.2.2 Neutron powder diffraction

The two samples of CeCuOS (non-oxidised and oxidised respectively) were investigated by neutron powder diffraction using the Polaris diffractometer at ISIS, UK. The non-oxidised (brown) sample was loaded into a vanadium can and sealed under an argon atmosphere with an indium gasket, while the oxidised (black) sample was contained in a similar vanadium can which was not air-tight. A previous study suggested that differences between the samples should be small,[41] and therefore measurements were taken at ambient temperature for both samples for a long period of approximately 6 hours (1100 μAhr) to ensure that correlations between structural parameters, thermal displacement parameters and fractional occupancy factors (amongst others) were minimised during the Rietveld refinement process.

For both samples, the ambient temperature data sets from three fixed detector banks (35°, 90° and 145°) were used for similar Rietveld refinements. Refined structural parameters are displayed in table 3.1 on the following page, and representative refinements are shown in figure 3.4. Tables of refined atomic co-ordinates, temperature factors, and refinement statistics are displayed in Appendix C. The material was found to have undergone significant structural changes on oxidation. The most obvious difference between the samples is a large decrease in the lattice parameters that has occurred on oxidation. The lattice parameters of the "green" sample are significantly larger than any previously reported for CeCuOS ($V = 132.405(1)$ Å^3), while those for the "black" sample are comparable to previous reports ($V = 128.955(5)$ Å^3). Both samples were found to contain a small but similar amount of elemental Cu (approximately 3.5 mol%). The refined values for the occupancy of the Cu site show that the non-exposed green sample is close to stoichiometric with composition $CeCu_{0.987(2)}OS$, while the oxidised black sample appears to be significantly deficient in Cu with a refined composition of $CeCu_{0.862(2)}OS$. A large decrease in the Ce-S distance (-1.76 %) appears to drive the contraction of the unit cell (-2.61 %), which is consistent with partial oxidation of Ce^{3+} to Ce^{4+} and reflects the fact that this

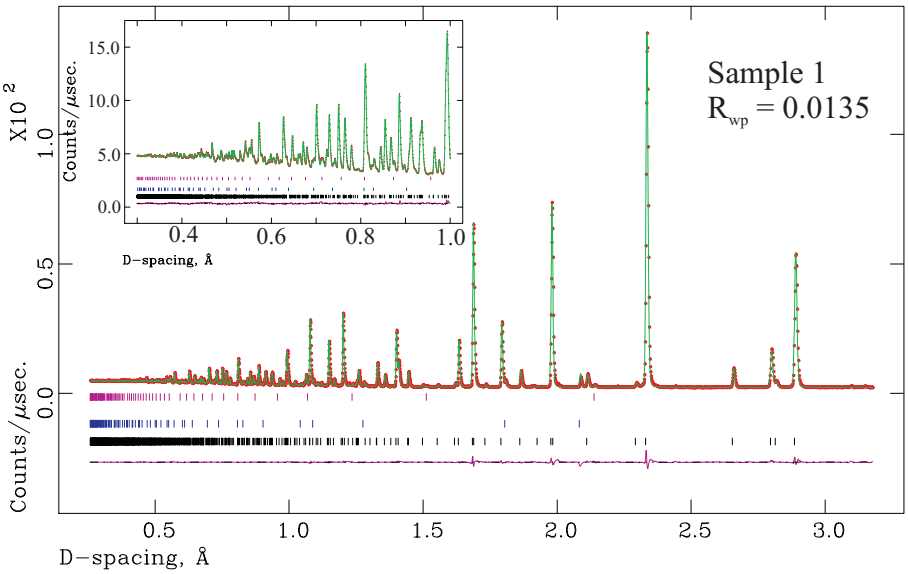
Table 3.1: Refined structural parameters, and a comparison with a previously reported Cu-deficient sample. Numbers in square brackets designate multiplicity.

	Sample 1	Sample 2	% change	$CeCu_{0.76}OS$ [34]
Cu occ.	0.987(2)	0.862(2)	-12.66	0.762
a / Å	3.95828(2)	3.92757	-0.78	3.9072(3)
c / Å	8.45071(5)	8.3596(2)	-1.08	8.2834(10)
c / *a*	2.135	2.128	-0.33	2.120
V / $Å^3$	132.405(1)	128.955(5)	-2.61	126.46(2)
Cu-S [4] / Å	2.4263(4)	2.4193(7)	-0.29	2.4064(9)
Ce-S [4] / Å	3.2129(3)	3.1562(5)	-1.76	3.1245(8)
Ce-O [4] / Å	2.3378(2)	2.3372(4)	-0.03	2.3342(2)
S-Cu-S [2] / deg	109.32(3)	108.53(5)	-0.72	108.55(6)
S-Cu-S [4] / deg	109.55(1)	109.95(2)	+0.37	109.93(3)

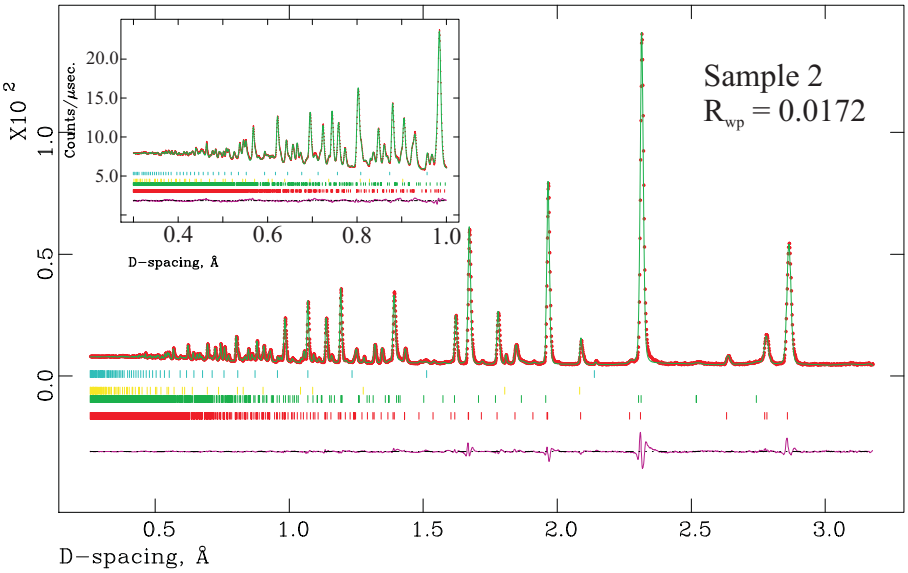
Cu deficiency leaves sulfide somewhat under-bonded. It should be noted that there is a negligible change in the Ce-O distance (-0.03 %), which implies that a purely ionic model for this cell contraction may be simplistic. There also appears to be a small amount of disruption to the structure of the CuS layer, as the CuS_4 tetrahedra are slightly distorted away from ideal T_d geometry, while the average Cu-S distance decreases by only a small amount (-0.29 %). These changes in bond distances are plotted in figure 3.7.

Inspection of the anisotropic displacement parameters of the Cu atoms shows an elongation in the *ab*-plane in the Cu-deficient compound (illustrated in figure 3.6). This type of anisotropic displacement is often seen in compounds with a high ionic mobility, and has been observed in neutron diffraction studies of the isostructural Ag analogue LaAgOS [19] as well as other Cu-deficient layered oxysulfides.[111]

A visual comparison of diffractograms from the two samples is displayed in figure 3.5. It is clear that the peaks from "black" CeCuOS are broader than those of "green" CeCuOS. This may be due to greater compositional inhomogeneity in the oxidised Cu-deficient sample. There are also several broad features of low intensity in the "black" diffractogram that are not present in the non-exposed sample. The *d*-spacings of these features are coincident with those of CuO. This appears to be evidence that the Cu extruded from the sulfide layer by exposure to moist oxygen is oxidised to a poorly-



(a) Sample 1 (pristine). Reflection markers: *Black* = $CeCu_{0.987(2)}OS$; *Blue* = Cu; *Purple* = V (sample container).



(b) Sample 2 (oxidised). Reflection markers: *Red* = $CeCu_{0.862(2)}OS$; *Green* = CuO; *Yellow* = Cu; *Cyan* = V (sample container).

Figure 3.4: Rietveld refinements against neutron powder diffraction data from the high-resolution 145° detector bank on Polaris. Red line = observed data; green line = calculated intensities; purple line = difference curve (observed - calculated). Phase markers are identified in sub-captions. Low *d*-spacings and weighted *R*-factors are inset. "Sample 1" is pristine green $CeCu_{0.987(2)}OS$; "Sample 2" is oxidised black $CeCu_{0.862(2)}OS$.

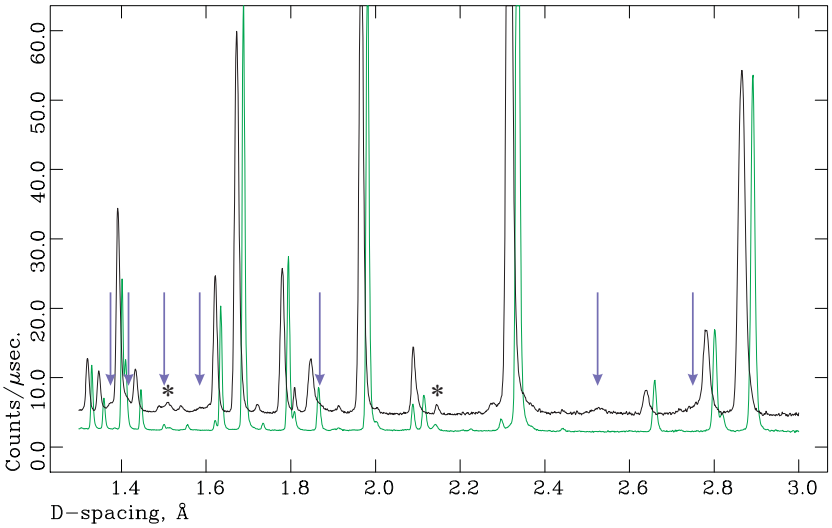


Figure 3.5: Detailed sections of the diffractograms for "Sample 1" (pristine $CeCu_{0.987(2)}OS$, green pattern) and "Sample 2" (oxidised $CeCu_{0.862(2)}OS$, black pattern). Blue arrows mark positions of Bragg peaks due to poorly crystalline CuO. Asterisks indicate reflections from the vanadium containers.

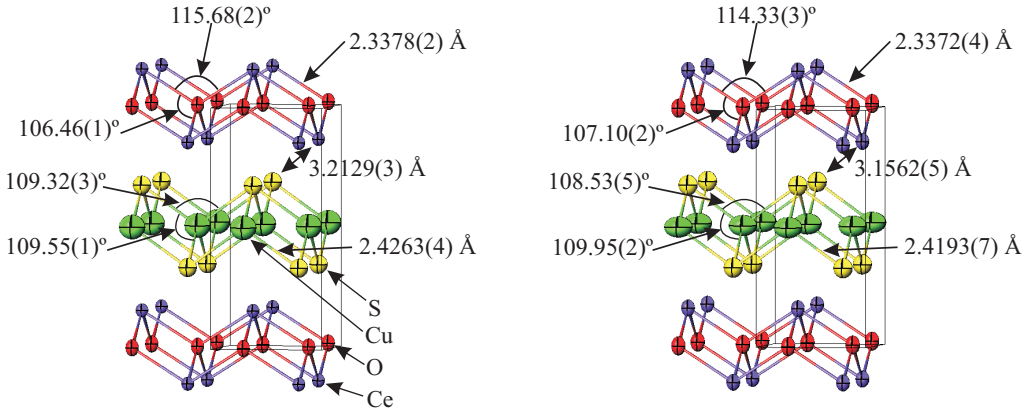


Figure 3.6: Thermal displacement ellipsoids (99 %) with refined bond lengths and angles (NPD) for "Sample 1" (pristine $CeCu_{0.987(2)}OS$, left hand side) and "Sample 2" (oxidised $CeCu_{0.862(2)}OS$, right hand side).

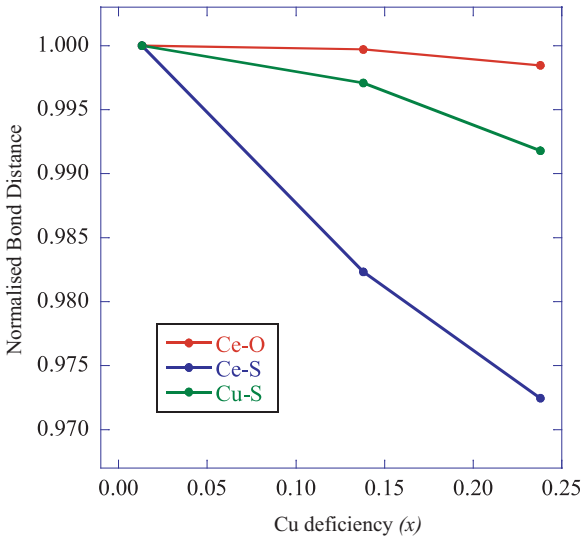


Figure 3.7: A plot of normalised Ce-O, Ce-S and Cu-S distances and their variation with refined Cu content for 3 samples of $CeCu_{1-x}OS$. The points at $x \approx 0.25$ are taken from a single-crystal XRD study (reference [34]).

crystalline form of CuO. It should be noted that this would be extremely difficult to observe by laboratory XRD techniques. CuO is black in colour, and it is possible that this is responsible (at least in part) for the green→black colour change observed on oxidation.

This type of air sensitivity caused by Cu-extrusion from an anti-PbO-type sulfide layer has since been observed in $Sr_2CoO_2Cu_2S_2$,[112] which also contains an oxidisable cation Co^{2+}. In this material, CuO peaks are also visible in the neutron diffraction pattern of the oxidised phase, but are less obscured by the majority phase.

3.2.3 SQUID Magnetometry

Previous studies on $CeCu_{(1-x)}OS$ and related compounds have shown that these materials exhibit Curie-Weiss paramagnetic behaviour, and therefore the oxidation state of Ce can be derived if the Curie constant is determined. Previous work has shown that magnetisation does not have a perfectly linear relationship to applied field below $H = 0.1$ T.[41] Magnetisation measurements were therefore taken on warming

from 5 - 300 K in applied fields of 3 T and 4 T, with the sample initially cooled in zero applied field. Magnetisation, which is recorded in c.g.s. units of emu by default, was converted to molar magnetic susceptibility by the following relation (where applied field H is in c.g.s. units of gauss):

$$\chi_{mol} = \frac{M_1 - M_2}{(H_1 - H_2)} = \frac{M_1 - M_2}{10^4} \tag{3.1}$$

The resulting plots of χ, $1/\chi$ *vs* T are shown in figure 3.8. The behaviour of $\chi(T)$ is similar in both samples, and plots of $1/\chi$ as a function of T are found to be linear above $T \approx 150$ K, which is consistent with a previous report [34] that ascribes this behaviour to crystal field splitting in the $J = 5/2$ ground state of Ce^{3+}. For each sample the molar Curie constant, and the effective magnetic moment (μ_{eff}) of Ce, were derived from the gradient of $1/\chi$ vs T in the region $T > 150$ K using the following equation (with all constants in c.g.s. units):

$$\chi_{mol} = \frac{N_A \mu_{eff}^2 \mu_B^2}{3 k_B T} = \frac{C}{T} \tag{3.2}$$

The values of μ_{eff} derived in this way were then corrected for core diamagnetism using standard tables.[113] The mass and spin-only paramagnetism of 0.14 molar equivalents CuO in the oxygen-exposed $CeCu_{0.862(2)}OS$ sample was then subtracted. This analysis yielded values of μ_{eff} of 2.38(4) μ_B for $CeCu_{0.862(2)}OS$ and 2.53(2) μ_B for $CeCu_{0.987(2)}OS$ (where errors are derived from linear fits to the $1/\chi$ plots). The theoretical free-ion value for Ce^{3+} is given by $\mu = g\sqrt{J(J+1)} = 2.54$ μ_B, which corresponds to a Curie constant of 0.80 emu K/mol. Ce^{4+} is diamagnetic, therefore a mixed-valence system of type $[Ce^{4+}_{0.14}Ce^{3+}_{0.86}]Cu^{+}_{0.86}OS$ is expected to have $C_{mol} = 0.69$ emu K/mol, which yields a theoretical μ_{eff} of 2.36 μ_B. These experimental values are therefore consistent with the partial oxidation of Ce^{3+} to Ce^{4+} as Cu is extruded from the sulfide layer, and with the refined compositions obtained by neutron diffraction.

Table 3.2: Calculated (free-ion) and experimentally-determined effective magnetic moments for 3 samples of $CeCu_{1-x}OS$. Values for $CeCu_{0.987(2)}OS$ ("Sample 1") and $CeCu_{0.862(2)}OS$ ("Sample 2") were derived from the data plotted in Figure 3.8.

Sample	$CeCu_{0.987(2)}OS$	$CeCu_{0.862(2)}OS$	$CeCu_{0.81}OS$[34]
Experimental / μ_B	2.53(2)	2.38(4)	2.13(6)
Calculated / μ_B	2.52	2.36	2.27

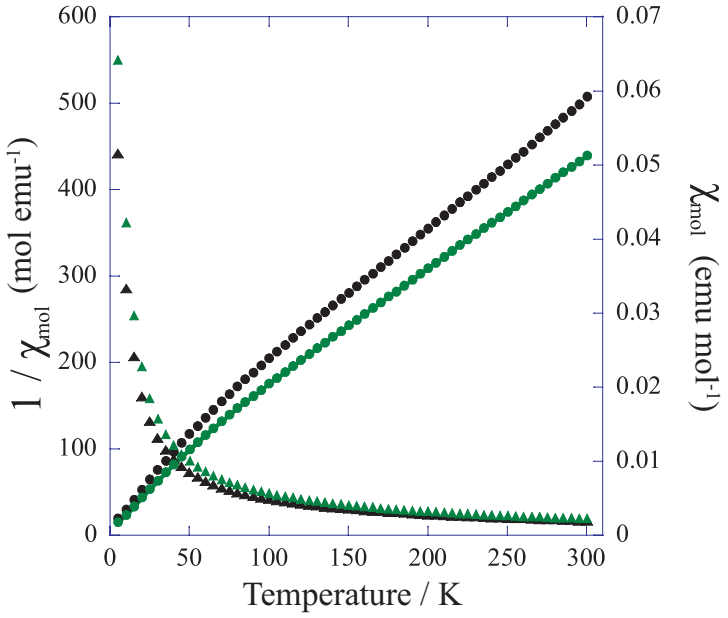


Figure 3.8: Plots of $1/\chi_{mol}$ *vs* T (circles) and χ_{mol} *vs* T (triangles) from magnetic susceptibility measurements of "Sample 1" (pristine $CeCu_{0.987(2)}OS$, green markers) and "Sample 2" (oxidised $CeCu_{0.862(2)}OS$, black markers) in the range $5-300$ K, showing Curie-Weiss paramagnetism above $T \approx 100$ K. These data were used to calculate the effective magnetic moments in Table 3.2.

3.3 Reaction of $CeCu_{(1-x)}OS$ with x.CuO under a reducing atmosphere

In the previous section, the investigation of 2 samples of CeCuOS by neutron powder diffraction showed that the air-sensitivity of nearly-stoichiometric green $CeCu_{(1-\delta)}OS$ ($\delta \simeq 0.01$) is due to the extrusion of Cu, to leave a black material with refined composition $CeCu_{0.862(2)}OS$. The extruded Cu then remains in the sample as poorly-crystalline CuO. In light of these results, and previous work showing that the green $\rightarrow$ black phase change can be reversed by heating under reducing conditions,[77, 41] the possibility of using CuO and $CeCu_{(1-x)}OS$ in a new synthetic route to fully stoichiometric CeCuOS was explored.

A copper deficient sample of nominal composition $CeCu_{0.85}OS$ was prepared by the methods described in section 3.2.1. The product was a black powder, and inspection by laboratory XRPD showed this sample to be $CeCu_{(1-x)}OS$ with a small amount (< 5 mol%) of crystalline Ce_2O_2S as a minority phase. A small portion of this sample was loaded into an alumina boat and sealed in a silica tube with two steel end caps fitted with three-way valves. This portion ("Sample A") was then heated to 400 °C under a flow of H_2/N_2 (5 % : 95 %) for 8 hours.

A second portion of the sample was then ground together with 0.15 molar equivalents of CuO. A small portion of the unreacted $CeCu_{0.85}OS$: CuO mixture was kept for inspection by XRPD, and the rest of the mixture ("Sample B") was subjected to the same reduction treatment as Sample A. On retrieval from the reduction apparatus, Sample A remained black while Sample B was found to be olive green in colour.

3.3.1 Laboratory XRD

Samples A and B, and the Sample B / CuO mixture, were examined by laboratory XRPD and lattice parameters were obtained by Rietveld refinement (shown in figure 3.9). The lattice parameters of Sample A (set out in table 3.3) showed negligible

change upon reduction, with a unit cell volume equal (within error) to that of the original material. However, the lattice parameters of Sample B were found to have increased significantly and the XRD pattern contained no Bragg reflections from crystalline CuO. These factors, and the fact that the colour of this sample has changed from black to green, are consistent with the consumption of CuO to form a non-Cu-deficient phase under reducing conditions:

$$CeCu_{0.85}OS + 0.15CuO \xrightarrow{400C,\ H_2/N_2} CeCuOS + 0.15H_2O$$

It is also worth noting that the lattice parameters of Sample B appear to be even larger than those of the nearly-stoichiometric sample $CeCu_{0.987(2)}OS$ investigated by neutron diffraction in section 3.2.2, which implies that Sample B may be genuinely fully-stoichiometric (although this claim should be made cautiously as the difference is subtle and the lattice parameters were obtained from different diffractometers). A plot of unit cell volume as a function of composition is shown in figure 3.10, which includes samples 1 and 2 from section 3.2 and also a sample of refined composition $CeCu_{0.762(4)}OS$ by single-crystal XRD from reference [34]. This plot shows a linear relationship between unit cell volume and refined composition, and is consistent with Sample B being fully stoichiometric. These parameters are compared with those of other *Ln*CuOS compounds in figure 3.11.

Examination of the unit cell parameters of Sample A suggests that the nominal composition of $CeCu_{0.85}OS$ is actually an underestimate of the true Cu occupancy, which may be closer to $CeCu_{0.90}OS$ (see figure 3.10). This is consistent with the presence of a small amount of Ce_2O_2S and may reflect high sensitivity of composition to the precise reaction conditions. Further investigation may be neccessary to investigate the relationship between the targeted composition and the actual (resulting) composition under various synthetic conditions. For this particular experiment, this discrepancy in starting composition is not expected to undermine the conclusions drawn from the properties of Sample B (although it does perhaps imply that an

Table 3.3: Lattice parameters obtained by Rietveld refinement against laboratory XRD data for Sample A ($CeCu_{0.85}OS$ heated under H_2/N_2) and Sample B ($CeCu_{0.85}OS$ + CuO, heated under H_2/N_2).

Sample	Original	A	B
a / Å	3.94155(16)	3.94105(8)	3.96379(8)
c / Å	8.3904(4)	8.3922(2)	8.4576(2)
V / Å^3	130.352(14)	130.347(8)	132.883(8)
c / a	2.1287	2.1294	2.1337

excessive amount of CuO was used).

3.3.2 SQUID Magnetometry

Samples A and B were cooled to 5 K in zero applied field, and measurements of magnetisation were taken between $5 - 300$ K in applied fields of 3 T and 4 T. The resulting magnetic susceptibility plots are shown in figure 3.12, and the resulting μ_{eff}^2 values are plotted in figure 3.13.

For both samples, the behaviour of $\chi(T)$ was found to be similar to that observed for the two samples in section 3.2.3, with $1/\chi$ exhibiting a linear region above T = 150 K. Curie constants and effective magnetic moments were calculated as before (see section 3.2.3), resulting in values of 2.38(4) μ_B for Sample A and 2.55(2) μ_B for Sample B. Again, the experimental values appear to correspond very well to calculated values of the free-ion moment for these compounds. This is consistent with the reduction of Ce^{4+} with insertion of Cu to fill the vacancies in the sulfide layer. As with unit cell volume, the effective magnetic moment μ_{eff} of Ce in Sample B is slightly higher than that observed for $CeCu_{0.987(2)}OS$, which appears to suggest that Sample B is fully stoichiometric.

3.4 Structural ordering in $CeCu_{(1-x)}OS$

As discussed in section 3.1, there are several oxysulfide compounds with intrinsically Cu-deficient sulfide layers that are known to exhibit long-range ordering of Cu ions

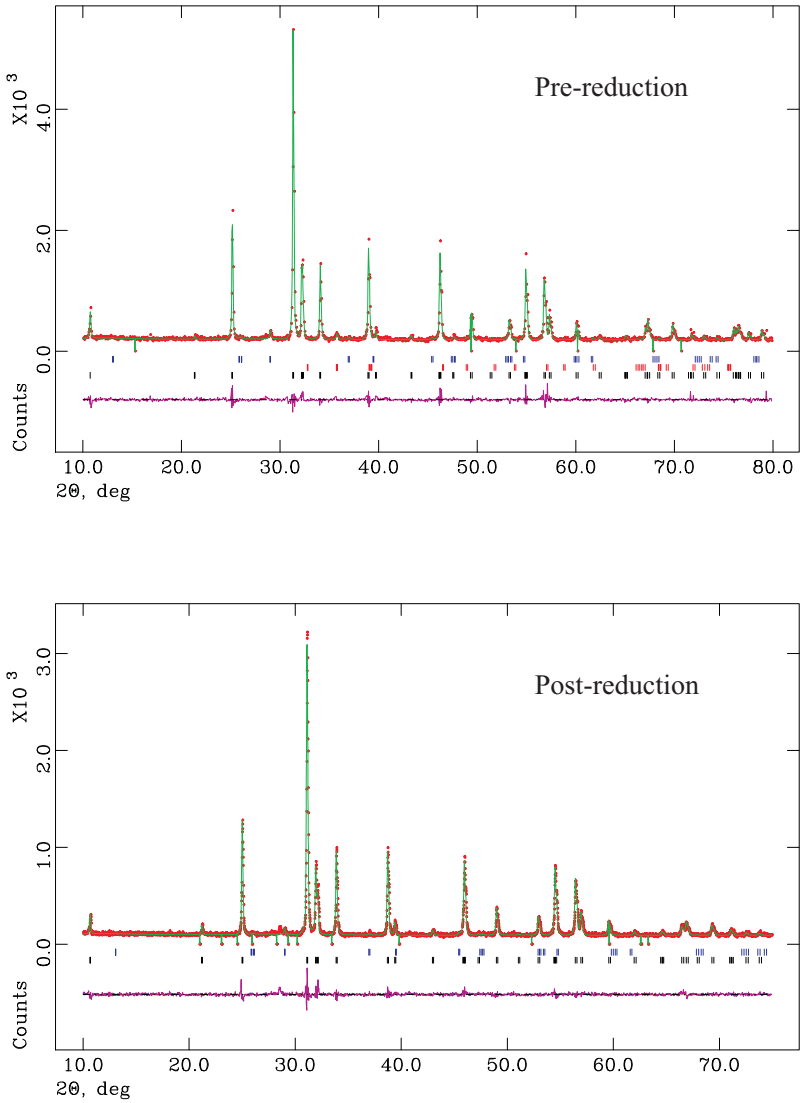


Figure 3.9: Rietveld refinement against laboratory XRPD data, before and after reduction treatment. A small number of individual data points are excluded due to electrical noise in the X-ray detector. Reflection markers: *Black* = CeCuOS; *blue* = Ce_2O_2S; *red* = CuO.

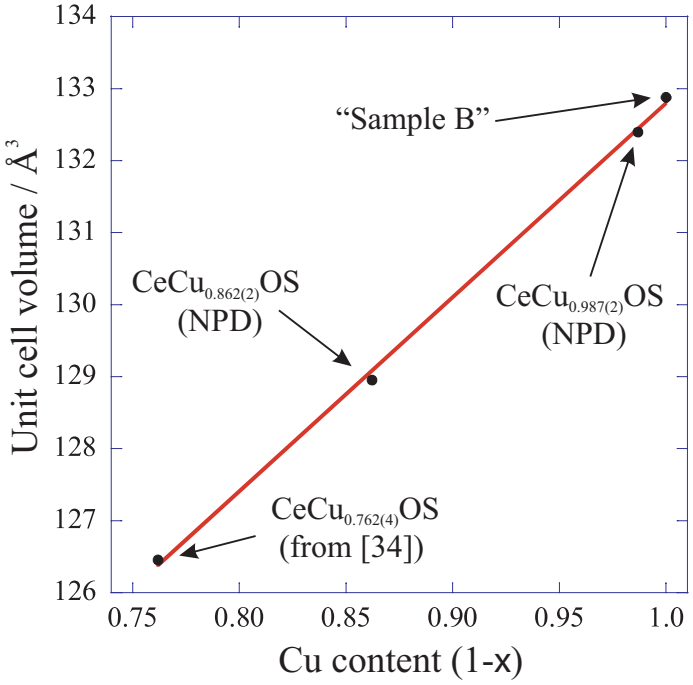


Figure 3.10: A plot of V vs. $(1-x)$ for several samples of CeCu$_{(1-x)}$OS. Error bars corresponding to statistical errors in the refinements are smaller than the points, although these are likely to underestimate the true error in refined composition (x-axis) by up to an order of magnitude.

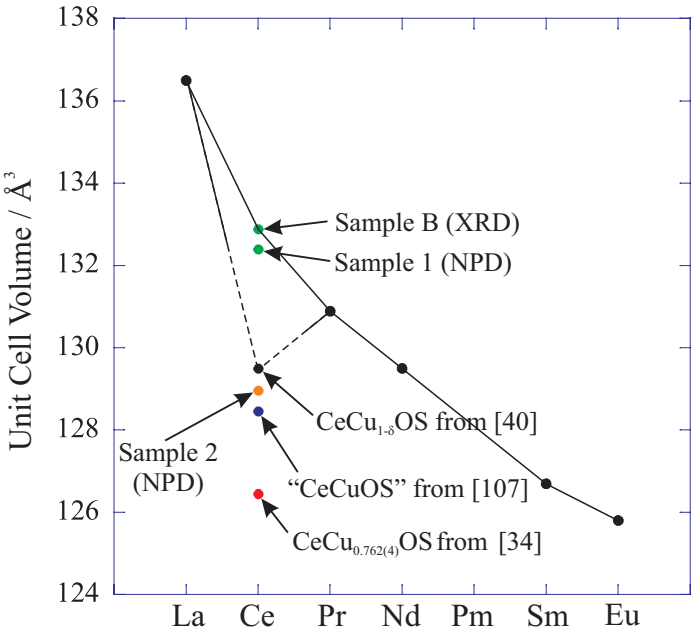


Figure 3.11: Trend in unit cell volumes for *Ln*CuOS plotted with six different samples of *Ln* =Ce, which appear either in the literature or in this work. It can be seen that the nearly/fully-stoichiometric "Sample 1" and "Sample B" from this work have the values expected from the lanthanide contraction. In contrast, the three samples that appear in the literature (references [34, 40, 109]) have a variety of anomalously small unit cell volumes, consistent with the Cu-deficient "Sample 2" described in the text.

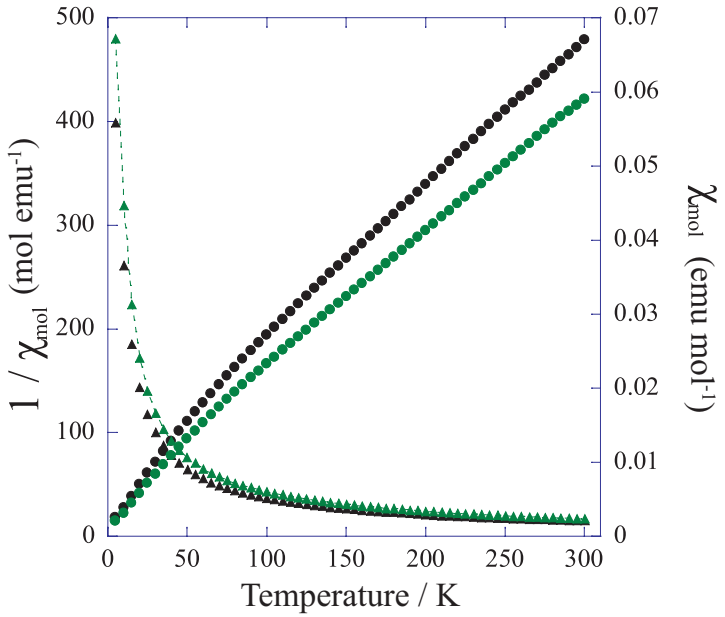


Figure 3.12: Plots of $1/\chi_{mol}$ *vs* T (circles) and χ_{mol} *vs* T (triangles) from magnetic susceptibility measurements of "Sample A" ($CeCu_{0.85}OS$ after heating/reduction *without* CuO, black markers) and "Sample B" ($CeCu_{0.85}OS$ after heating/reduction *with* CuO, green markers). Curie-Weiss behaviour is observed in the region $T > 100$ K.

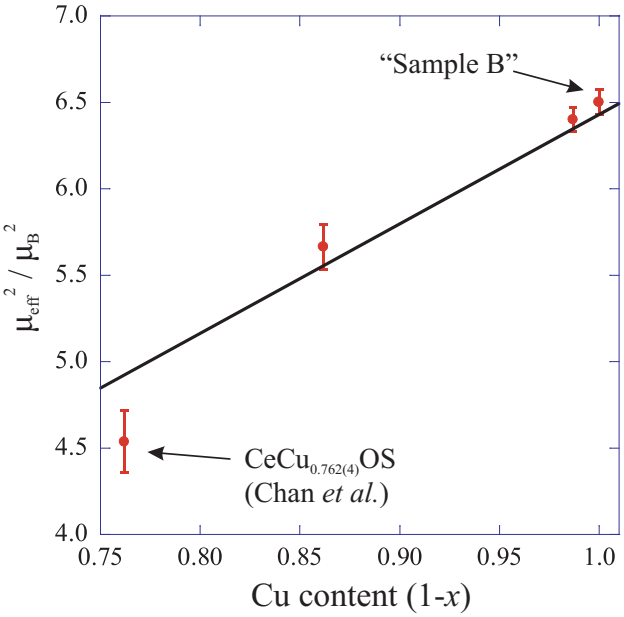


Figure 3.13: A plot of effective magnetic moment squared against refined Cu content for 4 samples of $CeCu_{(1-x)}OS$. The black line represents the calculated trend in free-ion μ^2_{eff} values for a system with one Ce^{3+} per Cu^{+} ion. The point at $(1-x) \approx 0.75$ is taken from reference [34].

and vacancies to form low temperature superstructures. Two significant studies of CeCuOS,[34, 40] and the work described in the previous section of this chapter, have shown that CeCuOS readily forms with a Cu-deficient deficient sulfide layer. Recent work[41, 114] has also confirmed that stable $CeCu_{(1-x)}OS$ phases can be formed with discrete values of x between values of $0 - 0.25$. Hence, this compound is a strong candidate for Cu/vacancy ordering, and the compositional flexibility of the CuS layer leaves open the possibility that there may be more than one stable superstructure dependent on the size of x.

3.4.1 Sample preparation

Two Cu-deficient samples with different nominal compositions were prepared. Sample X, with nominal composition $CeCu_{0.80}OS$, was prepared by a similar method to the samples in section 3.2.1. This sample was examined by laboratory XRPD and found to contain $CeCu_{(1-x)}OS$ as the major phase, with a very small amount (< 2 mol%) of CeO_2 impurity. A second XRPD experiment on this sample, with Si added as a calibrant, yielded a unit cell volume after Rietveld refinement of $V = 127.542(2)$ Å^3, which is consistent with its nominal composition (see figure 3.10 for comparison). This powder was dark brown in colour.

Sample Y, with nominal composition $CeCu_{0.75}OS$, was prepared by a slightly different method that had previously been employed in the successful syntheses of $CeCu_{(1-x)}OS$ compounds.[41] A stoichiometric mixture of $CeCuS_2$, CeO_2 and Cu (1 : 1 : 0.5) was thoroughly ground and pressed into a pellet, then loaded into an alumina crucible and sealed in an evacuated silica tube (pre-dried at 1000 °C under vacuum to remove all traces of adsorbed moisture). The reaction was then heated to 1100 °C for 6 days and cooled radiatively to room temperature. On cooling, it was noted that the tube contained a pale yellow vapour which condensed into orange droplets on further cooling, signifying the presence of excess elemental sulfur in the mixture. This had not been observed in previous syntheses. The pellet was found to be coated

by a very thin layer of indigo-coloured material but became dark brown on grinding. Laboratory XRPD measurements on this sample found that it was almost phase-pure $CeCu_{(1-x)}OS$, with a small amount (< 2 mol%) of Ce_2O_2S as a minority phase. The fact that Ce_2O_2S and excess S were present suggests that this sample of $CeCu_{(1-x)}OS$ should be richer in Cu than its nominal value states. A larger-than-expected unit cell volume of $V = 127.286(7)$ Å^3 confirms this, suggesting that the true composition of the sample is closer to $CeCu_{0.80}OS$. This was confirmed by a neutron diffraction experiment (discussed later in section 3.4.3), which yielded a refined composition of $CeCu_{0.790(2)}OS$.

3.4.2 High resolution XRPD

An initial investigation of the low-T behaviour of Sample Y by neutron powder diffraction revealed extra Bragg reflections that were not readily indexed. As these new reflections were not restricted to long d-spacings, and there was no evidence of a magnetic transition from magnetometry measurements, these new reflections were assumed to be due to structural ordering. To probe this further, a series of high-resolution XRPD experiments were conducted on Sample X and Sample Y using the I11 diffractometer at the Diamond Light Source with the intention of indexing and solving the low temperature structure for each sample, and determining the transition temperature. The neutron diffraction data were then re-visited, and this is addressed later in section 3.4.3.

Experiment 1: Determination of the transition temperature

The first experiment aimed to determine the ordering temperature for the system by taking multiple scans on increasing temperature. The instrument wavelength for this experiment was 0.6010 Å. Sample Y was mounted inside a PheniX cryostat, which was used to attain an initial base temperature of 12 K. The sample was contained in a 0.7 mm aluminium capillary in order to maximise heat transfer and avoid spurious effects

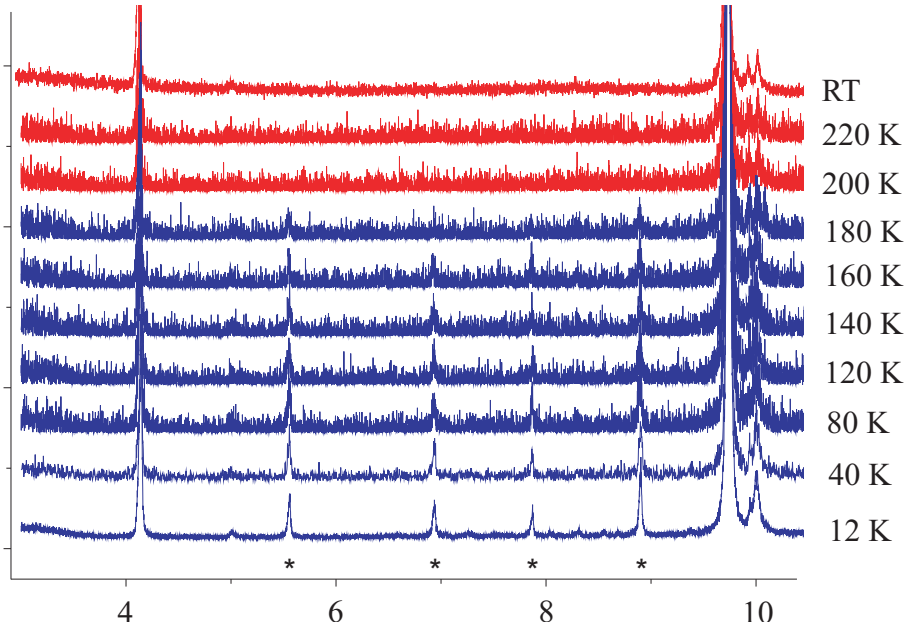


Figure 3.14: Scans of "Sample Y" ($CeCu_{0.790(2)}OS$) at a variety of temperatures (note that some temperatures have been omitted for clarity). Asterisks mark the positions of low-temperature superstructure peaks. Patterns plotted in blue contain discernible superstructure peaks, while patterns plotted in red do not.

caused by the beam heating the sample. This capillary contributes several very intense Bragg peaks to the observed pattern. To obtain high quality structural information about the ordered phase, a long measurement was taken at 12 K. Temperature was then increased to 20 K and short (5 minute) measurements were taken in 20 K increments up to 220 K. A separate scan at ambient temperature was conducted with the sample out of the cryostat contained in a sealed 0.5 mm borosilicate capillary. These scans are plotted in figure 3.14. Each scan was subjected to a Rietveld refinement (using a ZrSiCuAs-type disordered structural model for all temperatures with Al peaks excluded) to obtain a trend in lattice parameters, which is plotted in figure 3.15.

At 12 K, several sharp superstructure peaks are observed at high d-spacings. On heating, these peaks persist until $T > 180$ K, when the material goes through a phase transition to the high temperature ZrSiCuAs structure. This shows lattice parameters decreasing smoothly as T decreases, suggesting that the sample is genuinely in equilibrium with the cryostat environment with no spurious beam-heating effects

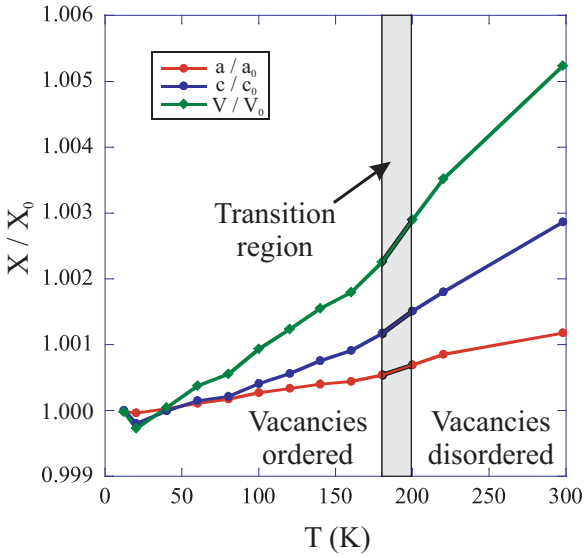


Figure 3.15: A plot of normalised unit cell parameters from "Sample Y" ($CeCu_{0.790(2)}OS$) as a function of increasing temperature, with the structural transition region highlighted in grey. These lattice parameters were obtained by Rietveld refinement against XRPD data from the I11 diffractometer.

(which can sometimes occur if the exchange gas inside the capillary condenses - see the Supporting Information from reference [112]).

Experiment 2: Solving the Low-*T* Structure

In a second experiment on I11, the vacancy-ordered crystal structures of Samples X and Y were investigated at a temperature of 100 K. The incident beam wavelength for this experiment was 0.8269 Å. Samples were sealed in 0.5 mm borosilicate capillaries and mounted on a spinning sample stage. A nitrogen cryostream was used to cool the samples to 100 K. Sample X was cooled rapidly to 200 K (just above the transition temperature), then cooled slowly to 100 K at a rate of 3 K min^{-1} to avoid freezing any disorder into the system. Sample Y was treated similarly, and cooled at a slower rate of 1 K min^{-1}. Both samples were also measured at ambient temperature.

Visual comparison of the patterns obtained by cooling slowly to 100 K shows that low-*T* Bragg reflections occur at the same *d*-spacings in each sample, indicating that the superstructure is the same in both. However, there is a striking difference in the peak profiles of the two samples. Sample X exhibits Bragg reflections that are

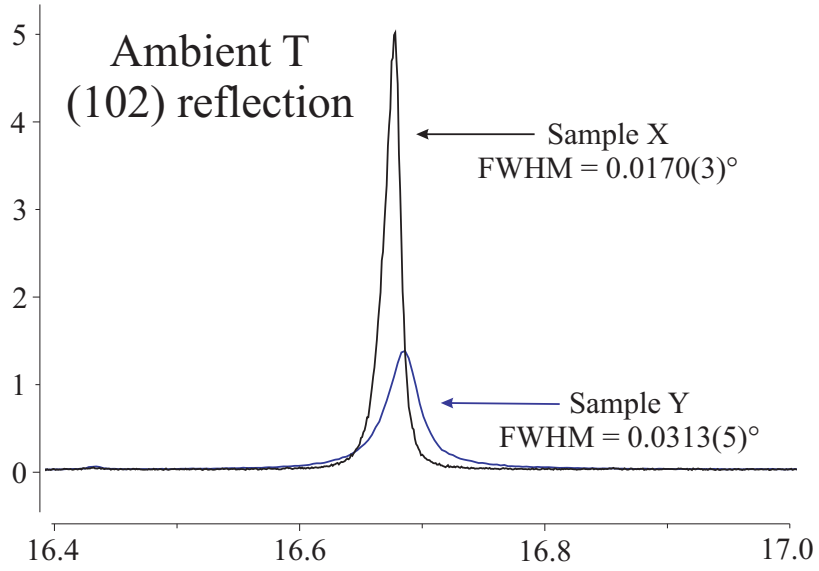


Figure 3.16: The (102) Bragg reflection, obtained from the I11 diffractometer at ambient T, illustrating the typical peak shapes for "Sample X" (approximate composition $CeCu_{0.8}OS$) and "Sample Y" (refined composition $CeCu_{0.790(2)}OS$ - see section 3.4.3). FWHM values were obtained from peak fits using the program CMPR.[115]

significantly more intense and sharper than those of Sample Y (illustrated in figure 3.16). Consequently, at 100 K the superstructure peaks in Sample X can be seen across a broader range of d-spacings than those in Sample Y, making Sample X more favourable to index.

The first 35 Bragg reflections of the 100 K pattern of Sample X were subsequently indexed using the Crysfire powder indexing suite.[116] The five results with the highest figures of merit all successfully indexed the first 20 peaks and all corresponded to a tetragonal unit cell with lattice parameters $a \simeq 8.74$ Å and $c \simeq 8.29$ Å. This result was then processed using the Celref/Chekcell program to generate a possible space group, which yielded best estimates for $P4/nmm$ and $P4/n$.

Comparison of the indexed low-temperature unit cell with the refined high-temperature unit cell shows that the a-parameter has expanded by a factor of $\sqrt{5}$ on ordering, while there is no significant change in the c-parameter. If this expanded unit cell is overlaid on to the high-T cell (as in figure 3.17), it can be seen that the

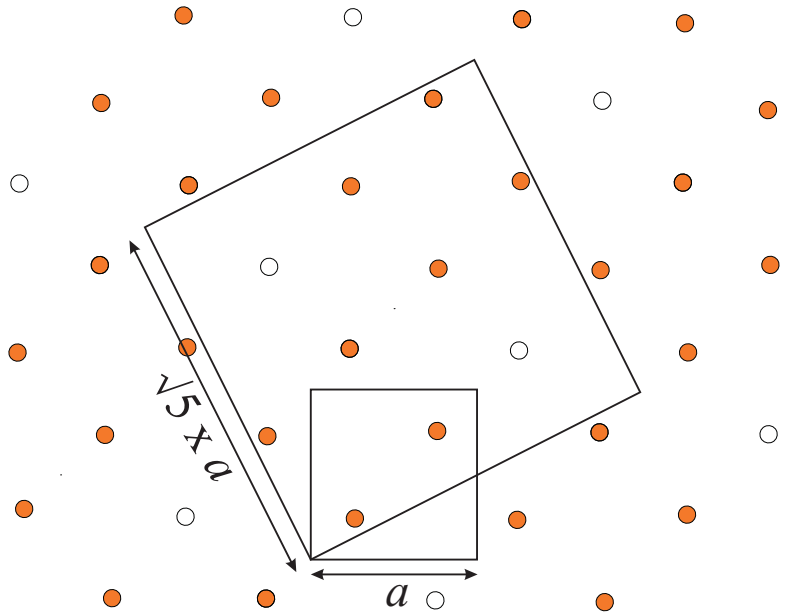


Figure 3.17: Atomic arrangement of the Cu plane viewed along the c-axis, illustrating the basal expansion of the unit cell with a loss of mirror symmetry. White circles indicate possible Cu vacancies.

internal symmetry must be lower than that of the original cell, as the positions of the Cu ions can no longer be described by the orthogonal mirror planes of the $P4/nmm$ space group. However, an n glide plane (perpendicular to the c-axis) is still present, which is consistent with the $P4/n$ space group.

These indexing results were used to construct a new crystallographic model for low temperature $CeCu_{0.8}OS$, with lattice parameters derived from the high-temperature phase ($\sqrt{5}a \times \sqrt{5}a \times c$) and atomic positions transformed from the high-temperature cell into the space group $P4/n$. This space group has two alternative origins; origin choice 1 (at $\bar{1}$) is transformed to origin choice 2 (at $\bar{4}$) by a translation of $+x/4 - y/4$. Origin choice 2 was used for this model. Cu atoms are therefore located on the $8g$ and $2b$ positions. It was noted that, if the $2b$ position were to be entirely unoccupied and the $8g$ position fully occupied, the correct stoichiometry for the compound is obtained, and the vacancies are ordered crystallographically.

Rietveld refinement was then conducted against the data collected from Sample X. Due to a relatively short data collection time and significant beam absorption, attempts to allow the thermal displacement parameters to refine anisotropically yielded several

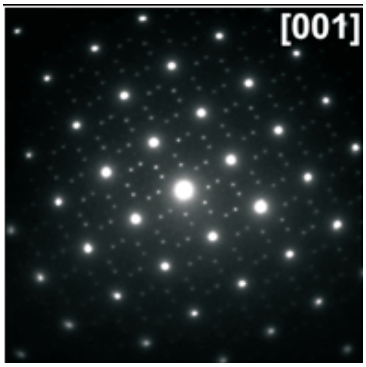
Table 3.4: Atom site symmetries, refined atomic positions, fractional site occupancies and isotropic displacement parameters for vacancy-ordered $CeCu_{0.8}OS$ (Sample X) at 100 K. Errors represent 1 estimated standard deviation, as calculated by GSAS.

Space Group = P4 / *n* (origin 2) *a* = *b* = 8.742511(4) Å; *c* = 8.283150(7) Å; *V* = 633.094(1) Å^3						
Atom	Site	x	y	z	Occupancy	U_{iso} ($\times$100)
Ce	8*g*	0.55308(6)	0.35068(8)	0.15773(3)	1.0	0.526(3)
Ce	2*c*	3/4	3/4	0.13507(8)	1.0	0.654(10)
Cu	8*g*	0.5426(1)	0.8456(2)	0.4992(2)	1.0	0.158(9)
Cu	2*b*	1/4	3/4	1/2	0.025(6)	0.158(9)
O	8*g*	0.5534(8)	0.8448(8)	0.0016(9)	1.0	0.714(35)
O	2*a*	1/4	3/4	0	1.0	0.714(35)
S	8*g*	0.5437(3)	0.3501(3)	0.6698(1)	1.0	0.714(17)
S	2*c*	1/4	1/4	0.6690(4)	1.0	0.614(46)

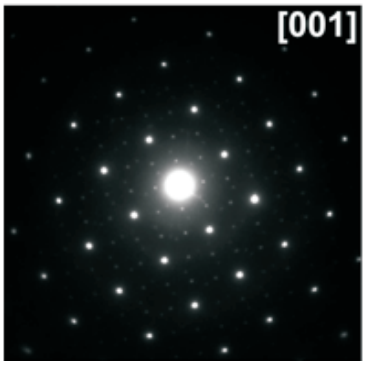
negative values (which have no physical foundation). These parameters were therefore allowed to refine isotropically. The starting model included a small amount of Cu on the 2*b* site, where the occupancy level was allowed to refine freely and the thermal displacement parameter was constrained to be equal to that of the principal Cu (8*g*) site. The U_{iso} values of both oxide sites were also constrained to be equal (due to the relatively weak scattering power of O^{2-}). The model was found to account for all of the superstructure peaks observed at low T (see the Rietveld refinement illustrated in figure 3.19), and some of the results are displayed in table 3.4.

Subsequent low temperature electron diffraction measurements on a sample of $CeCu_{0.8}OS$ were conducted by Prof. Joke Hadermann, who also analysed the results. These experiments confirmed that the space group $P4/n$, deduced from XRPD, is the correct one for the low temperature structure. These results were also consistent with a $(\sqrt{5}a \times \sqrt{5}a \times c)$ expansion of the high-temperature cell with vacancies on the 2*a* Cu site (in $P4/n$ with origin choice 1). Images from several temperatures, and a diagram of the indexed peaks, are shown in figure 3.18 on the next page.

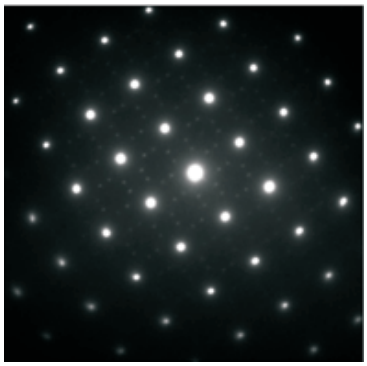
Consideration of the multiplicities of the atomic sites suggests that a negligible occupancy of the 2*b* site by Cu, with full occupancy of the 8*g* site, could account for both vacancy ordering and the nominal stoichiometry of the phase. Refinement of the Cu occupancy on the 2*b* site appears to confirm this, as it resulted in a very small



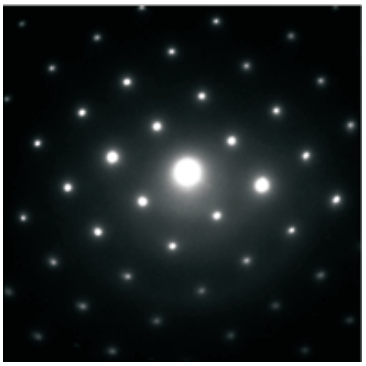
203 K
(twinned crystals)



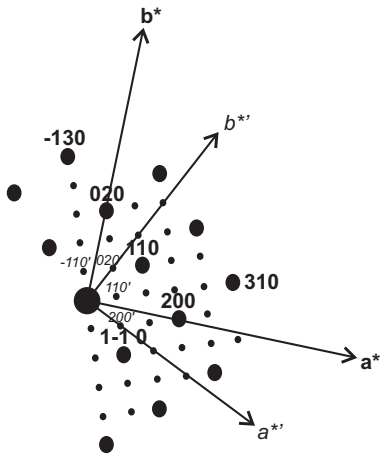
203 K
(after attempt to separate twins)



223 K
(twinned)



243 K



This font for the parent cell

This font for the supercell, in which hk0: h+k = 2n

Figure 3.18: Low temperature electron diffraction data from crystals of $CeCu_{0.8}OS$, measured along the *c*-axis. (Figure supplied by Prof. J. Hadermann).

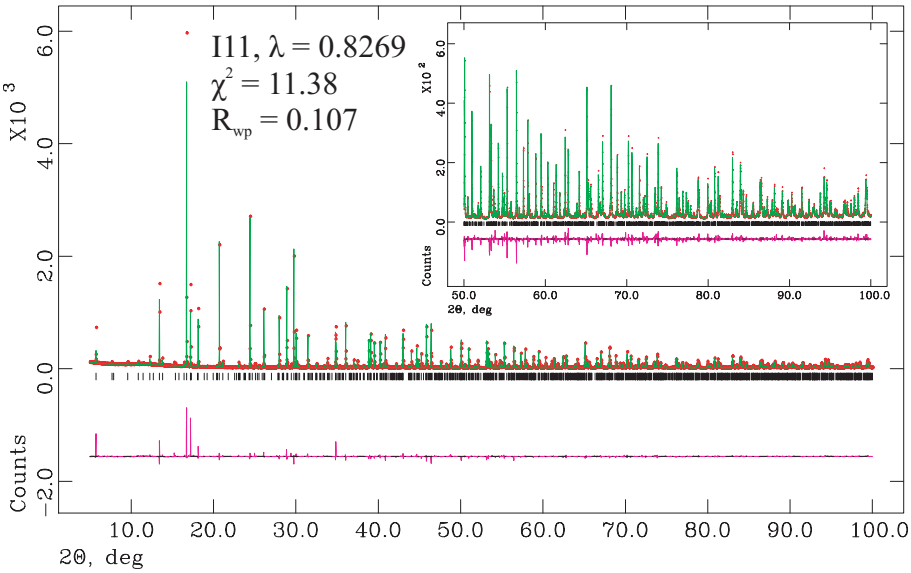


Figure 3.19: Rietveld refinement against low temperature (100 K) XRD data from I11 ($\lambda = 0.8269$ Å). Data from the region $100 \leq 2\theta < 150°$ were also used in the refinement but are not displayed here for clarity. Black markers indicate Bragg reflections due to $CeCu_{0.80}OS$ (Sample X). Inset shows the region $50 \leq 2\theta \leq 100°$.

value of 0.025(6). It can be seen from atomic co-ordinates and from the inter-atomic distances that a subtle relaxation of the crystal structure occurs about the immobile Cu-vacancies, with 4 discrete Cu-S distances becoming apparent. The sulfide ions on the 2*c* site are fully co-ordinated by 4 Cu and 4 Ce in a square anti-prismatic environment (as in the high temperature phase), with 4 equivalent S-Cu distances of 2.442(2) Å. This distance is significantly longer than those exhibited by sulfide ions on the general-symmetry 8*g* site, which are each adjacent to one Cu vacancy and therefore only 7-coordinate, with three inequivalent S-Cu distances of 2.336(3), 2.401(3) and 2.416(3) Å. There are also some differences in S-Ce distances between the two S sites: 8-coordinate S has 4 equivalent S-Ce distances of 3.139(2) Å, while 7-coordinate S has two short S-Ce distances (3.16 Å) and two long S-Ce distances (3.10 Å). However, the mean Ce-S distance is almost the same for each site. This ordering scheme is illustrated in figure 3.20, and the two different sulfide coordination environments are shown in figure 1.3.

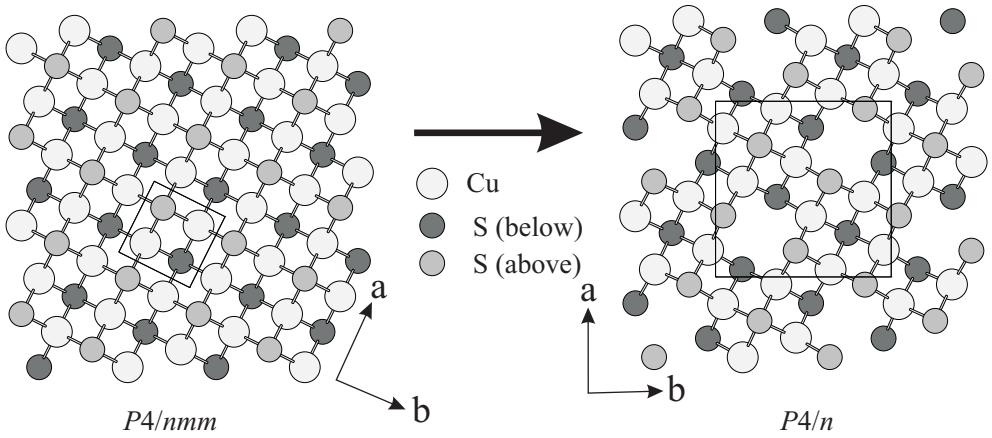


Figure 3.20: The $Cu_{0.8}S$ layer at high temperature (left) where Cu ions and vacancies are disordered; and below 180 K (right) where the vacancies are ordered. The square outlines indicate the respective unit cells.

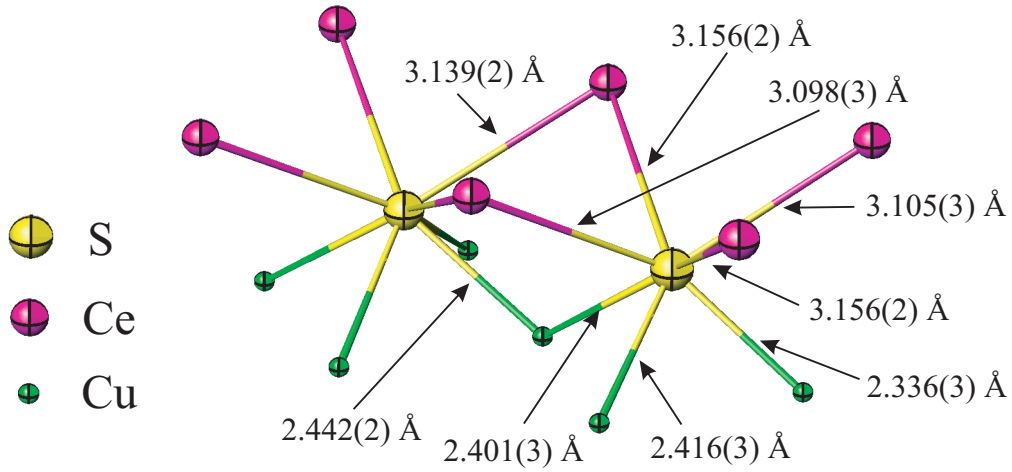


Figure 3.21: Thermal displacement ellipsoids (99 % probability) showing S-Cu and S-Ce distances for 8-coordinate S (left hand side) and 7-coordinate S (right hand side).

After successfully deriving and refining an appropriate structural model for vacancy-ordered $CeCu_{0.80}OS$ (using the highly crystalline Sample X), the same model was used for low temperature Rietveld refinement against data from Sample Y. This refinement was conducted in a similar way to that of Sample X, and it was again found that thermal displacement parameters could not be refined anisotropically. Refined lattice parameters of $a = 8.73989(3)$ Å, $c = 8.28487(5)$ Å and $V = 632.846(6)$ Å^3 are very similar to those of Sample X and consistent with the refined composition of $CeCu_{0.79(1)}OS$ (from section 3.4.3). Occupancy of the 2*b* site by Cu was again allowed to refine freely and yielded a value of 0.05(1).

Effect of cooling rate on ordering

To assess the effect of cooling rate on the superstructure, Sample Y was subjected to two different cooling regimes: the first (discussed above) was very slow cooling at 1 K min^{-1} from 200 K to 100 K, with rapid (5 min) scans taken at 20 K intervals. For the second cooling run, the cryostream was cooled to 100 K off-line, then used to quench the sample from ambient *T* down to 100 K. The effect of quenching the sample through the transition temperature is illustrated in figure 3.22. It can be seen that Bragg reflections due to the superstructure are strongly suppressed by this rapid cooling, although they are not completely absent, suggesting that there is still some small degree of ion/vacancy ordering in the $Cu_{0.8}OS$ layer (although this would be extremely difficult to see with a conventional laboratory diffractometer). It is reasonable to assume that the inherent disorder of the high-temperature phase has been frozen in to the layer by quenching.

3.4.3 Neutron diffraction

Prior to the high-resolution XRD experiments described above, the Polaris diffractometer at ISIS was used to obtain neutron diffraction patterns from Sample Y at both ambient temperature and at 5 K. Structural parameters were obtained from

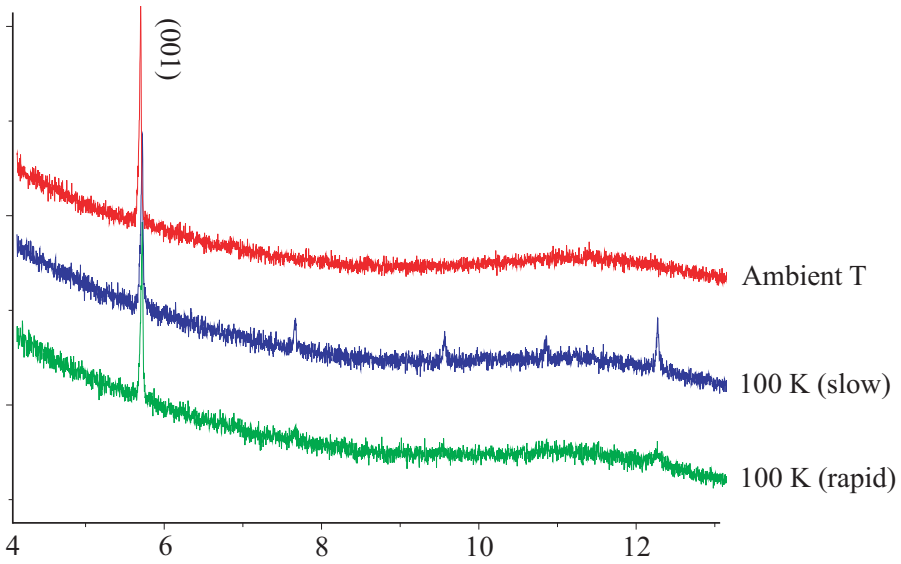


Figure 3.22: X-ray powder diffraction patterns of "Sample Y" ($CeCu_{0.790(2)}OS$) obtained from the I11 diffractometer at ambient T (red), and at 100 K by slow cooling (blue) or rapid quenching (green). Note that the superstructure peaks are far more prominent after slow-cooling.

the ambient temperature data by Rietveld refinement (shown in figure 3.23 along with a refinement against low temperature data). Refinement of the fractional occupancy of Cu yielded a composition of $CeCu_{0.790(2)}OS$, consistent with the refined lattice parameters of $a = 3.91138(3)$ Å, $c = 8.30746(7)$ Å and $V = 127.095(2)$ Å^3. A comparison of the patterns taken at the two temperatures revealed that several new Bragg reflections at high d-spacings had appeared on cooling, consistent with long range vacancy ordering (as the X-ray diffraction experiments have now ruled out a magnetic origin). These peaks could not be modelled by a standard ZrCuSiAs structure (space group $P4/nmm$), but attempts to index the low temperature pattern were unsuccessful, due to the small number of discernible peaks and the low resolution of the high d-spacing 35° detector bank. However, Rietveld refinement became possible after a model of the superstructure was obtained by high-resolution XRD.

Data from all three detector banks (35°, 90° and 145°) were used in the refinement. Isotropic thermal displacement parameters were constrained for each atom type (such that each element has the same U_{iso} whether it is on a 2-fold site or an 8-fold site). The fractional occupancies of the two Cu sites were allowed to refine,

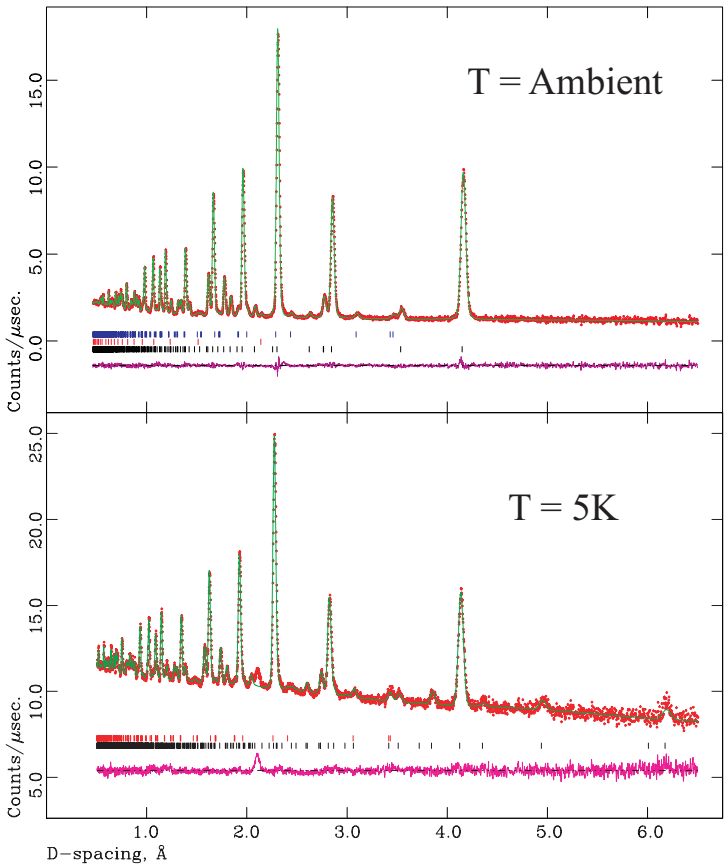


Figure 3.23: Rietveld refinements against data from the Polaris low-angle (35°) detector bank for "Sample Y" ($CeCu_{0.790(2)}OS$). Data were collected at ambient temperature and at 5 K. Reflection markers: *Black* = $CeCu_{0.790(2)}OS$; *red* = Ce_2O_2S; *blue* = V (from the sample container).

with initial occupancy values of 1.0 for $8g$ and 0.0 for $2c$ (corresponding to a composition of $CeCu_{0.80}OS$). An appropriate constraint was applied to maintain this initial stoichiometry.

3.4.4 Comparison with a family of iron selenides $K_xFe_{2-y}Se_2$

This type of $\sqrt{5}a \times \sqrt{5}a \times c$ vacancy-ordered superstructure is not unique to $CeCu_{0.8}OS$. For example, a similar vacancy-ordered superstructure is exhibited by the antiferromagnetic iron selenide $TlFe_{1.7}Se_2$, which has a layered $ThCr_2Si_2$-type substructure.[117] Very recently, research into layered Fe-based chalcogenides has investigated other compounds of type $K_xFe_{2-y}Se_2$, some of which are found to be superconducting at high temperatures.[47] The structures of these compounds are also

Table 3.5: Refined atomic coordinates, site occupancies and isotropic thermal displacement parameters for disordered $CeCu_{0.8}OS$ from Rietveld refinement against ambient temperature neutron diffraction data from Polaris.

Space Group = P4 / *nmm* (origin 2) $a = b = 3.911381(27)$ Å; $c = 8.30746(7)$ Å; $V = 127.095(2)$ Å^3 $\chi^2 = 1.421$; $R_{wp} = 0.0176$							
Atom	Site	x	y	z	Occupancy	U_{11} ($\times 100$)	U_{33} ($\times 100$)
Ce	2*c*	1/4	1/4	0.15315(6)	1.0	0.453(11)	1.123(18)
Cu	2*b*	1/4	3/4	1/2	0.790(2)	2.096(19)	1.326(24)
O	2*c*	1/4	1/4	0.6697(1)	1.0	0.898(21)	0.84(4)
S	2*a*	1/4	3/4	0	1.0	0.588(9)	0.956(19)

Table 3.6: Refined atomic coordinates, site occupancies and isotropic thermal displacement parameters for vacancy ordered $CeCu_{0.8}OS$ from Rietveld refinement against neutron diffraction data from Polaris (T = 5 K).

Space Group = P4 / *n* (origin 2) $a = b = 8.74574(14)$ Å; $c = 8.29377(17)$ Å; $V = 634.374(19)$ Å^3 $\chi^2 = 2.131$; $R_{wp} = 0.0096$						
Atom	Site	x	y	z	Occupancy	U_{iso} ($\times 100$)
Ce	8*g*	0.552747	0.347066	0.157394	1.0	0.447(32)
Ce	2*c*	3/4	3/4	0.1384(6)	1.0	0.447(32)
Cu	8*g*	0.54370(31)	0.84699(30)	0.50629(29)	0.960(3)	0.170(22)
Cu	2*b*	1/4	3/4	1/2	0.159(13)	0.170(22)
O	8*g*	0.5503(4)	0.8428(4)	0.0021(6)	1.0	0.507(33)
O	2*a*	1/4	3/4	0	1.0	0.507(33)
S	8*g*	0.5463(9)	0.3445(9)	0.6698(5)	1.0	0.11(4)
S	2*c*	1/4	1/4	0.6725(17)	1.0	0.11(4)

based on the layered $ThCr_2Si_2$ structure, with anti-PbO-type $Fe_{2-y}Se_2$ layers separated by K^+ ions. It has been shown that both cation sites host an appreciable number of vacancies in these materials, with typical values of $y \simeq 0.4$ and $x \simeq 0.25$.

Single crystal XRD experiments on $K_{0.774(4)}Fe_{1.613(3)}Se_2$, $K_{0.738(6)}Fe_{1.631(3)}Se_2$ and $Cs_{0.748(2)}Fe_{1.626(1)}Se_2$ have shown that cations and vacancies are ordered at room temperature in the $Fe_{2-x}Se_2$ layer to create a $\sqrt{5}a \times \sqrt{5}a \times c$ supercell of the $ThCr_2Si_2$ structure, with symmetry reduced from $I4/mmm$ to $I4/m$.[48] The superstructures are very similar to that described above for $CeCu_{0.8}OS$. The order/disorder transition temperature has been reported as 578 K in $K_{0.8}Fe_{1.6}Se_2$,[118] and the structural ordering is apparently intimitely involved in the establishment of long-range antiferromagnetic order ($T_N = 559$ K). This ordering temperature is considerably higher than the typical ordering temperatures observed in copper sulfides (typically ~ 220 K),[111, 35] and may reflect the difference in ion mobility in these two types of layer. Interestingly, vacancy ordering is yet to be reported in Cu-deficient Se layers, and has not been observed in low-temperature diffraction measurements of Se-rich members of the series $Sr_2MnO_2Cu_{1.5}S_{2-x}Se_x$.[35] The reasons for this are currently unclear, but it may be that Cu has a lower mobility in the selenide which inhibits the formation of the ordered state. An alternative scenario is that better screening of the Cu^+ charges by Se^{2-} and/or the larger lattice parameters of the selenides (compared to the sulfides) decrease the Coulombic driving force for ordering in these compounds.

3.5 Summary and conclusions

The work described in the first part of this chapter aimed to establish the nature of the air sensitivity of CeCuOS, by determining the compositional change that accompanies a colour change from green/brown to black when the compound is exposed to air. This problem was addressed using crystallographic methods (primarily neutron powder diffraction) and by SQUID magnetometry. Neutron diffraction measurements showed

that, on exposure to air, a significant amount of Cu is extruded from the sulfide layer to leave a Cu-deficient phase with a refined composition of $CeCu_{0.862(2)}OS$. The extruded Cu was found to be oxidised to Cu^{2+}, forming CuO of low crystallinity. It is possible that this CuO (which is black) is at least partially responsible for the observed colour change. Magnetometry measurements showed that the effective magnetic moment of Ce was diminished from $2.53\mu_B$ in non-air-exposed $CeCu_{0.987(2)}OS$ to a value of $2.38\mu_B$ in oxidised $CeCu_{0.862(2)}OS$, indicating that a transition from a formally trivalent Ce^{3+} compound to a mixed-valence $Ce^{3+/4+}$ compound has occurred. This is consistent with observations of mixed-valence Ce in this compound in other studies, and implies that several studies of nominally stoichiometric CeCuOS have actually been conducted on Cu-deficient mixed-valence samples of type $CeCu_{(1-x)}OS$.

Once the role of Cu-extrusion in the oxidation of CeCuOS had been identified, a new synthesis route to stoichiometric CeCuOS was devised. This utilised the presence of reducible Cu^{2+} to reductively insert Cu^{+} ions into a Cu-deficient sample $CeCu_{0.85}OS$ at moderate temperatures (400 °C) under a reducing H_2/N_2 (5 : 95) atmosphere. This was found to generate a sample of CeCuOS with the largest unit cell volume and highest effective magnetic moment for Ce than any other reported sample, which is consistent with a genuine Ce^{3+} compound of fully-stoichiometric composition CeCuOS. This method may represent the most reliable route to this fully stoichiometric phase.

The second part of this chapter describes the study of the low temperature structure of two samples of composition $CeCu_{0.8}OS$ by variable-temperature neutron powder diffraction and high-resolution X-ray diffraction. This material was found to undergo a structural phase transition as it was cooled below 200 K, with the appearance of a superstructure due to ordering of Cu^{+} ions and vacancies. The superstructure was solved by indexing high-resolution XRPD data (taken at 100 K) and found to have a unit cell equivalent to a $\sqrt{5}a \times \sqrt{5}a$ basal plane expansion of the high-temperature (ZrSiCuAs) unit cell, with a change in space group from $P4/nmm$ to a $P4/n$, reflecting a decrease in internal symmetry. This was subsequently confirmed

by a low temperature electron diffraction experiment. This new model was used in Rietveld refinements against low-temperature XRPD and NPD data and found to account for all of the superstructure peaks. The ordering scheme of the Cu^{+} ions and vacancies in this material is different from that which occurs in similar Cu-deficient layers of composition $Cu_{0.75}S$ (as in the layered oxysulfide $Sr_2MnO_2Cu_{1.5}S_2$), but several studies have demonstrated the stability of $CeCu_{(1-x)}OS$ compounds with different discrete value of x from $0 \leq x \leq 0.25$. It is therefore possible that the low-T ordering scheme in $CeCu_{(1-x)}OS$ could be controlled by tuning the composition of the compound.

Chapter 4

Structure and Superconductivity of LiFeAs and $Li_{1-y}Fe_{1+y}As$

4.1 Introduction

The report of superconductivity below 26 K in fluoride-doped $LaFeAsO_{(1-x)}F_x$ by Kamihara *et al* [21] triggered a period of intense research into the superconducting properties of isostructural ZrSiCuAs-type compounds with anti-PbO-type iron arsenide layers. For this class of compounds, the superconducting transition temperature was quickly optimised by substituting smaller isovalent lanthanides for La^{3+}, leading to a reported maximum T_c of 55 K in $SmFeAsO_{0.9}F_{0.1}$,[61] while similar high T_cs were reported for compounds that were nominally oxide-deficient.[119] Further investigation showed that aliovalent doping on the rare-earth site could also induce superconductivity, as demonstrated by the Th^{4+} compound $Gd_{0.8}Th_{0.2}FeAsO$ [120] with a T_c of 56 K, currently the highest reported T_c of all known Fe-based superconductors.

Research then began to focus on the synthesis of new compounds containing anti-PbO-type FeAs layers. A major breakthrough in this area came with a report by Rotter *et al* [46] of superconductivity below 38 K in $Ba_{0.6}K_{0.4}Fe_2As_2$, which takes the common layered $ThCr_2Si_2$ structure. This uncovered the possibility of

a whole family of structurally-related Fe-based superconductors, similar to that of the superconducting cuprates. As with the LaFeAsO-type superconductors, it was apparent that the non-superconducting "parent" phase $BaFe_2As_2$ must be doped in order to attain a superconducting phase.

In response to this work, we conducted an extensive literature search and utilised the Inorganic Crystal Structure Database [121] to identify other known compounds with anti-PbO-type FeAs layers, with the intention of synthesising such compounds and assessing their magnetic properties. In the course of this investigation, we identified LiFeAs as a possible candidate for superconductivity.

The synthesis of LiFeAs was first reported by Juza and Langer in 1968,[78] and the compound had received very little attention since. The structure was determined by XRPD, and shown to consist of anti-PbO-type layers of FeAs with Li in the inter-layer space. Their discussion includes detailed consideration of the precise location of the Li ions, with their analysis favouring a pseudo-octahedral co-ordination environment (which is perhaps described more accurately as square-pyramidal) over an alternative tetrahedral site (which they find to be occupied in the analogous layered compound LiMnAs), although they were unable to draw firm conclusions. The suggested structures are illustrated in figure 4.1. The composition was inferred from the molar ratios of the starting materials and assessed by density measurements, and reported to be Li-rich with stoichiometry $Li_{1.1}FeAs$. This conclusion adds to the uncertainty over the Li position: assuming the Fe and As sites are fully occupied, where should the extra 0.1 Li reside? One suggestion is that both possible inter-layer sites are occupied to some extent (e.g. 1.0 Li on a square-pyramidal site and 0.1 Li on a tetrahedral site), which may contribute to the ambiguity over the average Li position. However, this model requires 0.1 Li ions to occupy a site with four other Li in its nearest-neighbour co-ordination sphere, which does not seem reasonable. Alternatively this scenario could be accommodated by a 90 % occupancy of both the Fe and As sites, with the Li site fully occupied, although this also seems unlikely.

Their study also demonstrates that there is considerable compositional phase-

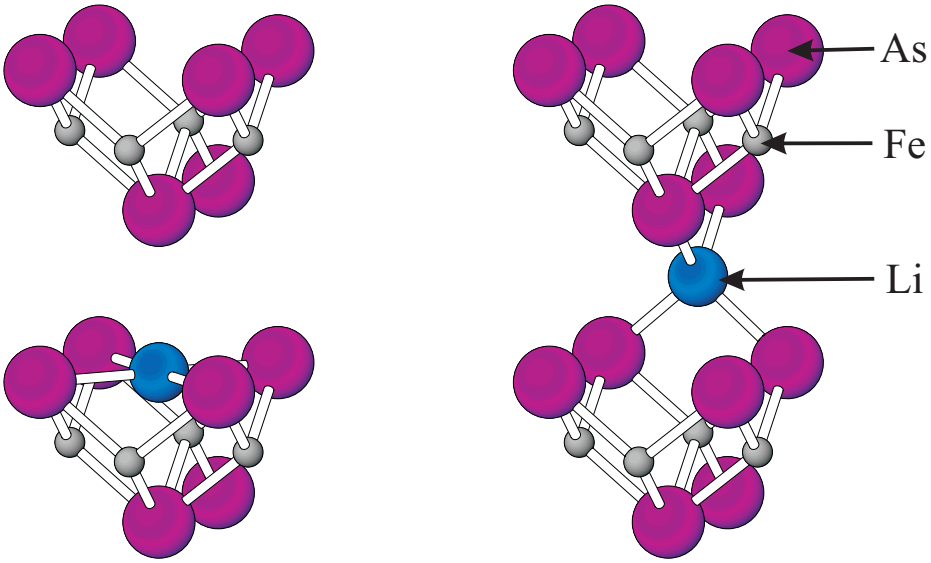


Figure 4.1: A fragment of the LiFeAs structure illustrating the two possible Li sites proposed by Juza and Langer:[78] a pseudo-octahedral/square-pyramidal site corresponding to the PbFCl structure (left hand side), or a tetrahedral site corresponding to an ordered fluorite structure (right hand side). Note that, for clarity, only one Li ion has been plotted for each structure.

width in this compound, and a series of samples of type $Li_{1.1-y}Fe_{1+y}As$ were synthesised with nominal metal:arsenide ratios of 2.1:1. It was shown that lattice parameters decrease linearly as Fe-content is increased, with $x = 0.14$ as the limiting composition. Beyond this limit, the samples became mixtures of "$Li_{0.96}Fe_{1.14}As$" and the isostructural binary arsenide Fe_2As. Again this raises questions over the location of the extra 0.1 metal ions, but more importantly it implies that Li and Fe are able to share the same site within the structure.

The large question marks still hanging over the structure and composition of this compound provided an obvious starting point for a new investigation into LiFeAs, and needed to be addressed before any meaningful study into possible superconducting properties could go ahead. For these purposes it was clear that investigation by X-ray diffraction alone may not be sufficient due to the weak scattering amplitude of Li, which proved to be a serious handicap in the original study. The use of neutron diffraction alone could also be problematic due to the possibility of site sharing between Li and Fe and consequent null-scattering effects (coherent scattering lengths of Li and Fe are -1.90 fm $+9.45$ fm respectively). The work in this chapter involves an initial structural and compositional characterisation of two samples of LiFeAs by combined XRPD-NPD to determine unambiguously the site occupied by Li and the M:As ratio.

This is followed up by a combined XRPD-NPD study of a series of Fe-rich compositions of type $Li_{1-y}Fe_{1+y}As$, to confirm the range of compositions adopted by the system and the location of the extra Fe ions. Finally, magnetic/superconducting properties were investigated by D.C. SQUID magnetometry and correlated with structural properties and composition.

4.2 Initial synthesis of two samples of LiFeAs

The first attempts to synthesise LiFeAs loosely followed the techniques used by Juza and Langer.[78] One sample, with nominal composition LiFeAs, was synthesised by

sealing stoichiometric quantities of Li metal and FeAs powder (previously synthesised from the elements - see Chapter 2) in a welded tantalum tube under flowing argon, then heating at 800 °C for 36 hours. The product was then re-ground, pelletised and sealed in a fresh Ta tube, and held at 800 °C for a further 72 hours, before being quenched into cold water. The resulting black powder was inspected by laboratory XRPD and found to contain LiFeAs as the major phase (89.5(5) mol%), with a smaller quantity of FeAs as a minor component (10.5(5) mol%). The lattice parameters of this sample were $a = 3.775(1)$ Å and $c = 6.358(2)$ Å. Magnetometry measurements showed a strong transition to a diamagnetic state below $\sim$ 16 K, with a splitting between field cooled (FC) and zero-field cooled (ZFC) scans. This is a manifestation of the Meissner-Ochsenfeld effect, and the sample is therefore superconducting below 16 K.

This sample proved to be highly unstable in air, with rapid decomposition evident from an XRPD experiment conducted on an open slide. All subsequent laboratory XRPD studies on LiFeAs (and derivatives) utilised an air-tight sample cell, loaded under an argon atmosphere, to avoid this decomposition.

A large ($\sim$ 3 g) second sample ("sample 2") was prepared with a nominal composition $Li_{1.1}FeAs$ using stoichiometric quantities of Li_3As powder, FeAs powder, and Fe powder. The ground mixture was pelletised and sealed in an alumina-lined evacuated silica ampoule, then heated at 800 °C for 48 hours and quenched in air. On removal from the furnace, it was noted that the inside of the silica tube was discoloured. However, inspection of the product by laboratory XRPD revealed that this sample contained no crystalline impurities, and had lattice parameters $a = 3.774(1)$ Å and $c = 6.354(2)$ Å, equal within experimental uncertainty to those of sample 1. This sample was also characterised by SQUID magnetometry and showed a diamagnetic transition below $\sim$ 12 K, with splitting of FC and ZFC scans, but the diamagnetism was weaker than that of Sample 1. The magnetometry results for the two samples are compared in figure 4.2, and also in figure 4.4.

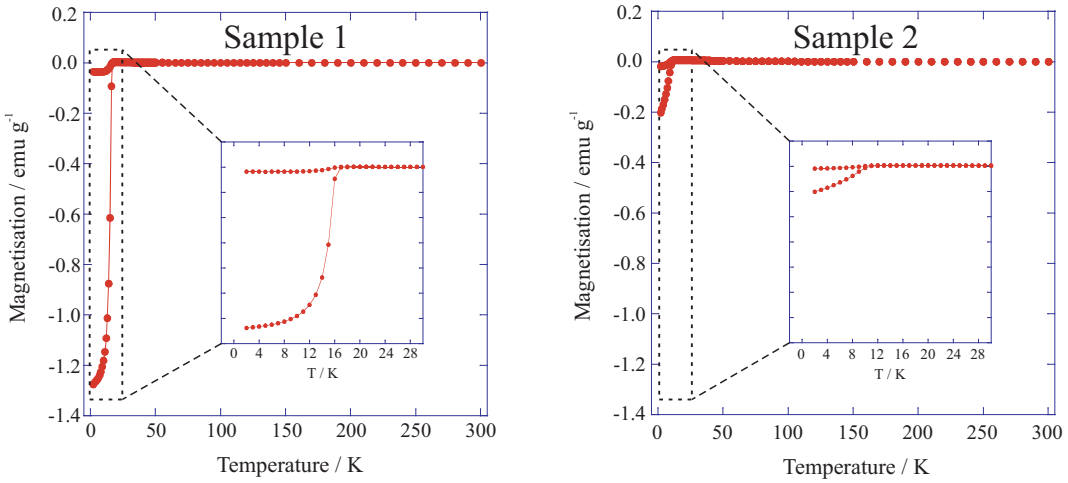


Figure 4.2: Plots (on the same scale) of magnetisation *vs* temperature showing the Meissner transition in two samples of LiFeAs (referred to in the text as "Sample 1" and "Sample 2"). The region containing the transition ($T \leq 20$ K) is inset.

4.3 Magnetometry studies of two samples of LiFeAs

Samples 1 and 2, described in section 4.4, were both studied by D.C. SQUID magnetometry to investigate their magnetic and superconducting properties. Two sets of measurements were taken in a small applied field of 50 Oe, between temperatures of $2 - 300$ K. For one set of measurements the sample was cooled in zero applied field (zero field cooled, or "ZFC"); the second set were conducted after the sample had been cooled in the 50 Oe applied field (field cooled, or "FC"). A small applied field is important when studying the onset temperature of the superconducting state, as the critical fields H_{c1} (the "lower critical field", where magnetic flux begins to penetrate the superconductor) and H_{c2} (the "upper critical field", where magnetic flux fully penetrates the sample, destroying superconductivity) must not be exceeded. The data in figure 4.3 show that a measuring field of 50 Oe is not strong enough to penetrate the superconductor.

For the ZFC measurements, care was taken to avoid the presence of a small residual field (usually $\mid H_{residual} \mid \leq 2$ Oe) by taking a measurement at 300 K in a nominal applied field of 0 Oe. If a signal due to sample magnetisation was detected, the applied field was adjusted accordingly and the measurement repeated until $H_{applied} =$

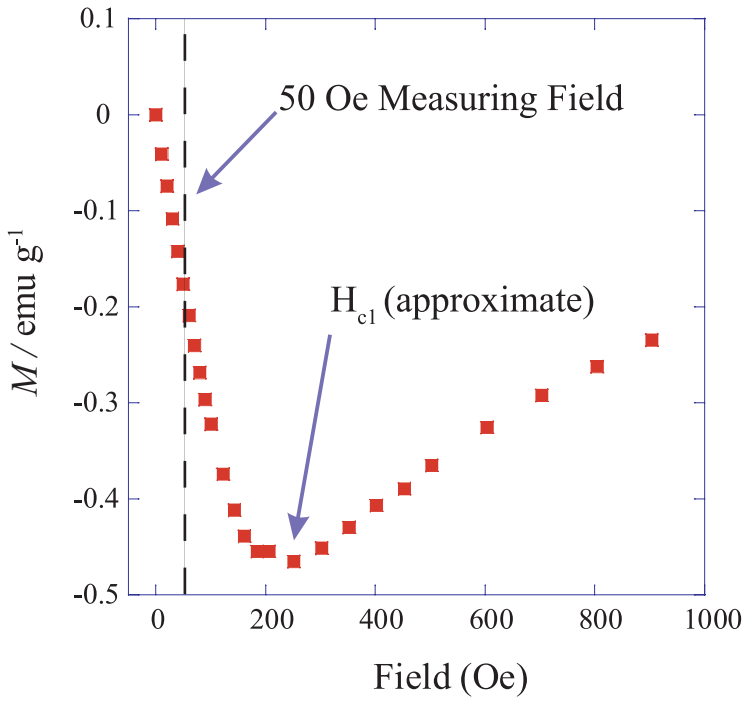


Figure 4.3: A plot of magnetisation *vs* applied field at 2 K for one sample of LiFeAs (referred to in the text as "Sample 2"). The dashed line indicates the measuring field used in scans of M *vs* T throughout this work, which is below the lower critical field (H_{c1}) for this sample.

$-H_{residual}$ and the net flux density about the sample is zero. The sample was then cooled in this corrected zero field.

The results for both samples are plotted together in figure 4.4. In the temperature range $T > 18$ K the samples show very similar behaviour, with both exhibiting weak paramagnetism above T_c and no indication of any magnetic transition (e.g. a spin-density wave, which is exhibited at around 140 K by the "parent" materials $BaFe_2As_2$ and LaFeAsO).[66, 122] The paramagnetism in both samples has a temperature-dependent component, as shown in figure 4.5.

At low temperatures where $T < 18$ K, the first major differences between these samples becomes apparent. Both samples undergo a transition to a strongly diamagnetic state with a large splitting between FC and ZFC scans, characteristic of the Meissner effect, but the transitions differ in two respects. Firstly, they occur at different temperatures. Sample 1 becomes diamagnetic between $16 - 17$ K, while Sample 2 remains paramagnetic above $T \approx 11$ K. Secondly, Sample 1 exhibits a

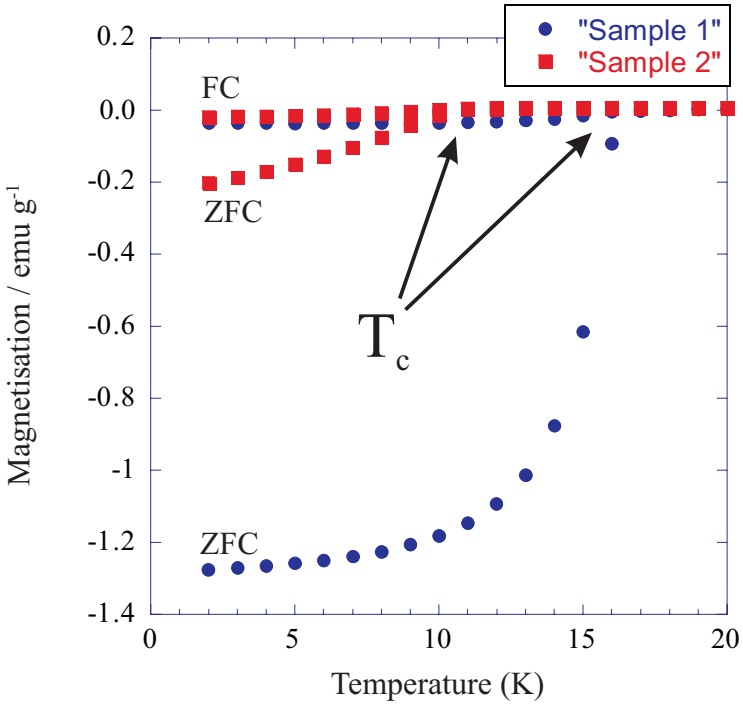


Figure 4.4: Field cooled and zero-field cooled magnetisation measurements for two samples of LiFeAs (referred to in the text as "Sample 1" and "Sample 2"), taken in the temperature range $2-20$ K, using an applied field $H = 50$ Oe. Blue markers correspond to Sample 1; red markers correspond to Sample 2.

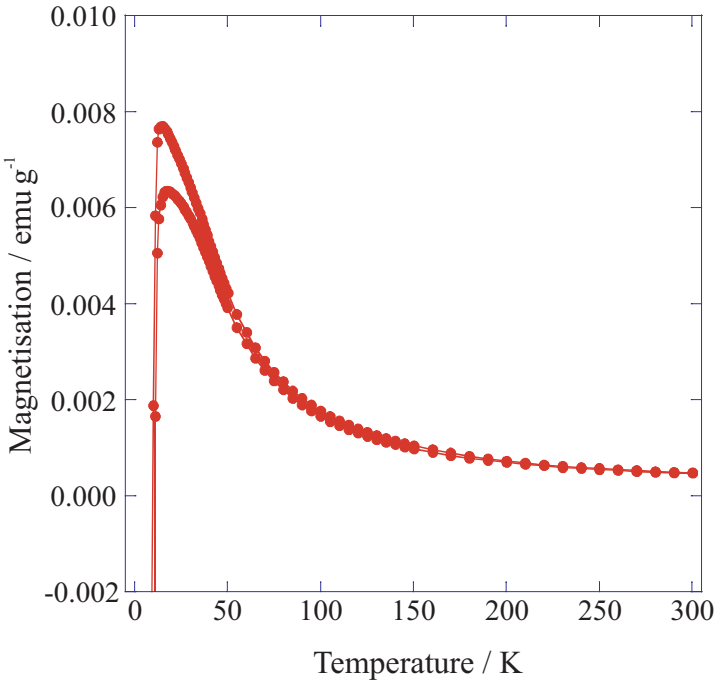


Figure 4.5: Plot of M *vs* T for one sample of LiFeAs (referred to in the text as "Sample 2"), expanded in the region $-0.002 \leq M \leq 0.01$ emu g^{-1} to show the paramagnetic region above T_c. Note that this paramagnetic behaviour, although T-dependent, does not obey the Curie-Weiss law.

sharper transition and a much stronger diamagnetic signal than Sample 2, indicating a significant difference in the superconducting volume fractions. This result, taken with the conclusions drawn in section 4.4, suggests that there could be a difference in composition between the two samples which is too small to be fully resolved by isolated diffraction measurements, with an implication that the superconducting properties are extremely sensitive to the precise composition.

If the assumption is made that the compositional difference is due to $Li_{1-y}Fe_{1+y}As$ type non-stoichiometry (the occurrence of which has already been demonstrated by Juza and Langer), then a systematic study to correlate y with the superconducting properties T_c and volume fraction could help to clarify the relationship between samples 1 and 2, as well as being of more general interest (especially for comparison with $Fe_{1+y}Se$ phases which show similar behaviour).[123]

4.4 Diffraction studies of two samples of LiFeAs

Sample 2, which is phase-pure with a large mass, was selected for detailed study by neutron powder diffraction using HRPD, the high-resolution time-of-flight diffractometer at ISIS; and for high-resolution X-ray powder diffraction using the ID31 diffractometer at the ESRF. The refinement results discussed in this section are supported by the tables of refined parameters (including bond distances and angles) in Appendix D.

For neutron diffraction, the sample was loaded into a cylindrical vanadium can under an argon atmosphere and sealed with a gasket of indium wire. Measurements were taken at ambient temperature and at 6.5 K by Dr. Richard Ibberson, and Rietveld refinement was performed against data from the 90° and 168° banks. For the refinement, the data sets were treated jointly using two separate high- and low-T phases, with the site occupancy factors for Li and As constrained such that the high- and low-T phases remained identical in composition.

Two different starting models were tried, both taken from the original report by

Juza and Langer; the first with square-pyramidal Li and the second with tetrahedral Li (i.e. the LiMnAs structure). Rietveld refinements for both models are displayed in figure 4.6. The model with square-pyramidal Li yielded a very good fit to the observed peak intensities ($R_{wp} = 0.0389$, $\chi^2 = 7.035$), and refinement of the z-coordinate and fractional occupancy of the Li site resulted in values of 0.6538(1) and 0.963(4) respectively. Fractional occupancy of the As site was also refined and gave a value of 0.972(1). A small amount of FeAs (1.5 mol%) was identified as a minor impurity phase.

An attempted refinement using the LiMnAs-type model yielded a comparatively poor fit ($R_{wp} = 0.1243$, $\chi^2 = 31.33$), and refinement of the fractional occupancy of the tetrahedral Li site gave a value of 0.080(4). It is perhaps unsurprising that this refinement was unstable when the isotropic temperature factor (U_{iso}) for Li was allowed to refine freely.

When assessing composition in this way, particularly with an element such as Li which has a small, negative neutron scattering length, great care must be taken in the interpretation of Rietveld refinement results. The fractional occupancy parameter is essentially a scale factor applied to the scattering factor f_n of a particular element at a given crystallographic site; it therefore directly affects the intensities of any peaks with contributions from this element. The small scattering length of Li means that, in this case, small changes in the fractional occupancy parameter do not greatly affect peak intensities. There are also several other important (but unrelated) parameters that affect peak intensities, which can counter-balance each other during the refinement process. Sets of parameters that are related in this way are said to be "correlated". Typical parameters that can become correlated to fractional occupancy when freely refined include the thermal displacement parameters, absorption factors and atomic co-ordinates. A change in any of these parameters might be expected to affect the value obtained for fractional occupancy. For a one-off experiment of this type, the presence of a very large degree of error on the fractional occupancy values of Li is anticipated, with the effective error perhaps up to an order of magnitude greater than

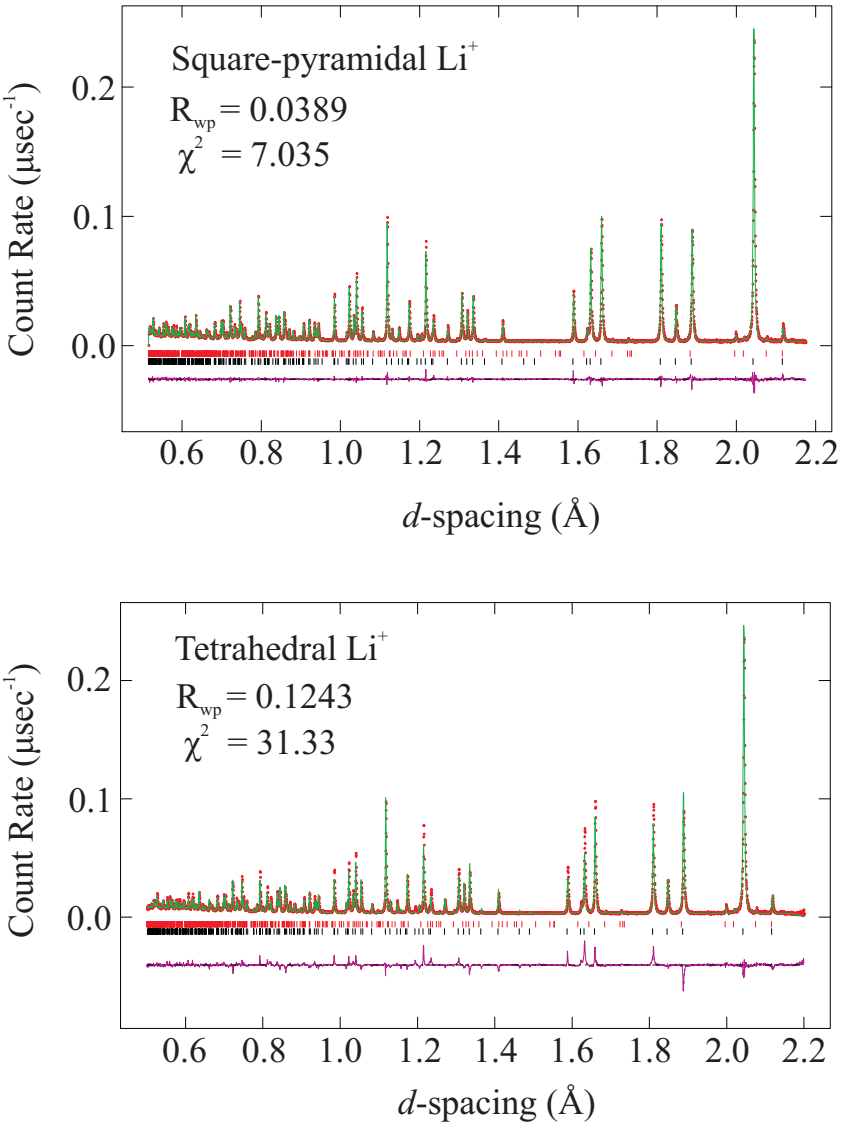


Figure 4.6: Rietveld refinements against time-of-flight NPD data, obtained from one sample of LiFeAs ("Sample 2" from the text) at ambient temperature using the HRPD diffractometer (168° bank). The two refinements correspond to different starting models (PbFCl model with square-pyramidal Li above, and an ordered-fluorite model with tetrahedral Li below), and indicate that Li is located in a square-pyramidal coordination environment. Reflection markers: *Black* = LiFeAs; *red* = FeAs.

the estimated standard deviation calculated by GSAS.

Taking the potentially large error into consideration, it is possible to draw the conclusion from these refinements that Li resides almost entirely on a square-pyramidal site, with very little scattering from an alternative tetrahedral site, and that the material is close to fully stoichiometric. However, a very small amount of disorder over the two sites cannot be ruled out entirely. Neither is it possible to rule out a small deficiency ($\leq 5\%$) of Li on the square-pyramidal site, or the incorporation of a very small amount of Fe on the site (which would have the same effect on the Bragg intensities as a Li deficiency due to the opposite phases of the scattering factors of Li and Fe).

In contrast to the behaviour of the non-superconducting parent compounds $BaFe_2As_2$ and $SrFe_2As_2$, which undergo a structural distortion to an orthorhombic phase with concomitant antiferromagnetic ordering in the Fe layer, cooling the sample to 6.5 K did not cause any apparent distortion away from tetragonal symmetry and no extra Bragg reflections appeared in the diffraction pattern. This is consistent with the existence of superconductivity in this sample, but contrasts with the other layered arsenide systems as the sample composition is very close to stoichiometric. From NPD alone, the uncertainty in the exact occupancy of the Li site is enough to leave open the possibility that the sample is Li-deficient, or that the Li site may be partially occupied by a very small amount of Fe.

In order to address the ambiguities left by neutron diffraction, a high-quality powder X-ray diffraction measurement was made at ambient temperature by Dr. Michela Brunelli using ID31 at the ESRF. The sample was contained in a sealed borosilicate capillary loaded under an argon atmosphere. Refinement against these data showed good agreement with the parameters obtained by NPD, indicating that both the square-pyramidal Li site and the As site were fully occupied.

The XRPD data were then used in a simultaneous refinement with the ambient-temperature NPD data, with equally weighted histograms and a constrained starting model with Li shared by two sites. The resulting Li and As site occupancies were

0.997(4) and 0.995(1) respectively, with only a very small refined occupancy of the proposed tetrahedral site by Li of 0.011(2). The very small value for the refined occupancy of the tetrahedral site is consistent with a single crystal study of LiFeAs by Tapp *et al*,[64] and is an order of magnitude lower than the values reported by Juza and Langer,[78] suggesting that their proposed M:As ratio of 2.1 : 1 is not attainable in this system. Consideration of these X-ray diffraction data appears to support the conclusion that the square-pyramidal Li site does not host a significant number of vacancies. However, it is still possible that a very small amount ($\leq 1\%$) of Fe is accommodated on this site in place of Li, which would decrease the average neutron scattering power of the site but increase its X-ray scattering power with the results of the joint refinement reflecting this balance.

This detailed study of Sample 2 leads to the conclusions that Li almost exclusively occupies a square-pyramidal inter-layer site, and that the sample is, within experimental uncertainty, stoichiometric LiFeAs. However, its superconducting properties appear to be significantly different from those of "Sample 1", and the two are indistinguishable by laboratory XRPD. To investigate this further, "Sample 1" (which has a smaller mass and a significant amount of FeAs impurity) was subjected to ambient-temperature neutron powder diffraction using the Polaris instrument at ISIS, and some of the results of a Rietveld refinement against these data are included in table 4.2. The refined lattice parameters were $a = 3.7773(7)$ Å, $c = 6.3565(1)$ Å, with unit cell volume $V = 90.696(5)$ Å^3. The values are very close to those obtained from sample 2, and the refined Li-site occupancies and temperature factors of the two samples are equal within experimental uncertainty. The respective z-coordinates of Li and As are also very similar in the two samples. (Again, neutron diffraction alone suggests a small deficiency on the As site). From this experiment, the composition of sample 1 cannot be distinguished from sample 2, and is very close to stoichiometric LiFeAs.

Table 4.1: Refined parameters for LiFeAs "Sample 2" from joint XRPD-NPD refinements at ambient temperature. U_{equiv} is the mean of the anisotropic temperature factors. Errors represent one standard deviation generated by GSAS.

Atom	Site	x	y	z	U_{equiv} / Å^2 x 100	Refined Site Occupancy
Fe	2*a*	0.75	0.25	0	0.68(1)	1 (not refined)
Li	2*c*	0.25	0.25	0.6536(2)	1.78(5)	0.997(4)
As	2*c*	0.25	0.25	0.23715(3)	0.74(1)	0.995(4)
$a = 3.776360(4)$ Å ; $c = 6.35679(1)$ Å ; $V = 90.6536(2)$ Å^3						

Table 4.2: Refined parameters for LiFeAs "Sample 1" from refinements against NPD data from the Polaris diffractometer.

Atom	Site	x	y	z	U_{equiv} / Å^2 x 100	Refined Site Occupancy
Fe	2*a*	0.75	0.25	0	0.65(2)	1 (not refined)
Li	2*c*	0.25	0.25	0.6551(4)	1.77(9)	0.99(1)
As	2*c*	0.25	0.25	0.23654(9)	0.65(2)	0.977(3)
$a = 3.7773(7)$ Å ; $c = 6.3565(1)$ Å ; $V = 90.696(5)$ Å^3						

4.5 Synthesis of an Fe-rich series $Li_{1-y}Fe_{1+y}As$

It appeared likely from the structural and compositional similarity of two samples of LiFeAs, which have different superconducting transition temperatures, that the superconducting properties of LiFeAs are highly sensitive to extremely small changes in composition. In order to investigate the true nature of these compositional differences it was necessary to follow up the work of Juza and Langer to establish the range of non-stoichiometric compositions available to this system, and to investigate the relationships between composition and superconductivity in these phases.

Five large 3g powder samples of $Li_{(1-y)}Fe_{(1+y)}As$, with nominal y values of 0.01, 0.02, 0.03, 0.04, 0.05, and a new fully stoichiometric member, were prepared by combining a pre-ground stoichiometric mixture of Fe powder and As (ground pieces) with Li pieces. This mixture was contained in a niobium tube which was sealed under a flowing argon atmosphere by arc welding. The reaction was heated to 220 °C for $1-2$ hours to allow all of the Li metal to react. The resulting inhomogeneous crystalline powder, containing a mixture of binary arsenides, was thoroughly ground and pressed into pellet form, then sealed in a fresh niobium tube. This vessel was then sealed

within a protective evacuated silica ampoule, and heated to 800 °C for 48 hours. The resulting dark brown powders were examined by laboratory XRPD and found to be single-phase.

The fact that LiFeAs and Fe_2As are isostructural strongly suggests that any realistic model for $Li_{(1-y)}Fe_{(1+y)}As$ should have Li and Fe sharing the 2*c* site. The 2-electron lithium ion is a very weak scatterer of X-rays, but a reasonable scatterer of neutrons, so neutron diffraction methods should normally be preferred for the location of this ion. However, the neutron scattering length of Li is negative (-1.90) while that of Fe is positive (9.54), leading to null scattering effects whereby a deficiency on the Li site would have the same effect on the intensities of the Bragg reflections as the incorporation of a small amount of Fe (e.g. $Li_{0.97}Fe_{1.03}As$ and $Li_{0.82}FeAs$ cannot be distinguished by neutron diffraction). Hence, it is desirable to combine neutron diffraction with high quality X-ray diffraction (in which both scattering factors have the same sign) for investigations of this site.

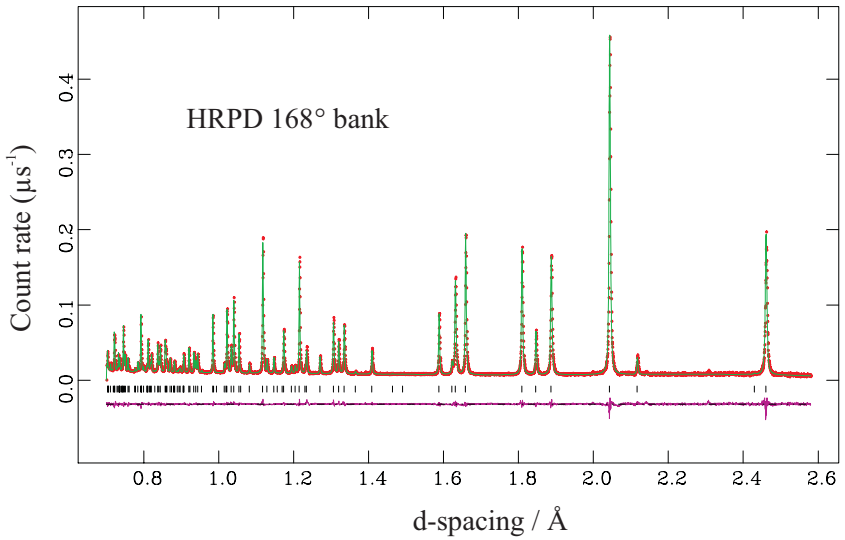
Neutron diffraction data were collected from all of these samples at ambient temperature using HRPD, with samples contained in thin-walled cylindrical vanadium cans. Only data from the 90° and 168° detector banks were used in the Rietveld analysis. Two samples, with $y = 0$ and $y = 0.05$ (both synthesised prior to the intermediate samples), were measured using the Polaris high-intensity diffractometer. X-ray diffraction data were collected at ambient temperature using I11, the high-resolution powder diffractometer at the Diamond Light Source, with a Si-calibrated incident wavelength $\lambda = 0.8272$ Å and samples loaded in spinning 0.5 mm borosilicate capillaries. The apparently stoichiometric "Sample 2" (discussed in section 4.4) was also measured using I11 to allow reliable comparisons to be drawn when addressing the possibility of non-stoichiometry in this sample. The results of these experiments, discussed below, are supported by the tables of refined structural parameters (including bond distances and angles) in Appendix D.

Analysis of both NPD and XRD patterns showed that all but one of these samples were phase-pure, with the exception of $x = 0.03$ which contained a small amount of

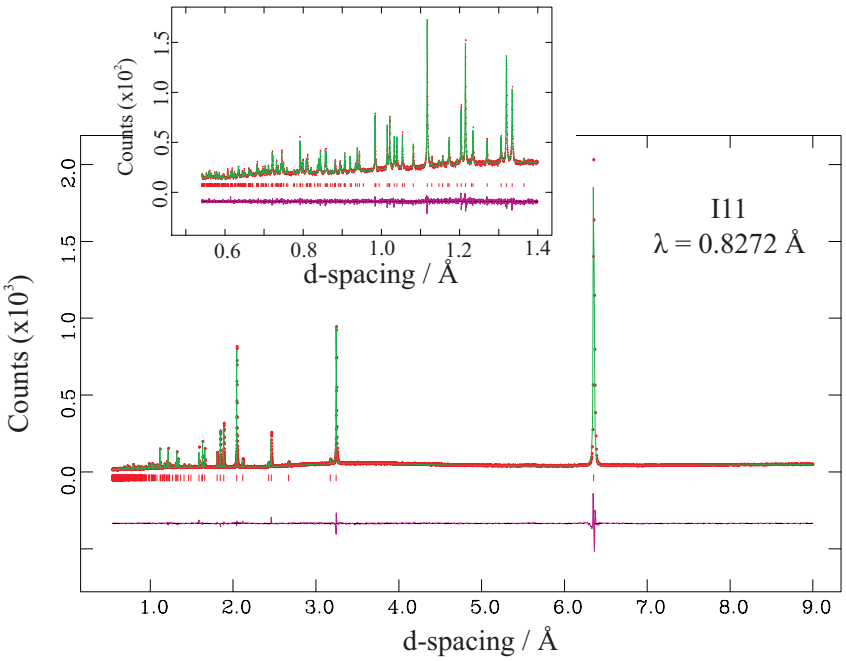
FeAs impurity (5.4 mol%). Initial refinements against I11 data were conducted in order to precisely and accurately determine comparable lattice parameters which is important when such small changes in composition are made. During these refinements, it was noted that strong absorption of the 0.8272 Å beam caused the refined temperature factors to take negative values, which are not physically meaningful. To correct for this absorption, the anisotropic temperature factors were derived from refinements against ToF NPD data, and inserted into the X-ray refinements as constant values. An absorption factor was then applied (using GSAS absorption function 0, an empirical Lobanov & alte da Veiga function, as described in the GSAS manual [83]) and refined manually for one sample to a value of 0.350 $Å^{-1}$. This value for the absorption factor was then applied to each X-ray refinement. The samples also exhibited a small degree of preferred orientation, and this was accounted for using a low-order spherical harmonic correction.

The three data sets (two neutron detector banks and one XRD pattern) were combined in a joint Rietveld refinement for each sample, and these are displayed in figure 4.7. The starting model was based on that obtained from LiFeAs in section 4.4, with a nominal amount of Fe substituted on to the Li 2*c* site with the tetrahedral 2*a* site left vacant. The initial stages of the refinement used constant lattice parameters obtained from I11 to calibrate the DIFC parameter (an instrument parameter corresponding to a sample position correction) for the two NPD data sets. DIFC was then fixed, with lattice parameters allowed to refine throughout the remainder of the refinement process. An absorption correction was applied to each XRD histogram as described above. The fractional occupancies of the 2*c* site by Li and Fe were constrained so that $f_{Li} + f_{Fe} = 1$ (i.e. the site is always fully occupied).

Figure 4.8 shows the variation in the refined lattice parameters with refined values of *y*. It is clear that there is a very good correlation between these two variables, with lattice parameters and c/a ratio decreasing linearly as the amount of Fe on the site increases. This trend is consistent with the report of non-stoichiometry by Juza and Langer, and should be expected as the lattice parameters of the isostructural



(a) Refinement against ToF neutron diffraction data from the back-scattering detector bank of HRPD. Reflection markers: *Black* = LiFeAs.



(b) Refinement against XRPD data from I11, plotted as a function of *d*-spacing for ease of comparison with the NPD refinement (figure 4.7a). The low-*d* region is shown inset. Reflection markers: *Red* = LiFeAs.

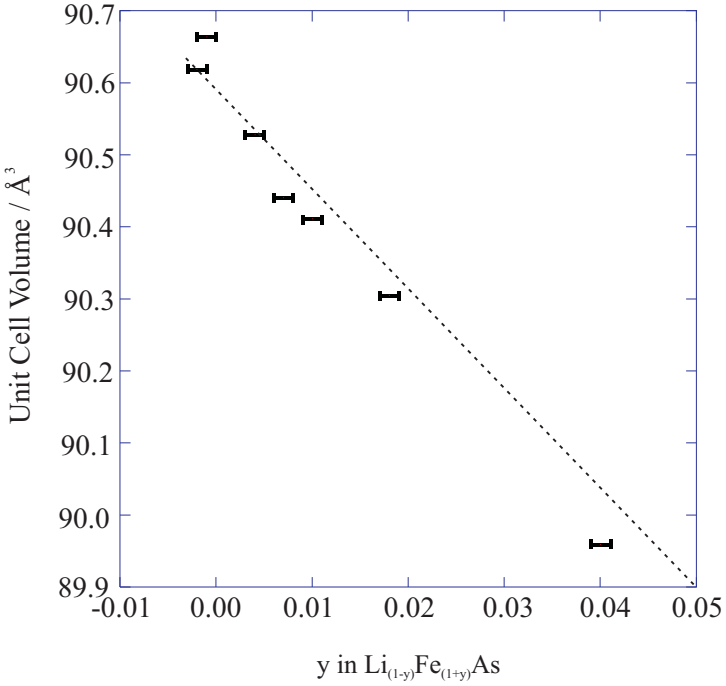
Figure 4.7: A representative joint NPD/XRD Rietveld refinement for a sample of $Li_{1-y}Fe_{1+y}As$, against data obtained from the HRPD time-of-flight neutron diffractometer and the I11 synchrotron X-ray diffractometer. This sample has a nominal composition of $y = 0.04$.

end-member of the series, Fe_2As, are significantly smaller than those of LiFeAs ($a = 3.6379(6)$, $c = 5.9834(15)$ for Fe_2As from reference [124]). Although the error in the determination of composition is generally very high for an isolated sample (the statistical errors generated by GSAS may underestimate the true error by as much as an order of magnitude), this level of correlation with the lattice parameters indicates that the data are of high enough quality for the refined values of y to be valid in this case. This is a significant result, as it suggests that unit cell volume can be used as a measure of composition for compounds of this type.

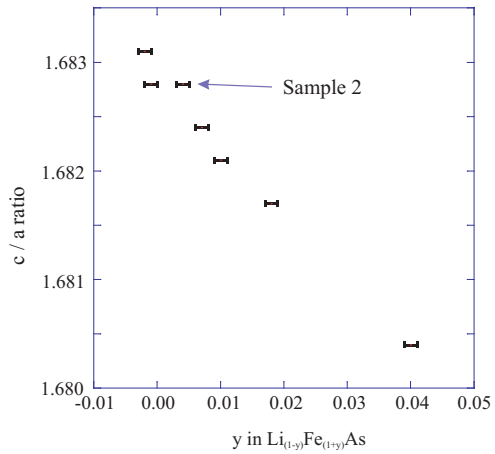
The geometry of the $FeAs_4$ tetrahedron appears to be a very important parameter in superconducting FeAs compounds which has a strong influence over T_c, with the highest transition temperatures occurring in compounds when the Fe co-ordination environment is close to an ideal tetrahedron. In LiFeAs, the FeAs layer is highly compressed in the basal plane, with the $FeAs_4$ tetrahedra correspondingly distorted in comparison to those in $BaFe_2As_2$ and LaFeAsO. A plot of the two tetrahedral angles (labelled α and β) as a function of refined lattice parameter is shown in figure 4.9. This plot shows that there is a systematic change in the As-Fe-As angles as the $2c$ site becomes increasingly occupied by Fe, with the layer becoming more distorted by compression in the basal plane. The trends in Fe-As bond distance and intra-plane Fe-Fe bond distance are consistent with this; as y increases to 0.04 the Fe-Fe distance ($= a/\sqrt{2}$) decreases by approximately 0.2%, while there is no discernible change in Fe-As distance.

This is consistent with the As-Fe-As bond angles in the isostructural Fe_2As, where the layers are extremely distorted with angles $\alpha = 96.6°$ and $\beta = 116.3°$ (as determined from neutron diffraction by Nuss *et al.* [124]).

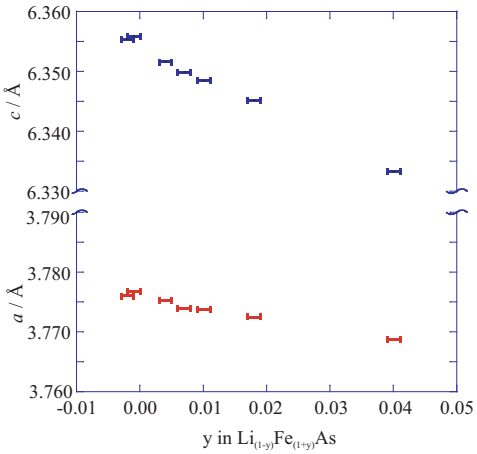
The structural changes about the Li site, plotted in figures 4.10 and 4.11, are small. As y increases, the 4-fold intra-planar Li-As distance exhibits no significant change, while the single bond to the apical As shows a contraction of approximately 1.5 % as y increases to 0.04. The bond angles also show exhibit a subtle trend: δ decreases very slightly while γ exhibits a very small increase. Taken together with the decreasing As-



(a) Refined unit cell volume *vs* refined *y*. The dotted line represents the results of Juza and Langer (reference [78]).



(b) Plot of c/a ratio *vs* refined *y*.



(c) *a*- and *c*-parameters *vs* refined *y*.

Figure 4.8: Variation in refined lattice parameters of $Li_{1-y}Fe_{1+y}As$ as a function of refined *y*, derived from joint XRPD-NPD refinements using the HRPD or Polaris time-of-flight diffractometers and the I11 synchrotron X-ray diffractometer. LiFeAs "Sample 2" is included in all plots (clearly indicated in 4.8b). Error bars represent one estimated standard deviation obtained from GSAS.

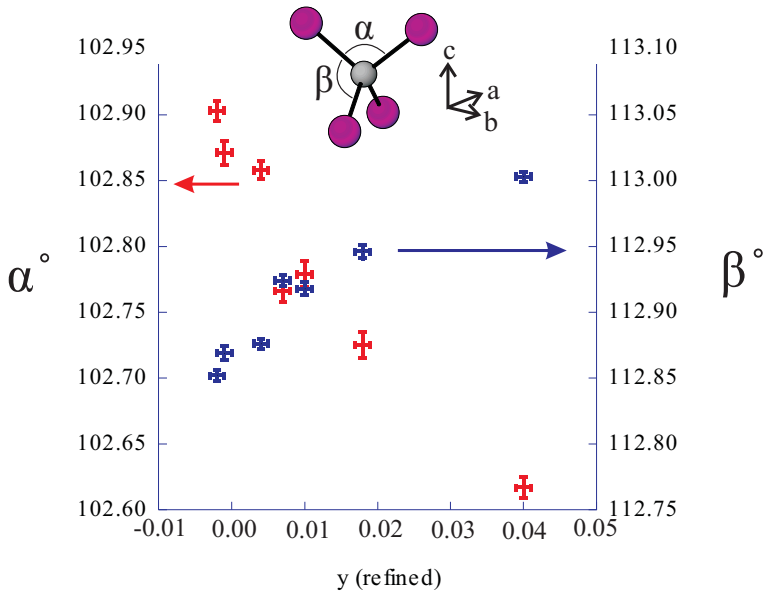


Figure 4.9: Refined As-Fe-As angles of $Li_{1-y}Fe_{1+y}As$ as a function of refined y, derived from joint XRPD-NPD refinements using the HRPD or Polaris time-of-flight diffractometers and the I11 synchrotron X-ray diffractometer. This shows the distortion of the $FeAs_4$ tetrahedra as Fe content increases. Error bars represent 1 estimated standard deviation calculated by GSAS.

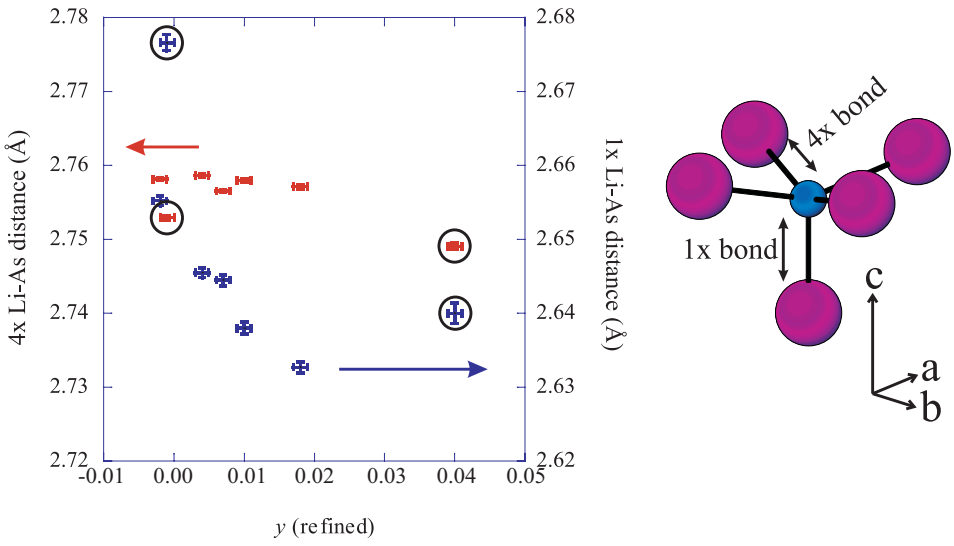


Figure 4.10: Plot of refined Li-As distances in $Li_{1-y}Fe_{1+y}As$ as a function of refined y. Data are derived from joint XRPD-NPD refinements using the HRPD or Polaris time-of-flight diffractometers and the I11 synchrotron X-ray diffractometer. The four circled data points are derived from I11-Polaris joint refinements.

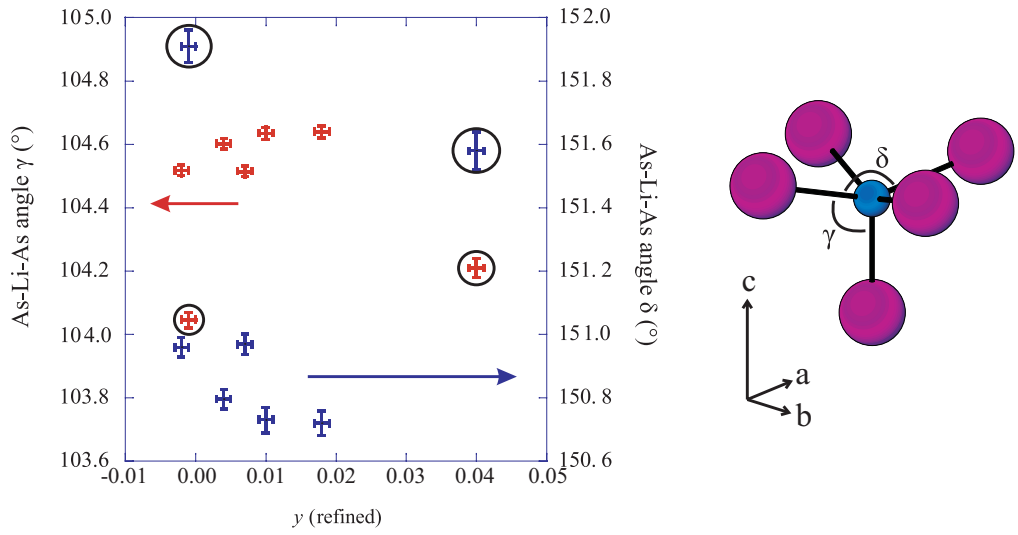


Figure 4.11: Plot of two refined As-Li-As angles in $Li_{1-y}Fe_{1+y}As$ plotted as a function of refined *y*. Data are derived from joint XRPD-NPD refinements using the HRPD or Polaris time-of-flight diffractometers and the I11 synchrotron X-ray diffractometer. The four circled data points are derived from I11-Polaris joint refinements.

As distances in the *ab*-plane, these indicate that the average *M* position moves slightly towards the centre of the square-based As_5 pyramid as the site becomes richer in Fe. It should be noted that the scattering from this site is much stronger in the neutron diffraction patterns than in the XRD patterns, and from these plots it is evident that the absolute value obtained for these parameters is somewhat dependent on the neutron diffractometer used (see the highlighted points in figure 4.11). However, it can be seen that the gradients $\frac{\partial(parameter)}{\partial y}$ are similar for a set of I11-HRPD refinements and for a set of I11-Polaris refinements, suggesting that the observed trends in the $LiAs_5$ environment is real.

On close inspection of the high-resolution XRD patterns (see figure 4.12), it was noted that the peak widths (FWHM) of the Bragg reflections increase as the the 2*c* site accommodates more Fe. This may be an indication that the sample compositions become less homogeneous as Fe content increases - the lattice parameters do show a strong dependence on Fe content so in this case even a small distribution of compositions would be expected to broaden the Bragg reflections to some extent.

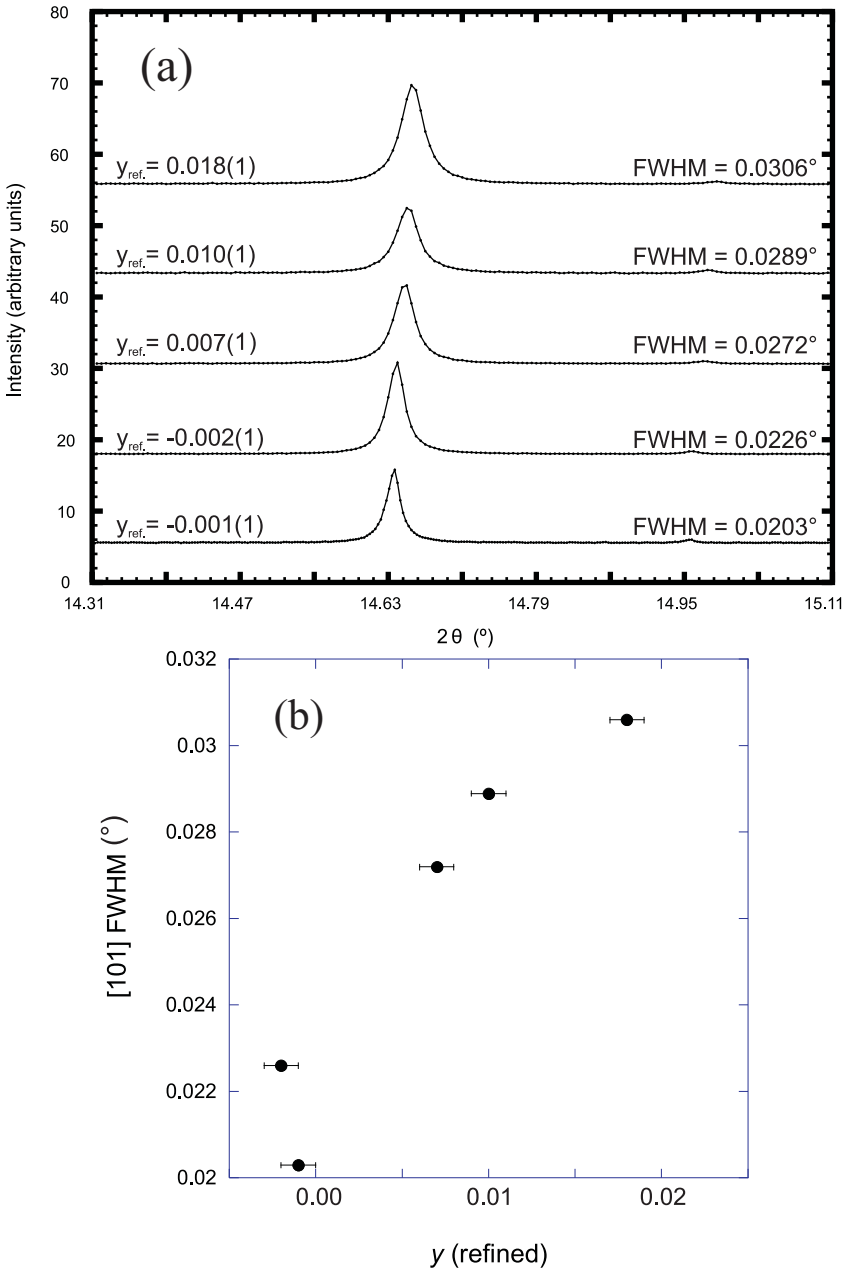


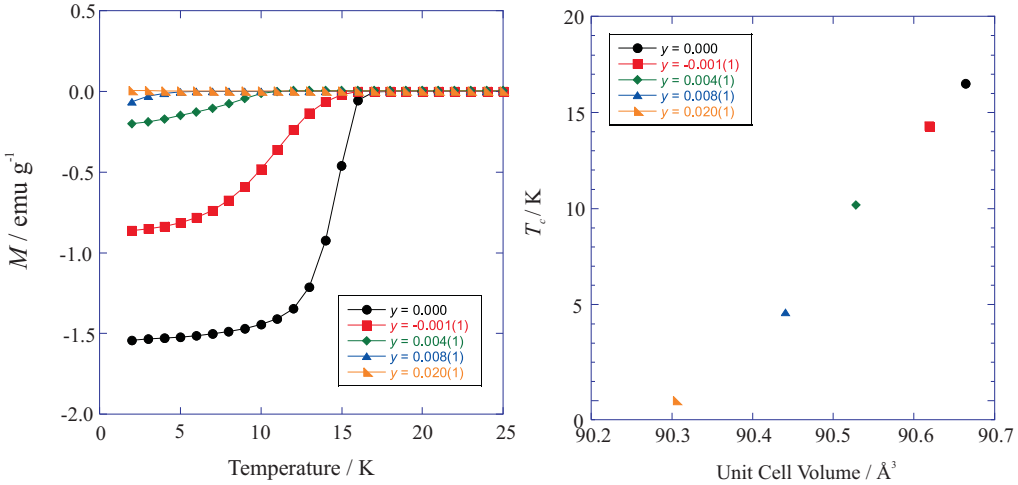
Figure 4.12: (a) Normalised (101) reflections for several $Li_{1-y}Fe_{1+y}As$, measured using I11 with $\lambda = 0.82720$ Å, with peak widths (FWHM) derived from Rietveld refinements; (b) a plot of peak widths against refined y values, showing a gradual broadening as the system becomes increasingly non-stoichiometric. Note that statistical errors for FWHM values are not calculated by GSAS.

4.6 Magnetometry studies of an Fe-rich series $Li_{1-y}Fe_{1+y}As$

Magnetic characterisation was carried out using similar methods to those in section 4.3. Magnetisation was measured as a function of temperature in a small measuring field of 50 Oe, after both field-cooling and zero-field-cooling. The ZFC scans of samples with 5 different refined y values are displayed in figure 4.13a. It can be seen from this figure that the incorporation of Fe has a dramatic effect on both the superconducting transition temperature and the superconducting volume fraction. The transition temperature shows an apparently linear dependence on y (inferred from its proportional relationship to unit cell volume), with the incorporation of 1% Fe on the Li site enough to reduce T_c from approximately 17 K to 5 K. The superconducting volume fraction is also sharply reduced by the presence of extra Fe, and superconductivity is eventually quenched when the unit cell volumes become smaller than approximately 90.42 $Å^3$, which can be equated to the point at which $y \approx 0.02$. As well as a reduction in volume fraction, the transitions also appear to become less sharply defined, which could be due to some degree of compositional inhomogeneity (i.e. the samples would contain some Fe-rich regions with lower transition temperatures and some relatively Fe-poor regions with higher temperature transitions). This is consistent with the peak broadening observed in the XRD patterns.

Figure 4.13 includes data for Sample 2 from section 4.3. The superconducting and structural properties of this sample are both consistent with a slightly non-stoichiometric composition with y in the range $0.00 < y < 0.01$ (refined value = 0.004(1) - see section 4.5).

The extreme sensitivity of the superconducting properties to the presence of Fe on the 2c site is not observable in the most commonly studied $BaFe_2As_2$ and LaFeAsO-derived superconductors, which do not exhibit any appreciable disorder over cation sites and have not been reported to accommodate ions on interstitial sites, but these characteristics are shared by the chalcogenide superconductor $Fe_{(1+x)}Se$. This material



(a) Magnetisation *vs* T, measured in an applied field of 50 Oe.

(b) T_c *vs* refined unit cell volume

Figure 4.13: Measurements of magnetisation *vs* T and correlation of T_c with refined unit cell volume for 5 samples of type $Li_{1-y}Fe_{1+y}As$ (with refined y values inset, as described in section 4.5). These two plots illustrate the suppression of superconductivity as y increases.

is formally isoelectronic with LiFeAs and takes the anti-PbO structure (therefore containing no inter-layer cations). Just as LiFeAs can become non-stoichiometric by accommodating Fe in place of some Li ions, FeSe will also accommodate Fe ions in a similar inter-layer square-pyramidal site. McQueen and co-workers [123] reported the magnetic response to the presence of Fe-interstitials in samples of stoichiometry $Fe_{(1+y)}Se$, with both T_c and the apparent superconducting volume fraction decreasing, with superconductivity eventually suppressed when $x = 0.03$ (although the precise location of the interstitial Fe ions was not addressed in this work).

Neutron diffraction experiments by Li *et. al.* [125] confirmed that interstitial Fe ions do occupy this pseudo-octahedral (square pyramidal) site in the isostructural compounds $Fe_{(1+y)}Te$ and $Fe_{(1+y)}Te_{(1-x)}Se_x$, and also suggest that they carry a localised magnetic moment (in contrast to the more delocalised electrons in the Fe-based orbitals of the metal ions in the Fe*Ch* layer). This was found to be consistent with density-functional-theory calculations [126] that suggest that such interstitials should carry a significant magnetic moment (e.g. $2.4\mu_B$ for $Fe_{1+y}Te$), which should persist independently of magnetic ordering or superconductivity in the Fe*Ch* layer.

The magnitude of this moment, and its independence from (and proximity to) the Fe*Ch* layer, raises the possibility that magnetic pair-breaking by Fe interstitials is responsible for the suppression of the superconducting state in $Fe_{1+y}Se$. By direct analogy, it may be concluded that a similar effect causes this behaviour in Fe-rich $Li_{1-y}Fe_{1+y}As$. Despite the existence of many iron-based superconductors containing strongly paramagnetic ions (such as $Eu_{0.7}Na_{0.3}Fe_2As_2$ which superconducts below 34 K, [127] and most of those with the ZrSiCuAs-type structure), this type of behaviour appears to be unique to $Fe_{1+y}Se$ and $Li_{1-y}Fe_{1+y}As$.

4.7 Summary and Conclusions

The work described in this chapter was intended to examine the structure of LiFeAs and its non-stoichiometric derivatives of type $Li_{1-y}Fe_{1+y}As$, and correlate structural and superconducting properties. These materials were found to be highly air-sensitive with decomposition occurring in a matter of minutes. Rietveld refinement against combined NPD-XRD data sets showed that LiFeAs takes the anti-PbFCl structure with Li co-ordinated by five As ions in a square-pyramidal site (alternatively referred to as a pseudo-octahedral site), which appears to be fully occupied, while scattering from an alternative tetrahedral site is negligible. This is in agreement with one of two structures proposed by Juza and Langer in the original structural report,[78] but more importantly it is confirmed by an independent single-crystal XRD experiment.[64] This apparently fully-stoichiometric phase was found to superconduct at temperatures below $\sim$ 17 K, in contrast to the behaviour of other known FeAs superconductors such as $BaFe_2As_2$ and LaFeAsO, where superconductivity must be induced by doping. However, two different samples of LiFeAs, which were structurally indistinguishable and very close to stoichiometric, exhibited quite different superconducting properties.

To investigate the effects of non-stoichiometry (and to help elucidate some difference between the two samples mentioned above), a series of non-stoichiometric samples of type $Li_{1-y}Fe_{1+y}As$ was synthesised and investigated by NPD, XRPD and

SQUID magnetometry. Rietveld refinement against combined NPD-XRD data sets showed a strong correlation between the lattice parameters and the refined values of y, with unit cell volume decreasing as Fe is substituted onto the Li site (in agreement with a previous study).[78] This was accompanied by an extremely strong dependence of T_c on y, with even very small values of $y \approx 0.02$ able to quench superconductivity completely. This observation reflects the behaviour of the non-stoichiometric iron chalcogenide superconductor $Fe_{1+y}Se$, and may be due to the magnetic pair-breaking effect of strong local magnetic moments very close to the superconducting layers. It was concluded from both structural and magnetic trends that "Sample 2" is in fact slightly non-stoichiometric, with an estimated composition of $Li_{0.994}Fe_{1.006}As$. This degree of non-stoichiometry would not be quantifiable from the isolated measurements reported in reference [63].

Chapter 5

The Effect of Doping in $LiFe_{1-x}M_xAs$ (M =Mn, Co, Ni)

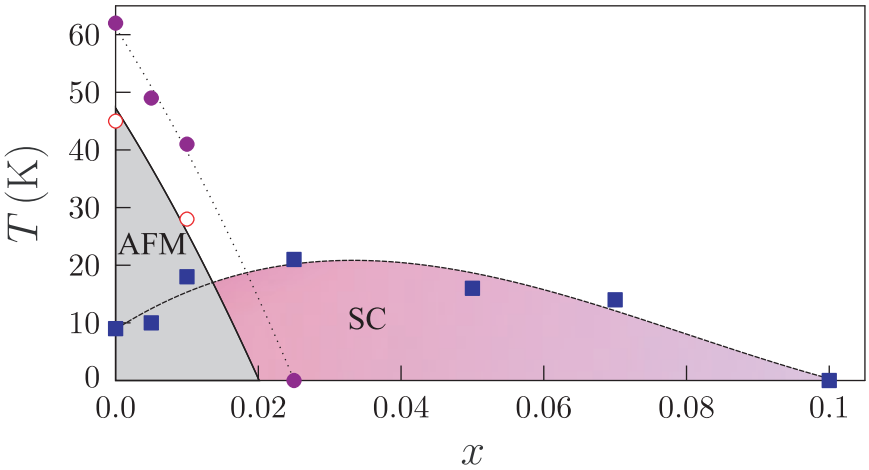
5.1 Introduction

The discovery of superconductivity below 38 K in potassium-doped $Ba_{0.6}K_{0.4}Fe_2As_2$ in 2008,[46] coming shortly after a report of superconductivity below 26 K in $LaFeAsO_{1-x}F_x$,[21] marked the realisation of a new family of layered high temperature superconductors. By this time, much research had been conducted in trying to optimise the superconducting transition temperatures in the *Ln*FeAsO-type materials, and an empirical relationship between the regularity of the $FeAs_4$ tetrahedra and T_c had been realised.[128, 129] It was also clear that electron count played an important rôle, and a study of the effect of electron-doping in $LnFeAsO_{(1-x)}$ [119] showed that T_c increased with dopant concentration. However, compositional studies on *Ln*FeAsO-type materials are complicated by the low levels of doping that could be achieved (typically < 0.2) and the difficulty in assessing the precise dopant concentration.[130, 131]

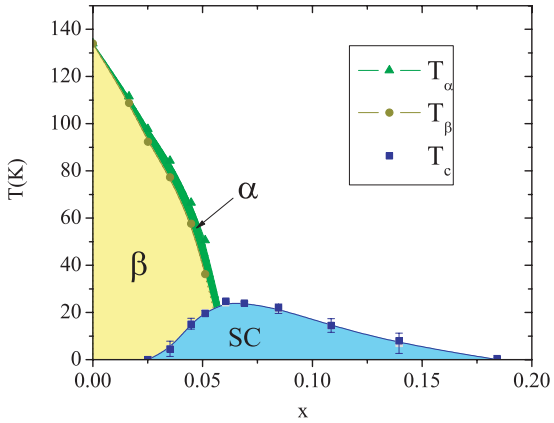
The $BaFe_2As_2$-type materials were found to provide a better platform for the investigation of the doping dependence of superconductivity, due to their ease of formation and crystallisation and their stability in air. The earliest investigation of

electron-doping in these materials was conducted by Rotter *et al.* [132] on a series of solid solutions of type $Ba_{1-x}K_xFe_2As_2$. The end members of this series, $BaFe_2As_2$ and KFe_2As_2, are stable isostructural compounds with the common $ThCr_2Si_2$ structure, and it was found that a complete series could be formed with $0 \leq x \leq 1$. At low doping levels $(0 \leq x \leq 0.1)$ the material undergoes a structural distortion to an orthorhombic phase and orders antiferromagnetically at low temperatures. With compositions of $0.3 \leq x < 1.0$ there is no structural distortion or magnetic order at low temperatures and the material exhibits superconductivity. A peak in T_c occurs at $x = 0.4$. In the region $0.2 \leq x \leq 0.3$ the two states appear to overlap, with samples exhibiting both magnetic order *and* superconductivity. This co-existence has also been observed in other systems and it is currently a matter of some debate over whether it is a manifestation of microscopic co-existence of the two states (i.e. with each Fe atom involved in both states) as suggested by recent NMR experiments,[133] or if it is due to sample inhomogeneity with separate antiferromagnetic and superconducting domains as suggested in a wide-ranging study by Park *et al*.[134]

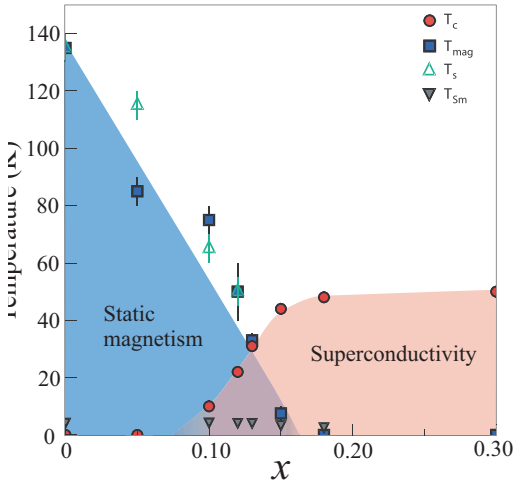
A second mode of doping in these materials involves the partial substitution of Fe for a different transition metal. In this way, the electron count can be increased by adding metals such as Co or Ni, or decreased by a metal such as Mn. In the high temperature cuprate superconductors, this type of modification of the superconducting copper-oxide layers results in a strong suppression of the superconducting state due to magnetic pair-breaking effects,[135] and it is of interest to compare the reaction of iron-based superconductors with this behaviour. A study of cobalt-doped $BaFe_{2-x}Co_xAs_2$ [136] showed that superconductivity could be induced when $x \approx 0.2$ in a system of this type, despite the associated disorder in the superconducting layer (phase diagrams for three Co-doped iron-based superconductors are shown in figure 5.1). Subsequent work [67] then showed a similar phase diagram to that obtained for the $Ba_{(1-x)}K_xFe_2As_2$ series, with the magnetic ordering and associated structural distortion suppressed as x increases to ≈ 0.05, with superconductivity exhibited by samples with $0.036 \leq x \leq 0.14$ and the maximum T_c of 22 K observed when $x \approx 0.06$.



(a) $NaFe_{1-x}Co_xAs$ (from reference [69]).



(b) $BaFe_{2-x}Co_xAs_2$ (from reference [67]).



(c) $LaFeAsO_{1-x}F_x$ (from reference [68]).

Figure 5.1: Phase diagrams, taken from the literature, for the normal/magnetic/superconducting regions of three electron-doped iron-based superconductors with different crystal structures (which were illustrated in section 1.4). In (b) the β-region is orthorhombically distorted and ordered antiferromagnetically, while the α-region is orthorhombic but not magnetically ordered.

The synthesis and characterisation of LiFeAs (described in Chapter 4) showed that, in contrast to *Ln*FeAsO and AeFe$_2$As$_2$-type materials, this material exhibits superconductivity in the un-doped state and does not exhibit long-range magnetic order or undergo any associated structural transition. Clearly the phase diagram of this system is significantly different to these more extensively explored materials, and it is of interest to discover the effects of doping in this material and explore the phase diagram further. In order to address the questions over the compositional range that supports superconductivity, whether the modest T_c can be enhanced, and whether the superconductivity occurs in the proximity of a magnetically ordered domain, three series of compounds were synthesised with the transition metals Mn, Co or Ni substituted for Fe.

5.2 The synthesis of LiFe$_{1-x}M_x$As (M =Mn, Co, Ni)

Derivatives of LiFeAs doped with Mn, Co or Ni were prepared by a similar method to the iron-rich series Li$_{(1-y)}$Fe$_{(1+y)}$As described in the previous chapter. A series of cobalt-doped samples of type LiFe$_{1-x}$Co$_x$As was prepared with nominal values of $x = 0.025$, 0.050, 0.075, 0.100, 0.150 and 0.200; nickel-doped samples were prepared with nominal values of $x = 0.005$, 0.010, 0.015, 0.020, 0.025, 0.050 and 0.10; and manganese-doped samples were prepared with nominal values of $x = 0.01$, 0.02, and 0.05.

Stoichiometric mixtures of Fe powder, As powder and dopant transition metal powder were thoroughly ground in an agate pestle and mortar under an inert argon atmosphere and placed in a niobium tube with lithium pieces. This tube was sealed by arc welding under an argon gas flow, then heated to 220 °C and held for one hour to allow the lithium metal to react. The resulting inhomogeneous powder, consisting of binary arsenides and unreacted transition metals, was thoroughly re-ground and pressed into a pellet before being sealed in a fresh niobium tube by arc welding. For the synthesis of the cobalt-doped series, this tube was sealed in a protective evacuated

silica tube and heated to 800 °C, where it was held for 48 hours. The tube was then quenched in air by removal from the furnace at high temperature. This method yielded products that appeared to be single phase by laboratory X-ray powder diffraction. Preliminary work on a similar Co-doped series by W. Trevelyan Thomas [137] found that solid solutions of this type ($LiFe_{1-x}Co_xAs$) form stable compounds across the entire range of x, reflecting the fact that LiFeAs and LiCoAs are isostructural with very similar distorted tetrahedral MAs_4 metal environments. However, work in this chapter will focus on the superconducting Fe-rich end of the series where $x \leq 0.20$.

For the nickel-doped and manganese-doped derivatives, this protocol was not adopted as it tends to yield a mixture of products. Instead, it was found that the desired single-phase products could only be obtained within certain compositional limits by very rapid quenching from high temperatures. To increase the cooling rate, the niobium reaction tube was not sealed in an evacuated silica jacket (which provides significant thermal insulation), but was instead heated in a tube furnace under a protective flowing-argon atmosphere. After being held at 800 °C for 48 hours, the tube was withdrawn from the furnace by an attached molybdenum wire, and immediately quenched in a bucket of iced water.

The nickel-containing series $LiFe_{1-x}Ni_xAs$ was found to have a limiting composition at $x \approx 0.40$,[137] beyond which several competing phases such as $Li_{5.2}Ni_{10.8}As_7$, NiAs, $FeAs_2$ and Li_3As begin to form. This is perhaps unsurprising, as the existence of the notional end-member of the series "LiNiAs" has not been reported to date. However, the system appears to be even less tolerant to substitution of Fe by Mn. No single-phase products were obtained for Mn-doped compositions with $x > 0.05$, as compositions beyond this limit resulted in mixtures of $LiFe_{1-x}Mn_xAs$ and LiMnAs.[137]

LiMnAs takes a slightly different structure to LiFeAs, as both cations are in tetrahedral sites and it may be thought of as an ordered derivative of the anti-fluorite structure. The two compounds have a very different geometry about the MAs_4 tetrahedra (which are close to regular in LiMnAs)[138] and presumably it is these

differences that cause the instability of $LiFe_{1-x}Mn_xAs$-type compounds. Mn has also been reported to show a limited solubility in the ZrCuSiAs-type solid solution $CaFe_{1-x}Mn_xAsF$, which has a limiting composition of $x \simeq 0.15$.[139]

5.3 Structural Characterisation of $LiFe_{1-x}Co_xAs$

5.3.1 High-resolution X-ray powder diffraction

The structural characterisation of the $LiFe_{(1-x)}Co_xAs$ compounds was conducted primarily by a series of room-temperature X-ray powder diffraction experiments, using the I11 instrument at the Diamond Light Source (UK) and the ID31 instrument at the ESRF (France). Consequently, different incident wavelengths were employed, with the majority of the samples measured using $\lambda = 0.6010$ Å (I11) or $\lambda = 0.3994$ Å (ID31). The un-doped member LiFeAs and one other sample with $x = 0.10$ were measured in a separate I11 experiment using a longer wavelength of $\lambda = 0.8272$ Å. The refinement results discussed in this section (and throughout the rest of this chapter) are supported by the tables of refined parameters in Appendix E.

The powdered air-sensitive samples were loaded into 0.5 mm borosilicate capillaries under an argon atmosphere and sealed with a gas/oxygen torch. Measurements were taken from spinning capillaries to improve the powder average. In total, measurements were taken from 12 samples with $0 \leq x \leq 0.2$, with lattice and structural parameters obtained by Rietveld refinement. Four of these samples were also studied by neutron powder diffraction using the Polaris (3 samples) and HRPD (1 sample) diffractometers (ISIS, UK), and subjected to joint Rietveld refinements with their corresponding XRD data sets. In these joint refinements, lattice parameters were initially determined by refinement against the XRD data sets, and these values used to calibrate the neutron instrument parameter DIFC (a sample position correction). Lattice parameters are therefore strongly weighted by the XRD histograms. Neutron diffraction offers a superior contrast between Fe and Co (which

have neutron scattering lengths of 9.54 fm and 2.45 fm respectively), allowing for refinement of the composition in the arsenide layer.

Figure 5.2 shows representative Rietveld refinements from I11 and ID31. Close inspection of the diffraction patterns revealed that, while most of the samples were single phase (consistent with laboratory XRPD), four samples were found to contain small amounts of Li_3As (< 5.4 mol%) as the sole impurity, which were not observed in all of the laboratory XRPD patterns. Furthermore, three samples were found to contain small amounts of FeAs (< 3.7 mol%). These secondary phases were included in the Rietveld refinement process.

For wavelengths $\lambda > 0.6$ Å, absorption by the sample becomes significant (as illustrated in figure 5.3). Absorption is λ-dependent and θ-dependent, and in Debye-Scherrer geometry is also dependent on the radius of the sample, the sample composition, and the packing density of the sample. This effect, which changes the observed intensities of diffraction peaks, can be treated by GSAS during the Rietveld refinement process by including an appropriate absorption function. For fixed-wavelength experiments, this function cannot be refined and must be derived manually.

During the course of these experiments, absorption corrections were derived in two stages. First, crude absorption corrections (which are dependent on the unknown sample packing density) were calculated using the web utility Absorb [140] and applied to the initial refinements. Absorption is strongly correlated with thermal displacement parameters, which were found to refine to strongly negative values before absorption corrections were applied. Such values are not physically meaningful and are usually an indication that some other factor (typically absorption) is incorrect or unreliable. When the calculated values were applied, these U_{iso} values became strongly positive, which was taken as an indication that absorption had been overestimated (perhaps due to an overestimate of the sample packing density).

The second stage relied upon the strong dependence of U_{iso} values on absorption to refine the absorption correction manually by comparison with U values obtained

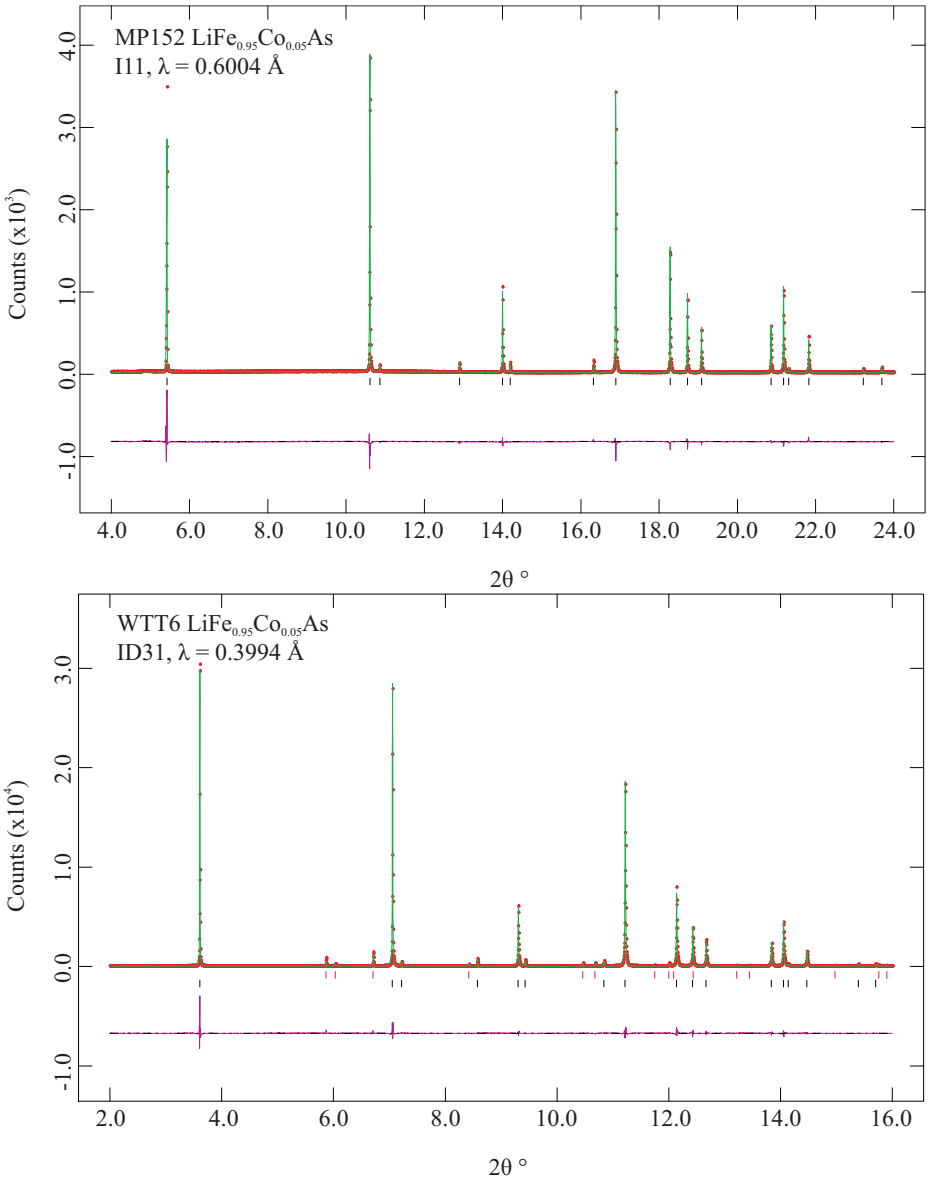


Figure 5.2: Representative Rietveld refinements against synchrotron-XRPD data from two different samples of $LiFe_{0.95}Co_{0.05}As$, using the I11 and ID31 diffractometers (incident wavelengths inset). Only the low-angle region is displayed. Reflection markers: *Black* = $LiFe_{0.95}Co_{0.05}As$; *red* = Li_3As.

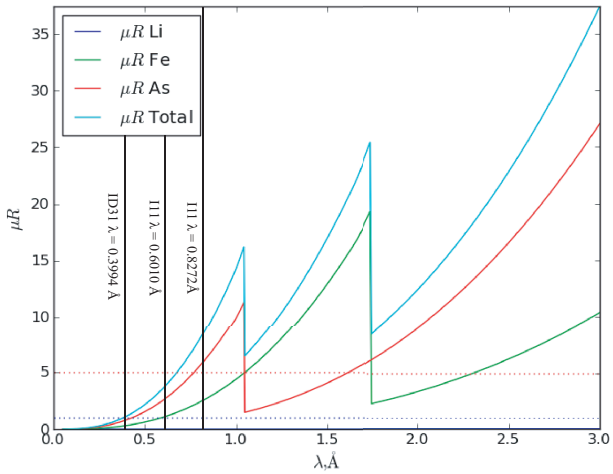


Figure 5.3: A plot of the λ-dependent absorption of X-rays by LiFeAs. The incident wavelengths used in this study are marked by the vertical black lines. The region above the horizontal dashed-red line may be considered as a problematic amount of absorption. Image generated by the web-utility Absorb.[140]

from time-of-flight neutron diffraction. In this way, three dimensionless absorption factors were calculated, with each corresponding to a particular incident wavelength: values of 1.030, 3.248 and 5.619 were used with their respective wavelengths of 0.3994 Å, 0.6004 Å and 0.8272 Å. Consequently, all of the thermal displacement parameters included in the XRD refinements have not been derived directly from these experiments and their absolute values carry little significance, although their relative values may still be useful.

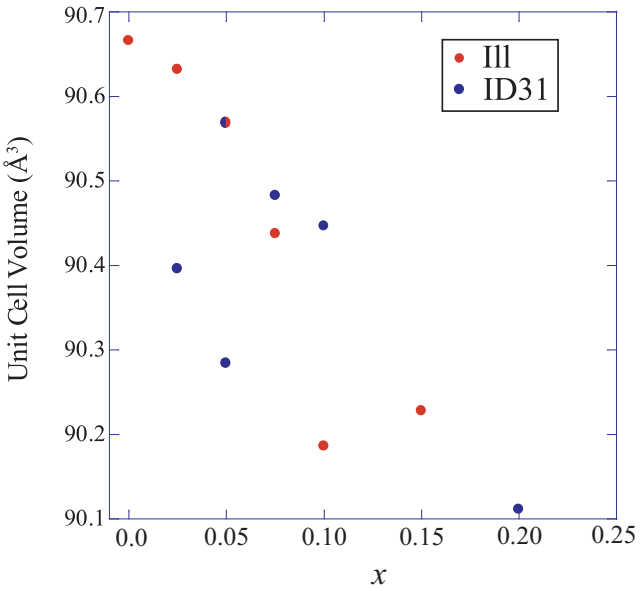
All samples were subjected to similar Rietveld refinements. The similar X-ray scattering factors of Fe and Co precluded any attempts to refine the compositions of the samples using X-rays alone, therefore the 2*a* site (space group $P4/nmm$, with origin choice 2) was modelled with Fe sharing with a nominal amount of Co. For samples subjected to joint NPD-XRPD refinements, with nominal compositions of $x = 0.10$, $x = 0.15$ and $x = 0.20$, the fractional occupancies of Fe and Co were refined and subjected to the constraint that $f_{Fe} + f_{Co} = 1$ (i.e. the site was assumed not to host vacancies). This yielded values of $x = 0.083(2)$, $x = 0.143(3)$ and $x = 0.188(1)$, where the number in brackets is the estimated standard deviation derived from GSAS (usually an underestimate of the true error in this type of refinement, as discussed in

Chapter 4). These refined values are consistent with the nominal values, although each is underestimated by a similar amount which may suggest a systematic error in the Rietveld refinements.

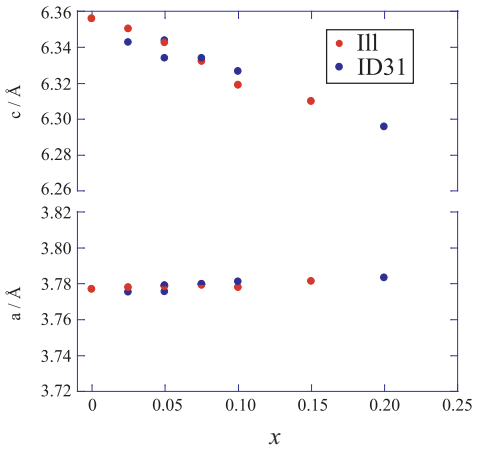
Figure 5.4a illustrates the relationship between the lattice parameters and the Co concentration x. It is clear to see that as x increases, the unit cell volume decreases approximately linearly. This decrease occurs despite a small increase in the value of the a parameter, which is overwhelmed by a relatively large decrease in c. The decrease in unit cell volume is consistent with the replacement of Fe with a metal of smaller ionic radius. The trends do not appear to be affected by the identity of the diffractometer, reflecting that the wavelengths of both instruments were correctly calibrated prior to the measurements.

The three FeAs-containing samples were found to lie a long way below the general trend, with significantly smaller parameters than anticipated from their nominal compositions. The behaviour of the c and a parameters of these samples is not consistent with the simple substitution of Co for Fe, as both parameters are significantly smaller than in stoichiometric LiFeAs. Such characteristics are reminiscent of the non-stoichiometric $Li_{1-y}Fe_{1+y}As$ phases investigated in Chapter 4, suggesting that there may be some incorporation of Fe/Co on to the Li site. All have unit cell volumes smaller by $0.25-0.30$ Å^3; this would correspond to metal-rich compositions with approximately 2% of the Li ions replaced by a mixture of Fe and Co, of formula $Li_{1-y}Fe_{(1-x)(1+y)}Co_{x(1+y)}As$. The fact that these samples contain small amounts of FeAs suggests may be consistent with some deficiency of Li in the reaction mixture (caused by its volatility at high temperatures) resulting in a sample rich in Fe, with the Fe that cannot be incorporated into the ternary phase left over to form binary FeAs.

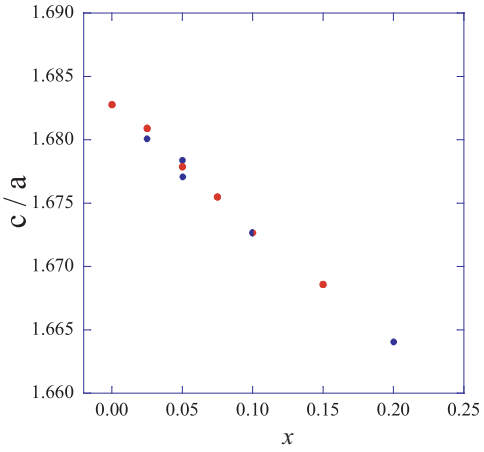
Structural parameters were found to follow smooth trends with increasing x_{Co}. The tetrahedral angles in the FeAs layer, illustrated in figure 5.5, show that the co-ordination environment of Fe becomes slightly more regular as x_{Co} increases. This is presumably driven by a small decrease in M-As distance as Co is substituted for the



(a) Refined unit cell volume..

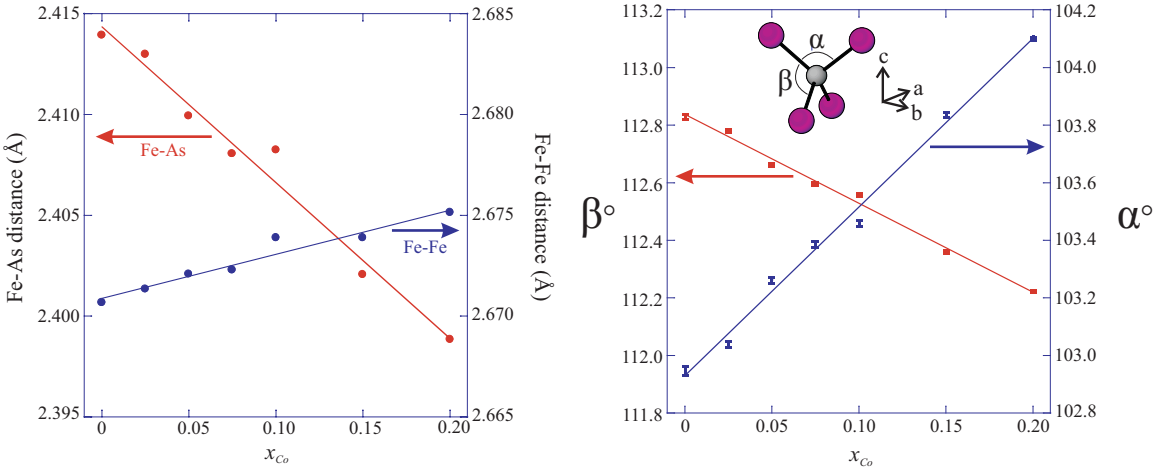


(b) Refined a and c-parameters



(c) c/a ratio.

Figure 5.4: Plots of the variation of lattice parameters with x (unrefined) for $LiFe_{1-x}Co_xAs$, obtained by Rietveld refinement against synchrotron XRPD data from either the I11 (red points) or ID31 diffractometer (blue points). Each data point represents an individual sample (i.e. no samples were measured on both I11 and ID31). Error bars (1 e.s.d. from GSAS) are smaller than the points. Note that figure (a) contains 3 samples with anomalously small unit cell volumes, which were later found to be non-stoichiometric (of type $Li_{1-y}Fe_{1+y}As$).



(a) Nearest-neighbour Fe-As and Fe-Fe distances *vs* composition (x_{Co}).

(b) $FeAs_4$ tetrahedral bond angles *vs* composition (x_{Co}).

Figure 5.5: Variation in refined Fe-As and Fe-Fe bond distances and tetrahedral $FeAs_4$ angles with composition for $LiFe_{1-x}Co_xAs$ between $0 \leq x \leq 0.20$. Error bars represent 1 e.s.d. from GSAS (which are smaller than the markers in (a)). The anomalous Fe-rich samples seen in figure 5.4 are not plotted here.

larger Fe ions. It can also be seen that the *M*-*M* distance increases (as required by the expansion of the *a* parameter) despite the larger decrease in *M*-As.

Although Li-As distances cannot be determined directly by these methods (due to the weak X-ray scattering power of Li), the structural changes about the Li atom can be inferred from changes in As-As distances. Li occupies a square-pyramidal site and there are two discrete As-As distances that define its co-ordination geometry: the basal As-As distance (i.e. the length of the square base) and the apical As-As distance from a basal vertex to the apical vertex. It should be noted that the refinement errors are much smaller for the basal As-As distance because this parameter has no dependence on the refined As *z*-coordinate. It can be seen from figure 5.6 that increasing Co content increases the basal area of the pyramids, while the apical distance does not change significantly. Overall this represents an increase in the volume of the $LiAs_5$ environment, which implies a small increase in the mean Li-As distance.

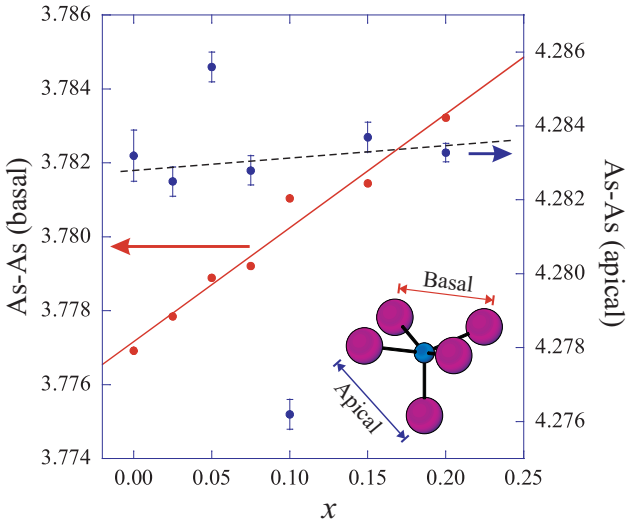


Figure 5.6: Changes to the Li coordination environment with x in $LiFe_{1-x}Co_xAs$, inferred from As-As distances (derived from Rietveld refinements against synchrotron XRPD data). The red line represents a linear best fit to the basal distance data. The dashed line is a guide to the eye for the apical distance data. Error bars represent 1 e.s.d. from GSAS (which are smaller than the markers for basal distances).

5.4 Structural characterisation of $LiFe_{1-x}Ni_xAs$

5.4.1 Laboratory X-Ray Powder Diffraction

Eight samples of type $LiFe_{1-x}Ni_xAs$ (with $0.005 \leq x \leq 0.200$) were synthesised and initially characterised by Si-calibrated XRPD using a PanAlytical XPert Pro, with monochromated Cu K_{α_1} radiation. Preliminary XRPD investigations on a sample of LiFeAs suggested that this compound is not only highly air-sensitive but is also able to react with vacuum grease, which is routinely used to fix the powder to a glass slide. To avoid any sample decomposition by this route, small amounts of the highly air-sensitive samples were ground together with high purity silicon in a 3:1 mass ratio, loaded into a depression in an aluminium slide, and sealed inside an air-tight cell under an argon atmosphere.

The samples in this series are separated by very small steps in composition, and the substitution of Fe by Ni is expected to produce only a small structural change. When attempting to detect such small differences by laboratory XRPD, experimental errors (e.g. small variations in location of the sample relative to the incident beam

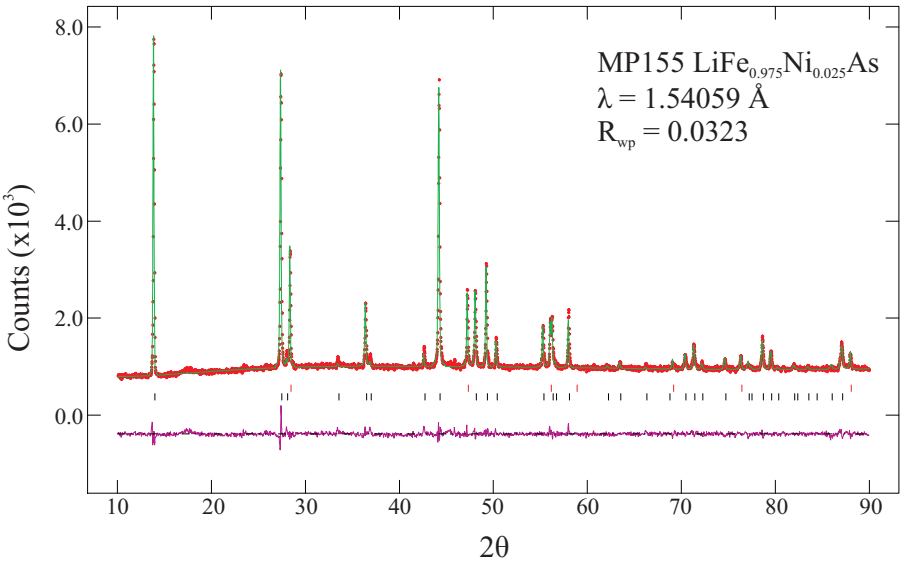


Figure 5.7: Representative Si-calibrated Rietveld refinement against laboratory XRD data for $LiFe_{1-x}Ni_xAs$. Reflection markers: *Black* = $LiFe_{0.975}Ni_{0.025}As$; *red* = Si.

and the detector) can become significant and must be minimised. For this reason, the same aluminium slide and cell were used for each member of the series, and for each experiment the cell was carefully mounted in the diffractometer to try to ensure a consistent and reproducible sample height.

For the purposes of collecting data of high enough quality to perform reliable Rietveld refinements, patterns are typically collected over a period of 3 hours from this instrument. However, the air-tight cells used in this work do not provide a perfect seal against the atmosphere and any air-sensitive sample contained within will degrade after a period of time. During the course of these experiments, sample degradation (signified by the appearance of poorly-crystalline FeAs in the diffraction patterns and a small shift in the Bragg peaks of the main phase) became noticeable after approximately 2 hours. Each sample was therefore measured using a standard program, with a 2θ range 10-90°, and a duration of 100 minutes.

Rietveld refinements were conducted by initially including only the silicon phase with fixed lattice parameters, and refining the *shift* profile parameter (which is a sample displacement correction).[83] A representative refinement is shown in figure 5.7. The $LiFe_{1-x}Ni_xAs$ phase was then added and the fixed *shift* correction applied. Lattice

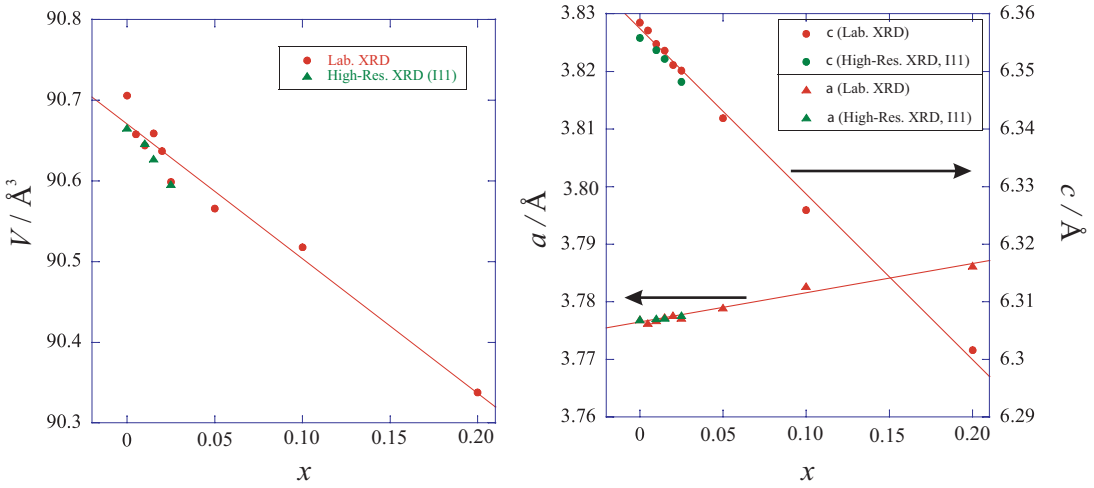
parameters were then allowed to refine freely. Samples mounted in this way exhibited varying degrees of preferred orientation, which was accounted for by a spherical harmonic function. Tables of refined parameters from these experiments are included in Appendix E.

The lattice parameter trends obtained by these methods, displayed in figure 5.8, showed similar behaviour to the Co-doped series. As the concentration of Ni increases, the unit cell volume decreases, which is driven by a decrease in the c parameter. Like the Co-doped series, there is also an increase in the a-parameter, which is even more pronounced here. In the compositional range $x \leq 0.025$ the trend is not completely smooth. Here, the extremely small steps in composition combined with the subtle structural change make it very difficult to resolve the differences between similar samples under these experimental conditions.

It was also noted that samples that had degraded slightly, with small broad peaks corresponding to FeAs, had refined lattice parameters that lay below the general trend. Again, this behaviour is reminiscent of the Fe-rich materials discussed in Chapter 4, and hints that the facile extrusion of Li could be the reason for this compound's instability in air. It should be noted that the isostructural Na analogue NaFeAs is also highly sensitive to the presence of air, and that Na may be deintercalated to leave a poorly-crystalline phase of stoichiometry $NaFe_2As_2$,[141] although in the case of LiFeAs the equivalent $ThCr_2Si_2$-type compound $LiFe_2As_2$ has not been observed, as the reaction appears to proceed directly to FeAs.

5.4.2 High Resolution XRPD

Three Ni-doped samples, with compositions $x_{Ni} = 0.010$, 0.015 and 0.025, were also studied by high resolution synchrotron XRPD using I11 at the Diamond Light Source, UK. Measurement conditions were identical to those used for the Co-doped samples in section 5.3, with an incident wavelength $\lambda = 0.60036$ Å. No internal standards were used. These data are expected to yield highly accurate and reproducible



(a) Refined unit cell volume.

(b) Refined a and c-parameters.

Figure 5.8: Refined lattice parameters plotted against nominal composition *(x)* for a series of $LiFe_{1-x}Ni_xAs$, obtained from Si-calibrated laboratory XRPD data presented in section 5.4.1 (red markers) and high-resolution synchrotron-XRPD data presented in section 5.4.2 (green markers). Error bars (1 e.s.d. from GSAS) are similar to the marker sizes.

lattice parameter values due to the very high resolution of the instrument (with narrow peak widths maximising the precision in the peak position values), extensive instrument calibration, and the highly reproducible sample positioning and diffraction geometry. Rietveld refinements against these data (illustrated in figure 5.9 with parameters included in figure 5.8a) show good agreement with the results obtained from laboratory Si-calibrated XRD experiments. The unit cell volume is shown to decrease consistently, even in the low-doping region where there appears to be significant uncertainty in the laboratory XRD parameters. Due to the limited number of samples studied using I11, detailed analysis of the structural parameters is discussed together with NPD results in section 5.4.3.

5.4.3 Neutron powder diffraction

All of the Ni-doped samples (with the exception of $x = 0.010$) were studied at ambient temperature by time-of-flight neutron diffraction using the Polaris instrument at ISIS. Samples were contained in thin-walled vanadium cans of 6 mm diameter, which

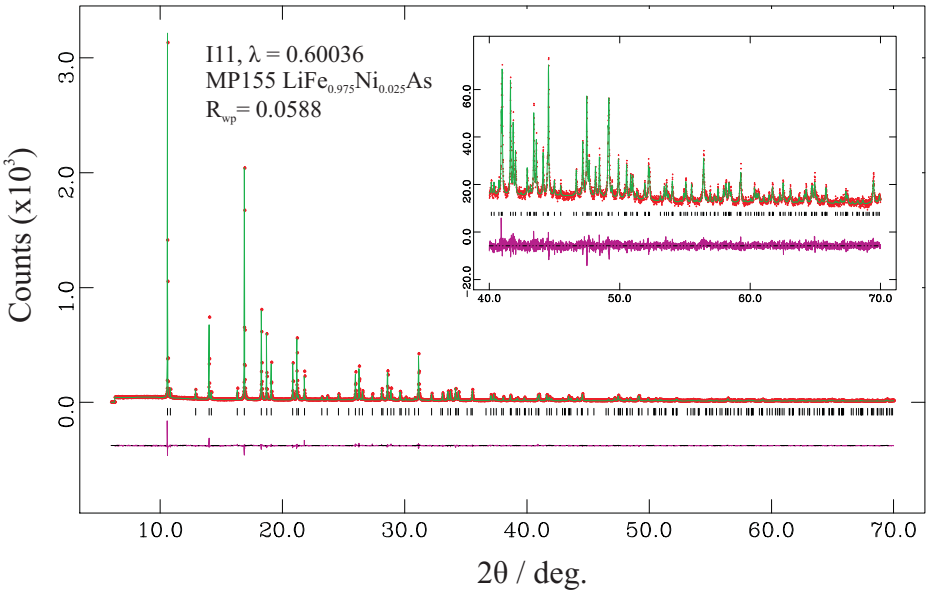


Figure 5.9: Representative Rietveld refinement against high-resolution XRPD data (I11 diffractometer) for a typical sample of $LiFe_{1-x}Ni_xAs$. High angle data ($40 \leq 2\theta \leq 70°$) are inset. Reflection markers: *Black* = $LiFe_{1-x}Ni_xAs$.

were loaded and sealed with an indium gasket under an argon atmosphere. Rietveld refinement was used to obtain structural parameters. A representative refinement is displayed in figure 5.10. The compositions were not refined, due to the fairly similar neutron scattering lengths of Fe and Ni (9.54 fm and 10.3 fm, respectively), and nominal values are used throughout this section. Refined parameters are displayed in the tables in Appendix E.

The refined lattice parameters (plotted in figure 5.11) are consistent with the trends derived from laboratory X-ray diffraction, and show excellent correlation between the c/a ratio and the nominal Ni content. The structural parameters also show smooth changes with x. The $M\text{As}_4$ environment, which is highly distorted in the end member LiFeAs, is found to exhibit a small relaxation toward regular tetrahedral geometry. This is accompanied by a small decrease in the M-As distance (-0.4%) as x increases from 0 to 0.20; this is expected from the slightly smaller ionic radius of Ni^{2+} (0.55 Å *vs* 0.63 Å for tetrahedral Fe^{2+}).[142] Over the same x range the M-M distance (which is equal to $a/\sqrt{2}$) increases by approximately $+0.3\%$. These distances are plotted in

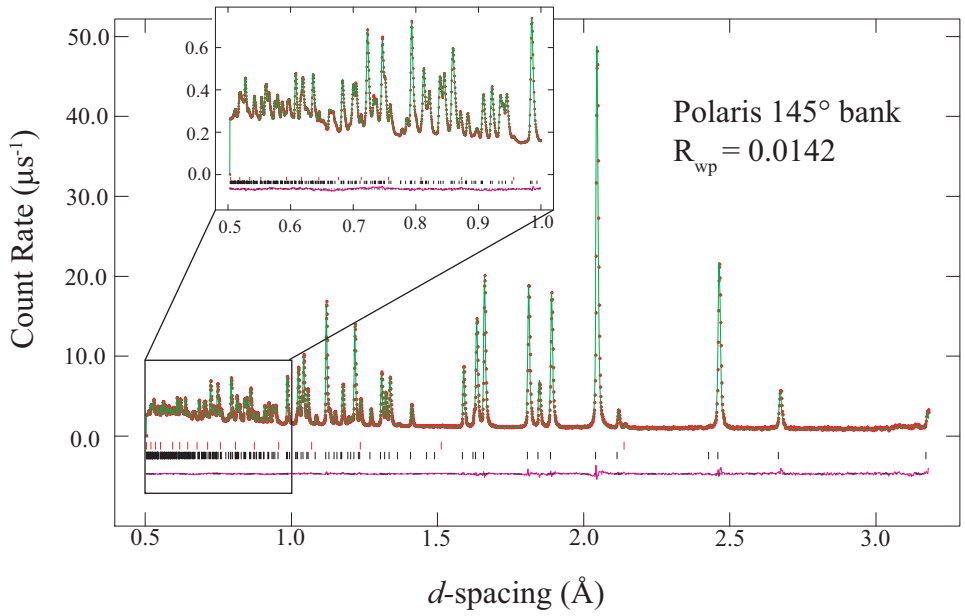
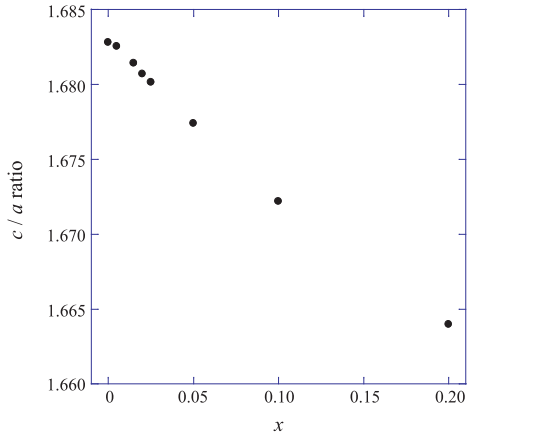


Figure 5.10: Representative Rietveld refinement against neutron powder diffraction data from the 145° bank of Polaris, for a sample of $LiFe_{1-x}Ni_xAs$ with $x = 0.015$. The low *d*-spacing region is inset. Reflection markers: *Black* = $LiFe_{1-x}Ni_xAs$; *red* = V (sample container).

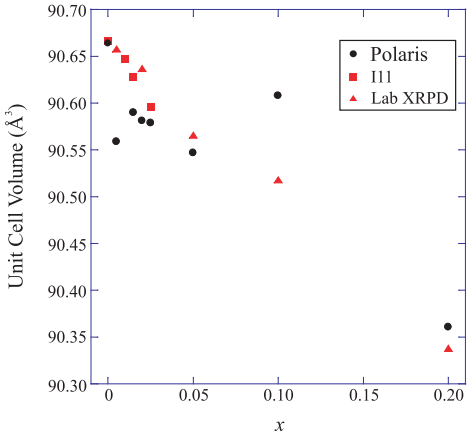
figure 5.12.

Small changes also occur in the square-pyramidal $LiAs_5$ environment, with both Li-As distances increasing with Ni content. This is consistent with the changes observed on Co substitution (see figure 5.6 on page 139). Considering that the overall trend is to decrease the unit cell volume, it is perhaps surprising that the effective size of the Li^+ site should increase in this manner. As the MAs_4 tetrahedra relax and the *a*-parameter increases, the As-As distance must increase and drive a basal expansion of the As_5 square pyramid. The increase in the Li^+ *z*-coordinate occurs as the ion is drawn towards the base of the pyramid.

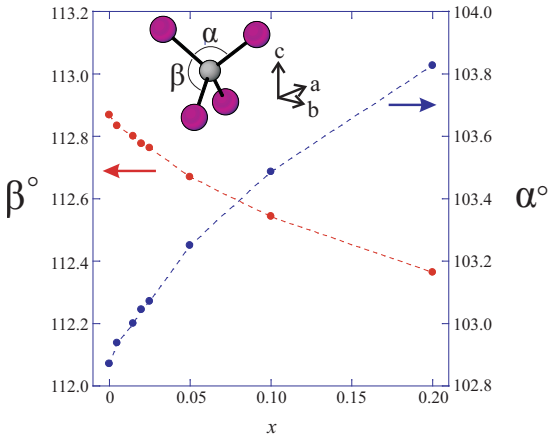
The excellent correlation between structural parameters and the nominal compositions reflect the high quality of the diffraction data and suggest that these nominal values are highly accurate. However, the trend in unit cell volume contains a number of anomalous points which occur despite the excellent agreement between observed data and the refined model and do not arise in the Si-calibrated XRPD



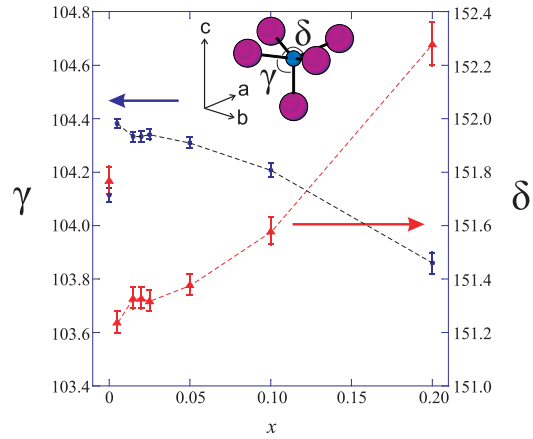
(a) Refined c / a ratios.



(b) Refined unit cell volume.



(c) Refined As-Fe-As angles.



(d) Refined $LiAs_5$ bond angles.

Figure 5.11: Selected lattice and structural parameters plotted against nominal composition *(x)* for the series $LiFe_{1-x}Ni_xAs$. Values were obtained from Rietveld refinement against NPD data. Note that the values for sample with $x = 0$ were obtained from a joint XRD-NPD refinement.

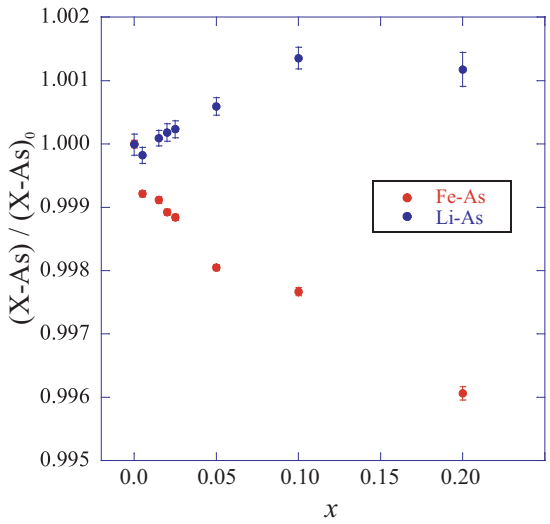


Figure 5.12: Normalised nearest-neighbour Fe-As and Li-As distances plotted against nominal composition *(x)* for $LiFe_{1-x}Ni_xAs$. Values were obtained by Rietveld refinement against NPD data (Polaris diffractometer). Error bars represent the statistical error in the refinements (1 e.s.d. from GSAS).

experiments (detailed in section 5.4.1). The very smooth trend in c/a ratio suggests that the relative positions of the Bragg peaks are reliable; it is therefore likely that differences in the *absolute* positions of the peaks are the cause of these anomalies. The absolute positions can be determined very precisely but their accuracies are affected by the position of the sample in the diffractometer and uncertainties in the value of the path length/time-of-flight, which directly affects the values derived for lattice parameters.

The samples studied by NPD contained no internal standard (e.g. Si) and it is therefore difficult to discern differences in the effective zero-points of the diffraction patterns. In general, lattice parameters are determined most accurately using X-ray radiation, as the incident wavelength is known to a higher degree of accuracy (it is either characteristic radiation such as Cu $K_{\alpha 1}$ or highly monochromated synchrotron radiation). This has been demonstrated by an extensive comparative study of Rietveld refinements against XRPD and constant-wavelength NPD data for several standard samples.[143, 144]

5.5 Structural characterisation of $LiFe_{1-x}Mn_xAs$

A very limited number of $LiFe_{1-x}Mn_xAs$ samples were synthesised as they could only be made phase-pure for compositions with $x \leq 0.05$. Samples with x = 0.01, 0.02 and 0.05 were prepared by the methods outlined in section 5.2 and found to be single phase by laboratory X-ray diffraction. These samples were studied by neutron powder diffraction using the D2B diffractometer at the Institut Laue-Langevin, with an incident wavelength $\lambda = 1.5943$ Å. Structural parameters were obtained by Rietveld refinements, which were conducted similarly for each sample. A representative refinement is displayed in figure 5.13. In the starting model, the Li site was shared with a small amount of Fe, and the relative occupancy of the site by these two atoms was refined in the later stages (with the constraint that the total occupancy of the site must be 1). Tables of refined parameters are displayed in Appendix E.

Replacement of Fe by Mn is expected to cause an increase in lattice parameters due to the slightly greater ionic radius of Mn (0.66 Å *vs* 0.63 Å for tetrahedral Fe^{2+}),[10] and this is observed from a comparison of the isostructural PbFCl-type compounds NaFeAs ($a = 3.9494$, $c = 7.0396$ Å)[145] and NaMnAs ($a = 4.212$, $c = 7.112$ Å).[146] However, in contrast to this expected change, the refined lattice parameters for $LiFe_{1-x}Mn_xAs$ (displayed in figure 5.14) show an initial increase followed by a decrease beyond $x = 0.02$. Inspection of the refined occupancy factors for Li and Fe on the 2*c* site does suggest that this site becomes occupied by an increasing amount of Fe as x increases, although the true errors on these values are expected to be significantly higher than the statistical errors generated by GSAS. It is also apparent, from consideration of the trends in unit cell volume for $NaFe_{1-x}Mn_xAs$ (inferred by assuming a linear change in cell parameters between the end members) and $Li_{(1-y)}Fe_{(1+y)}As$, that the incorporation of 2.4(3) % Fe on the Li site in $LiFe_{0.95}Mn_{0.05}As$ is unlikely to be enough to cause such a strong deviation from the expected lattice parameters.

Examination of the effect of Mn substitution on other structural parameters shows

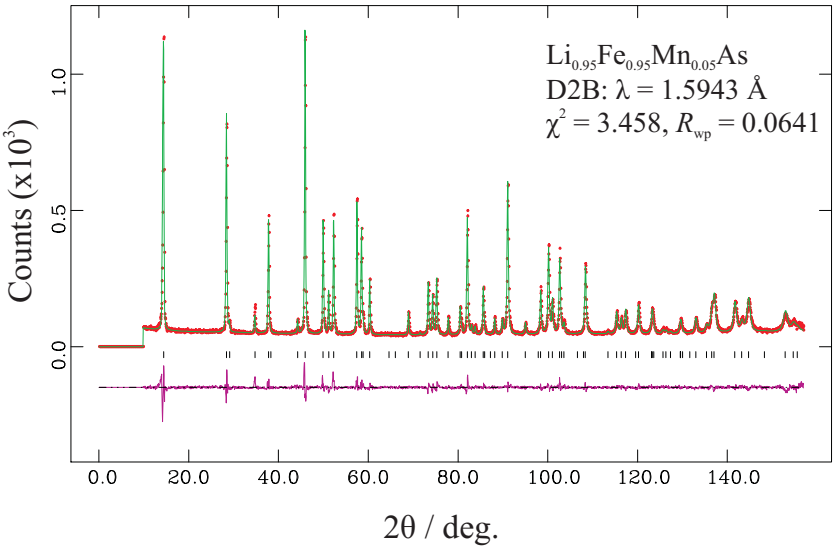


Figure 5.13: Representative Rietveld refinement against constant-wavelength neutron diffraction data from D2B for $LiFe_{0.95}Mn_{0.05}As$. Reflection markers: *Black* = $LiFe_{0.95}Mn_{0.05}As$.

a small increase in the *M*-As distances at the lowest doping levels, which then appears to decline as x is increased to 0.05. Relatively large statistical errors make it difficult to discern any real trend in the weighted Li-As distance for comparison. As with Co- and Ni-substitution, the $FeAs_4$ tetrahedra again become slightly more distorted as x increases (plotted in figure 5.15). The analysis of these trends is somewhat hampered by the small number of samples, and it is possible that some small anomaly in the refined As z-coordinate causes this apparent discontinuity between $x = 0.02$ and $x = 0.05$.

5.6 Structural comparisons between M = Mn, Co, Ni and $Li_{1-y}Fe_{1+y}As$

The work presented in the first part of this chapter, together with the work contained in Chapter 4, describes two important ways in which the composition of LiFeAs can be modified: the partial substitution of Fe by Mn, Co or Ni ($LiFe_{1-x}M_xAs$), and the partial occupancy of the Li-site by a small amount of Fe ($Li_{1-y}Fe_{1+y}As$). In order to

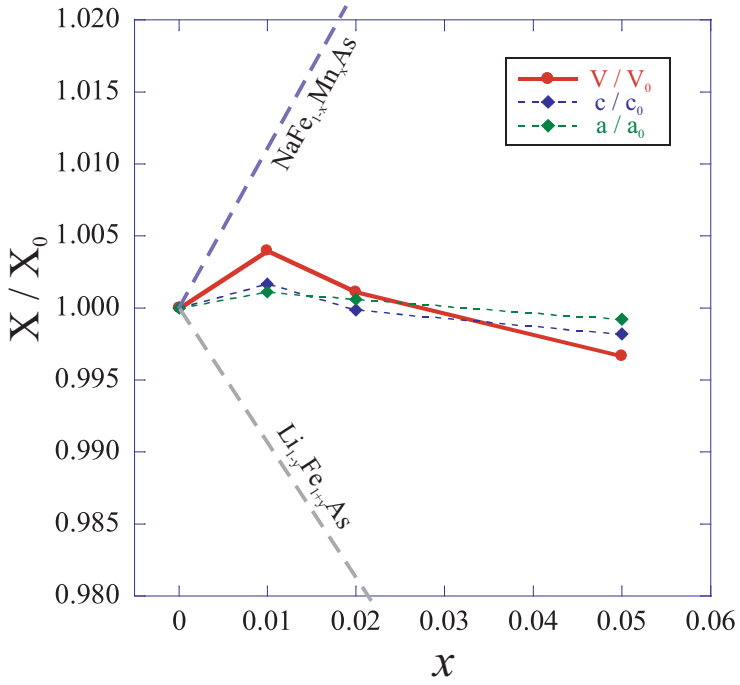
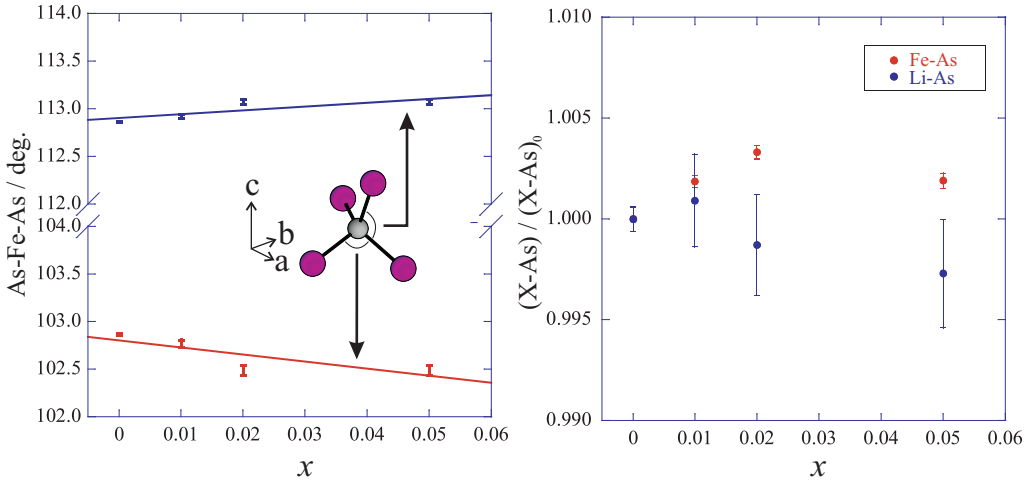


Figure 5.14: Normalised lattice parameters for $LiFe_{(1-x)}Mn_xAs$, from Rietveld refinement against NPD data. Dashed lines represent trends in unit cell volume for the isostructural $NaFe_{(1-x)}Mn_xAs$ system (blue line, estimated from the parameters of the end members) and $Li_{(1-y)}Fe_{(1+y)}As$ (grey line, from Chapter 4). Refinement errors are smaller than the points.



(a) Refined As-Fe-As angles.

(b) Refined Fe-As distances and weighted Li-As distances, both normalised.

Figure 5.15: Trends in bond angles and normalised bond distances plotted against nominal composition *(x)* for the series $LiFe_{1-x}Mn_xAs$, obtained by Rietveld refinement against constant-wavelength NPD data. Error bars represent 1 e.s.d. from GSAS.

compare these changes directly, normalised structural changes accompanying each of these substitutions are illustrated in figures 5.16, 5.17 and 5.18.

As might be anticipated from ionic radius arguments, the structural response to Co- and Ni-substitution in $LiFe_{1-x}M_xAs$ is generally very similar for both metals. It can be seen that the resulting decrease in V is very slightly stronger when M = Co, while Ni-substituted samples show the strongest decrease in c/a ratio (arising from a more pronounced increase in the a-parameter). These changes are presumably driven by a steadily decreasing nearest-neighbour Fe(Co,Ni)-As distance. For both metals, the geometry of the $FeAs_4$ tetrahedron relaxes slightly towards regularity as x increases. It may be significant that the Fe-Fe distance (equal to $a/\sqrt{2}$), which is thought to have a strong influence on T_c, increases with x in these materials. These structural changes are all very similar those observed on Co- and Ni-substitution in the related compounds $NaFe_{1-x}M_xAs$[69] (where the a-parameter is almost invariant with x), $CaFe_{1-x}M_xAsF$,[139] and $BaFe_{2-x}M_xAs_2$.[147]

While the Co and Ni series are reasonably well-behaved, the structural changes observed on Mn-substitution do not seem to be entirely consistent with an increased ionic radius, and they are not anticipated from inspection of the isostructural compounds NaFeAs and NaMnAs. This type of substitution does result in an increase in Fe-As distance and an apparent increase in V between $x = 0.0$ and $x = 0.01$. Beyond $x = 0.01$, V appears to decrease sharply. Neutron diffraction experiments hinted that this deviation from the anticipated trend might be due, in some part, to incorporation of Fe on the Li site. Unfortunately a more meaningful discussion of these (potentially complicated) trends is hampered by the small number of samples studied, due to the fact that single-phase samples with $x > 0.05$ could not be synthesised.

Materials of type $Li_{1-y}Fe_{1+y}As$ exhibit structural changes that are quite distinct from those of $LiFe_{1-x}M_xAs$ (especially M = Co, Ni), due to the much stronger dependence of any given parameter on the amount of substituent y. Figure 5.16 shows a sharp decrease in V as y increases, which is due to a decrease in both a and c parameters (in contrast to the changes seen in $LiFe_{1-x}M_xAs$, where V decreases despite

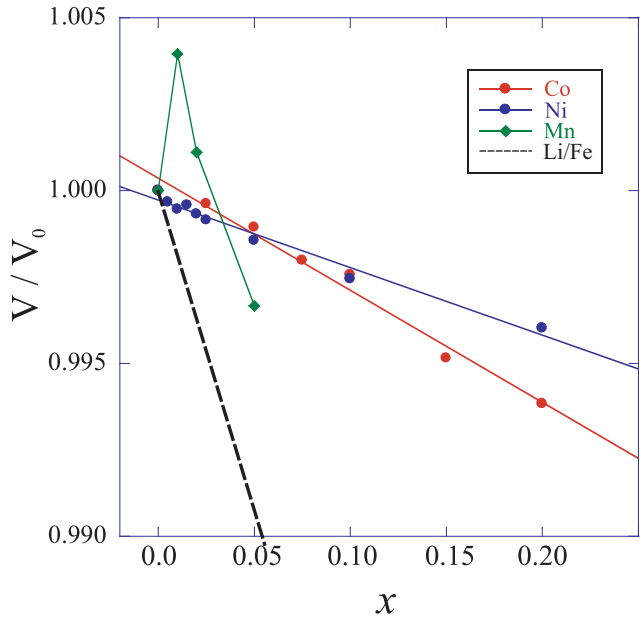
an increase in the a-parameter). These more dramatic changes are also reflected in the increased distortion of the $FeAs_4$ tetrahedra. However, there is little discernible change in the Fe-As distance with y, presumably because the substituent does not directly affect the FeAs layer (unlike in $LiFe_{1-x}M_xAs$, where the FeAs layer hosts the substituent atoms). During the structural investigation of $LiFe_{1-x}Co_xAs$ (section 5.3.1), several Fe-rich samples of this type were synthesised inadvertently, but due to their distinctive structural and superconducting features (a unit cell volume that is much smaller than expected and a strongly suppressed superconducting transition) they could be easily identified.

5.7 Magnetic characterisation of $LiFe_{1-x}M_xAs$

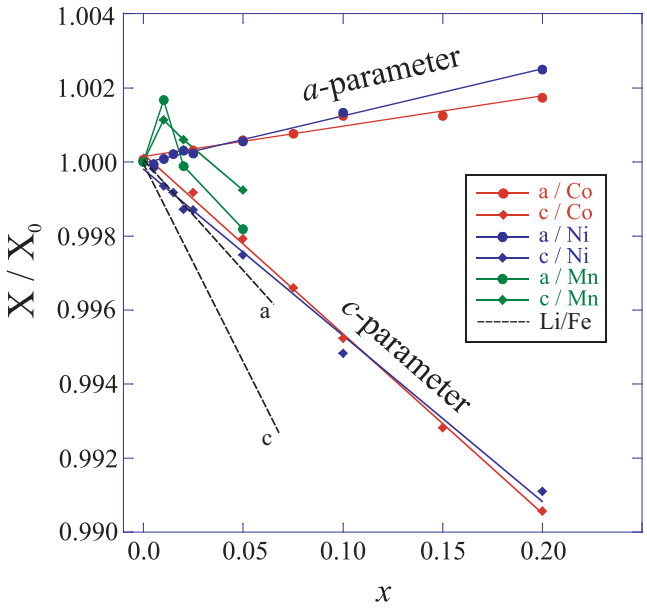
5.7.1 dc-SQUID Magnetometry

Each member of the series was characterised by dc-SQUID magnetometry, under similar conditions to those employed in Chapter 4. Measurements of magnetisation were taken in the temperature range $2 \leq T \leq 300$ K, using small steps of 1 K for temperatures in the region of the superconducting transition ($T < 30$ K), and larger steps of 5 K thereafter. A small constant measuring field of 50 Oe was applied, with a field cooled scan and a zero-field cooled scan (corrected for residual field if necessary) for each sample.

Superconducting transition temperatures were derived by drawing a tangent to the sharpest part of the transition and extrapolating the paramagnetic regions; the intercept of the two was rounded to the nearest 0.5 K and taken to be T_c. The results from the Co- and Ni-doped series are illustrated in figure 5.19. Figures 5.19a and 5.19c illustrate the trend in superconducting volume fraction, which becomes progressively smaller as x increases (i.e. as electrons are added to the system). This is clearest for the Co-doped series, which has larger differences in composition between samples. For the Ni-doped series, there is some overlap between adjacent samples, which may



(a) Refined unit cell volume



(b) Refined a- and c-parameters

Figure 5.16: Normalised lattice parameters for three series of $LiFe_{1-x}M_xAs$ where $M =$ Mn, Co, or Ni (from data presented in sections 5.3 – 5.5). Red and blue lines represent linear best fits to the data for $M =$ Co and Ni, respectively. The green lines represent $M =$ Mn and are a guide to the eye. Dashed black lines represent the trends observed for non-stoichiometric materials of type $Li_{1-y}Fe_{1+y}As$ (discussed in Chapter 4). For clarity, the dashed lines are extrapolated beyond the natural end of the series (at $x = 0.04$).

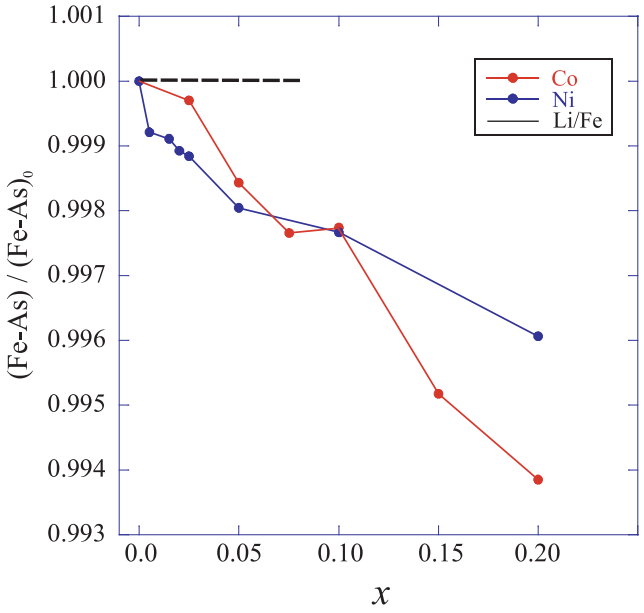


Figure 5.17: Variation in normalised Fe-As distances with composition for $LiFe_{1-x}Co_xAs$ (red line/markers) and $LiFe_{1-x}Ni_xAs$ (blue line/markers), obtained by Rietveld refinement against data presented in sections 5.3 (synchrotron XRPD) and 5.4 (t.o.f. NPD). Blue/red lines are a guide to the eye. The black dashed line represents non-stoichiometric materials of type $Li_{1-y}Fe_{1+y}As$ (discussed in Chapter 4) and is extrapolated beyond $x = 0.04$ for ease of comparison.

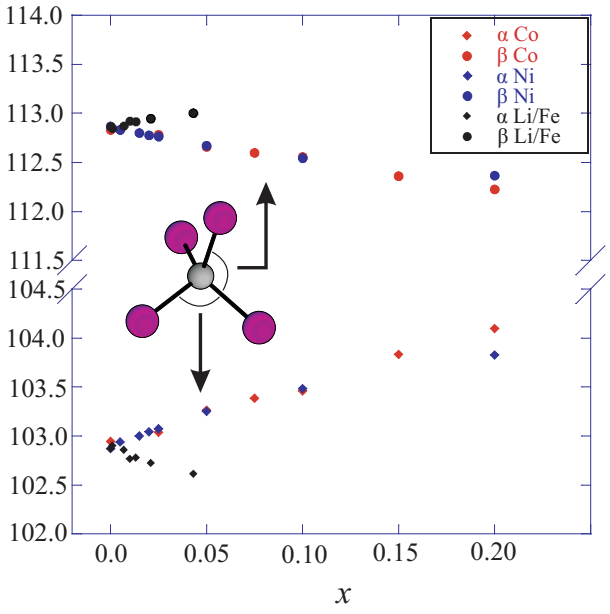
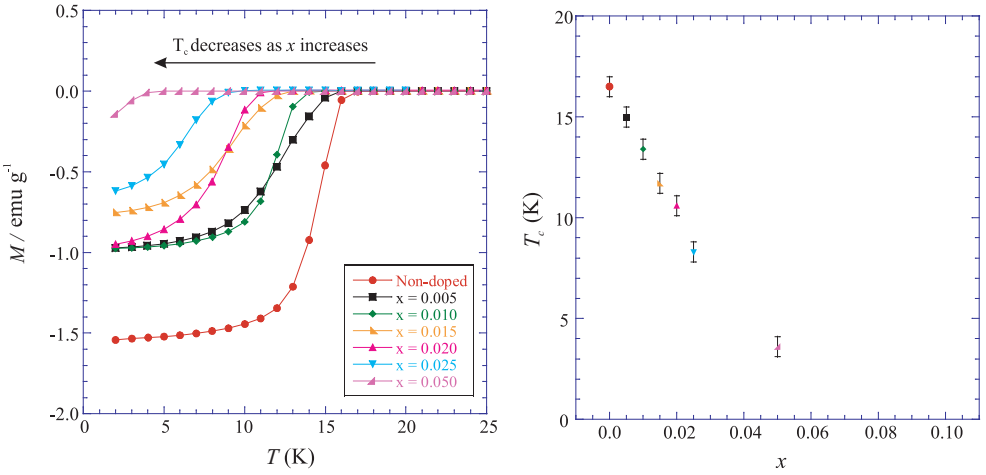
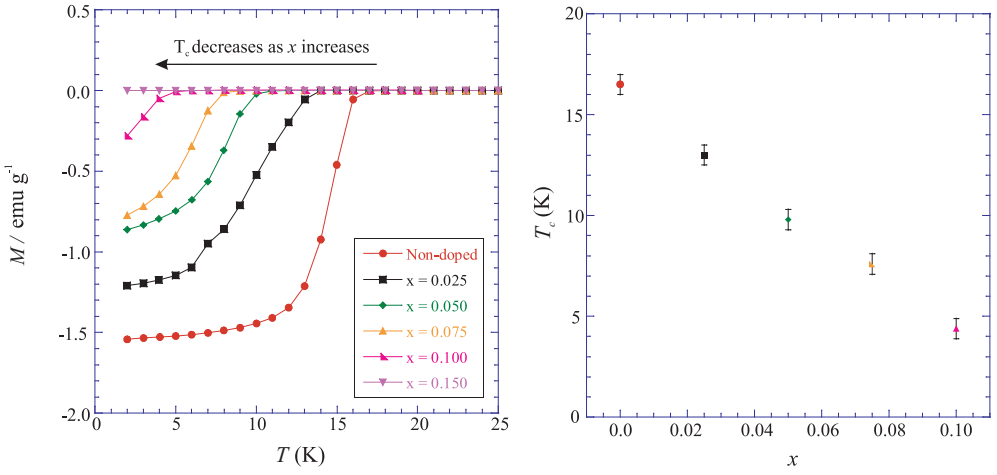


Figure 5.18: Plot of As-Fe-As angles for $LiFe_{1-x}M_xAs$ (M = Ni, Co) and $Li_{1-y}Fe_{1+y}As$ (data from Chapter 4) against composition, illustrating the contrasting relaxation/distortion of the $FeAs_4$ tetrahedra in the two systems. Error bars (representing 1 e.s.d. from GSAS) are smaller than the markers.



(a) M *vs* T for $LiFe_{1-x}Ni_xAs$ ($0.0 \leq x \leq 0.05$, (b) T_c *vs* composition *(x)* for $LiFe_{1-x}Ni_xAs$. compositions inset).



(c) M vs T for $LiFe_{1-x}Co_xAs$ ($0.0 \leq x \leq 0.150$, (d) T_c *vs* composition *(x)* for $LiFe_{1-x}Co_xAs$. compositions inset).

Figure 5.19: Plots of Magnetisation *vs* Temperature (d.c. SQUID magnetometry in a 50 Oe measuring field), and T_c *vs* Composition *(x)* (T_c derived from the M *vs* T plots), for superconducting samples of two series of $LiFe_{1-x}M_xAs$ (M =Co or Ni). Precise compositions are inset.

be due to the inherent uncertainties involved in measuring a superconducting volume fraction quantitatively from a powder (as discussed in Chapter 2).

The superconducting transition temperatures, derived from these data, are plotted in figures 5.19b and 5.19d. These plots show a well-behaved linear relationship between T_c and x, with the former strongly suppressed as x increases in both series. Superconductivity is no longer observed beyond compositions of $x = 0.10$ (Co) and $x = 0.05$ (Ni). One crucial difference between the two series is derived from these plots: the negative gradient of the Ni-doped series is considerably steeper than that of the Co-doped series. A line of best fit was applied to each data set using the Kaleidagraph software package, and yielded approximate values for $^{dT}/_{dx}$ of -118 K per Co for the Co-doped series and -261 K per Ni for the Ni-doped series. It should be noted that these values are very approximate, as the errors inherent in the T_c values undermine the precision of the values obtained from the fitting program. However, it is clear that the substitution of x Ni atoms is approximately twice as effective at suppressing T_c than the substitution of x Co atoms.

On first inspection this is perhaps not surprising: each Ni (d^8) dopant atom brings twice as many extra electrons to the system as each Co (d^7) dopant atom. A plot of T_c versus the number of dopant electrons per formula unit (i.e. the number of extra electrons per Fe), shown in figure 5.20, underlines this apparently more fundamental dependence on electron count which is independent of dopant identity. Hence, a sample of formula $LiFe_{1-x}Co_xAs$ has very similar properties to a sample of formula $LiFe_{1-x/2}Ni_{x/2}As$. This dependence on the number of dopant electrons appears to be universal as it has also been observed in the isostructural Na analogue $NaFe_{1-x}M_xAs$,[69] in $BaFe_{2-x}M_xAs_2$ (M = Co, Ni and Cu)[147] and also for $4d$ electron dopants in this system (M = Rh, Pd, which have the same d-shell configuration as Co and Ni respectively),[148] and in the ZrCuSiAs-type $CaFe_{1-x}M_xAsF$ (M = Co, Ni).[139, 149]

In all of these examples, superconductivity is induced at low doping levels, then T_c goes through a maximum before superconductivity is destroyed, which typically

occurs at doping levels of above 0.2 electrons per Fe. This "superconducting dome" was illustrated in figures 5.1a, 5.1b and 5.1c on page 129. The dependence of the magnetic and superconducting properties on electron count (i.e. the shape of the superconducting dome) has generally been considered in terms of a band-filling effect, with the dopant electrons delocalised throughout the solid and the Fermi level rising with progressive doping. This scenario is expected for a broad conduction band with dopant *d*-orbitals that are of similar energy to the Fe *d*-orbitals. DFT band structure calculations and experiments have suggested that this model may be reasonable for $SrFe_{2-x}M_xAs_2$.[150] However, there is currently no clear theoretical consensus over the validity of this model. In particular, a very recent DFT study by Wadati *et al.*[151] on $BaFe_{2-x}M_xAs_2$ (M = Co, Ni, Cu, Ru, Rh, Pd and Zn) has suggested that the band-filling assumption is flawed. Instead, they suggest that the extra electrons should remain strongly localised in the *d*-orbitals of the dopant atoms, which then act as electron-scattering centres to interfere with magnetic order and superconductivity. It should be noted that this scattering model has yet to be reconciled with the 1:2 relationship between Co and Ni doping, and details of how this could induce superconductivity or enhance T_c have not yet been addressed, although a plausible scenario is that the effectiveness of a dopant at destroying superconductivity and magnetic order correlates with its electronegativity (i.e. the energy of its *d*-states relative to those of Fe).[152]

These models represent two extreme cases (complete delocalisation *vs* complete localisation) and it may be possible that the compounds discussed here represent a range of intermediate cases. In any case, it is clear that further studies (both theoretical and experimental) are required before the origin of these observations can be satisfactorily explained. In LiFeAs, the suppression of T_c and the significant decrease in the superconducting volume fraction by Co and Ni does appear to be consistent with such an impurity model.

As noted in section 5.3, three samples with nominal $x_{Co} = 0.025$, 0.05 and 0.10 were found to have anomalously small unit cell volumes and other structural features

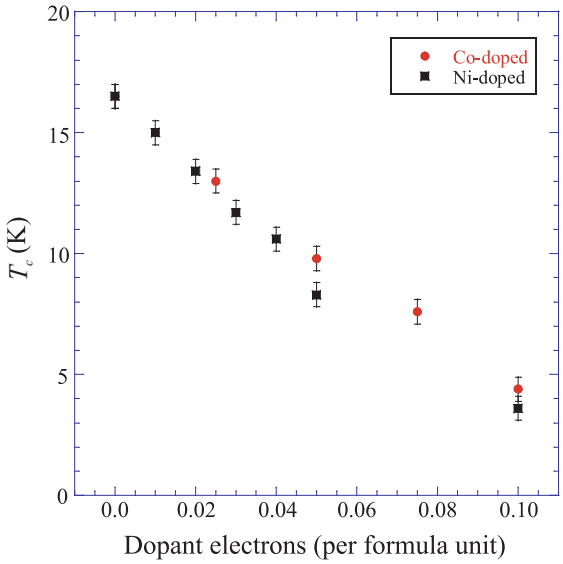


Figure 5.20: Variation of T_c with electron count for both Co-doped (red markers) and Ni-doped (black markers) series. T_c values were derived from the magnetisation data displayed in figure 5.19.

associated with non-stoichiometric $Li_{(1-y)}Fe_{(1+y)}As$ type materials with $y \approx 0.02$. Their magnetic properties were found to be consistent with this conclusion, as all remained paramagnetic down to 2 K, in contrast to their superconducting counterparts with non-anomalous structures.

Beyond the superconducting regime (in the region $x_{Co} > 0.10$ and $x_{Ni} > 0.05$) the materials show weak temperature-dependent paramagnetism (approximately 3 orders of magnitude weaker than a typical Meissner signal) that does not obey the Curie-Weiss law, with evidence for a magnetic transition when $T \approx 10$ K. This behaviour is well exemplified by $x_{Co} = 0.15$ (figure 5.21), and is echoed in the behaviour of non-superconducting $Li_{(1-y)}Fe_{(1+y)}As$ materials. The splitting of the FC and ZFC scans (with a decrease in magnetic susceptibility most strongly evident in the ZFC scan), along with the very low transition temperature, suggests that compositional inhomogeneity may be the cause of this apparent transition, with some tiny fraction of the sample exhibiting the diamagnetism associated with the Meissner effect. The relative strengths of the Meissner signal and the paramagnetic signal means that an amount of superconducting impurity of the order of 0.001 mol% could cause this effect. Alternatively, a transition to a ferromagnetically ordered state cannot be ruled

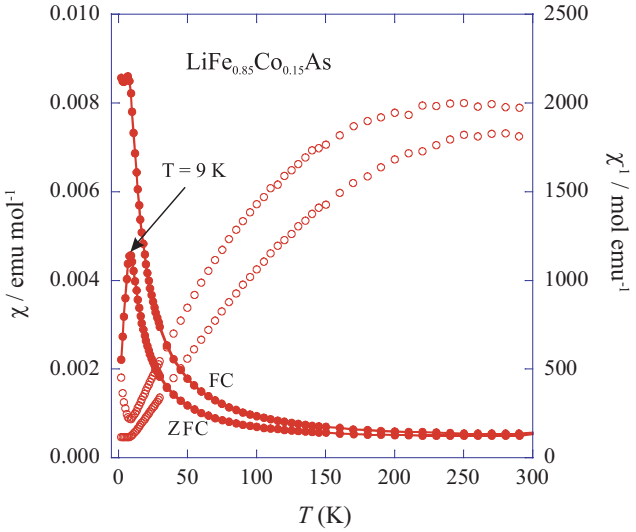


Figure 5.21: Typical magnetic behaviour of non-superconducting $LiFe_{1-x}Co_xAs$ showing non-Curie-Weiss paramagnetism. Data were taken from a sample of composition $LiFe_{0.85}Co_{0.15}As$ using d.c. SQUID magnetometry with an applied field of 50 Oe. Filled circles represent magnetic susceptibility (χ), while open circles represent $1/\chi$.

out. In this case, the small applied field may have been insufficient to align the ferromagnetic domains after zero-field cooling, resulting in an increasing susceptibility up to the Curie temperature. However, it should also be noted that the existence of magnetic order when the system is doped beyond the superconducting region would be unprecedented. Measurements at higher field could be used to distinguish between these possibilities.

In contrast to samples doped with cobalt and nickel, those doped with manganese are formally hole-doped (i.e. decrease the electron count). If the suppression of superconductivity by electron-doping is due to band-filling (as discussed above), this might imply that hole-doping will enhance T_c. However, this is not borne out by experiment. Instead, it is clear from the magnetisation measurements plotted in figure 5.22 that superconductivity is suppressed by the introduction of Mn, and this suppression is significantly stronger than that caused by Co or Ni. The gradient $\delta T/\delta x$ (obtained in the same way as for Co and Ni-doped series) is approximately -325 K per Mn, which is similar in magnitude to that of Ni-doping (-261 K per Ni). The superconducting volume fraction is also very strongly suppressed; the sample with

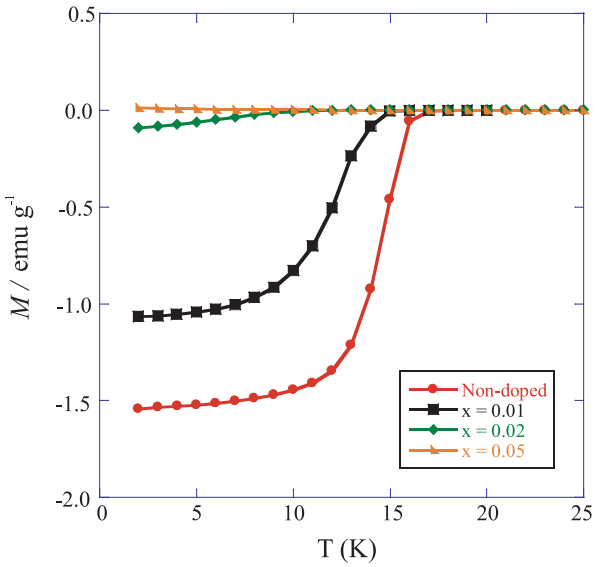


Figure 5.22: Variable-temperature magnetisation measurements for three samples of $LiFe_{1-x}Mn_xAs$ ($x = 0.01,\ 0.02,\ 0.05$) and non-doped LiFeAs, obtained using d.c. SQUID magnetometry with an applied field of 50 Oe. These data illustrate the suppression of superconductivity with increasing Mn content.

$x_{Mn} = 0.05$ did not exhibit superconductivity, while $x_{Mn} = 0.02$ exhibits a very weak diamagnetic signal relative to samples with $(x_{Co},\ x_{Ni}) = 0.02$. A magnetic phase diagram for $LiFe_{1-x}M_xAs$, constructed from these results and those for M =Co and Ni, is plotted in figure 5.23.

This type of behaviour is reminiscent of the Fe-rich $Li_{1-y}Fe_{1+y}As$ samples discussed in Chapter 4. In these materials, the strong suppression of superconductivity at very low doping levels ($y \leq 0.02$) was ascribed to scattering of Cooper-pair electrons by a paramagnetic Fe^{2+} impurity, which lies in close proximity to the FeAs layer. Doping by Mn does not induce superconductivity in $SrFe_{2-x}Mn_xAs_2$[150] or $CaFe_{1-x}Mn_xAsF$[139] (where it is found to dramatically increase the resistivity of the normal state). Unless LiFeAs happens to have precisely the optimal electron configuration for superconductivity, it seems likely that effects other than simple removal of electrons are occurring upon Mn-doping, and magnetic scattering is a likely candidate. As discussed above, impurity scattering may be the principal effect of all dopants in LiFeAs.

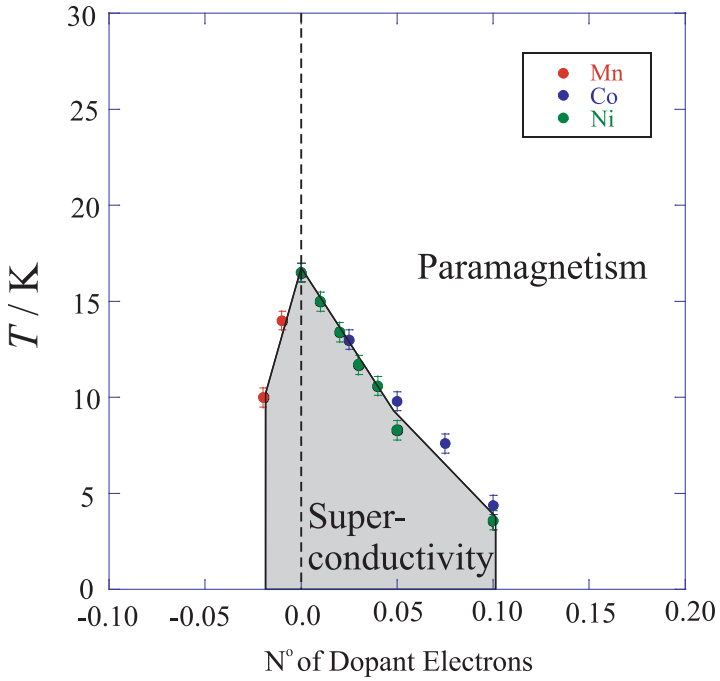


Figure 5.23: A magnetic phase diagram for $LiFe_{1-x}M_xAs$, constructed from the T_c values obtained by d.c. SQUID magnetometry. Marker colours: red = Mn-doped; blue = Co-doped; green = Ni-doped.

5.7.2 Muon Spin Rotation

Several superconducting samples, with Co-doped compositions $x_{Co} = 0.025$, 0.05, 0.075 and Ni-doped compositions $x_{Ni} = 0.01$ and 0.02, as well as Fe-rich $Li_{0.993}Fe_{1.007}As$ ("Sample 2" from Chapter 4) and non-doped LiFeAs, were studied by muon-spin rotation (μ-SR) spectroscopy using the MuSR instrument at ISIS (UK) and the GPS instrument at P.S.I. (Switzerland). Measurements and analysis were carried out by the group of Prof. S. J. Blundell (Dept. of Physics, University of Oxford) with Dr. P. J. Baker and Dr. F. L. Pratt (ISIS, UK). This technique allows the accurate determination of T_c but is used primarily to probe fundamental properties of the superconducting state such as the superfluid stiffness ρ_s which is related to London penetration depth λ. These properties can then be compared with those of other type-II superconductors using an Uemura plot: this is a plot of T_c *vs* λ^{-2} which has been shown empirically to obey a linear scaling relation in type-II superconductors and is frequently used to compare the properties of cuprates, [101, 102] and more recently other Fe-based superconductors. [153, 154]

Samples were subjected to a magnetic field of 10 mT, applied perpendicular to the direction of the spin polarisation (i.e."transverse-field" μSR), which induces a vortex lattice about the partially-penetrating flux lines (in the superconducting state). Measurements were taken at a range of temperatures above and below T_c, between $2-20$ K. T_c can be derived from the observation of an extra damping component of the muon-spin polarisation due to the presence of the vortex lattice (which can be seen in figure 5.24). The derivation of T_c, the in-plane penetration depth λ_{ab} and the superfluid stiffness $\rho_s = {}^{n_s}/_{m*} \propto {}^{1}/_{\lambda^2}$ (where n_s is carrier density and m^* is effective mass) from the properties of the vortex lattice is described in detail in references [155] and [156]. T_c values are displayed in table 5.1 with values obtained from SQUID magnetometry for comparison.

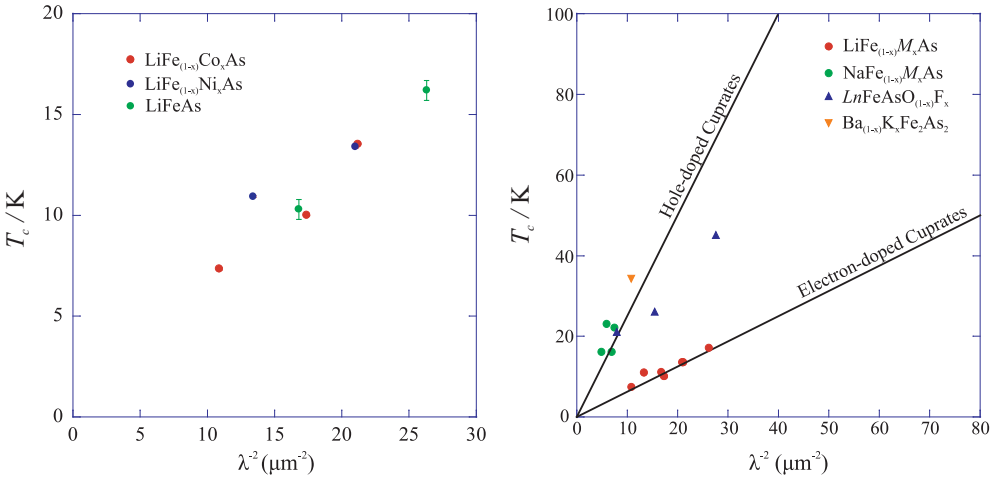
All samples were found to be fully superconducting at low temperatures, with no suggestion of any magnetic ordering (in contrast to the situation found in isostructural

The material originally presented here is not currently available in ORA

Figure 5.24: Transverse-field μSR data for $LiFe_{0.99}Ni_{0.01}As$, both above T_c (grey data points) and below T_c (red data points). Taken from reference [155].

Table 5.1: Superconducting transition temperatures and inverse-square in-plane (*ab*) penetration depths obtained by μSR.

Sample	T_c / K (Magnetometry)	T_c / K (μSR)	λ^{-2} (μm)
LiFeAs	16.2(5)	-	26.3(2)
$Li_{0.993}Fe_{1.007}As$	10.3(5)	-	16.8(2)
$x_{Co} = 0.025$	13.0(5)	13.52(1)	21.2(1)
$x_{Co} = 0.050$	9.8(5)	10.00(1)	17.4(6)
$x_{Co} = 0.075$	7.6(5)	7.35(5)	10.9(2)
$x_{Ni} = 0.010$	13.4(5)	13.41(8)	21.0(9)
$x_{Ni} = 0.020$	10.6(5)	10.93(4)	13.4(2)



(a) Uemura plot for $LiFe_{1-x}M_xAs$.

(b) Extended Uemura plot. With points taken from references [154, 153, 69, 157].

Figure 5.25: Two Uemura plots illustrating (a) the linear relationship between T_c and λ^{-2} for $LiFe_{1-x}M_xAs$, and (b) a comparison with other Fe-based superconductors and the cuprates, with $LiFe_{1-x}M_xAs$ closely following the Uemura line of the electron-doped cuprates. Note that λ is penetration depth in μm.

and isoelectronic NaFeAs).[145] It can be seen that the superfluid stiffness ($\rho_s \propto \lambda^{-2}$) decreases with increasing dopant concentration in both Co- and Ni-substituted series, indicating that the superconductivity is becoming less robust. This is also observed in the Fe-rich "Sample 2" from Chapter 4. The Uemura plot of T_c vs λ^{-2} (figure 5.25a) indicates that all of these samples obey the same scaling relation. LiFeAs can be compared to other important high-T superconductors by expanding the Uemura plot to include two other arsenide series (the isostructural $NaFe_{1-x}M_xAs$ and ZrCuSiAs-type $LnFeAsO_{1-x}F_x$) and two classes of cuprate superconductors, shown in figure 5.25b.

Other μSR studies on Fe-based superconductors (including LnFeAsO,[154, 153] $AeFe_2As_2$,[157] and NaFeAs [69]) have shown that these materials generally lie on the Uemura line obeyed by the broad class of hole-doped cuprate superconductors. However, the expanded Uemura plot (figure 5.25b) shows that LiFeAs and its derivatives conform to the Uemura line of the electron-doped cuprate superconductors, indicating that the nature of superconductivity in LiFeAs could be fundamentally different to that which occurs in other iron-based superconductors.

5.8 Summary and Conclusions

The work described in this chapter aimed to establish the response of the structure and superconductivity of LiFeAs to substitution of Fe by Co, Ni and Mn, to explore the possibility of a higher T_c or the existence of a magnetically ordered domain, and for comparison with other Fe-based superconductors.

An extensive series of X-ray and neutron powder diffraction experiments found that the structural changes that occur on Co- and Ni-substitution are small and very similar for both metals, as expected from the relative sizes of their ionic radii, and results in a slight relaxation of the $FeAs_4$ tetrahedra towards ideal geometry. This contrasts strongly with the changes observed in materials of type $Li_{1-y}Fe_{1+y}As$ described in Chapter 4. However, substitution of Fe by Mn apparently leads to a more complex structural response which does not follow a simple linear increase in unit cell volume (as might be expected from the introduction of an ion with greater ionic radius, and by consideration of the unit cell dimensions of the isostructural compounds NaFeAs and NaMnAs). Further work may be required to confirm and fully rationalise these results.

SQUID magnetometry measurements allowed the derivation of a magnetic / superconducting phase diagram for the system. It was found that increasing the electron count by Co- or Ni-substitution causes a monotonic decrease in T_c, which is dependent on the number of doping electrons regardless of the identity of the substituent. This dependence on electron count has also been observed in other Fe-based superconductors including the analogous Na-based compounds $NaFe_{1-x}Co_xAs$ and $NaFe_{1-x}Ni_xAs$.[69] The suppression of T_c is accompanied by a decrease in the superconducting volume fraction, while μSR measurements show that the London penetration depth increases. Both of these observations suggest that the superconducting state is becoming less robust, which may be consistent with Co or Ni impurities acting as scatterers (as suggested by DFT studies).[151] Beyond the superconducting regime ($x_{Co} > 0.10$ or $x_{Ni} > 0.05$) the system reverts to the normal state. Magnetic order was not observed in any samples by magnetometry or μSR.

Attempts to hole-dope the material by Mn-substitution were also found to suppress T_c, while the superconducting volume fraction decreases very sharply. This behaviour is more reminiscent of that seen in $Li_{1-y}Fe_{1+y}As$, and neutron powder diffraction measurements suggest that some Fe may also partially occupy the Li site in the Mn-substituted samples studied here. In all of these doped systems (and particularly in Mn-substituted derivatives) it is quite possible that the suppression of superconductivity is due to disruptive scattering by the substituent atoms, although the possibility that for Co- and Ni-substituted derivatives the suppression is due to a band-filling effect can not be ruled out. Future developments in theory and experiment (e.g. angle-resolved photoelectron spectroscopy) may help to rationalise this fully.

Chapter 6

Effect of Pressure on the Structure and Superconductivity of LiFeAs and NaFeAs

6.1 Introduction

The first report of high temperature superconductivity in $LaFeAsO_{1-x}F_x$ [21] was quickly followed by simple substitutions of smaller lanthanides for La in attempts to establish the maximum T_c for this system. The replacement of one lanthanide by another is not expected to affect the electron count of the system, as all of the ions tend to take the Ln^{3+} oxidation state in compounds of this structure type (although Ce is a possible exception, as it is known in some similar cases [34, 158] to exist in a mixed $Ce^{3+/4+}$ state - see Chapter 3), and the 4*f* electrons exhibit very weak covalent bonding interactions. The effect of this type of substitution is therefore expected to be primarily structural, and this is confirmed by band structure calculations. [159]

During this flurry of early work on lanthanide substitution, it became apparent that the maximum value of T_c in *Re*FeAsO compounds is somewhat dependent on certain structural parameters. A neutron powder diffraction study of oxide-deficient $LaFeAsO_{1-x}$ and $NdFeAsO_{1-x}$ by Lee and co-workers [129] was among the first to

note the apparent correlation between T_c and the geometry of the $FeAs_4$ tetrahedra, with high T_c values favoured by the most regular tetrahedra. This correlation is neatly illustrated by a plot of T_c(max.) for each optimally-doped compound against tetrahedral angle (figure 6.1), which follows a curve with a peak around $\alpha = 109°$. This relationship also seems to be valid for other systems, and if LiFeAs is included in the plot its T_c of ~ 17 K is seen to lie on an extrapolation of a curve which is assumed to be symmetrical about $\alpha = 109°$ (see figure 168).

Subsequent theoretical studies found that tetrahedral geometry has a strong influence on the properties of the Fermi surface,[160] and structural changes that occurred on chemical substitution in materials such as $CeFeAsO_{(1-x)}F_x$ [161] and $BaFe_2As_2$ [132] were also consistent with this observation. There are also several studies that approach these changes in terms of changes in pnictogen coordinate.[162] It should be noted that, if a constant Fe-As distance is assumed in these compounds, then any change in bond angle (or pnictogen height) will be correlated to a change in the Fe-Fe distance, which may be of more fundamental importance for the superconducting state.[163] However, many of the values for atomic coordinates found in the literature are derived from lattice parameter trends or refinements from laboratory powder X-ray diffraction, as to date there has been no systematic study of the series by high quality diffraction measurements.

Inducing structural changes in the FeAs layer without changing the electron count by substituting larger or smaller ions is commonly discussed as the application of "chemical pressure" to the system. Another way of modifying structural parameters without changing the electron count is the application of an external physical pressure. The use of external pressure in this way is extremely important in systems that are difficult to tune chemically, such as $FeSe_{1-x}Te_x$, LiFeAs and NaFeAs. External pressures can also induce structural changes that are different from, or larger than, those obtained by chemical substitution. Taken to the extreme, this can often result in a structural transition.

There are two conditions under which external pressure can be applied. It is

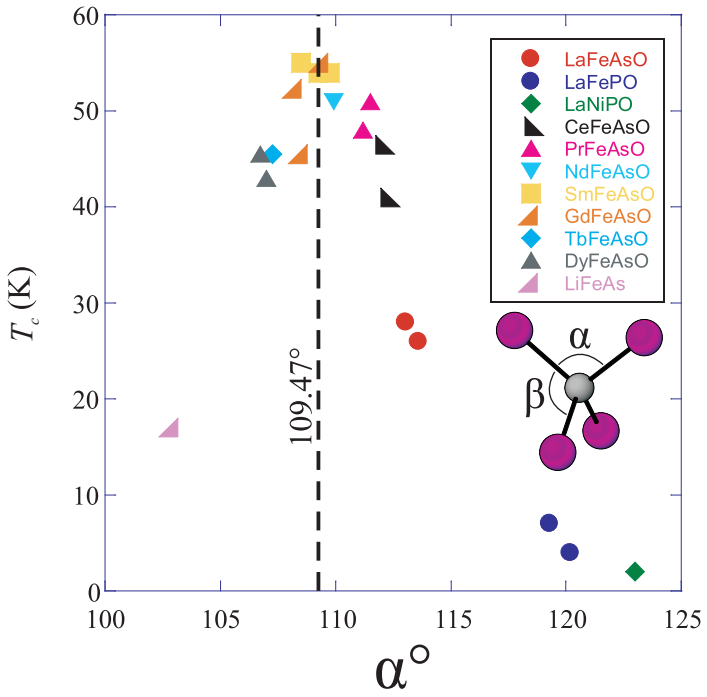


Figure 6.1: Empirical relationship between optimal T_c and tetrahedral angle for a selection of Fe-based superconductors (adapted from reference [129]).

most conventional to conduct experiments under hydrostatic pressure, where the pressure-transmitting medium is fluid, and pressure is applied to a sample equally in all directions. If the pressure transmitting medium is solid, an experiment can be conducted under uniaxial (or "non-hydrostatic") conditions. The two modes of pressure application are expected to produce different structural responses in a sample. For most applications, hydrostatic conditions are preferred, as these conditions are universal (i.e. not dependent on the identity of the pressure transmitting medium) and can be easily reproduced. In contrast, uniaxial conditions are more difficult to control and reproduce, as the degree of non-hydrostaticity is usually characteristic of a particular pressure-transmitting medium. In powder diffraction experiments, non-hydrostaticity causes peak broadening due to anisotropic strain on the crystallites, degrading the quality of the diffractogram. Consequently, efforts are usually made to avoid freezing the pressure transmitting medium under high pressures (especially if low temperatures are employed) and if this cannot be avoided a distinction is drawn between results obtained from the hydrostatic and non-hydrostatic regions.

Early high-pressure conductivity studies on $LaFeAsO_{1-x}F_x$ [164, 165, 166] showed that T_c has a complicated pressure dependence which shows a steep initial increase at low pressures before decreasing at higher pressures. In contrast, in several other *Ln*FeAsO superconductors (*Ln* = Ce, Nd, Sm) T_c has been found to decrease monotonically with increasing pressure.[167, 168, 169] Compounds related to $BaFe_2As_2$ show similarly enigmatic behaviour.[170] LiFeAs is structurally quite different from LaFeAsO and $BaFe_2As_2$ due to its highly distorted $FeAs_4$ tetrahedra and short Fe-Fe distances of 2.67 Å, which are smaller than those in any reported iron-based superconductor with the exception of FeSe. Hence, the response of the crystal structure and the superconducting properties to applied pressure in this system will be interesting to compare to the responses of other materials, and may help to rationalise the influence of structure on superconductivity in these materials.

The compound NaFeAs is isostructural with LiFeAs but it behaves much more similarly to the *Re*FeAsO and *Ae*Fe_2As_2-type materials. The $FeAs_4$ tetrahedra of NaFeAs are almost regular and the Fe-Fe distance of 2.79 Å is typical of other layered arsenides. Like the non-superconducting "parent" compounds LaFeAsO and $BaFe_2As_2$, at low temperatures NaFeAs undergoes a structural phase transtion from a tetragonal to an orthorhombic unit cell (below $T = 55$ K) which is associated with the onset of antiferromagnetism with $T_N = 45$ K, with a small ordered moment of the order of 0.1 μ_B.[69, 145] However, all samples prepared with nominal composition "NaFeAs" also exhibit a small superconducting volume fraction (typically 10 %) with $T_c \approx 9$ K. The nature of this co-existance (which also occurs in some electron-doped samples with a strong superconducting fraction) is discussed in more detail elsewhere,[69, 145] but it is presently unclear whether this is due to compositional inhomogeneity (perhaps caused by oxidation or hydrolysis at the surface)[141] or to genuine microscopic co-existence of these two phenomena. Part of the work in this chapter investigates the response of structure and superconductivity of NaFeAs to applied hydrostatic pressures, for comparison with the response of LiFeAs and other layered Fe-based superconductors.

6.2 Response of the Structure and Superconductivity of LiFeAs to High Pressures

6.2.1 High pressure XRD from 0 – 17 GPa

X-ray powder diffraction measurements of LiFeAs were carried out by Dr. Gaston Garbarino and Dr. Wilson Crichton using the ID27 high-pressure beamline at the ESRF, Grenoble. The sample used was "Sample 2" from Chapter 4. At the time of these experiments this sample was thought to be stoichiometric LiFeAs [63, 171] but it should be noted that subsequent experiments (described in Chapter 4 and reference [155]) showed this sample to be slightly non-stoichiometric with approximate composition $Li_{0.994}Fe_{1.006}As$ inferred from the lattice parameter trends for a series of compounds. The incorporation of a small amount of Fe on the Li site was found to have a strong effect on the superconducting properties [155] but since it represents only a minor structural anomaly, it is not expected to affect the conclusions drawn from this experiment.

The sample was handled under inert atmospheric conditions at all times. The initial loading procedure was carried out in an argon-filled glovebox at the ESRF, where the sample was loaded into a membrane-driven diamond anvil cell (DAC) with a ruby (included in the sample space for fluorescence pressure calibration) and sealed with a stainless steel gasket. Once sealed, the DAC was transferred to the high-pressure gas-loading facility where it was opened and flushed with a clean atmosphere of helium, then re-sealed under a high pressure of helium, leaving an internal cell pressure of approximately 0.7 kbar.

For these experiments, two DACs with different diamond culet sizes (i.e. the flat faces of the diamond that are in contact with the sample/pressure-transmitting medium) were used. A small culet size is important for attaining the highest possible pressures, but can make the cell more prone to failure by rupturing the gasket or fracturing the diamonds. The first measurements were taken on increasing pressure up to 15 GPa,

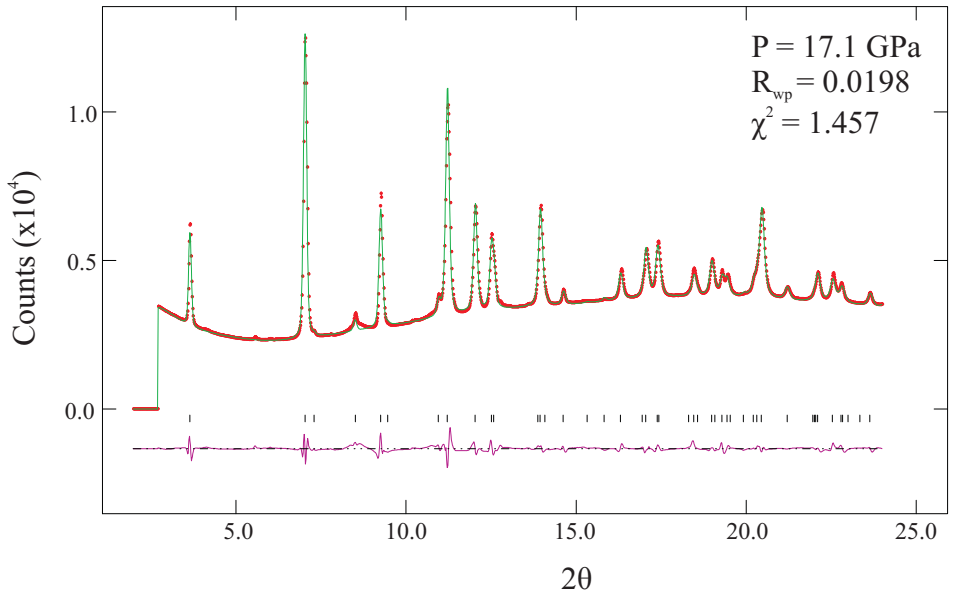


Figure 6.2: Representative Rietveld refinement against synchrotron XRPD data for LiFeAs under an applied hydrostatic pressure of 17.1 GPa. Data were collected from the ID27 instrument at the E.S.R.F. using an incident wavelength $\lambda = 0.3738$ Å. Red line represents observed data points; green line represents calculated intensities; purple line is a difference curve (observed - calculated). Reflection markers: *black* = LiFeAs.

using 350 μm culet diamonds. This cell failed at a pressure of approximately 15 GPa, and in order to complete the experiment a fresh portion of the sample was loaded into a new DAC with 600 μm culet diamond anvils, and measurements were taken at pressures up to 17 GPa using this cell. Measurements were taken at intervals of less than 0.5 GPa both on compression and on decompression, with data collected for 1 minute on a mar345 (345 mm diameter) image plate detector, with a beam size of 5×7 μm.

The compression ("upstroke") data from both runs were used to obtain lattice parameters by Lebail-type fits (providing model-independent peak intensities), as full Rietveld refinement was found to be unstable for data taken at the lowest pressures (possibly due to strong correlations between thermal displacement, structural and preferred-orientation parameters). The decompression ("downstroke") data were used to obtain the As z-coordinate by full Rietveld refinement. A representative Rietveld refinement is shown in figure 6.2. All of the collected patterns were affected by preferred orientation of the sample crystallites, and this was modelled with a March-

Table 6.1: Parameters derived from Birch-Murnaghan equation of state (equation 6.1).

Parameter	X_0 (Å^3)	K_0 (GPa)	K_0'
V	90.356(4)	57.3(6)	4.5(1)
a^3	53.675(4)	65.6(8)	4.9(15)
c^3	256.124(5)	45.3(6)	3.9(1)

Dollase function. Both Lebail fitting and Rietveld refinement were carried out using GSAS. Tables of refined parameters are displayed in Appendix F.

The lattice parameters (illustrated in figures 6.3 and 6.4) show a smooth decrease across the entire pressure range (up to 17 GPa). From finite strain analysis (conducted by Dr. W. Crichton) the bulk modulus K ($= -V\frac{\partial P}{\partial V}$) of the sample was estimated to be 56.7 GPa, and a third-order Birch-Murnaghan equation of state [172] was fitted to the trend in unit cell volume:

$$P = \frac{3K_0}{2}\left[\left(\frac{V_0}{V}\right)^{\frac{7}{3}} - \left(\frac{V_0}{V}\right)^{\frac{5}{3}}\right]\left\{1 - \frac{3}{4}(4 - K_0')\left[\left(\frac{V_0}{V}\right)^{\frac{2}{3}} - 1\right]\right\} \qquad (6.1)$$

The EosFit5.2 software [173] was used to derive parameters V_0, ambient bulk modulus K_0, and first pressure derivative of ambient bulk modulus K_0'. Similar parameterised equations were also found to be valid for the behaviour of the a and c parameters, with the variable V replaced by a^3 and c^3 respectively. All derived parameters are displayed in table 6.1. A K_0 value of 57.3(6) GPa for LiFeAs is significatly lower than values reported for $LaFeAsO_{0.88}F_{0.12}$ ($K_0 = 78$ GPa) [174] and $NdFeAsO_{0.88}F_{0.12}$ ($K_0 = 102$ GPa),[128] which are much less compressible due to the PbO-type oxide spacing layers in these compounds. A later study of α-FeSe (which contains no ions in the inter-layer space) by Margadonna and co-workers [175] reports that FeSe is more compressible than LiFeAs, with a value of $K_0 = 30.7$ GPa.

As expected from the observed trend in c/a ratio and from the normalised trends in a and c (figures 6.5 and 6.4), the equation of state reveals that the c-axis is more compressible than the a-axis ($K_c = 45.3$ GPa versus $K_a = 65.6$ GPa) with a stiffness that increases less sharply with increasing pressure ($K_c' < K_a'$). These relative compressibilities are consistent with the tetragonal nature of the crystal structure,

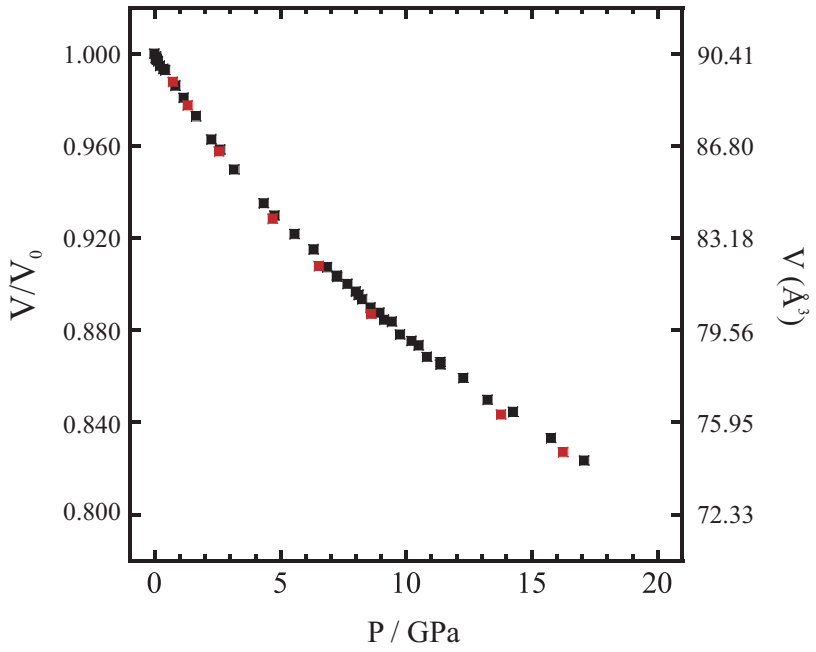


Figure 6.3: Unit cell volume (V) and normalised unit cell volume (V/V_0) for LiFeAs as a function of applied hydrostatic pressure. Data are derived from synchrotron XRPD (with sample contained in a diamond anvil cell), either by Rietveld refinement against downstroke data (red markers), or by Lebail fits to upstroke data (black markers).

which has a lower density of atoms along the stacking direction and a higher density in the basal plane.

Changes in the structural parameters are shown in figures 6.6, 6.7 and 6.8. The region of the structure that is of the greatest interest is the $FeAs_4$ tetrahedra, which are highly distorted even at ambient pressures, with angles 102.79° and 112.91°. Figure 6.6 shows that as pressure increases, the $FeAs_4$ tetrahedra become distorted even further away from the ideal tetrahedral angle. This is perhaps surprising, as the trends in lattice parameters clearly show a decrease in the c/a ratio (figure 6.5), as the compression along the c-axis is greater than that which occurs in the ab-plane, and it might therefore be expected that the $FeAs_4$ angles would reflect this trend by becoming less distorted. However, the trends in As-As distances (illustrated in figure 6.8) show that different regions of the structure respond quite differently to applied pressure. It can be seen that As-As distance B (the only edge of the $FeAs_4$ tetrahedron with a component along the c-axis) barely changes across this pressure range, while distance A (which lies entirely in the ab-plane) exhibits a significant decrease. On first

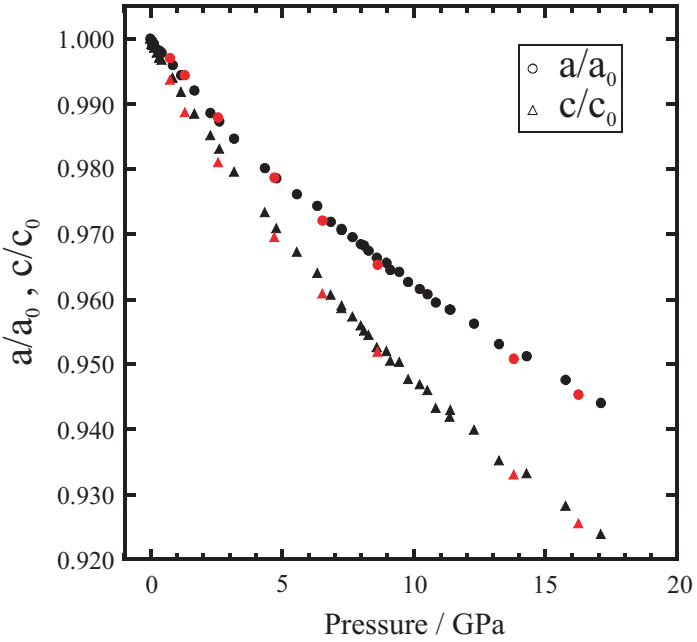


Figure 6.4: Normalised lattice parameters for LiFeAs as a function of applied hydrostatic pressure, derived from Lebail fits to synchrotron XRPD data collected on increasing pressure (*black* markers), and by Rietveld refinement against data collected on decreasing pressure (*red* markers).

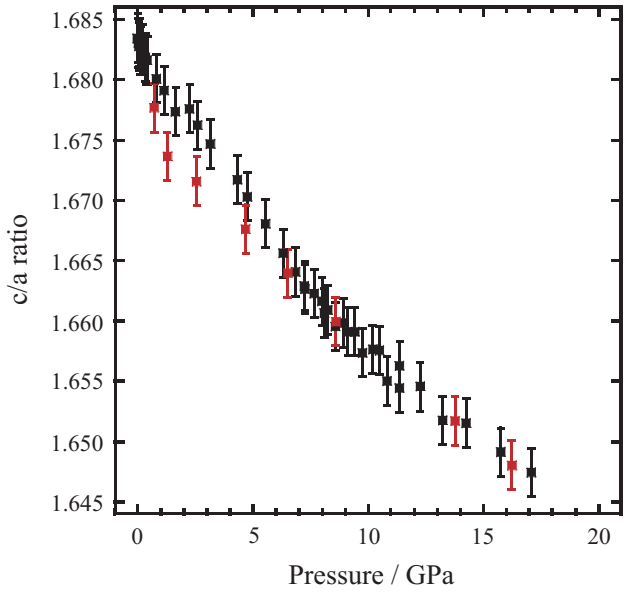


Figure 6.5: Refined c/a ratio for LiFeAs as a function of applied hydrostatic pressure, from Lebail fits (upstroke, black markers) and Rietveld refinement (downstroke, red markers).

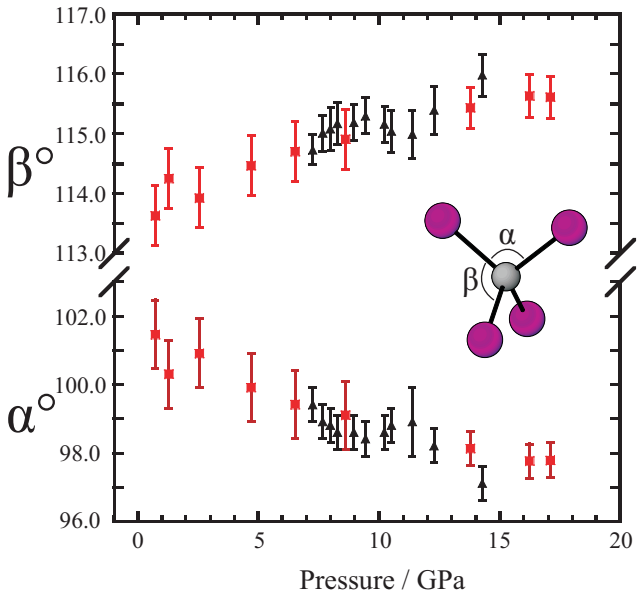


Figure 6.6: Refined tetrahedral As-Fe-As angles for LiFeAs as a function of applied hydrostatic pressure. Data were obtained by Rietveld refinement against synchrotron XRPD data on upstroke (black markers) and downstroke (red markers). Errors are equal to 5x the e.s.d. obtained from GSAS.

inspection, these changes do not appear to be consistent with the observed trends in c and a.

However, distance C (the apical edge of the $LiAs_5$ square pyramid, with a major component along the c-axis) shows a strong decrease, while distance A is equivalent to the basal parameter of the square pyramid. The changes in both of these parameters show that the compression of the $LiAs_5$ pyramids is far more significant than that which occurs in the $FeAs_4$ tetrahedra, presumably because the Li-As bond is weaker than the Fe-As bond. This suggests that the changes observed in the $FeAs_4$ tetrahedral angles, which move even further away from ideal tetrahedral geometry, are facilitated by this preferential compression of $LiAs_5$. The Fe-As distance shows a decrease of approximately 3% at 17 GPa, but Li-As distances were not refined in this experiment due to the weak X-ray scattering of Li and are addressed in section 6.2.2. Over the same pressure range, the Fe-Fe distance ($= a/\sqrt{2}$) decreases by almost 6 %.

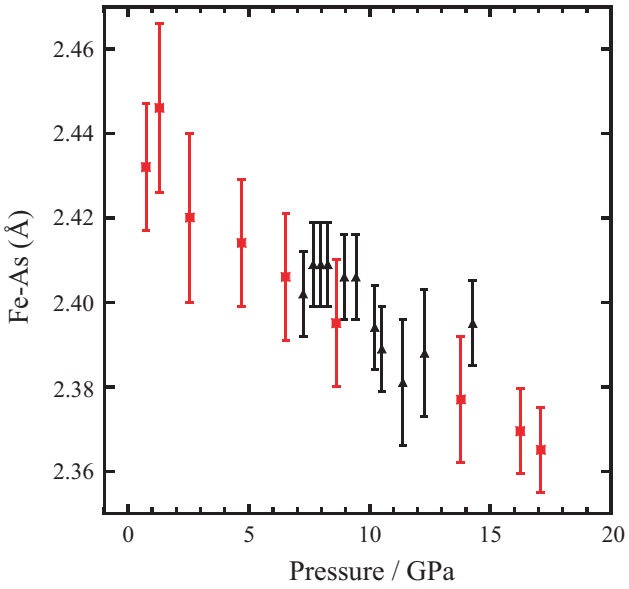


Figure 6.7: Plot showing the variation in nearest-neighbour Fe-As distance as a function of pressure, obtained by Rietveld refinement against upstroke data (red markers) and downstroke data (black markers). Errors are equal to 5x the e.s.d. obtained from GSAS.

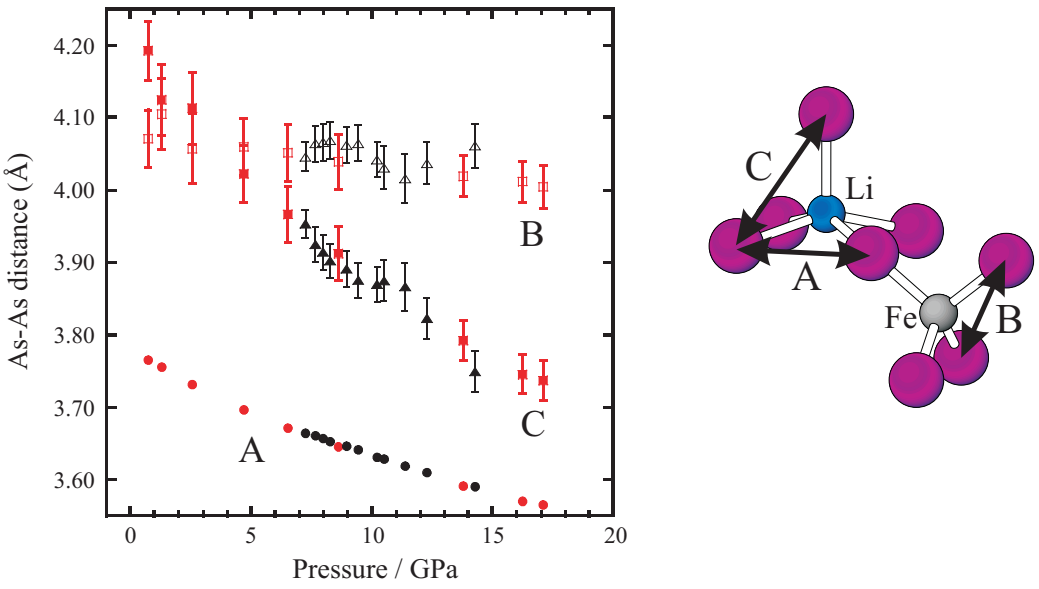


Figure 6.8: Plot showing the variation of three different As-As distances (A, B and C in the structural diagram) as a function of pressure, obtained from synchrotron XRPD by Rietveld refinement against upstroke data (red markers) and downstroke data (black markers). Distance A is dependent only on the basal cell parameter a and therefore has much smaller error bars than distances B and C, which are dependent on both the a-parameter and the As z-coordinate.

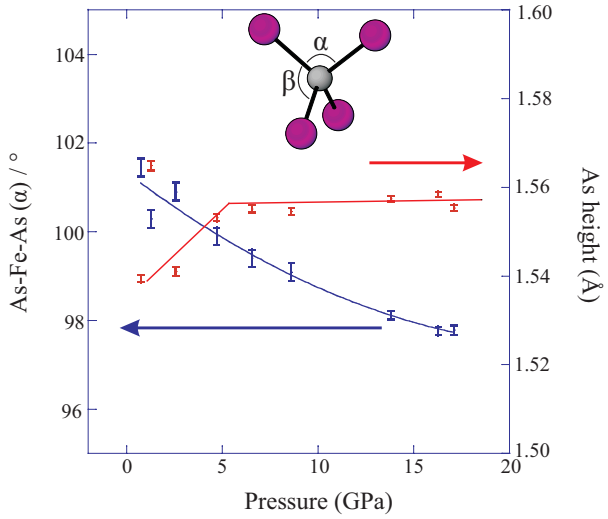


Figure 6.9: Plot comparing the variation in tetrahedral As-Fe-As angle α (blue markers) with the height of arsenide ion above the Fe plane (red markers) as a function of applied hydrostatic pressure. Data were obtained from synchrotron XRPD by Rietveld refinement against downstroke data. Lines are a guide to the eye.

6.2.2 High pressure NPD from 0 – 10 GPa

6.2.2.1 Helium gas cell

As discussed in section 6.2.1, XRPD is an excellent tool for determining the structural response to high pressures and has allowed the accurate determination of lattice parameters and the coordinates of As as a function of pressure in LiFeAs. However, the extremely weak X-ray scattering power of Li^+ does not enable any detailed information about the Li-coordinate to be extracted, and hence the information derived from XRPD for the $LiAs_5$ environment is incomplete. The neutron scattering length of Li is still relatively small (-1.90 fm) but much more significant than its X-ray scattering factor, which allows neutron diffraction methods to probe this region of the crystal structure in more detail.

The XRPD measurements used "Sample 2" (from Chapter 4 and reference [63]) which was later found to be slightly non-stoichiometric.[155] For neutron diffraction measurements, a large sample of LiFeAs (of approximate mass 10 g) was prepared by similar methods to those described in Chapter 4. This sample was inspected by laboratory XRPD and found to be single phase, while a scan of magnetisation

versus temperature in an applied field of 50 Oe confirmed the presence of bulk superconductivity below 17 K. Further diffraction and magnetisation measurements on this sample are described in Chapter 4 and reference [155]. Care was taken to ensure that the sample was handled under an inert atmosphere at all times.

A portion of the sample (approximately 4 g) was loaded into a null-scattering Ti:Zr gas pressure cell (described in detail in Chapter 2) in an argon-filled dry box. This was enough powder to fill the sample void in the cell, which has dimensions of 6 mm diameter by 30 mm height. This volume of sample is very similar to that used in a regular ambient-pressure neutron diffraction experiment, exemplifying the major advantage that gas cells have over other high pressure techniques where small sample volumes are problematic for neutron diffraction measurements. Once loaded and sealed in a glass vessel under argon, the pressure cell was transported to ISIS where it was mounted on a customised sample control stick. In order to exchange the Ar gas within the cell for He, the mounted cell was enclosed within a disposable glove-bag, which was purged several times with helium gas to minimise the O_2 and H_2O content. The cell was then opened and re-sealed under the helium atmosphere and transported to the beamline, where it was connected to the gas intensifier by a stainless steel capillary. A small pressure of 0.2 kbar was then applied to engage the Bridgman seal. The gas intensifier system includes a piezoelectric pressure sensor, allowing pressure to be monitored in real time. When the desired pressure had been reached, the gas cell was isolated and measurements commenced.

Due to the arrangement of the boron nitride jacket and the cadmium snout shielding of the pressure cell (illustrated in figure 6.11), which are used in combination to minimise the background signal from the cell itself as described in reference [176], data are only collected from the medium-resolution bank at 90° to the incident beam. This diffraction geometry is a general feature of experiments where samples are contained in complex environments, such as high-pressure cells or in-situ reaction cells.

Prior to Rietveld refinement, the data were corrected for absorption of the higher

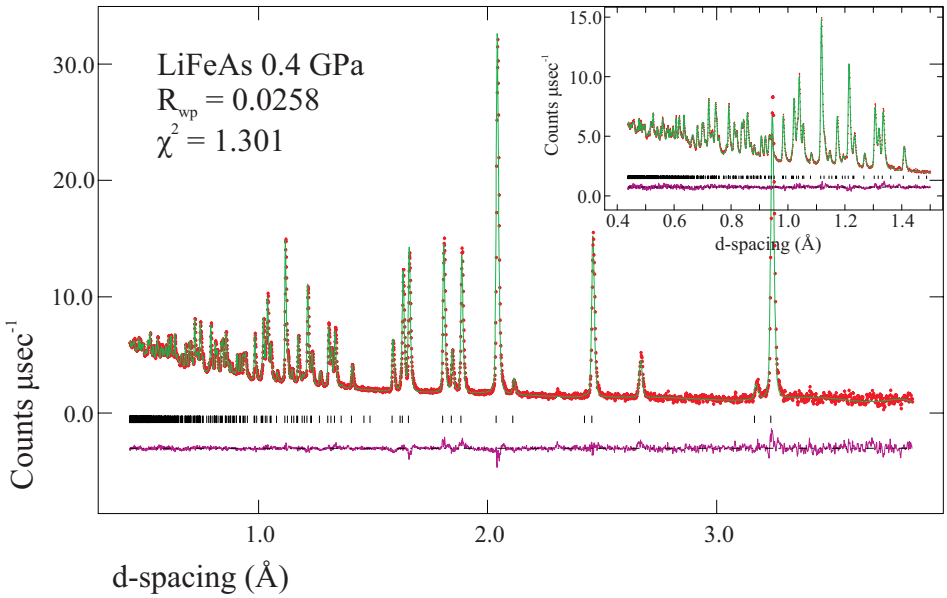


Figure 6.10: Representative Rietveld refinement against NPD data for a sample of LiFeAs under an applied pressure of 0.4 GPa, with sample contained in a Ti:Zr He-gas pressure cell (described in detail in Chapter 2). Low *d*-spacings are inset. Data shown here have been corrected for absorption by the Ti:Zr alloy of the pressure cell. Reflection markers: *Black* = LiFeAs.

energy incident neutrons by the Ti:Zr alloy, which has the effect of strongly increasing the background signal at small *d*-spacings. This treatment was carried out by Dr. Ron Smith, and subsequent Rietveld refinements were conducted in the same way as regular ambient pressure refinements with no special measures. Thermal displacement parameters for all atoms - including Li - were allowed to refine anisotropically. A representative Rietveld refinement is displayed in figure 6.10; tables of refined parameters are displayed in Appendix F.

The results of these refinements show lattice parameters that decrease steadily with a decrease in c/a ratio (see figure 6.12), in agreemement with the results obtained from high pressure XRPD in section 6.2.1. Inspection of the $LiAs_5$ environment reveals that both Li-As distances (the longer 4-fold bond to the basal As ions, and the shorter bond to the apical As ion) decrease at a very similar rate, as illustrated in figure 6.14. There is a corresponding change in As-Li-As bond angles, which is very small over this pressure range, but with the result that the Li ion is effectively moving towards the base of the pyramid despite the equality in bond distance changes. This is consistent

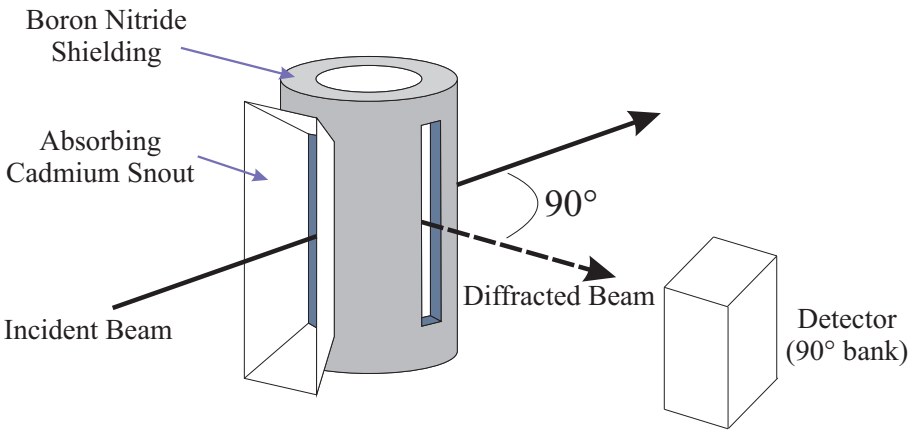


Figure 6.11: Diagram of the null-scattering He-gas pressure cell, including the shielding/sample arrangement and diffraction geometry, which was used for high-pressure neutron diffraction measurements of LiFeAs on the Polaris t-o-f diffractometer.

with the negative change in c/a ratio, as the base of the pyramid lies in the *ab*-plane while its height is dependent on c and the As z-coordinate. Comparison of the Li-As distances with the Fe-As distances in figure 6.13 shows that the Li-As distance contracts far more quickly than the Fe-As distance under applied pressure. This is consistent with the enhanced compressibility of the $LiAs_5$ square pyramids observed by high-pressure XRPD.

6.2.2.2 Paris-Edinburgh cell

A similar sample of LiFeAs, with $T_c = 17$ K, was prepared as before and found to be phase pure by laboratory XRPD. The Paris-Edinburgh cell (described in Chapter 2) applies pressure mechanically through two tungsten carbide anvils using a hydraulic press. The setup requires that a liquid pressure transmitting medium is used. To ensure hydrostatic conditions at pressures of up to 10.5 GPa,[99] a deuterated 4:1 mixture of methanol-ethanol is a commonly used medium. At pressures greater than 10.5 GPa, the mixture becomes glassy and hydrostaticity is lost. However, LiFeAs has already been found to decompose rapidly under atmospheric conditions, and it was therefore important to check its stability in methanol-ethanol in advance of the experiment. To do this, a small quantity of degassed methanol was added to a Schlenk tube with

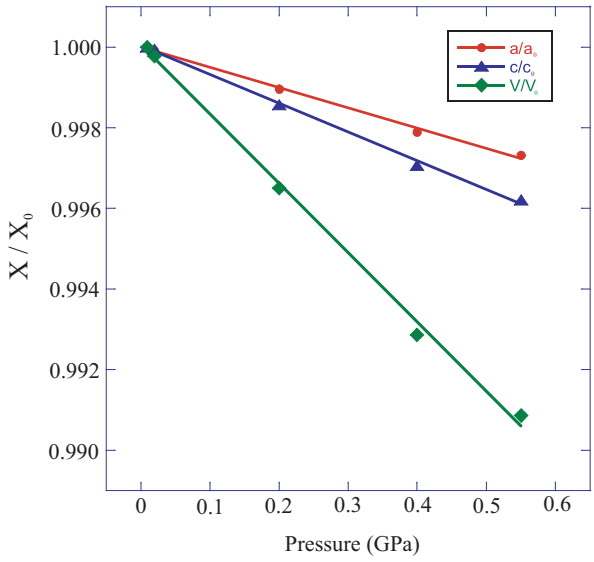


Figure 6.12: Normalised unit cell parameters of LiFeAs as a function of applied hydrostatic pressure. Data were derived by Rietveld refinement against NPD data (Polaris), with the sample contained within the He-gas pressure cell. Error bars (1 e.s.d. from GSAS) are smaller than the markers. *Green = V; blue = c; red= a.*

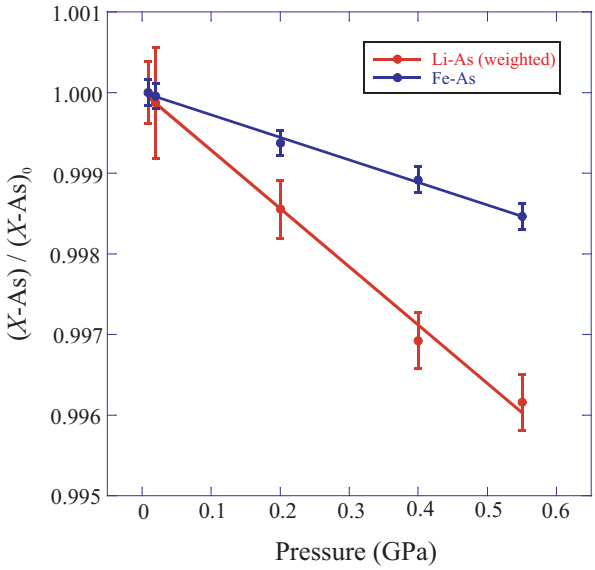
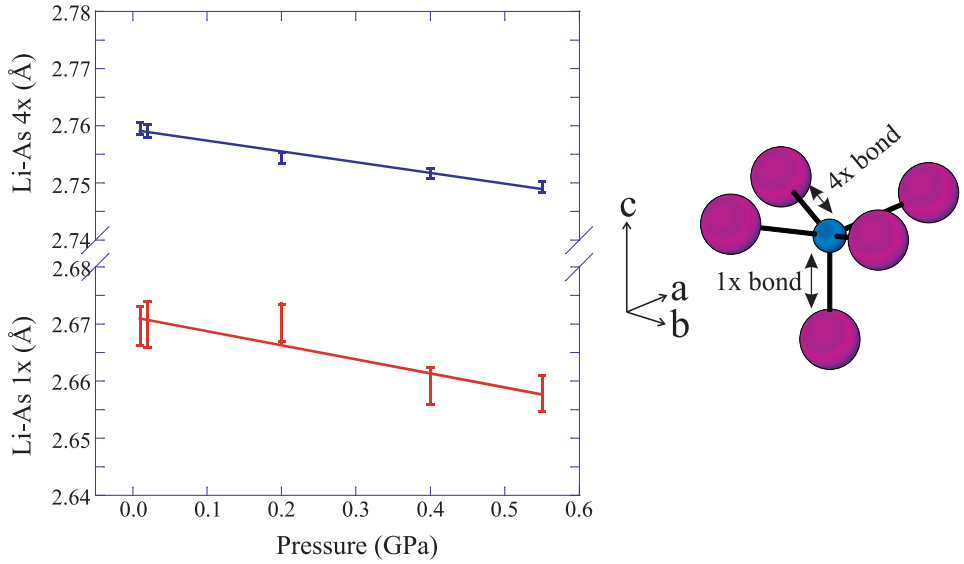
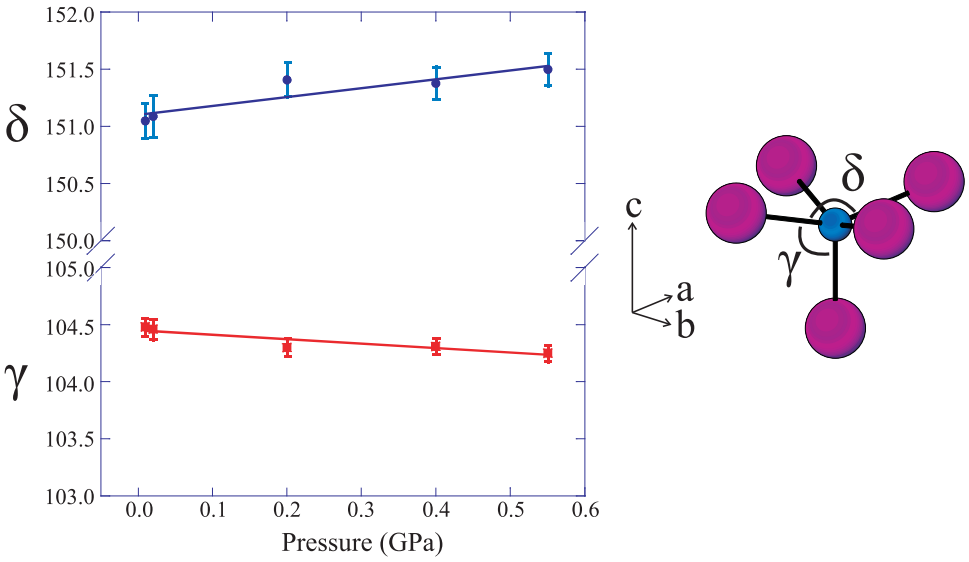


Figure 6.13: Normalised Fe-As distances and normalised weighted (mean) Li-As distances, as a function of increasing pressure. Data were derived by Rietveld refinement against NPD data (Polaris), with the sample contained within the He-gas pressure cell. Errors bars represent one e.s.d. from GSAS. Lines represent linear best-fits calculated by the Kaleidagraph spreadsheet software. *Blue = Li-As; red = Fe-As.*



(a) Li-As distances. *Red = 1x distance; blue = 4x distance.*



(b) As-Li-As angles. *Red = γ; blue = δ.*

Figure 6.14: Response of the structural parameters about the $LiAs_5$ site to applied pressure, obtained by Rietveld refinement against NPD data with LiFeAs contained in the He-gas pressure cell. Error bars represent 1 e.s.d. from GSAS. Lines represent linear best fits are generated by the Kaleidagraph spreadsheet software.

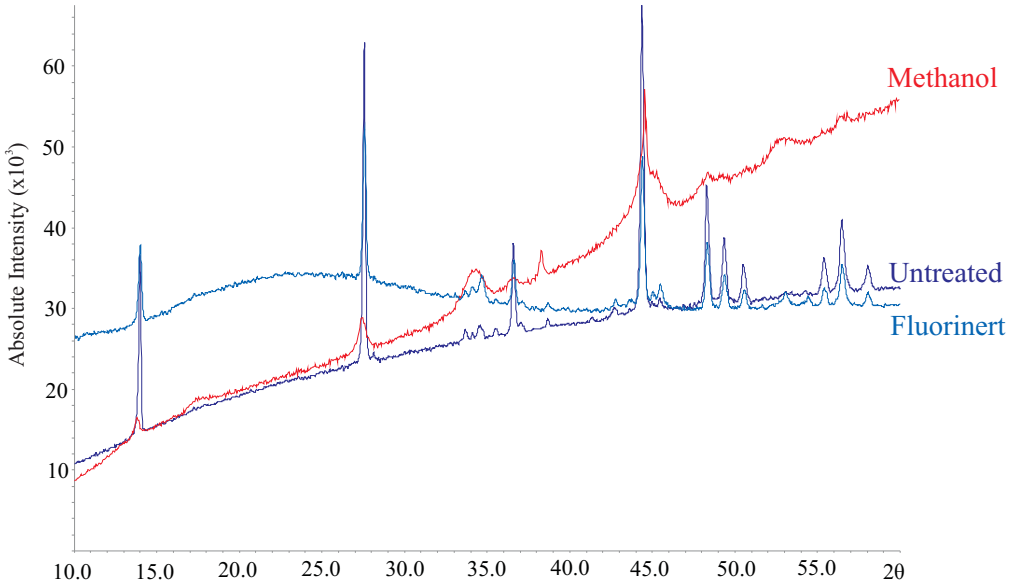


Figure 6.15: Laboratory XRPD patterns of LiFeAs after exposure to methanol and Fluorinert. Broad features in the "methanol" pattern (red) correspond to poorly-crystalline FeAs.

a small amount of LiFeAs and left overnight under an inert nitrogen atmosphere. The methanol was then removed and the powder thoroughly dried under vacuum. An X-ray diffraction pattern from this powder showed that, while some of the main "LiFeAs" phase was still present, a significant amount of decomposition had occurred, and methanol-ethanol was therefore discarded as a candidate for the pressure medium. These XRPD patterns are compared in figure 6.15.

An alternative medium, used for highly reactive samples, is the liquid perfluorocarbon Fluorinert (molecular formula C_8F_{18}). To assess the suitability of this medium, the above experiment was repeated, and the sample was retrieved without having undergone significant decomposition. However, unlike the methanol-ethanol mixture, Fluorinert does not provide a hydrostatic environment at pressures greater than 2.3 GPa[98, 99] so this would place a constraint on the experiment.

The sample, of approximate volume 30 mm^3, was loaded into the Ti:Zr gasket in an argon-filled glovebox at ISIS. Upon removal, a small amount of Fluorinert was added through a syringe, then the gasket/sample was inserted into the pressure cell and a small load of 70 bar applied to seal the sample environment. This procedure was

carried out as quickly as possible, and the sample spent approximately 2 minutes in air without a perfect seal. A pressure marker was not included with the sample, as pressure could be derived using the known equation of state for LiFeAs obtained from the high pressure X-ray powder diffraction measurements (equation 6.1 on page 172) without contributing extra Bragg reflections to the pattern.

Prior to the insertion of the PE cell into the sample area, a cursory measurement of the sample under ambient conditions in a vanadium can was taken for comparison with the high pressure data, and to help to identify any decomposition that may have occurred upon loading the cell. Hydrostatic pressure measurements were then taken on increasing pressures up to 2.3 GPa, and two further measurements were taken in the non-hydrostatic regime for comparison. Most of the data sets were collected over the course of 8 hours, equivalent to a beam current of 1200 μAhr. At the highest pressures, data collection times were increased to 1500 μAhr to compensate for the increased beam attenuation caused by deformation of the Ti:Zr gasket. Rietveld refinements were carried out after the application of an absorption correction to the data (similar to that for the gas cell in the previous section). Thermal displacement parameters were allowed to refine isotropically, and the Li and As z-coordinates were allowed to refine freely. Tables of refined parameters are displayed in Appendix F.

The equation of state derived from X-ray diffraction (see page 172) was used to calculate the pressure in the cell from the refined unit cell volumes. It should be noted that, due to the difference between the fitted value of V_0 (= 90.365 Å from section 6.2.1) and the crystallographic value of V_0 (= 91.058(6) Å^3 obtained by Rietveld refinement against these neutron diffraction data), the calculated P takes a negative value (-0.35 GPa) at base pressure indicating a systematic underestimate of the P values. By replacing V_{fit} with V_{cryst} in equation 6.1, this error is minimised, but the validity of the constants K_0 and K_0' is somewhat undermined; error limits for pressure were therefore set equal to the difference between $P(V_{fit})$ and $P(V_{cryst})$. This uncertainty is significantly greater than that of the XRD experiments (where pressure is directly measured by ruby fluorescence) and the gas cell NPD experiments (where

Table 6.2: Pressure parameters for each measurement derived using equation 6.1.

Applied Load [bar]	V [Å^3]	$P_1(V_0 = V_{cryst})$ [GPa]	$P_2(V_0 = V_{fit})$ [GPa]	$P_1 - P_2$ [GPa]
120	91.058(6)	0	-0.43	0.43
170	90.914(8)	0.09	-0.35	0.44
240	90.044(11)	0.66	0.21	0.45
310	88.518(13)	1.74	1.25	0.49
340	87.780(14)	2.29	1.79	0.50
540	83.363(17)	6.21	5.56	0.65
900	80.115(20)	9.85	9.10	0.75

it is directly measured by a piezoelectric device), but due to the large steps in pressure between measurements this is acceptable in the current experiment.

As anticipated, clear differences can be seen between data taken below and above the hydrostatic limits, as illustrated in figure 6.16. The two diffractograms taken in the non-hydrostatic regime (at 6.2 GPa and 9.9 GPa) have significantly broader Bragg reflections due to the non-isotropic strain in the crystallites, which is expected to reduce the reliability of the refined lattice parameters (and hence the calculated pressure) and the structural parameters. Refined structural parameters across the full range of pressures (up to 10 GPa) are illusrated in figures 6.17 to 6.19.

The greatly increased pressure range permitted by the Paris-Edinburgh cell allows meaningful comparisons to be drawn between the results from high pressure neutron and X-ray diffraction. Figure 6.18 shows a plot comparing the Fe-As distances obtained by X-ray diffraction (section 6.2.1) with those obtained by neutron diffraction in this experiment, and highlights the effect of the different experimental conditions. There appears to be some systematic difference in the absolute values obtained, and this is also apparent in plots of As-Fe-As tetrahedral angles (see figure 6.19). Both Fe-As distance and As-Fe-As angle are strongly dependent on the refined value of the As z-coordinate, and these differences may be partially a result of the differences of instrument calibration, detectors and sample effects (such as the preferred orientation observed in the XRD patterns). It is also possible that the centres of the scattering objects (atomic nuclei for neutrons, centres of electron density for X-rays) are in

slightly different positions for the two techniques, and this would be expected to cause discrepancies between the refined As z-coordinates.

It is also apparent that the gradients of the trends are different, with the Fe-As distance derived from NPD decreasing at a slightly faster rate. This can be attributed to the inherent uncertainties in the refined parameters. Estimated standard deviations (refinement errors from GSAS) are similar for the two experiments but the gradient derived from XRD is likely to be more reliable, as the entire pressure region lies well within the hydrostatic regime for He gas, and there are also a significantly greater number of observations (due to the rapid XRD collection times). For NPD, there are only two observations at $P > 2.3$ GPa, which both lie within the non-hydrostatic region for Fluorinert. The error in these data points is certainly underestimated by the statistical errors from GSAS, and is expected to be significantly larger than those in the hydrostatic region.

A plot of normalised Fe-As and Li-As distances in figure 6.17 shows good agreement with the results obtained from the gas pressure cell in section 6.2.2.1. It can be seen that, as expected, the weighted Li-As distance is compressed far more than the Fe-As distance as pressure increases. However, the weighted Li-As distance is also strongly affected by the As z-coordinate and is therefore subject to the same sources of error as the Fe-As distances discussed above. While this may not strongly influence the relative changes in the two parameters plotted here, the absolute values obtained at the highest pressures from the non-hydrostatic regime may over-estimate the true contraction of both Li-As and Fe-As distances.

While reasonably neat trends are observed for the Li-As distance, the trends in bond angles of the $LiAs_5$ tetrahedra are less well defined than those observed over a small pressure range in the He gas cell. These angles are critically dependent on the refined value of the z-coordinate for Li, and hence an increased uncertainty in this parameter significantly increases the error in the refined angles. The poorer quality of the data obtained from the PE cell compared to the gas cell, combined with the relatively small changes that occur to As-Li-As, means that a significant amount of precision is lost as

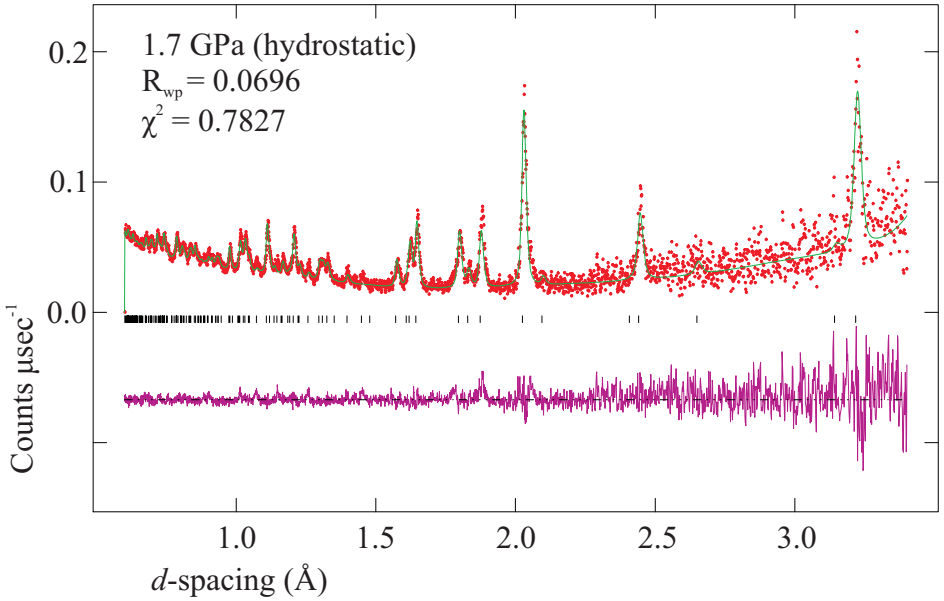
errors (even 1 ESD from GSAS) outweigh the changes that occur over this pressure region.

6.2.3 High pressure magnetometry from 0 – 4.3 GPa

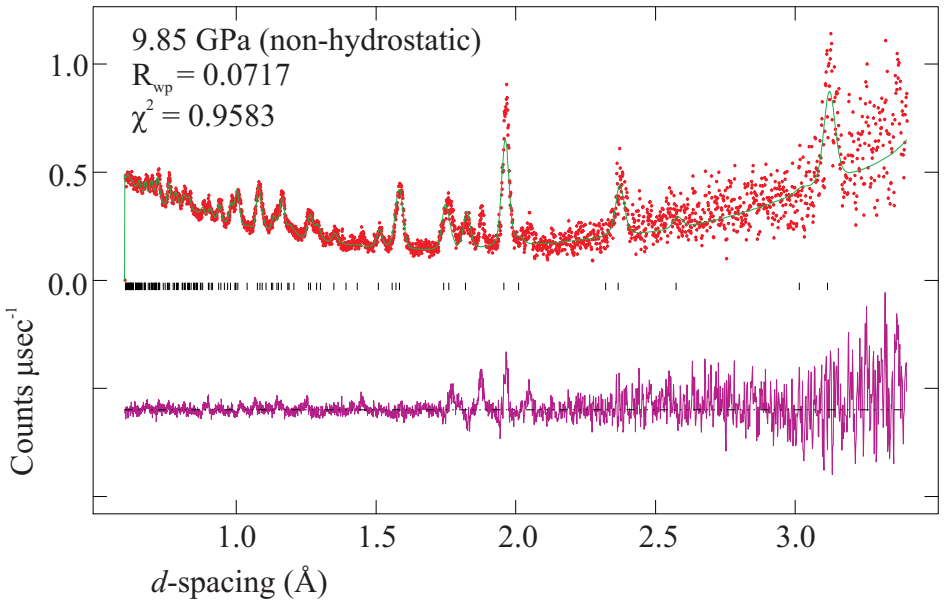
The superconducting properties of two samples of LiFeAs were assessed by magnetic susceptibility measurements taken using a.c. SQUID magnetometry. All measurements detailed in this section were carried out by Dr. Masaki Mito in the Department of Physics, University of Oxford, or later at Kyushu Institute of Technology, Kitakyushu, Japan. The samples ("Sample 1" and "Sample 2" with different superconducting properties, from Chapter 4 and reference [63]) were mixed with a liquid pressure transmitting medium (Apiezon J-oil) and loaded in a Teflon cell under inert conditions in an argon-filled glovebox, with care taken to exclude gas bubbles from the cell. The design of the piston cylinder cell (discussed in Chapter 2) means that such bubbles will significantly decrease the maximum pressure attained. A small piece of high-purity elemental tin (which exhibits a very sharp pressure-dependent superconducting transition below 4 K) was also included as a pressure marker. The viscous pressure transmitting medium is also a convenient means of protecting the sample from the atmosphere, allowing the Teflon cell to be removed from the glovebox and loaded into the piston-cylinder pressure cell on the open bench with greater dexterity.

A.C. susceptibility measurements were taken in an applied field of 4 Oe with a driving frequency of 10 Hz. The samples were cooled in zero field, and measurements were taken on warming between 2 – 30 K. At ambient pressures these two samples were found to superconduct with a relatively sharp and strong transition below 16 K ("Sample 1"), and with a relatively broad and weak transition below 12 K ("Sample 2").[63] For these initial measurements, applied pressure was varied between 0 – 1.4 GPa.

The results for Sample 1 and Sample 2 are shown in figure 6.20. For both, it can be



(a) Hydrostatic region, P = 1.74 GPa (310 bar load)



(b) Non-hydrostatic region, P = 9.85GPa (900 bar load)

Figure 6.16: Comparison of Rietveld refinements against NPD data taken from the hydrostatic and non-hydrostatic regimes, from the same sample of LiFeAs, using the Paris-Edinburgh cell with Fluorinert as the pressure-transmitting medium.

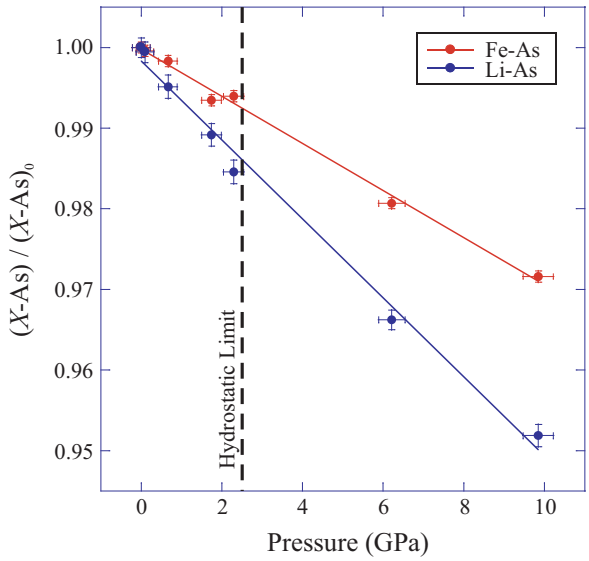


Figure 6.17: Normalised weighted (mean) Li-As and normalised Fe-As distances obtained by Rietveld refinement against NPD data, with pressure applied by the Paris-Edinburgh cell. The dashed line represents the hydrostatic limit of the pressure-transmitting medium (Fluorinert).

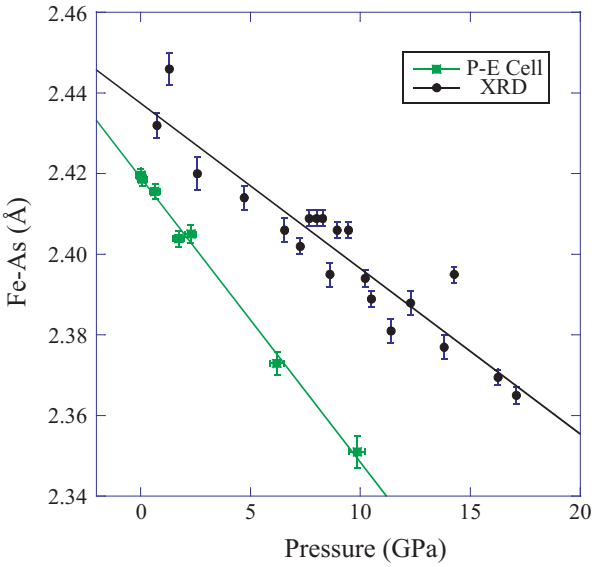


Figure 6.18: Comparison of the changes in Fe-As distance under applied pressure obtained by Rietveld refinement against XRD data (sample contained in diamond anvil cell, black line) and NPD data (sample contained in P-E cell, green line).

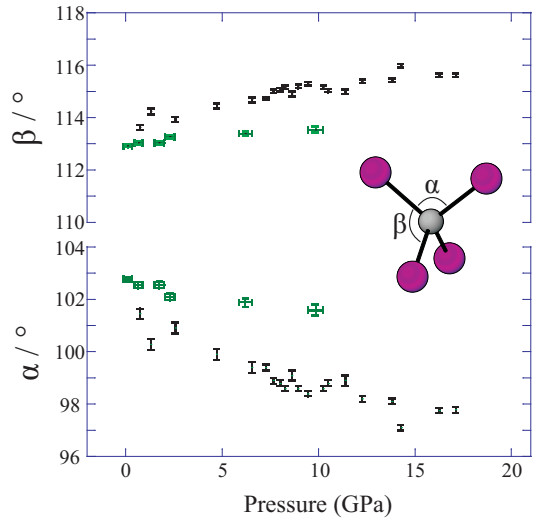
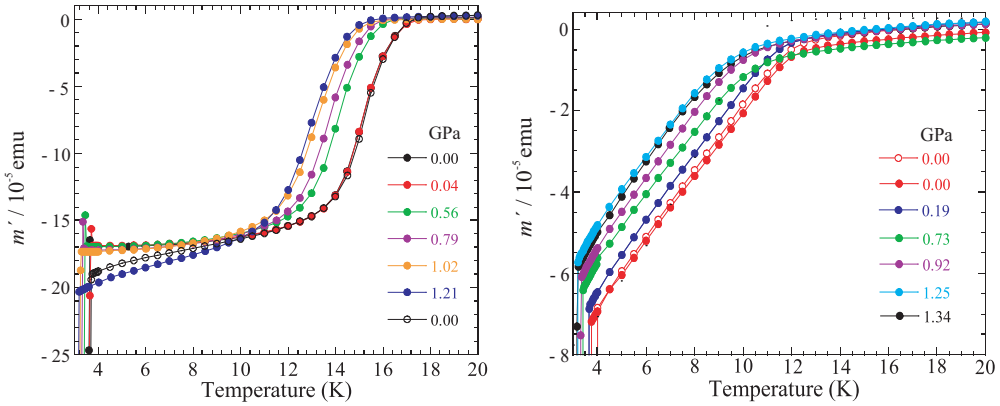


Figure 6.19: Comparison of the changes in As-Fe-As angles under applied pressure, obtained by Rietveld refinement against XRD data (sample contained in diamond anvil cell, black markers) and NPD data (sample contained in P-E cell, green markers).

seen that T_c is lowered by increasing the pressure. Values for T_c were obtained from the real part of the a.c. susceptibility by extrapolating the steepest part of the gradient and taking the intersection with the extrapolated normal state susceptibility. A plot of T_c versus pressure (figure 6.21), shows that the pressure response of both samples is approximately linear with very similar gradients $\frac{\Delta T_c}{\Delta P}$ of -1.7(2) K GPa^{-1} and -2.0(2) K GPa^{-1} for samples 1 and 2 respectively. Therefore, superconductivity is expected to be completely suppressed beyond $P \approx 9.5$ GPa for Sample 1 and $P \approx 6.0$ GPa for Sample 2.

In order to probe the response of superconductivity at even higher pressures, a second experiment was conducted with the piston-cylinder cell replaced by a customised miniature diamond anvil cell (described in detail in reference [177]). Two experimental runs were carried out using this device with a fresh sample of LiFeAs ($T_c \simeq 17$ K). The first, using 1.0 mm culet diamonds and a CuBe gasket, allowed measurements at hydrostatic pressures of up to 4.3 GPa. The second run used 0.8 mm culet diamonds with a Re gasket to measure at pressures up to 7.1 GPa, although T_c at this pressure was not well characterised due to a relatively weak Meissner signal in close proximity to the signal from the pressure marker, and the highest pressure



(a) LiFeAs Sample 1 (b) LiFeAs Sample 2

Figure 6.20: High-pressure a.c. magnetisation measurements of LiFeAs ("Sample 1" and "Sample 2" in the main text), with an applied field of 4 Oe and a driving frequency of 10 Hz, using the piston-cylinder pressure cell. Due the nature of the loading process, precise values for the masses of the samples were not obtained, and therefore m' represents the magnetic moment of the sample (in emu, or erg G^{-1}). The sharp transition below 4 K is due to the Sn pressure calibrant.

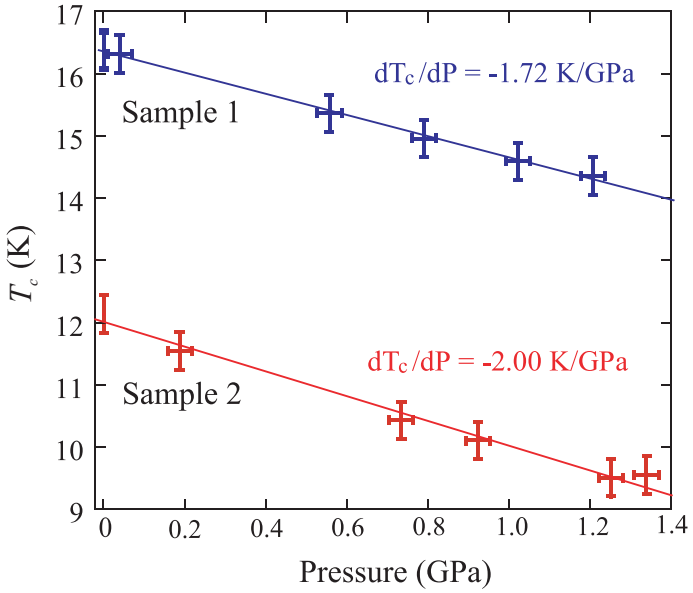


Figure 6.21: Variation of T_c with pressure for two samples of nominal stoichiometry LiFeAs ("Sample 1" and "Sample 2" from the text). Values are derived from the data in displayed in figure 6.20. dT_c/dP values are derived from linear best-fits.

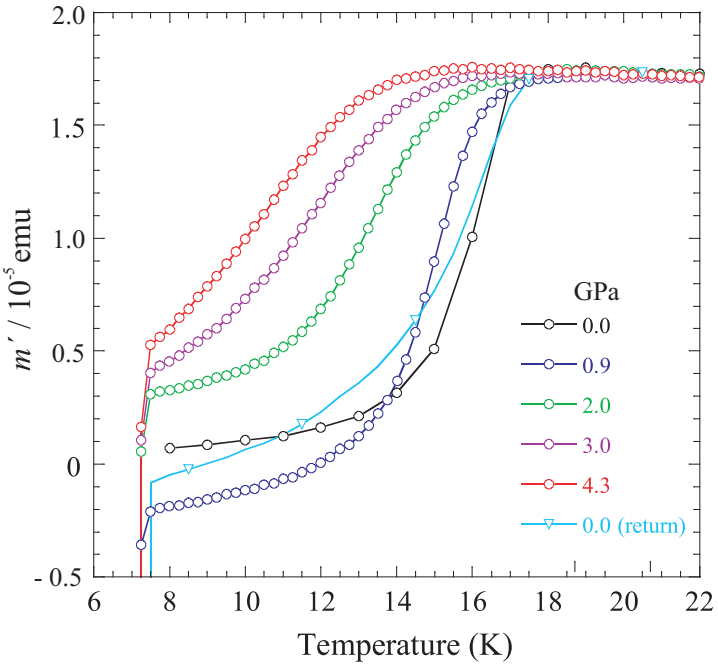


Figure 6.22: High-pressure a.c. magnetisation versus temperature for LiFeAs with pressure applied by a miniature diamond anvil cell. As for the piston cylinder cell (figure 6.20), a precise sample mass could not be obtained and m' represents the magnetic moment of the sample (in emu, or erg G^{-1}). The sharp transition below 8 K is due to the pressure marker.

at which a reliable measurement was taken was therefore 5.5 GPa. The following discussion is therefore limited to the data taken from the first run.

The results are shown in figures 6.22 and 6.23. It can be seen that T_c continues to decrease steadily as pressure is increased, with a similar gradient $\frac{\Delta T_c}{\Delta P} = -1.3(3)$ K GPa^{-1} to those obtained at lower pressures from the piston-cylinder cell (compared in figure 6.23). These observations are consistent with an early magnetic susceptibility study by Gooch *et al* [178] at modest pressures reporting that $\frac{\Delta T_C}{\Delta P} = -1.5$ K GPa^{-1}, and with resistivity experiments at higher pressures by Zhang *et al* [126] who report $\frac{\Delta T_C}{\Delta P}$ in the range -1.48 K GPa^{-1} to -1.22 K GPa^{-1}.

These results are consistent with the hypothesis that the regularity of the $FeAs_4$ tetrahedron is of critical importance to the superconducting transition temperature, as results from section 6.2.2 show that the tetrahedra become increasingly distorted with pressure. However, it is possible that the As-Fe-As angle is instead simply a proxy for some other structural parameter which affects T_c, such as the Fe-Fe distance, which

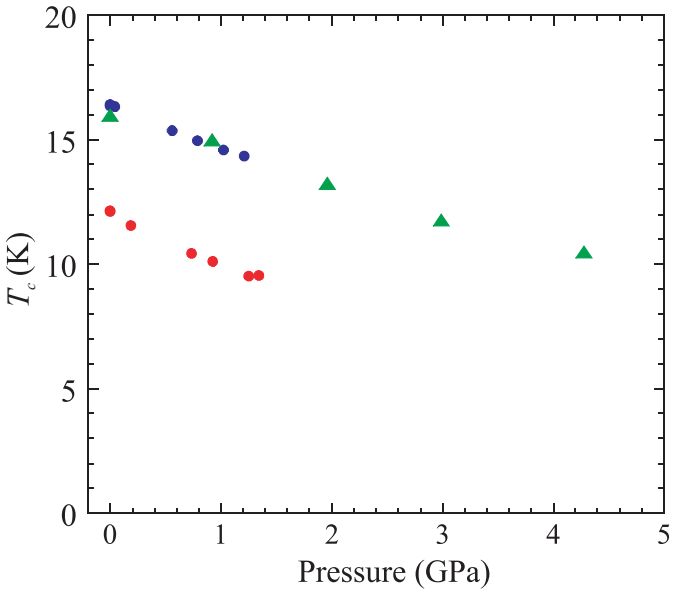


Figure 6.23: Variation of T_c with applied pressures of up to 4.3 GPa, for two samples of LiFeAs. Green triangles represent data from the miniature DAC; blue circles and red circles represent data from the piston-cylinder cell for Sample 1 and Sample 2 respectively.

may have more fundamental consequences for superconductivity in this system (as suggested by band structure calculations [163] for LaFeAsO). These two scenarios cannot be distinguished by the methods reported here.

However, it is clear from similar systems that the pressure dependence of T_c can be subject to factors other than As-Fe-As angle. A study of FeSe (which is isoelectronic with LiFeAs and structurally similar) by Margadonna and co-workers [175] shows a very different response of superconductivity to applied pressure at a low temperature of 16 K. FeSe has no ions in the inter-layer space and is therefore more compressible than LiFeAs (especially along the stacking direction), and on compression the $FeSe_4$ tetrahedra show a similar distortion away from ideal geometry, with the Fe-Fe distance decreasing from 2.67 Å at ambient pressure and temperature [123] (which is almost identical to the Fe-Fe distance in LiFeAs) to 2.52 Å under 12.1 GPa at 16 K. It is worth noting that this covers almost exactly the same range of Fe-Fe distances as the high-pressure XRPD experiment on LiFeAs in section 6.2.1. On increasing pressure, T_c is initially found to increase rapidly from 13 K to 37 K; it then goes through a maximum at $P \approx 6$ GPa before decreasing. The nature of this trend is ascribed to changes in

the band structure as inter-layer Se-Se interactions become stronger as the layers are forced together, but this does not fully explain why $\frac{\Delta T_C}{\Delta P}$ should be positive while that of LiFeAs is negative. Their results are confirmed by a later study by Okabe *et al.* [179] who suggested that the height of the anion above the Fe plane (which decreases), rather than Se-Fe-Se angle, is the controlling structural factor for T_c in FeSe.

Anion height (h_{An}) as a potential controlling parameter was proposed by Kukori *et al.* [162] who noted that the perpendicular distance between the pnictogen and the Fe plane has strong influence on the nesting properties of the Fermi surface (which is generally thought be be necessary for superconductivity in these systems). This has been used to empirically explain differing pressure responses in other compounds such as $Sr_2VFeAsO_3$ and the isostructural $Sr_2ScFePO_3$ [180] but does not appear to be universally applicable and requires the existence of some optimum height, which is not currently predicted by theory. The h_{An} value for LiFeAs is relatively high due to the large distortion of the $FeAs_4$ tetrahedra from regular geometry but its dependence on pressure appears to be very weak (see figure 6.9 on page 177), as it exhibits only a slight increase over the full range $0-17$ GPa. From these experiments, tetrahedral geometry appears to be a more credible controlling factor for T_c in LiFeAs than does h_{An}.

As mentioned previously, the extent of the correlation between bond angle, pnictide/chalcogenide height and Fe-Fe distance is dependent on the compressibility of the Fe-As or Fe-Se bonds. If this bond distance is considered to be fixed, these three parameters must be very strongly correlated. In section 6.2.1, the Fe-As distance in LiFeAs was found to be compressed at a rate of approximately -4.7×10^{-3} Å GPa^{-1}. This is comparable to the rates of -3.9×10^{-3} Å GPa^{-1} and -5.2×10^{-3} Å GPa^{-1} determined by X-ray diffraction for $BaFe_2As_2$ and $CaFe_2As_2$ respectively,[181] and -4.0×10^{-3} Å GPa^{-1} in $NdFeAsO_{1-x}$.[182] In FeSe, the Fe-Se distance is apparently more compressible and decreases at an approximate rate of -8.0×10^{-3} Å GPa^{-1}.[175] Presumably this is due to the lack of a *A-Ch* or *Ae-Ch* bond, which tend to be far less stiff (as demonstrated by the trends in Li-As distance in LiFeAs

in sections 6.2.1 and 6.2.2, the Ba-As distances in $BaFe_2As_2$[181] and the Nd-As distances in $NdFeAsO_{1-x}$).[182] Given the similarities of the Fe-As compressibility in all of these systems (perhaps with the exception of FeSe), it seems even more unreasonable to discuss their different structural and superconducting responses to pressure by treating bond angles, pnictide/chalcogenide heights and Fe-Fe distances as independent parameters.

Electronic factors also appear to have important consequences for the gradient of $\frac{\Delta T_C}{\Delta P}$: for example, in the compound $Sr_{1-x}K_xFe_2As_2$ the precise value of x causes $\frac{\Delta T_C}{\Delta P}$ to be positive, negative or zero [170] despite common structural changes. However, in LiFeAs the slight difference in composition between Sample 1 (stoichiometric LiFeAs) and Sample 2 (slightly non-stoichiometric $Li_{1-y}Fe_{1+y}As$, $y < 0.01$) does not appear to significantly affect the pressure response of the system, despite the suppression of T_c at ambient pressure. It may be of interest to investigate the pressure response of T_c in other doped derivatives of LiFeAs (such as $LiFe_{1-x}M_xAs$ where M = Co, Ni) for comparison with $Sr_{1-x}K_xFe_2As_2$.

6.3 Response of the Structure and Superconductivity of NaFeAs to High Pressures

6.3.1 High-pressure XRD from 0 – 24 GPa

A preliminary diffraction experiment on powdered NaFeAs under high pressures was conducted by Dr. Gaston Garbarino using the ID27 diffractometer (ESRF). Unfortunately the sample quality was too poor to determine structural parameters accurately, but the data did appear to show a phase transition at a pressure of approximately 22 GPa. This high-pressure phase could not be identified.

To follow up this experiment, with the aims of deriving an equation of state to describe the pressure response of the structural parameters and also solving the structure of the high-pressure phase, a second experiment was conducted using the

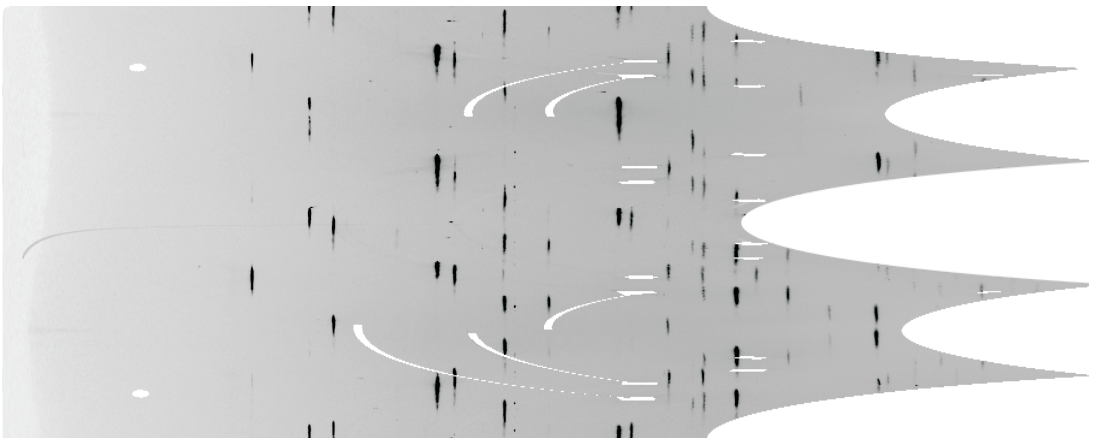


Figure 6.24: High-pressure X-ray diffraction pattern of NaFeAs taken from the 2D detector on ID09a, illustrating the graininess of the sample. White patches are masked Bragg reflections from the diamond anvils.

ID09a high-pressure diffractometer. This instrument is designed for angle-dispersive X-ray crystallography and is equipped with a 555 mm image-plate detector. The incident radiation was a monochromatic beam of wavelength $\lambda = 0.4141$ Å. A powder sample of NaFeAs was prepared by Dr. Dinah Parker by a method similar to that of LiFeAs.[69, 145] The sample was loaded into a diamond anvil cell (with a pressure-calibrating ruby) in an argon-filled dry box by Dr. Michael Hanfland, then sealed under a high pressure of He gas upon removal. All pressures are therefore considered to be fully hydrostatic.

Measurements were then taken on increasing pressure, with an exposure time of 4 s and the sample rotated through an angle of $\pm 30°$ to improve the powder average. In the first stage of the experiment, pressure was increased from a base value of 1.0 GPa to 4.3 GPa . The sample was then removed from the instrument for a short period and replaced for the second stage of the experiment, scanning through pressures from 5.2 GPa to a maximum of 24.1 GPa in steps of approximately 0.5 GPa. The observed powder rings from each scan were integrated using the program Fit2D [183, 184] to provide conventional plots of reflected intensity *vs* 2θ.

Visual inspection of the raw diffraction data (shown in figure 6.24) revealed that the Scherrer cones do not form rings of uniform intensity, which is a common symptom of a poor powder average (or "sample graininess"). In a fixed-wavelength

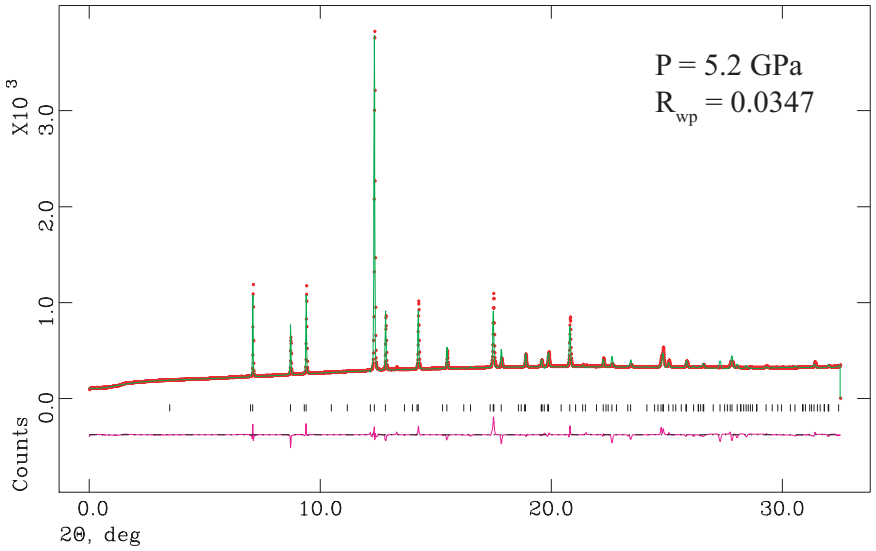


Figure 6.25: Representative Rietveld refinement of NaFeAs under 5.2 GPa applied pressure. Black markers indicate the positions of Bragg reflections (some of which are not observed due to preferred orientation). The incident wavelength is 0.4141 Å.

experiment with a 2θ-scanning detector, this phenomenon can have a very strong effect on observed peak intensities. In this experiment, the use of a 2D image-plate detector mitigates the problem to some degree, although a good powder average is still desirable. Despite this sample graininess, plots of integrated intensity *vs* 2θ clearly show that a transition to a new crystalline phase occurs when pressure is increased above 22 GPa, and this is illustrated in figure 6.30 on page 205.

Ambient-Pressure Phase

Rietveld refinement was used to determine lattice parameters of the low-pressure phase, using the sequential SEQGSAS routine from the GSAS suite. A representative refinement is shown in figure 6.25, and tables of refined parameters are displayed in Appendix F. The sample was found to exhibit very strong preferred orientation effects, with the result that several Bragg reflections were entirely absent from the observed patterns, and these effects were modelled by a spherical harmonic preferred orientation function. The refined lattice parameters show a smooth decrease above 5.2 GPa. Below this pressure, the lattice parameters are not so well-behaved, although the trend in c/a ratio follows a smooth curve throughout. Such behaviour is typical of a small

uncertainty in sample position, and it is therefore possible that the sample was not mounted securely in the first stage of the experiment. Furthermore, there is a slight discontinuity between the regions above and below 17.0 GPa which does not appear in a plot of c/a ratio. Again, this suggests some discrepancy in sample position.

The EoSFit5.2 software [173] was then used to fit a third order Birch-Murnaghan equation of state (see equation 6.1) to the refined lattice parameters, but the regions $P < 5.2$ GPa and $P > 17.0$ GPa were excluded for reasons outlined above. The fitted values are shown in table 6.3 on the next page. It should be noted that the statistical errors on these values are significantly higher than those obtained from LiFeAs, which may be due to the use of a smaller pressure region which in turn lies further from zero. The differing errors on the input data may also affect this. The fitted bulk modulus K_0 of NaFeAs is found to be smaller than that of LiFeAs (56.7 GPa), which means this compound is slightly more compressible. This effect appears to arise primarily as a result of the increased compressibility of the basal plane: in LiFeAs, the $FeAs_4$ are already effectively compressed in this plane under ambient conditions, with short Fe-Fe distances of 2.67 Å[63] making the basal plane relatively stiff ($K_0 = 65.6(8)$ GPa). In NaFeAs, the $FeAs_4$ tetrahedra are almost regular and the Fe-Fe distance is significantly longer (2.79 Å),[145] with the result that the stiffness of a^3 is relatively low ($K_0 = 51(3)$ GPa). The stiffness along the c-direction is comparable in the two materials with refined K_0 values of 42(2) GPa for NaFeAs against 45.3(6) GPa for LiFeAs. The derivative of the 3-dimensional bulk modulus K_0' is also similar for the two, indicating that stiffness increases at a similar rate as P increases, although along the c-direction K_0' is greater in NaFeAs than it is in LiFeAs.

A visual comparison of the lattice parameter trends from the two systems, shown in figure 6.26, is consistent with these conclusions. These plots are similar in most respects for LiFeAs and NaFeAs, but the trend in c/a ratio is quite different for each. The c/a ratio for LiFeAs shows a steady decrease following a smooth curve, while that of NaFeAs shows an initial decrease before passing through a shallow minimum at approximately 19 GPa and then increases sharply up to the phase transition at 22

Table 6.3: Fitted parameters for a third-order Birch-Murnaghan equation of state for NaFeAs.

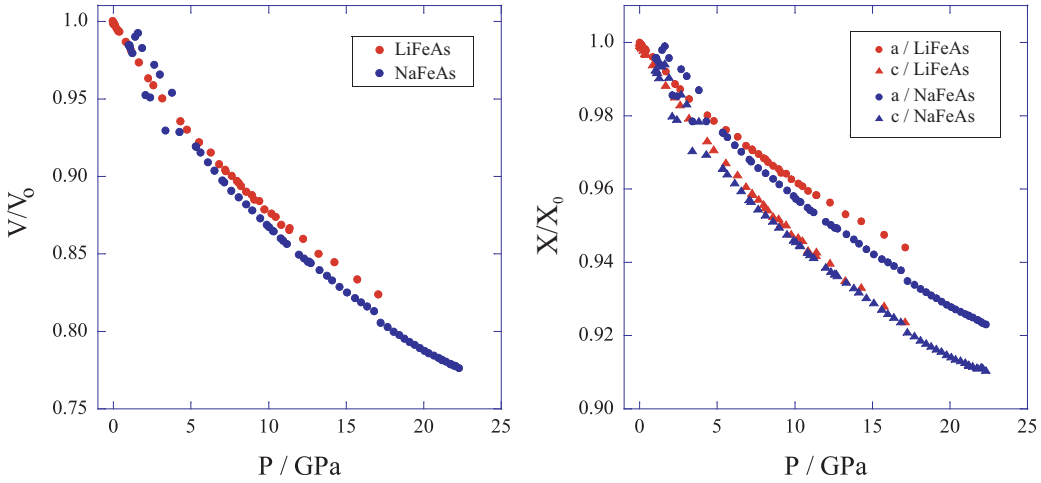
Parameter	X_0 (Å^3)	K_0 (GPa)	K_0'
V	110.4(2)	47(2)	4.8(2)
a^3	62.3(2)	51(3)	4.8(3)
c^3	347(1)	42(2)	4.6(2)

GPa. This trend reflects the higher K_0' in the c-parameter of NaFeAs and may be a significant factor for the occurrence of the phase transition.

Before discussing other structural parameters, it should be emphasised that the strong preferred-orientation effects (and the corresponding Rietveld corrections) for this sample mean that the integrated peak intensities - and hence the refined atomic coordinates - are inherently unreliable and conclusions drawn from them should be treated with caution. The parameters U_{iso} and z are expected to be correlated together with preferred-orientation parameters. However, meaningful conclusions may plausibly still be drawn if it is assumed that the extent of preferred-orientation is not strongly pressure-dependent. The z-coordinates of Na and As were therefore allowed to refine freely along with isotropic temperature factors.

Analysis of the bond angles in the FeAs layer, displayed in figure 6.26d, shows that the $FeAs_4$ tetrahedra become increasingly distorted as pressure increases. The mode of distortion is the same as that observed in LiFeAs, whereby the tetrahedra become relatively compressed in the basal plane. The greater X-ray scattering power of Na compared to that of Li allows some meaningful direct analysis of the Na-As distances in this sample. Comparison of the contraction of the Fe-As and Na-As bonds (shown in figures 6.27 and 6.28) is found to reflect the behaviour of LiFeAs, as the Na-As bond appears to be significantly more compressible than Fe-As.

However, the trend in Na-As distance does not vary smoothly throughout the pressure region $5 - 22$ GPa, and there is a clear discontinuity above 15 GPa. This discontinuity does not occur at the same pressure as that observed in the lattice parameter trends (approximately 17 GPa - see figure 6.26). Consequently, these two



(a) Unit cell volumes.

(b) c-parameters and a-parameters.

(c) c/a ratios.

(d) As-Fe-As angles.

Figure 6.26: Figures *a-c* show normalised lattice parameters trends as a function of applied hydrostatic pressure for NaFeAs (blue markers) and LiFeAs (red markers), obtained from synchrotron XRD data. Error bars are 1 ESD generated by GSAS and are smaller than the point markers. Figure *d* shows the distortion of the $FeAs_4$ tetrahedra on compression - error bars here represent 5x the ESDs generated by GSAS.

observations are unlikely to have been caused by the same external event (e.g. a small change in sample or detector position). Closer inspection reveals that the discontinuity corresponds to a sudden large increase in the refined z-coordinate of the Na atom which corresponds to a decrease in the mean Na-As distance. On visual inspection the refinement fits (and the patterns themselves) are not significantly different on either side of the discontinuity, while the weighted R-factor (R_{wp}) values do show a sudden decrease at this point (contrasting against the small prevailing increase in this parameter - see figure 6.29).

It is possible that this discontinuity is actually an artefact of the refinement sequence: for example, the initial refinement conditions may be close to two different minima, either of which may describe the system well. The balance between these minima may change with increasing pressure, with 15 GPa being a critical point at which one or the other becomes favoured. A plot of the weighted R-factor (R_{wp}) lends some support to this hypothesis, as this parameter shows a sudden sharp decrease co-incident with the observed discontinuity. To test this possibility, the sequential refinements were repeated in two ways: (i) the initial refinement conditions were modified by increasing the value of the Na z-coordinate to from 0.6 to 0.7 (a value obtained by extrapolating from the high-P region to 5 GPa), and (ii) the refinement sequence was run in reverse order.

Both procedures (i) and (ii) closely reproduced the initial results, with a general decrease in z and a discontinuity at 15 GPa. This suggests that the discontinuity is not merely an artefact of the sequential refinement process. Such a small transition resulting in shorter average Na-As bonds is chemically plausible, but it is very unusual for high-pressure transitions to occur with no change in co-ordination number or crystal symmetry - neither of which occur here - and no significant change in lattice parameters. One example of a high-pressure transition where coordination numbers and symmetry are preserved is the "collapsed" tetragonal phase of $CaFe_2As_2$,[80] but even in this case the transition is accompanied by a radical change in unit cell parameters. Further work, using a sample with a better powder average, may be

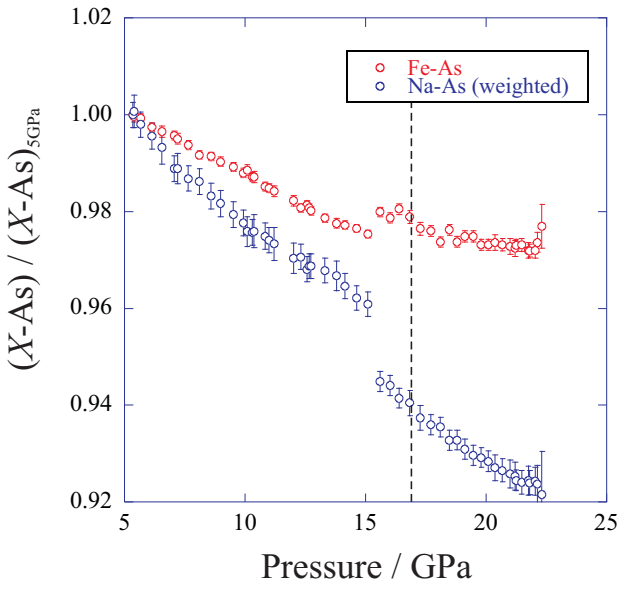


Figure 6.27: Fe-As and Na-As distances in NaFeAs as a function of applied pressure, normalised at 5.2 GPa. The black dashed line represents the position of the discontinuity observed in the lattice parameter trends (see figure 6.26). Error bars are equal to 1 ESD generated by GSAS: this is almost certainly an underestimate of the true uncertainty but these small values have been used to maintain the clarity of the plot.

required to confirm these observations.

High-Pressure Phase

Attempts were made to index the diffraction pattern of the high-pressure phase of NaFeAs using the automatic routines in CMPR and Crysfire, but no appropriate solution could be obtained. Presumably this is due to strong preferred orientation effects causing a number of Bragg reflections to be absent, which auto-indexing programs are not equipped to deal with. An attempt to index the pattern manually by trial-and-error, using the program CrystalCracker [185] to generate patterns arising from possible tetragonal, orthorhombic or hexagonal distortions with different combinations of lattice parameters, did not yield any satisfactory results. The possibility of a lower symmetry monoclinic unit cell was not investigated by this manual trial-and-error method, as the extra degree of freedom (variation in cell angle) would make this an extremely difficult and prohibitively time-consuming task.

High-pressure phase transitions are known to occur in the anti-isostructural (but

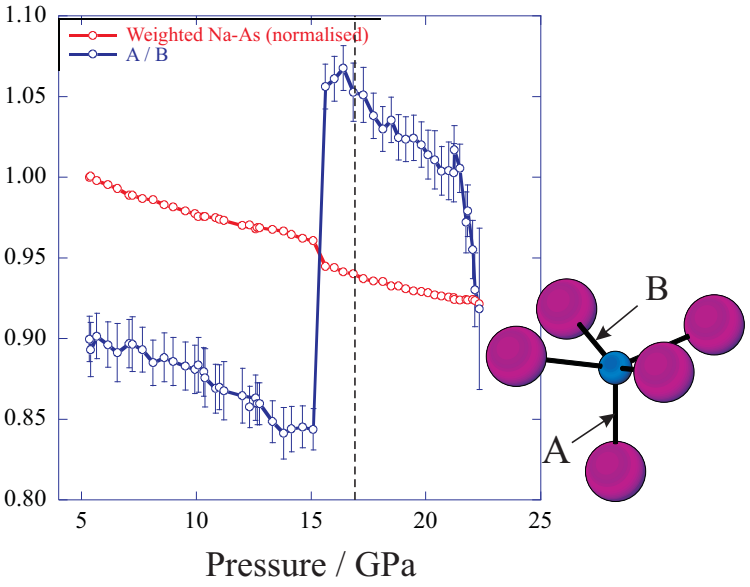
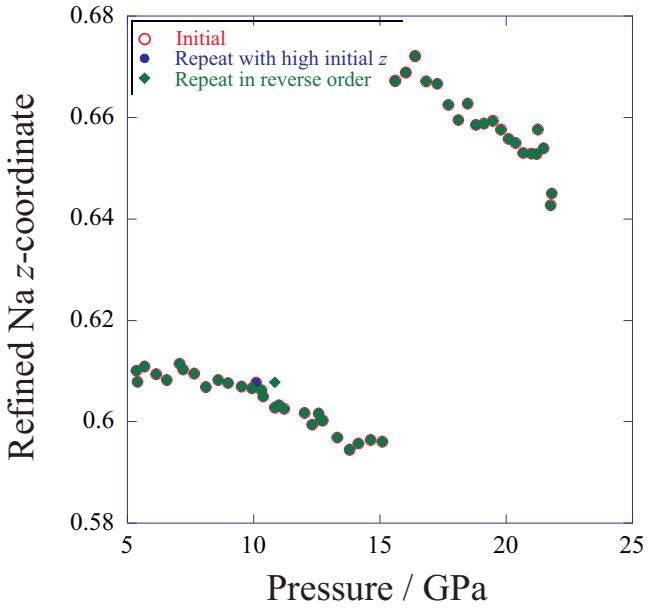


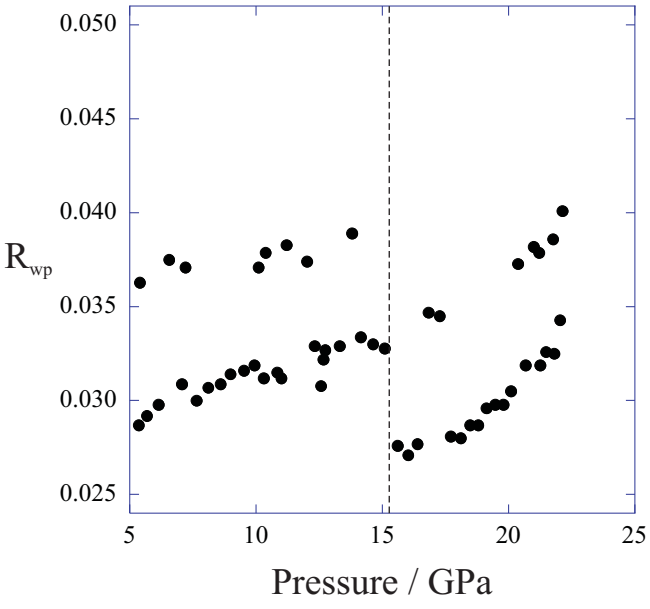
Figure 6.28: Ratio of the two Na-As distances (blue markers; A and B are labelled in the illustration), and the overall weighted Na-As distance (red markers) in NaFeAs, as a function of applied pressure. As in figure 6.27, the dashed line represents position of the discontinuity in the lattice parameter trends (see figure 6.26). Error bars are equal to 1 e.s.d. from GSAS.

comparatively strongly ionic) compounds BaFCl (at 21 GPa), BaFBr (at 27 GPa), SrFCl (at 41 GPa),[186] and BaFI (at 55 GPa).[187] These materials are found to distort from tetragonal to monoclinic symmetry at high pressures, with high-pressure BaFCl taking the space group $P2_1/m$ and maintaining its layered structure.[188] However, an attempt to use a monoclinic cell (with lattice parameters and angles estimated from the cell changes reported for BaFCl) to model the observed high-pressure NaFeAs pattern was again unsuccessful.

High-pressure phase transitions are also known for more covalent PbFCl-type compounds (also known as "Cu_2Sb-type")[49] such as Mn_2As[189] and MnFeAs.[190] Mn_2As undergoes a structural transition to the hexagonal Fe_2P structure above 6.5 GPa, while Fe_2P-type MnFeAs is stable at ambient pressure but must be synthesised under an applied pressure of 3.5 GPa. The Fe_2P structure is not layered, and therefore represents a more drastic structural change than that which occurs in BaFCl. However, attempts to match a Fe_2P-type model to the diffraction pattern from high-pressure NaFeAs by systematically varying the lattice parameters



(a) Refined Na z-coordinates.



(b) Weighted R-factors.

Figure 6.29: Refined Na z-coordinate and the corresponding weighted R-factor for NaFeAs, as a function of applied pressure. Data were obtained by sequential Rietveld refinements against variable-pressure XRD data. The discontinuity in Na z-coordinate is indicated in figure b by the black dashed line.

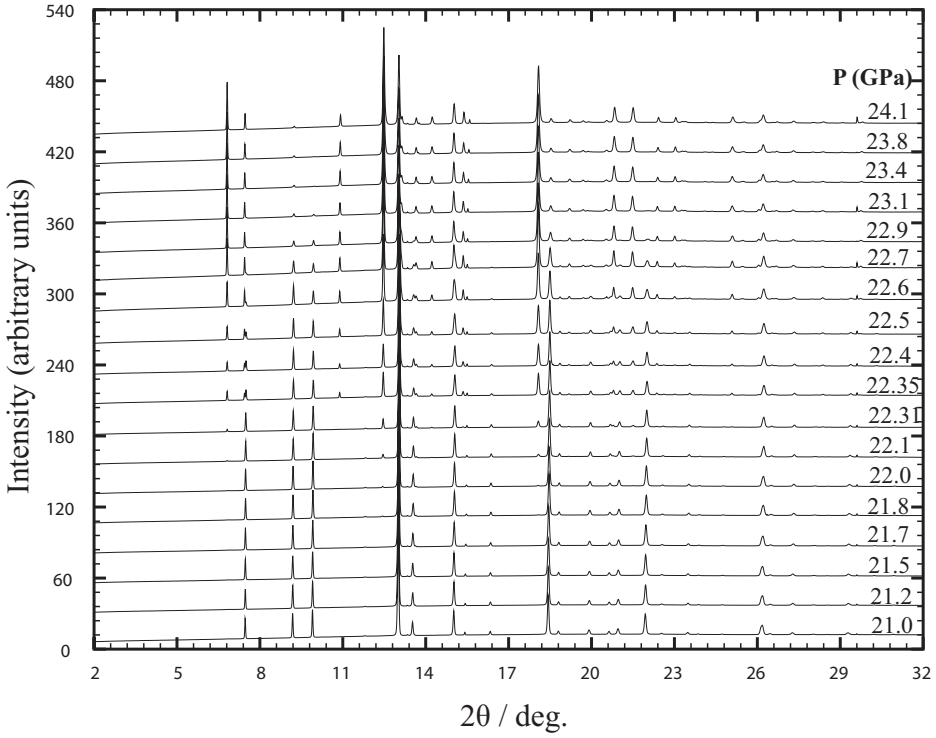


Figure 6.30: Synchrotron XRD patterns collected in the phase-transition region between $P = 21.0$ GPa and $P = 24.1$ GPa. The high pressure phase begins to appear above $P = 22.0$ GPa.

were repeatedly unsuccessful.

The comparison of NaFeAs with Mn_2As and MnFeAs is perhaps undermined by significant differences in ionic radii and the bonding preferences of Na and Mn. For example, the ratio of the 4-coordinate ionic radii $r_{Na^+}/r_{Fe^{2+}}$ is approximately 1.57 while $r_{Mn^{2+}}/r_{Fe^{2+}}$ is 1.05 [10] (although it should be noted that the assignment of a formal oxidation state to transition metals in highly covalent compounds such as MnFeAs is non-trivial and not always appropriate, it is still clear that these values are significantly different in the two compounds). While this is apparently enough to induce cation ordering in MnFeAs,[190] Mn^{2+} is sufficiently different to Na^+ (in both size and chemical characteristics) that it would not be unreasonable for these compounds to exhibit entirely different high-pressure phases. The ternary compound TiFeSi has a more similar ratio of metal radii (6-coordinate $r_{Ti^{2+}}/r_{Fe^{2+}}$ is approximately 1.41) to that in NaFeAs, and this material has a complicated ambient-pressure unit cell which is an orthorhombic supercell of the Fe_2P structure.[191] If NaFeAs were to take a high-pressure structure of this complexity it would be extremely difficult to assign manually (although in this situation a greater number of observed Bragg peaks would be expected, even though the preferred orientation is strong).

It should be noted that these failures to manually index the high-pressure pattern of NaFeAs to a monoclinic or hexagonal unit cell cannot be used to absolutely rule out the possibility of a monoclinic distortion (as in BaFCl) or a hexagonal distortion (as in Mn_2As), and comparison with these systems is still expected to be instructive even they prove not to be directly analogous. However, it appears that the collection of a diffraction pattern from a superior sample (either a non-oriented powder or a single crystal) will be crucial to the solution of the high-pressure structure of NaFeAs.

6.3.2 High pressure magnetometry from 0 – 1.6 GPa

In order to determine the pressure response of T_c in NaFeAs, A.C. magnetic susceptibility measurements were taken by Dr. Masaki Mito under hydrostatic

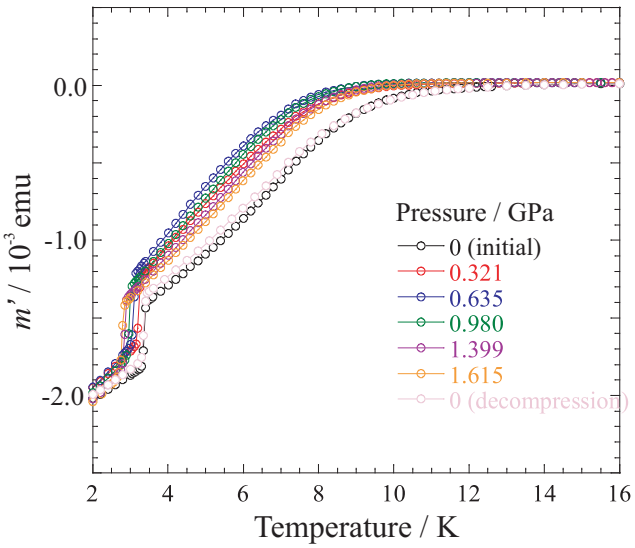
pressures of up to 1.6 GPa using a piston cylinder device (similar to that used for LiFeAs in the previous section). Measurements were taken with the sample in an applied field of 4 Oe with a driving frequency of 10 Hz. As before, T_c values were obtained by extrapolating the steepest section of the Meissner transition to intercept the extrapolated normal-state curve. The results are displayed in figure 6.31.

The system appears to exhibit a small initial decrease in T_c in the region $P < 0.6$ GPa, but as P is increased further $\frac{\Delta T_c}{\Delta P}$ becomes slightly positive. This is a more complex response than that exhibited by LiFeAs, and does not obviously correlate to a steadily changing structural parameter (such as Fe-Fe distance). Further experiments on samples of NaFeAs and superconducting $NaFe_{(1-x)}Co_xAs$, using the piston cylinder cell and miniature diamond anvil cell, are currently ongoing and aim to confirm these results and map out the behaviour of these systems up to (and possibly beyond) 5 GPa.

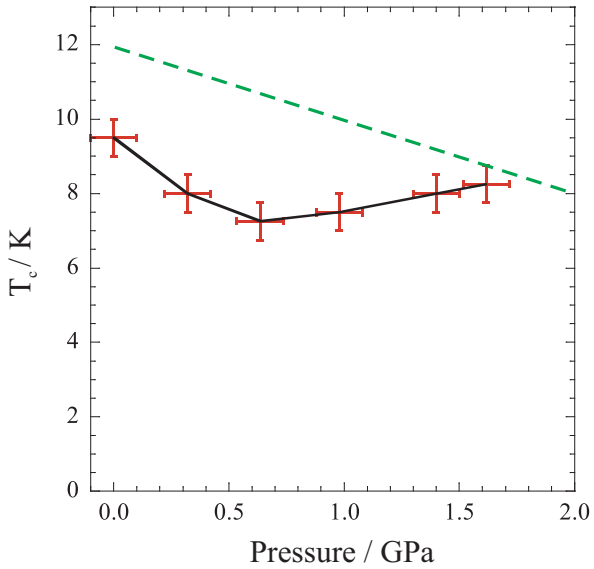
6.4 Summary and conclusions

Sections 6.2.1 and 6.2.2 detail the investigation of structural changes in LiFeAs under pressure by X-ray diffraction and neutron diffraction techniques, respectively. XRD allowed the pressure response to be investigated over the widest range of hydrostatic pressures, from $0-17$ GPa, and rapid collection times (60 seconds per measurement) allowed a large number of measurements to be taken in this region. This showed that LiFeAs is highly compressible compared to other arsenide superconductors, exhibiting a smooth contraction of the lattice parameters with a corresponding decrease in the c/a ratio. Inspection of the structural parameters revealed that the $LiAs_5$ environment is significantly more compressible than the $FeAs_4$ environment. Preferential compression of the $LiAs_5$ square-pyramids then causes the $FeAs_4$ tetrahedra to become more irregular (i.e. they are further compressed in the basal plane despite the negative change in c/a) as pressure is increased. These changes are illustrated together in figure 6.32.

To probe these structural changes further, two NPD experiments were carried out. The first, conducted over a small range of hydrostatic pressures (< 0.6 GPa) in a He-



(a) Plots of the magnetic moment of the sample m' (in emu, or erg G^{-1}) *vs* T for NaFeAs under several pressures below 1.6 GPa (values inset). Data were taken on increasing pressure.



(b) A plot of T_c vs P for NaFeAs (derived from the magnetisation plots in figure 6.31a, above). The green dashed line represents the trend obtained from LiFeAs "Sample 2". The black line is a guide to the eye.

Figure 6.31: The response of superconductivity to applied hydrostatic pressures of up to 1.6 GPa for a sample of NaFeAs, investigated using a.c. SQUID magnetometry with a piston-cylinder pressure cell (described in section 2.2.10).

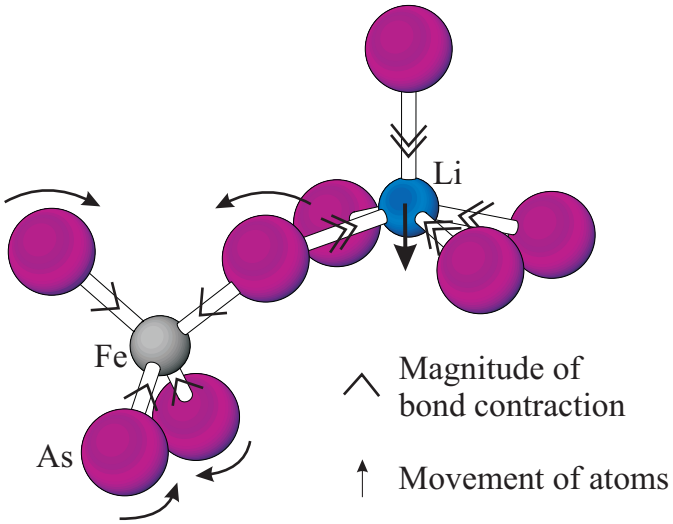


Figure 6.32: A diagram illustrating the structural changes occurring about the tetrahedral Fe position and the square-pyramidal Li position in LiFeAs as pressure is increased, highlighting the relatively high compressibility of the Li-As bonds and the increasing distortion of the $FeAs_4$ tetrahedra.

gas pressure cell, confirmed the changes observed by XRD and also showed more detailed (but small) changes to the $LiAs_5$ environment. This allowed the changes in Fe-As distance to be related to explicit changes in Li-As distance, which was found to contract at approximately double the rate. A tendency for the Li ion to move towards the base of the square pyramid was also identified from changes in As-Li-As angles.

The second NPD experiment was conducted using a Paris-Edinburgh cell to generate pressures of up to 10 GPa. This allowed structural parameters to be compared to those derived by XRD (due to similar pressure scales). While the agreement was generally good, the effects of a non-hydrostatic pressure environment caused some discrepancies at pressures above 2.3 GPa. This experiment complemented the results derived from the He gas cell which showed the Li-As distance contracting more rapidly than the Fe-As distance, but the decrease in data quality (caused by the small sample size and bulkier sample environment apparatus) meant an increased uncertainty in the refined Li z-coordinate with the result that meaningful trends in As-Li-As could not be discerned.

Changes in the superconducting transition temperature, determined by a.c. SQUID magnetometry in the pressure range $0 - 4.3$ GPa, show that T_c decreases with

increasing pressure. This is consistent with the hypothesis that T_c is dependent on the regularity of the $FeAs_4$ tetrahedra, which become increasingly distorted, but it is also possible that the Fe-Fe distance (which is already shorter at ambient pressure in LiFeAs than in any other reported iron arsenide superconductor) is the true controlling parameter. The thickness of the FeAs layers (i.e. the height of the As atoms above the Fe plane) shows a very weak dependence on pressure, and therefore does not adequately explain the observed trend in T_c. However, these factors can not be treated independently and there appear to be other important factors that affect the value of $\frac{\Delta T_C}{\Delta P}$ in similar systems, including electron count and various bond distances (which may affect the electronic structure), and as such there is no "typical" behaviour for comparison with LiFeAs, with even the structurally similar FeSe (which displays quite similar properties under addition of extra Fe) exhibiting a radically different superconducting response under pressure.

The behaviour of NaFeAs under high pressures is similar to that of LiFeAs but is slightly more complex with respect to both structural and magnetic properties. In NaFeAs, a smooth distortion of the $FeAs_4$ tetrahedra away from ideal geometry reflects the behaviour of LiFeAs, but in contrast to LiFeAs this does not correspond to a monotonic decrease in T_c. Instead, T_c shows an initial decrease and then increases slightly between $0.6 - 1.6$ GPa. It is possible that the T_c of this material could be enhanced considerably at higher pressures, and further high-pressure magnetometry experiments are on-going.

It is clear that further work is required to reinforce some of the conclusions drawn from a high-pressure XRD study on NaFeAs (described in section 6.3.1). This work showed a transition to a new crystalline phase at pressures greater than 22 GPa, but the diffraction pattern from this high-pressure phase could not be indexed due to the sample exhibiting strong preferred-orientation effects. Future experiments on a higher quality sample (possibly a single crystal) may lead to the identification of this structure, while X-ray powder diffraction experiments may have a rôle in refining the equation of state for NaFeAs, and investigating the reproducibility of a seemingly anomalous

change in the Na z-coordinate below the structural transition pressure.

Chapter 7

Summary

The work described in this thesis has mainly focused on two materials that have very closely related layered crystal structures, but which exhibit radically different physical and chemical properties. Work in Chapter 3 describes an investigation of the compositional range and low temperature crystal structure of the enigmatic ZrCuSiAs-type oxysulfide $CeCu_{1-x}OS$; while chapters $4-6$ contain a detailed study of the effects of structure and composition on superconductivity in the anti-PbFCl-type arsenide LiFeAs.

Prior to this work, several studies had detailed the anomalous structural and physical properties of CeCuOS. This compound is reported to be black in colour (in contrast to the green/brown colour of all other known *Ln*CuOS compounds) with anomalously small lattice parameters (in particular a contracted Ce-S distance), anomalous optical properties and a relatively high conductivity, and an effective magnetic moment that is significantly diminished from the free-ion value of 2.54 μ_B expected for Ce^{3+}. Furthermore, results published by different laboratories are not always consistent. It has previously been suggested that this compound is intrinsically Cu-deficient[40] and more recent work has confirmed that this material can host a significant Cu deficiency.[34] However, recent work in this laboratory [41, 77] has showed that it is possible to synthesise seemingly non-anomalous green/brown samples of CeCuOS that reverts to the more familiar (anomalous) black CeCuOS upon air

exposure in a process that can be reversed by heating under a reducing atmosphere of dilute hydrogen. Unfortunately this work did not establish the origin of this air-sensitivity and the relationship of these samples to those prevalent in the literature.

The investigation described in Chapter 3 has addressed these questions of compositional range and air-sensitivity in CeCuOS by using neutron powder diffraction to show that the green/brown material is almost-stoichiometric $CeCu_{0.987(2)}OS$. This material was found to have non-anomalous structural parameters with lattice parameter values between those of LaCuOS and PrCuOS, as expected from the lanthanide contraction, and these are significantly larger than any reported in the literature. Magnetometry measurements showed that this sample has an effective magnetic moment of 2.53(2) μ_B, again significantly higher than literature values and indicative of a bona-fide Ce^{3+} compound. Its partially-oxidised black counterpart was found to be significantly Cu-deficient with a refined composition of $CeCu_{0.862(2)}OS$ and correspondingly contracted lattice parameters, consistent with literature reports of "CeCuOS". This black sample exhibited a diminished paramagnetic moment of 2.38(4) μ_B, consistent with partial oxidation of Ce to leave a mixed-valence $Ce^{3+/4+}$ compound. In addition, the neutron diffraction patterns contained evidence for poorly-crystalline CuO in the oxidised black sample, which may be at least partially responsible for the colour change. This observation, coupled with the realisation that the oxidation can be reversed by heating under reducing conditions, has inspired a new synthetic route to fully stoichiometric CeCuOS which involves heating a ground mixture of $CeCu_{1-x}OS$ and xCuO under an atmosphere of dilute hydrogen. This method appears to be more reliable than the more conventional synthesis described in Chapter 3 and has been used to synthesise a sample with the largest lattice parameters yet observed.

The extrusion of Cu from the sulfide layer under atmospheric conditions explains the variable literature reports of the properties of CeCuOS. This realisation also has wider implications for the air-sensitivity of other compounds which contain a combination of anti-PbO-type CuS layers and oxidisable cations. It is significant that

this type of behaviour has subsequently been observed in $Sr_2CoO_2Cu_{2-x}S_2$.[112]

Variable-temperature X-ray diffraction studies of Cu-deficient $CeCu_{0.8}OS$ revealed extra Bragg reflections below 200 K due to crystallographic ordering of Cu ions and vacancies in the $Cu_{0.8}S$ layer. This low temperature XRPD pattern was successfully indexed and found to correspond to a $\sqrt{5}a \times \sqrt{5}a \times c$ basal expansion of the high temperature ZrCuSiAs unit cell, with a reduction in symmetry from the $P4/nmm$ space group to $P4/n$. This was subsequently confirmed by electron diffraction and the new structural model was used to obtain structural parameters by Rietveld refinement against XRPD data and NPD data. This observation of ion-vacancy ordering in $CeCu_{1-x}OS$, which has a range of stable compositions, raises the possibility that other ordering schemes may be attained by tuning the composition. This will be addressed in future work.

In February 2008, a report of superconductivity below 26 K in $LaFeAsO_{1-x}F_x$[21] was followed by a great surge in interest in layered iron pnictide compounds and a race to synthesise new high-T_c superconductors of this type. Consequently, LiFeAs (which contains anti-PbO-type FeAs layers separated by layers of Li cations) became a major synthetic target. The only previous study of LiFeAs[78] (by X-ray powder diffraction) was published in 1968 and left major ambiguity over the precise position of Li in the crystal structure; it was suggested that it lies in a square-pyramidal $LiAs_5$ site (as in the anti-PbFCl structure) but could alternatively occupy a tetrahedral site (as in the ordered fluorite-type LiMnAs).

In Chapter 4, this compound was synthesised and found to exhibit superconductivity below 16 K. This initial sample of LiFeAs was examined in detail by joint Rietveld refinements against high-resolution neutron diffraction and high-resolution X-ray diffraction, and unambiguously shown to take the anti-PbFCl structure with Li ions occupying a square-pyramidal site. The sample was found to be fully stoichiometric within experimental uncertaintly. The $FeAs_4$ tetrahedra were found to be highly distorted by compression in the basal plane, with shorter Fe-Fe distances than any other layered iron arsenides (but comparable with those of FeSe).

These results were in agreement with a single-crystal XRD experiment conducted by Tapp *et al.*[64] These results could not have been attained by conventional laboratory X-ray powder diffraction, as demonstrated by Wang *et al.*[192]

Joint XRD-NPD techniques were then used to explore the phase width of the system, which was found to readily adopt Fe-rich compositions of type $Li_{1-y}Fe_{1+y}As$ ($0 \leq y < 0.05$). It was found that the excess Fe ions share the square-pyramidal Li site, which causes a contraction of the lattice parameters and further distorts the $FeAs_4$ tetrahedra. This type of non-stoichiometry was found to strongly suppress superconductivity, probably by a magnetic pair-breaking effect,[193] such that compounds with $y \gtrsim 0.02$ no longer exhibit superconductivity. Superconductivity is similarly sensitive to this type of non-stoichiometry in tetragonal $Fe_{1+y}Se$. These non-stoichiometric compositions were found to form readily and several were synthesised inadvertently during the course of this work during attempts to synthesise fully stoichiometric materials, highlighting the care that needs to be taken when synthesising LiFeAs and its derivatives.

A significant amount of research has shown that the substitution of Fe by Co or Ni can induce superconductivity in $Ae Fe_2As_2$ and *Ln*FeAsO-type compounds, and that substitution strongly affects T_c in these systems by electron-doping. In Chapter 5, the effect of this type of substitution on the superconducting properties of LiFeAs was investigated, with Fe substituted by Co, Ni and Mn in three series of compounds of type $LiFe_{1-x}M_xAs$. Structural trends in each of these series were determined by high resolution XRPD and/or NPD measurements, and superconducting properties by SQUID magnetometry and μSR spectroscopy. The structure was found to respond similarly to Co- and Ni-substitution, with a slight relaxation of the $FeAs_4$ tetrahedra, in common with other systems of this type. Both of these substituents were found to suppress superconductivity with a decrease T_c and the superconducting volume fraction and an increase in the London penetration depth. The rate of suppression was found to be dependent the number of dopant electrons, with Ni found to be twice as effective as Co, and superconductivity was quenched entirely beyond 0.1 dopant electrons per Fe

atom (i.e. 10 % Co or 5 % Ni). This is consistent with the reported behaviour of other Co- or Ni-doped pnictide superconductors such as $NaFe_{1-x}M_xAs$ and $BaFe_{2-x}M_xAs_2$ and has generally been considered to be due to a band-filling effect (i.e. the dopant atoms contribute electrons to the conduction band),[155] although recent research[151] has suggested that the dopant electrons should instead be highly localised, acting as electron-scattering impurities. This impurity model could be more consistent with the inhibiting effect that Co- and Ni-substitution has on superconductivity in this system.

Phase-pure compounds with Fe substituted by Mn can not be synthesised beyond a very small range ($x \leq 0.05$), and the small number of samples (3) made the observed changes in lattice parameters difficult to interpret (with some suggestion from neutron diffraction that these samples may also be somewhat non-stoichiometric). Substitution of Fe by Mn was found to strongly suppress superconductivity. Comparison with the non-stoichiometric materials $Li_{1-y}Fe_{1+y}As$ and studies of the effects of Mn-substitution on the resistivity of other layered Fe-pnictides suggests that this is due to impurity scattering.

This study of the effect of substitution at the Fe site has allowed a phase diagram to be derived for $LiFe_{1-x}M_xAs$ for comparison with other iron-based superconductors. The diagram appears to be unique among this class of superconducting materials, as the material is superconducting in the un-doped state and does not appear to contain a magnetically-ordered region or a structural distortion.

The effect of structural changes on the superconducting properties of LiFeAs and the isostructural compound NaFeAs was investigated in Chapter 6 through a series of high-pressure X-ray diffraction, neutron diffraction and SQUID magnetometry experiments. The application of hydrostatic pressures has been shown to affect T_c in other iron-based superconductors, but this response can be complex and is not always predictable. Equations of state were derived for both compounds. These experiments showed that superconductivity is suppressed by the application of hydrostatic pressure in LiFeAs, as T_c follows a monotonic decrease which appears to be correlated to an increasing distortion of the $FeAs_4$ tetrahedra. This is consistent with empirical

observations that suggest a regular tetrahedral $FeAs_4$ geometry is important for a high T_c value,[129] but the relatively stiff Fe-As bond means that these bond angles cannot be de-coupled from other parameters such as Fe-Fe distance, which may have a more fundamental importance to superconductivity in these systems.

NaFeAs was found to show a broadly similar structural response to applied pressure, with the $FeAs_4$ tetrahedra becoming progressively distorted away from ideal geometry, and a similarly anisotropic compressibility. However, unlike in LiFeAs this distortion was not found to correlate with changes in T_c over a limited range of pressures. Interestingly, NaFeAs was found to undergo a structural transition above 22 GPa, but attempts to index the diffraction pattern of the high-pressure phase by XRPD failed due to strong preferred-orientation effects and a poor powder average. Future experiments, using either a superior powder sample (i.e. more crystallites with a more randomised orientation) or a single crystal, are required to characterise this phase.

References

[1] Schiffer, P.; Ramirez, A. P.; Bao, W.; Cheong, S. W. *Physical Review Letters* **1995,** *75,* 3336-3339.

[2] Mizushima, K.; Jones, P. C.; Wiseman, P. J.; Goodenough, J. B. *Materials Research Bulletin* **1980,** *15,* 783-789.

[3] Saha, D.; Bao, Z. B.; Jia, F.; Deng, S. G. *Environmental Science and Technology* **2010,** *44,* 1820-1826.

[4] Proch, S.; Herrmannsdorfer, J.; Kempe, R.; Kern, C.; Jess, A.; Seyfarth, L.; Senker, J. *Chemistry - a European Journal* **2008,** *14,* 8204-8212.

[5] Grochala, W.; Edwards, P. P. *Chemical Reviews* **2004,** *104,* 1283-1315.

[6] Xiong, Z. T.; Yong, C. K.; Wu, G. T.; Chen, P.; Shaw, W.; Karkamkar, A.; Autrey, T.; Jones, M. O.; Johnson, S. R.; Edwards, P. P.; David, W. I. F. *Nature Materials* **2008,** *7,* 138-141.

[7] Bednorz, J. G.; Muller, K. A. *Zeitschrift Fur Physik B* **1986,** *64,* 189-193.

[8] Jones, H. *Energy Policy* **2008,** *36,* 4342-4345.

[9] Flukiger, R.; Suo, H. L.; Musolino, N.; Beneduce, C.; Toulemonde, P.; Lezza, P. *Physica C* **2003,** *385,* 286-305.

[10] *Handbook of Chemistry and Physics;* CRC Press: 84 ed.; 2003-2004.

[11] Johnson, V.; Jeitschko, W. *Journal of Solid State Chemistry* **1974,** *11,* 161-166.

[12] Motomitsu, E.; Yanagi, H.; Kamiya, T.; Hirano, M.; Hosono, H. *Journal of Solid State Chemistry* **2006,** *179,* 1668-1673.

[13] Needs, R. L.; Weller, M. T.; Scheler, U.; Harris, R. K. *Journal of Materials Chemistry* **1996,** *6,* 1219-1224.

[14] Yamane, H.; DiSalvo, F. J. *Journal of Alloys and Compounds* **1996,** *234,* 203-206.

[15] Pottgen, R.; Johrendt, D. *Zeitschrift Fur Naturforschung B* **2008,** *63,* 1135-1148.

[16] Tegel, M.; Johansson, S.; Weiss, V.; Schellenberg, I.; Hermes, W.; Pottgen, R.; Johrendt, D. *EPL 84,* 5.

[17] Kaczorowski, D.; Albering, J. H.; Noel, H.; Jeitschko, W. *Journal of Alloys and Compounds* **1994,** *216,* 117-121.

[18] Albering, J. H.; Jeitschko, W. *Zeitschrift Fur Naturforschung B* **1996,** *51,* 257-262.

[19] Wilmer, D.; Jorgensen, J. D.; Wuensch, B. J. *Solid State Ionics* **2000,** *136,* 961-966.

[20] Kamihara, Y.; Hiramatsu, H.; Hirano, M.; Kawamura, R.; Yanagi, H.; Kamiya, T.; Hosono, H. *Journal of the American Chemical Society* **2006,** *128,* 10012-10013.

[21] Kamihara, Y.; Watanabe, T.; Hirano, M.; Hosono, H. *Journal of the American Chemical Society* **2008,** *130,* 3296.

[22] Brock, S. L.; Kauzlarich, S. M. *Journal of Alloys and Compounds* **1996,** *241,* 82-88.

[23] Zhu, W. J.; Hor, P. H. *Journal of Solid State Chemistry* **1997,** *130,* 319-321.

[24] Brechtel, E.; Cordier, G.; Schafer, H. *Zeitschrift Fur Naturforschung B* **1979,** *34,* 777-780.

[25] Brock, S. L.; Raju, N. P.; Greedan, J. E.; Kauzlarich, S. M. *Journal of Alloys and Compounds* **1996,** *237,* 9-19.

[26] Gal, Z. A.; Rutt, O. J.; Smura, C. F.; Overton, T. P.; Barrier, N.; Clarke, S. J.; Hadermann, J. *Journal of the American Chemical Society* **2006,** *128,* 8530-8540.

[27] Overton, T. P. *Part II Thesis,* Thesis, University of Oxford, 2003.

[28] Zhu, W. J.; Hor, P. H. *Journal of Solid State Chemistry* **2000,** *153,* 26-29.

[29] Ogino, H.; Sato, S.; Kishio, K.; Shimoyama, J.; Tohei, T.; Ikuhara, Y. *Applied Physics Letters* **2010,** *97,* 3.

[30] Ogino, H.; Machida, K.; Yamamoto, A.; Kishio, K.; Shimoyama, J.; Tohei, T.; Ikuhara, Y. *Superconductor Science and Technology* **2010,** *23,* 5.

[31] West, A. R. Solid State Chemistry and its Applications. In ; John Wiley and Sons Ltd.: 1984.

[32] Rutt, O. J.; Williams, G. R.; Clarke, S. J. *Chemical Communications* **2006,** 2869-2871.

[33] Indris, S.; Cabana, J.; Rutt, O. J.; Clarke, S. J.; Grey, C. P. *Journal of the American Chemical Society* **2006,** *128,* 13354-13355.

[34] Chan, G. H.; Deng, B.; Bertoni, M.; Ireland, J. R.; Hersam, M. C.; Mason, T. O.; Van Duyne, R. P.; Ibers, J. A. *Inorganic Chemistry* **2006,** *45,* 8264-8272.

[35] Adamson, P. *D.Phil Thesis,* Thesis, University of Oxford, 2010.

[36] Clarke, S. J.; Adamson, P.; Herkelrath, S. J. C.; Rutt, O. J.; Parker, D. R.; Pitcher, M. J.; Smura, C. F. *Inorganic Chemistry* **2008,** *47,* 8473-8486.

[37] Kim, J. S.; Lee, J. Y.; Swinnea, J. S.; Steinfink, H.; Reiff, W. M.; Lightfoot, P.; Pei, S.; Jorgensen, J. D. *Journal of Solid State Chemistry* **1991,** *90,* 331-343.

[38] Zabel, M.; Range, K. J. *Revue De Chimie Minerale* **1980,** *17,* 561-568.

[39] Hiramatsu, H.; Ueda, K.; Kamiya, T.; Ohta, H.; Hirano, M.; Hosono, H. *Journal of Materials Chemistry* **2004,** *14,* 2946-2950.

[40] Charkin, D. O.; Akopyan, A. V.; Dolgikh, V. A. *Russian Journal of Inorganic Chemistry* **1999,** *44,* 833-837.

[41] Pitcher, M. J. *Part II Thesis,* Thesis, University of Oxford, 2007.

[42] Just, G.; Paufler, P. *Journal of Alloys and Compounds* **1996,** *232,* 1-25.

[43] Raccah, P. M.; Longo, J. M.; Eick, H. A. *Inorganic Chemistry* **1967,** *6,* 1471.

[44] Reehuis, M.; Jeitschko, W.; Moller, M. H.; Brown, P. J. *Journal of Physics and Chemistry of Solids* **1992,** *53,* 687-690.

[45] Reehuis, M.; Jeitschko, W.; Kotzyba, G.; Zimmer, B.; Hu, X. *Journal of Alloys and Compounds* **1998,** *266,* 54-60.

[46] Rotter, M.; Tegel, M.; Johrendt, D. *Physical Review Letters* **2008,** *101,* 4.

[47] Guo, J.; Jin, S.; Wang, G.; Wang, S.; Zhu, K.; Zhou, T.; He, M.; Chen, X. *Physical Review B* **2011,** *82,* 180520.

[48] Zavalij, P.; Bao, W.; Wang, X. F.; Ying, J. J.; Chen, X. H.; Wang, D. M.; He, J. B.; Wang, X. Q.; Chen, G. F.; Hsieh, P.-Y.; Huang, Q.; Green, M. A. *arXiv 1101.4882* **2011,** .

[49] Pearson, W. B. *Zeitschrift Fur Kristallographie* **1985,** *171,* 23-39.

[50] Kamerlingh Onnes, H. *Communications from the Physical Laboratory at Leiden* **1911,** *120b,*.

[51] Kamerlingh Onnes, H. *Proceedings of the Koninklijke Nederlandse Akademie van Wetenschappen 13,* 1274.

[52] Bardeen, J.; Cooper, L. N.; Schrieffer, J. R. *Physical Review* **1957,** *108,* 1175-1204.

[53] Cava, R. J.; Vandover, R. B.; Batlogg, B.; Rietman, E. A. *Physical Review Letters* **1987,** *58,* 408-410.

[54] Wu, M. K.; Ashburn, J. R.; Torng, C. J.; Hor, P. H.; Meng, R. L.; Gao, L.; Huang, Z. J.; Wang, Y. Q.; Chu, C. W. *Physical Review Letters* **1987,** *58,* 908-910.

[55] Hazen, R. M. *et al. Physical Review Letters* **1988,** *60,* 1174-1177.

[56] Tallon, J. L.; Buckley, R. G.; Gilberd, P. W.; Presland, M. R.; Brown, I. W. M.; Bowden, M. E.; Christian, L. A.; Goguel, R. *Nature* **1988,** *333,* 153-156.

[57] Hazen, R. M.; Finger, L. W.; Angel, R. J.; Prewitt, C. T.; Ross, N. L.; Hadidiacos, C. G.; Heaney, P. J.; Veblen, D. R.; Sheng, Z. Z.; El Ali, A.; Hermann, A. M. *Physical Review Letters* **1988,** *60,* 1657.

[58] Schilling, A.; Cantoni, M.; Guo, J. D.; Ott, H. R. *Nature* **1993,** *363,* 56-58.

[59] Tranquada, J. M.; Moudden, A. H.; Goldman, A. I.; Zolliker, P.; Cox, D. E.; Shirane, G.; Sinha, S. K.; Vaknin, D.; Johnston, D. C.; Alvarez, M. S.; Jacobson, A. J.; Lewandowski, J. T.; Newsam, J. M. *Physical Review B* **1988,** *38,* 2477-2485.

[60] Burger, J. P.; Zanoun, Y. *Materials Chemistry and Physics* **1992,** *32,* 177-182.

[61] Ren, Z. A.; Lu, W.; Yang, J.; Yi, W.; Shen, X. L.; Li, Z. C.; Che, G. C.; Dong, X. L.; Sun, L. L.; Zhou, F.; Zhao, Z. X. *Chinese Physics Letters* **2008,** *25,* 2215-2216.

[62] Hsu, F. C.; Luo, J. Y.; Yeh, K. W.; Chen, T. K.; Huang, T. W.; Wu, P. M.; Lee, Y. C.; Huang, Y. L.; Chu, Y. Y.; Yan, D. C.; Wu, M. K. *Proceedings of the National Academy of Sciences* **2008,** *105,* 14262-14264.

[63] Pitcher, M. J.; Parker, D. R.; Adamson, P.; Herkelrath, S. J. C.; Boothroyd, A. T.; Ibberson, R. M.; Brunelli, M.; Clarke, S. J. *Chemical Communications* **2008,** 5918-5920.

[64] Tapp, J. H.; Tang, Z. J.; Lv, B.; Sasmal, K.; Lorenz, B.; Chu, P. C. W.; Guloy, A. M. *Physical Review B* **2008,** *78,* 4.

[65] Zhu, X. Y.; Han, F.; Mu, G.; Cheng, P.; Shen, B.; Zeng, B.; Wen, H. H. *Physical Review B* **2009,** *79,* 4.

[66] Rotter, M.; Tegel, M.; Johrendt, D.; Schellenberg, I.; Hermes, W.; Pottgen, R. *Physical Review B* **2008,** *78,* 4.

[67] Chu, J. H.; Analytis, J. G.; Kucharczyk, C.; Fisher, I. R. *Physical Review B* **2009,** *79,* 014506.

[68] Drew, A. J. *et al. Nature Materials* **2009,** *8,* 310-314.

[69] Parker, D. R.; Smith, M. J. P.; Lancaster, T.; Steele, A. J.; Franke, I.; Baker, P. J.; Pratt, F. L.; Pitcher, M. J.; Blundell, S. J.; Clarke, S. J. *Physical Review Letters* **2010,** *104,* 057007.

[70] Torikachvili, M. S.; Bud'ko, S. L.; Ni, N.; Canfield, P. C. *Physical Review Letters* **2008,** *101,* 4.

[71] Park, T.; Park, E.; Lee, H.; Klimczuk, T.; Bauer, E. D.; Ronning, F.; Thompson, J. D. *Journal of Physics - Condensed Matter* **2008,** *20,* 3.

[72] Yu, W.; Aczel, A. A.; Williams, T. J.; Bud'ko, S. L.; Ni, N.; Canfield, P. C.; Luke, G. M. *Physical Review B* **2009,** *79,* 4.

[73] Uemura, Y. J. *Nature Materials* **2009,** *8,* 253-255.

[74] Radaelli, P. G.; Cox, D. E.; Marezio, M.; Cheong, S. W.; Schiffer, P. E.; Ramirez, A. P. *Physical Review Letters* **1995,** *75,* 4488-4491.

[75] Orchard, A. F. *Magnetochemistry;* Oxford Chemistry Primers Oxford University Press: 2003.

[76] Jacobs, I. S.; Lawrence, P. E. *Physical Review* **1967,** *164,* 866.

[77] Smura, C. F. *Part II Thesis,* Thesis, University of Oxford, 2004.

[78] Juza, R.; Langer, K. *Zeitschrift Fur Anorganische Und Allgemeine Chemie* **1968,** *361,* 58.

[79] Wang, X. C.; Liu, Q. Q.; Lv, Y. X.; Gao, W. B.; Yang, L. X.; Yu, R. C.; Li, F. Y.; Jin, C. Q. *Solid State Communications* **2008,** *148,* 538-540.

[80] Kreyssig, A. *et al. Physical Review B* **2008,** *78,* 6.

[81] Komatsuzaki, S.; Takase, K.; Smura, C. F.; Takahashi, Y.; Takano, Y.; Sekizawaa, K.; Clarke, S. J. *Journal of Alloys and Compounds* **2006,** *408,* 586-588.

[82] Smura, C. F. *D.Phil Thesis,* Thesis, University of Oxford, 2008.

[83] Von Dreele, R. B.; Larsen, A. C. *GSAS Technical Manual;* University of California: 2004.

[84] Clegg, W.; Blake, A. J.; Gould, R. O.; Main, P. *Crystal Structure Analysis;* Oxford University Press: 2001.

[85] Shull, C. G.; Strauser, W. A.; Wollan, E. O. *Physical Review* **1951,** *83,* 333.

[86] Rietveld, H. M. *Acta Crystallographica* **1967,** *22,* 151.

[87] Rietveld, H. M. *Journal of Applied Crystallography* **1969,** *2,* 65.

[88] Larson, A. C.; Von Dreele, R. B. *General Structure Analysis System (GSAS);* Los Alamos National Laboratory Report 86-748: 2004.

[89] Toby, B. H. *Journal of Applied Crystallography* **2001,** *34,* 210-221.

[90] Young, R. A., Ed.; *The Rietveld Method;* Oxford University Press: 1995.

[91] Thompson, S. P.; Parker, J. E.; Potter, J.; Hill, T. P.; Birt, A.; Cobb, T. M.; Yuan, F.; Tang, C. C. *Review of Scientific Instruments* **2009,** *80,* 9.

[92] Tartoni, N.; Thompson, S. P.; Tang, C. C.; Willis, B. L.; Derbyshire, G. E.; Wright, A. G.; Jaye, S. C.; Homer, J. M.; Pizzey, J. D.; Bell, A. M. T. *Journal of Synchrotron Radiation* **2008,** *15,* 43-49.

[93] *The ILL Yellow Book;* 2008.

[94] Smith, R. I.; Hull, S. *User Guide for the Polaris Diffractometer at ISIS;*.

[95] Caglioti, G.; Paoletti, A.; Ricci, F. P. *Nuclear Instruments and Methods* **1958,** *3,* 223-228.

[96] Smith, R. I. ISIS Neutron Training Course Manual. In ; Hannon, A. C., Ed.; 2010.

[97] Kuhs, W. F.; Hensel, E.; Bartels, H. *Journal of Physics: Condensed Matter* **2005,** *17,* 3009-3015.

[98] Sidorov, V. A.; Sadykov, R. A. *Journal of Physics - Condensed Matter* **2005,** *17,* 3005-3008.

[99] Klotz, S.; Chervin, J. C.; Munsch, P.; Le Marchand, G. *Journal of Physics D* **2009,** *42,* 7.

[100] Mito, M. *Journal of the Physical Society of Japan* **2007,** *76,* 182-185.

[101] Uemura, Y. J. *et al. Physical Review Letters* **1989,** *62,* 2317-2320.

[102] Uemura, Y. J.; Le, L. P.; Luke, G. M.; Sternlieb, B. J.; Wu, W. D.; Brewer, J. H.; Riseman, T. M.; Seaman, C. L.; Maple, M. B.; Ishikawa, M.; Hinks, D. G.; Jorgensen, J. D.; Saito, G.; Yamochi, H. *Physical Review Letters* **1991,** *66,* 2665-2668.

[103] Berdonosov, P. S.; Kusainova, A. M.; Kholodkovskaya, L. N.; Dolgikh, V. A.; Akselrud, L. G.; Popovkin, B. A. *Journal of Solid State Chemistry* **1995,** *118,* 74-77.

[104] Ueda, K.; Hiramatsu, H.; Hirano, M.; Kamiya, T.; Hosono, H. *Thin Solid Films* **2006,** *496,* 8-15.

[105] Hosono, H. *Thin Solid Films* **2007,** *515,* 6000-6014.

[106] Nakao, H.; Takano, Y.; Takase, K.; Sato, K.; Hara, S.; Ikeda, S.; Takahashi, Y.; Sekizawa, K. *Journal of Alloys and Compounds* **2006,** *408,* 104-106.

[107] Ueda, K.; Takafuji, K.; Hiramatsu, H.; Ohta, H.; Kamiya, T.; Hirano, M.; Hosono, H. *Chemistry of Materials* **2003,** *15,* 3692-3695.

[108] Takano, Y.; Nakao, H.; Takahashi, Y.; Takase, K.; Misawa, S.; Clarke, J.; Smura, C. F.; Sekizawa, K. *Journal of Alloys and Compounds* **2006,** *408,* 101-103.

[109] Ueda, K.; Takafuji, K.; Hosono, H. *Journal of Solid State Chemistry* **2003,** *170,* 182-187.

[110] Sato, H.; Nishimoto, S.; Takase, K.; Nakao, H.; Yoshikawa, K.; Higashi, M.; Taniguchi, M.; Negishi, H.; Negishi, S.; Takahashi, Y.; Takano, Y.; Sekizawa, K. *Physica Status Solidi C* **2006,** *3,* 2884-2887.

[111] Rutt, O. J. *D.Phil Thesis,* Thesis, University of Oxford, 2006.

[112] Smura, C. F.; Parker, D. R.; Zbiri, M.; Johnson, M. R.; Gal, Z. A.; Clarke, S. J. *Journal of the American Chemical Society* **2011,** *133,* 2691-2705.

[113] *Magnetic properties of transition metal compounds, supplement 2;* Landolt-Bornstein New Series II/10 Springer-Verlag: Berlin, 1979.

[114] Shackleton, C. M. L. *Part II Thesis,* Thesis, University of Oxford, 2010.

[115] Toby, B. H. "CMPR", 2005.

[116] Shirley, R. "Crysfire", 2004.

[117] Haggstrom, L.; Verma, H. R.; Bjarman, S.; Wappling, R.; Berger, R. *Journal of Solid State Chemistry* **1986,** *63,* 401-408.

[118] Bao, W.; Huang, Q.; Chen, G. F.; Green, M. A.; Wang, D. M.; He, J. B.; Wang, X. Q.; Qiu, Y. *arXiv 1102.0830v1* **2011,** .

[119] Ren, Z. A.; Che, G. C.; Dong, X. L.; Yang, J.; Lu, W.; Yi, W.; Shen, X. L.; Li, Z. C.; Sun, L. L.; Zhou, F.; Zhao, Z. X. *EPL* **2008,** *83,* 17002.

[120] Wang, C.; Li, L. J.; Chi, S.; Zhu, Z. W.; Ren, Z.; Li, Y. K.; Wang, Y. T.; Lin, X.; Luo, Y. K.; Jiang, S. A.; Xu, X. F.; Cao, G. H.; Xu, Z. A. *EPL* **2008,** *83,* 4.

[121] Fletcher, D. A.; McMeeking, R. F.; Parkin, D. *Journal of Chemical Information and Computer Sciences* **1996,** *36,* 746-749.

[122] Dong, J.; Zhang, H. J.; Xu, G.; Li, Z.; Li, G.; Hu, W. Z.; Wu, D.; Chen, G. F.; Dai, X.; Luo, J. L.; Fang, Z.; Wang, N. L. *EPL* **2008,** *83,* 4.

[123] McQueen, T. M.; Huang, Q.; Ksenofontov, V.; Felser, C.; Xu, Q.; Zandbergen, H.; Hor, Y. S.; Allred, J.; Williams, A. J.; Qu, D.; Checkelsky, J.; Ong, N. P.; Cava, R. J. *Physical Review B* **2009,** *79,* 7.

[124] Nuss, J.; Wedig, U.; Jansen, M. *Zeitschrift Fur Kristallographie* **2006,** *221,* 554-562.

[125] Li, S.; de la Cruz, C.; Huang, Q.; Chen, Y.; Lynn, J. W.; Hu, J.; Huang, Y.-L.; Hsu, F.-C.; Yeh, K.-W.; Wu, M.-K.; Dai, P. *Physical Review B* **2009,** *79,* 054503.

[126] Zhang, S. J.; Wang, X. C.; Sammynaiken, R.; Tse, J. S.; Yang, L. X.; Li, Z.; Liu, Q. Q.; Desgreniers, S.; Yao, Y.; Liu, H. Z.; Jin, C. Q. *Physical Review B* **2009,** *80,* 014506.

[127] Qi, Y. P.; Gao, Z. S.; Wang, L.; Wang, D. L.; Zhang, X. P.; Ma, Y. W. *New Journal of Physics* **2008,** *10,* 6.

[128] Zhao, J.; Huang, Q.; de la Cruz, C.; Li, S. L.; Lynn, J. W.; Chen, Y.; Green, M. A.; Chen, G. F.; Li, G.; Li, Z.; Luo, J. L.; Wang, N. L.; Dai, P. C. *Nature Materials* **2008,** *7,* 953-959.

[129] Lee, C. H.; Iyo, A.; Eisaki, H.; Kito, H.; Fernandez-Diaz, M. T.; Ito, T.; Kihou, K.; Matsuhata, H.; Braden, M.; Yamada, K. *Journal of the Physical Society of Japan* **2008,** *77,* 4.

[130] Artioli, G. A.; Malavasi, L.; Mozzati, M. C.; Fernandez, Y. D. *Journal of the American Chemical Society* **2009,** *131,* 12044-12045.

[131] Malavasi, L.; Artioli, G. A.; Ritter, C.; Mozzati, M. C.; Maroni, B.; Pahari, B.; Caneschi, A. *Journal of the American Chemical Society* **2010,** *132,* 2417-2420.

[132] Rotter, M.; Pangerl, M.; Tegel, M.; Johrendt, D. *Angewandte Chemie* **2008,** *47,* 7949-7952.

[133] Laplace, Y.; Bobroff, J.; Rullier-Albenque, F.; Colson, D.; Forget, A. *Physical Review B* **2009,** *80,* 4.

[134] Park, J. T. *et al. Physical Review Letters* **2009,** *102,* 4.

[135] Gang, X.; Cieplak, M. Z.; Xiao, J. Q.; Chien, C. L. *Physical Review B* **1990,** *42,* 8752-8755.

[136] Sefat, A. S.; Jin, R.; McGuire, M. A.; Sales, B. C.; Singh, D. J.; Mandrus, D. *Physical Review Letters* **2008,** *101,* 117004.

[137] Trevelyan Thomas, W. *Part II Thesis,* Thesis, University of Oxford, 2009.

[138] Bronger, W.; Muller, P.; Hoppner, R.; Schuster, H. U. *Zeitschrift Fur Anorganische Und Allgemeine Chemie* **1986,** *539,* 175-182.

[139] Matsuishi, S.; Inoue, Y.; Nomura, T.; Kamihara, Y.; Hirano, M.; Hosono, H. *New Journal of Physics* **2009,** *11,* 9.

[140] von Dreele, R. B.; Suchomel, M. R.; Toby, B. H. "Absorb", 2010.

[141] Todorov, I.; Chung, D. Y.; Claus, H.; Malliakas, C. D.; Douvalis, A. P.; Bakas, T.; He, J. Q.; Dravid, V. P.; Kanatzidis, M. G. *Chemistry of Materials* **2010,** *22,* 3916-3925.

[142] Shannon, R. D. *Acta Crystallographica A* **1976,** *32,* 751-767.

[143] Hill, R. J. *Journal of Applied Crystallography* **1992,** *25,* 589-610.

[144] Hill, R. J.; Cranswick, L. M. D. *Journal of Applied Crystallography* **1994,** *27,* 802-844.

[145] Parker, D. R.; Pitcher, M. J.; Baker, P. J.; Franke, I.; Lancaster, T.; Blundell, S. J.; Clarke, S. J. *Chemical Communications* **2009,** 2189-2191.

[146] Schuster, H. U.; Achenbach, G. *Zeitschrift Fur Naturforschung B* **1978,** *33,* 113-114.

[147] Canfield, P. C.; Bud'ko, S. L.; Ni, N.; Yan, J. Q.; Kracher, A. *Physical Review B* **2009,** *80,* 060501.

[148] Ni, N.; Thaler, A.; Kracher, A.; Yan, J. Q.; Bud'ko, S. L.; Canfield, P. C. *Physical Review B* **2009,** *80,* 024511.

[149] Zhang, M.; Zhang, C. J.; Yu, Y.; Zhang, L.; Qu, Z.; Ling, L. S.; Xi, C. Y.; Tan, S.; Zhang, Y. H. *New Journal of Physics* **2010,** *12,* 11.

[150] Kasinathan, D.; Ormeci, A.; Koch, K.; Burkhardt, U.; Schnelle, W.; Leithe-Jasper, A.; Rosner, H. *New Journal of Physics* **2009,** *11,* 27.

[151] Wadati, H.; Elfimov, I.; Sawatzky, G. A. *Physical Review Letters* **2010,** *105,* 4.

[152] Sawatzky, G. A. "Private communication", .

[153] Luetkens, H.; Klauss, H. H.; Khasanov, R.; Amato, A.; Klingeler, R.; Hellmann, I.; Leps, N.; Kondrat, A.; Hess, C.; Kohler, A.; Behr, G.; Werner, J.; Buchner, B. *Physical Review Letters* **2008,** *101,* 4.

[154] Drew, A. J.; Pratt, F. L.; Lancaster, T.; Blundell, S. J.; Baker, P. J.; Liu, R. H.; Wu, G.; Chen, X. H.; Watanabe, I.; Malik, V. K.; Dubroka, A.; Kim, K. W.; Rossle, M.; Bernhard, C. *Physical Review Letters* **2008,** *101,* 4.

[155] Pitcher, M. J.; Lancaster, T.; Wright, J. D.; Franke, I.; Steele, A. J.; Baker, P. J.; Pratt, F. L.; Thomas, W. T.; Parker, D. R.; Blundell, S. J.; Clarke, S. J. *Journal of the American Chemical Society* **2010,** *132,* 10467-10476.

[156] Pratt, F. L.; Baker, P. J.; Blundell, S. J.; Lancaster, T.; Lewtas, H. J.; Adamson, P.; Pitcher, M. J.; Parker, D. R.; Clarke, S. J. *Physical Review B* **2009,** *79,* 4.

[157] Khasanov, R.; Evtushinsky, D. V.; Amato, A.; Klauss, H. H.; Luetkens, H.; Niedermayer, C.; uuml,; chner, B.; Sun, G. L.; Lin, C. T.; Park, J. T.; Inosov, D. S.; Hinkov, V. *Physical Review Letters* **2009,** *102,* 187005.

[158] Pitcher, M. J.; Smura, C. F.; Clarke, S. J. *Inorganic Chemistry* **2009,** *48,* 9054-9056.

[159] Nekrasov, I. A.; Pchelkina, Z. V.; Sadovskii, M. V. *JETP Letters* **2008,** *87,* 560-564.

[160] Calderon, M. J.; Valenzuela, B.; Bascones, E. *New Journal of Physics* **2009,** *11,* 9.

[161] Zhao, J.; Huang, Q.; de la Cruz, C.; Li, S. L.; Lynn, J. W.; Chen, Y.; Green, M. A.; Chen, G. F.; Li, G.; Li, Z.; Luo, J. L.; Wang, N. L.; Dai, P. C. *Nature Materials* **2008,** *7,* 953-959.

[162] Kuroki, K.; Usui, H.; Onari, S.; Arita, R.; Aoki, H. *Physical Review B* **2009,** *79,* 224511.

[163] Yin, Z. P.; Lebegue, S.; Han, M. J.; Neal, B. P.; Savrasov, S. Y.; Pickett, W. E. *Physical Review Letters* **2008,** *101,* 4.

[164] Okada, H.; Igawa, K.; Takahashi, H.; Kamihara, Y.; Hirano, M.; Hosono, H.; Matsubayashi, K.; Uwatoko, Y. *Journal of the Physical Society of Japan* **2008,** *77,* 4.

[165] Takahashi, H.; Igawa, K.; Arii, K.; Kamihara, Y.; Hirano, M.; Hosono, H. *Nature* **2008,** *453,* 376-378.

[166] Takahashi, H.; Igawa, K.; Arii, K.; Kamihara, Y.; Hirano, M.; Hosono, H. *Nature* **2008,** *453,* 376-378.

[167] Zocco, D. A.; Hamlin, J. J.; Baumbach, R. E.; Maple, M. B.; McGuire, M. A.; Sefat, A. S.; Sales, B. C.; Jin, R.; Mandrus, D.; Jeffries, J. R.; Weir, S. T.; Vohra, Y. K. *Physica C* **2008,** *468,* 2229-2232.

[168] Yi, W.; Sun, L. L.; Ren, Z. A.; Lu, W.; Dong, X. L.; Zhang, H. J.; Dai, X.; Fang, Z.; Li, Z. C.; Che, G. C.; Yang, J.; Shen, X. L.; Zhou, F.; Zhao, Z. X. *EPL* **2008,** *83,* 4.

[169] Takeshita, N.; Iyo, A.; Eisaki, H.; Kito, H.; Ito, T. *Journal of the Physical Society of Japan* **2008,** *77,* 2.

[170] Gooch, M.; Lv, B.; Lorenz, B.; Guloy, A. M.; Chu, C.-W. *Physical Review B* **2008,** *78,* 180508.

[171] Mito, M.; Pitcher, M. J.; Crichton, W.; Garbarino, G.; Baker, P. J.; Blundell, S. J.; Adamson, P.; Parker, D. R.; Clarke, S. J. *Journal of the American Chemical Society* **2009,** *131,* 2986-2992.

[172] Birch, F. *Physical Review* **1947,** *71,* 809.

[173] Angel, R. J. Equations of state. In *High-Temperature and High-Pressure Crystal Chemistry*, Vol. 41; Mineralogical Soc America: 2000.

[174] Garbarino, G.; Toulemonde, P.; Alvarez-Murga, M.; Sow, A.; Mezouar, M.; Nunez-Regueiro, M. *Physical Review B* **2008,** *78,* 4.

[175] Margadonna, S.; Takabayashi, Y.; Ohishi, Y.; Mizuguchi, Y.; Takano, Y.; Kagayama, T.; Nakagawa, T.; Takata, M.; Prassides, K. *Physical Review B* **2009,** *80,* 064506.

[176] Gray, E. M.; Smith, R. I.; Pitt, M. P. *Journal of Applied Crystallography* **2007,** *40,* 399-408.

[177] Mito, M.; Hitaka, M.; Kawae, T.; Takeda, K.; Kitai, T.; Toyoshima, N. *Japanese Journal of Applied Physics* **2001,** *40,* 6641-6644.

[178] Gooch, M.; Lv, B.; Tapp, J. H.; Tang, Z.; Lorenz, B.; Guloy, A. M.; Chu, P. C. W. *EPL* **2009,** *85,* 3.

[179] Okabe, H.; Takeshita, N.; Horigane, K.; Muranaka, T.; Akimitsu, J. *Physical Review B* **2010,** *81,* 6.

[180] Kotegawa, H.; Kawazoe, T.; Tou, H.; Murata, K.; Ogino, H.; Kishio, K.; Shimoyama, J. *Journal of the Physical Society of Japan* **2009,** *78,* 4.

[181] Mittal, R.; Mishra, S. K.; Chaplot, S. L.; Ovsyannikov, S. V.; Greenberg, E.; Trots, D. M.; Dubrovinsky, L.; Su, Y.; Brueckel, T.; Matsuishi, S.; Hosono, H.; Garbarino, G. *Physical Review B* **2011,** *83,* 054503.

[182] Kumai, R.; Takeshita, N.; Ito, T.; Kito, H.; Iyo, A.; Eisaki, H. *Journal of the Physical Society of Japan* **2009,** *78,* 013705.

[183] Hammersley, A. P.; Svensson, S. O.; Hanfland, M.; Fitch, A. N.; Hausermann, D. *High Pressure Research* **1996,** *14,* 235-248.

[184] Hammersley, A. P. *ESRF Internal Report* **1997,** .

[185] Leinenweber, K. "Crystal Cracker", 2005.

[186] Shen, Y. R.; Englisch, U.; Chudinovskikh, L.; Porsch, F.; Haberkorn, R.; Beck, H. P.; Holzapfel, W. B. *Journal of Physics - Condensed Matter* **1994,** *6,* 3197-3206.

[187] Decremps, F.; Fischer, M.; Polian, A.; Itie, J. P.; Sieskind, M. *Physical Review B* **1999,** *59,* 4011-4022.

[188] Subramanian, N.; Shekar, N. V. C.; Sahu, P. C.; Yousuf, M.; Rajan, K. G. *Physical Review B* **1998,** *58,* R555-R558.

[189] Jeitschk.W,; Johnson, V. *Acta Crystallographica B* **1972,** *28,* 1971-1973.

[190] Tobola, J.; Bacmann, M.; Fruchart, B.; Wolfers, P.; Kaprzyk, S.; Koumina, A. A. *Journal of Alloys and Compounds* **2001,** *317,* 274-279.

[191] Jeitschk.W, *Acta Crystallographica A* **1969,** *25,* 815-822.

[192] Wang, X. C.; Liu, Q. Q.; Lv, Y. X.; Gao, W. B.; Yang, L. X.; Yu, R. C.; Li, F. Y.; Jin, C. Q. *arXiv:0806.4688v1* **2008,** .

[193] Zhang, L.; Singh, D. J.; Du, M. H. *Physical Review B* **2009,** *79,* 012506.

Appendix A: Diffuse Reflectance Spectroscopy on $CeCu_{1-x}OS$

Much of the previous research into CeCuOS (and *Ln*CuOS materials in general) is focused on the optical properties of this material. In order to assess the effect of variable Cu occupancy on these properties, diffuse reflectance spectra were measured using a Perkin Elmer Lambda 750S UV/visible/NIR spectrometer. A thin layer of each powder was pressed on to a KBr substrate using a 13 mm pellet die. Air exposure of the samples in the spectrometer could not be avoided, and it is therefore possible that some in-situ decomposition may have occurred in the stoichiometric and nearly-stoichiometric samples. The results for 3 samples in the range $250 \leq \lambda \leq 2500$ nm are illustrated in figure 7.1. It can be seen that, at short wavelengths ($\lambda \lesssim 500$ nm), the samples exhibit similar behaviour. In the visible region the fully stoichiometric and nearly-stoichiometric are less absorbing than the significantly Cu-deficient sample (consistent with their difference in colour), while at longer wavelengths in the near infra-red ($\lambda \gtrsim 1000$ nm, 1.24 eV) the Cu deficient samples are significantly more absorbing.

These results appear to be very similar to those reported by Ueda *et al.* [107] which are obtained from a sample which is likely to be significantly Cu-deficient (as discussed in section 3.1). These results are compared in figure 7.2. In contrast with LaCuOS, PrCuOS and NdCuOS, none of the samples of $CeCu_{(1-x)}OS$ reported here exhibit an absorption edge at 400 nm (3 eV). This is somewhat surprising, as a fully (or nearly) stoichiometric sample of CeCuOS might be expected to have very

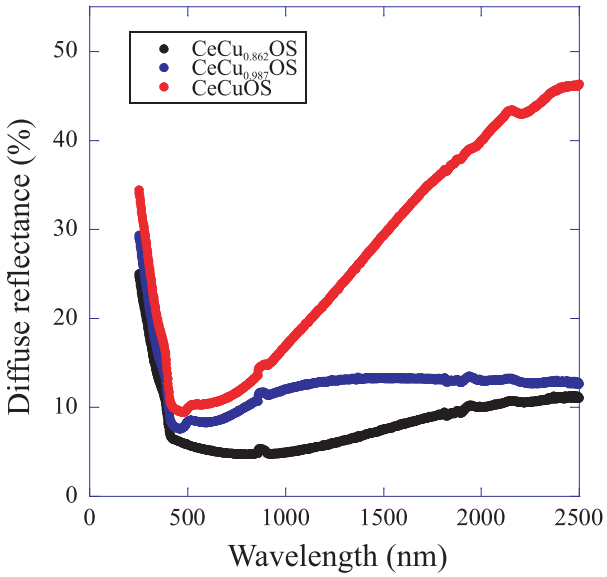


Figure 7.1: Diffuse reflectance spectra of Sample 1, 2 and B

similar optical properties to these materials. For a material of nominal composition $CeCu_{0.8}OS$, Chan *et al.* calculated that the band gap should be approximately 0.6 eV / 2000 nm, but this is not observed in a sample of $CeCu_{0.862(2)}OS$ in these experiments.

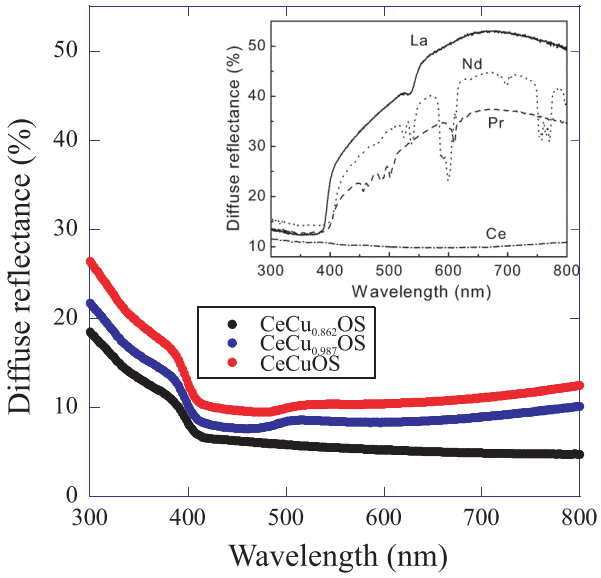
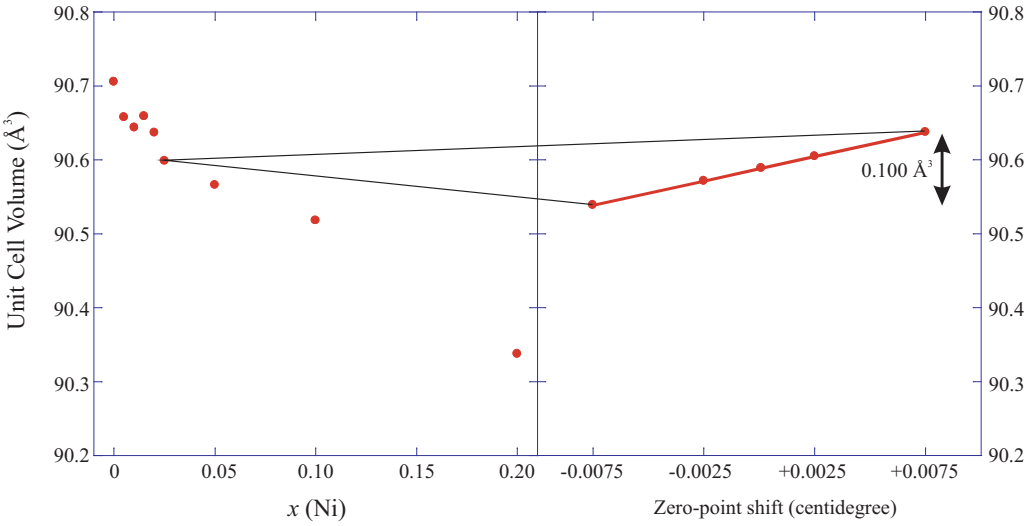


Figure 7.2: Diffuse reflectance spectra between $300 \leq \lambda \leq 800$ nm. Inset are results for other stoichiometric *Ln*CuOS from reference [107].

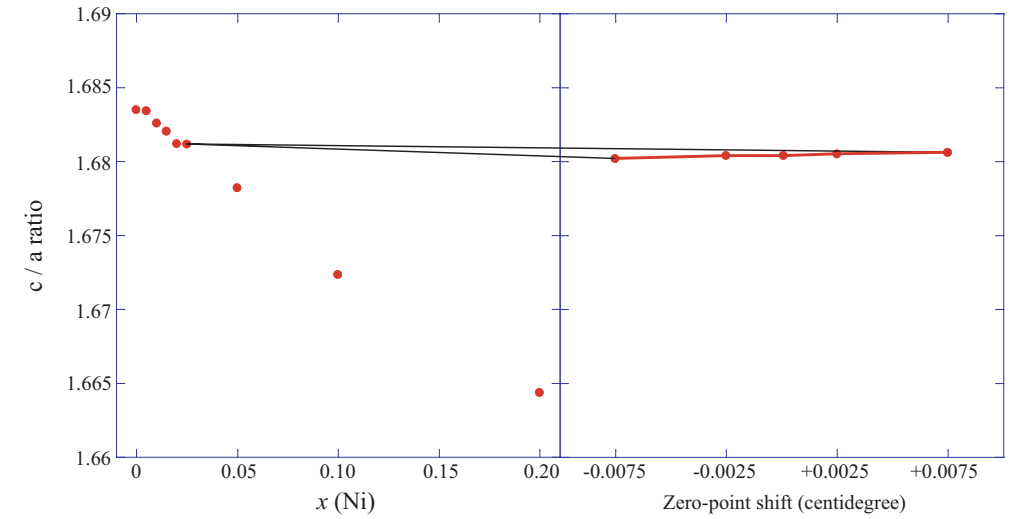
Appendix B: The Sensitivity of Refined Lattice Parameters to Zero-Point Errors in XRD Experiments on $LiFe_{1-x}Ni_xAs$

It is clear from the results detailed in Chapter 5 that the values obtained for unit cell volume by laboratory XRPD are highly sensitive to experimental conditions, which is especially important as the structural changes on Ni-substitution are small and the sample compositions are very closely spaces (i.e. x increasing in steps of 0.005). In order to quantify the effect of diffractogram zero-point on the unit cell volume and lattice parameter ratio c/a, the Si-calibrated Rietveld refinement for a sample with $x_{Ni} = 0.025$ was selected. This refinement was repeated with different fixed values for the "zero" diffractometer constant, with 2θ shifted by $-0.0075°$, $-0.0025°$, $+0.0025°$ and $+0.0075°$ while lattice parameters were refined freely.

The effects of these changes are illustrated in figures 7.3 and 7.4. It can be seen from figure 7.4 that modifying zero within these limits does not cause large changes in the quality of the refinement. For example, by any statistical measurement of refinement quality the difference between $2\theta_0 = +0.0025°$ and $2\theta_0 = +0.0075°$ is negligible, while negative shifts increase R_{wp} and χ^2 by only a very small amount. Visual inspection of the difference curve confirms this conclusion. However, consideration of the results in figure 7.3 indicates that these extremely small (or



(a) Effect of zero-point shift on refined unit cell volume



(b) c / a ratio

Figure 7.3: Effect of small zero-point shifts on unit cell volumes and c/a ratio (original values reported in Chapter 5), showing the strong dependence of unit cell volume and weak dependence of c/a on zero-point error.

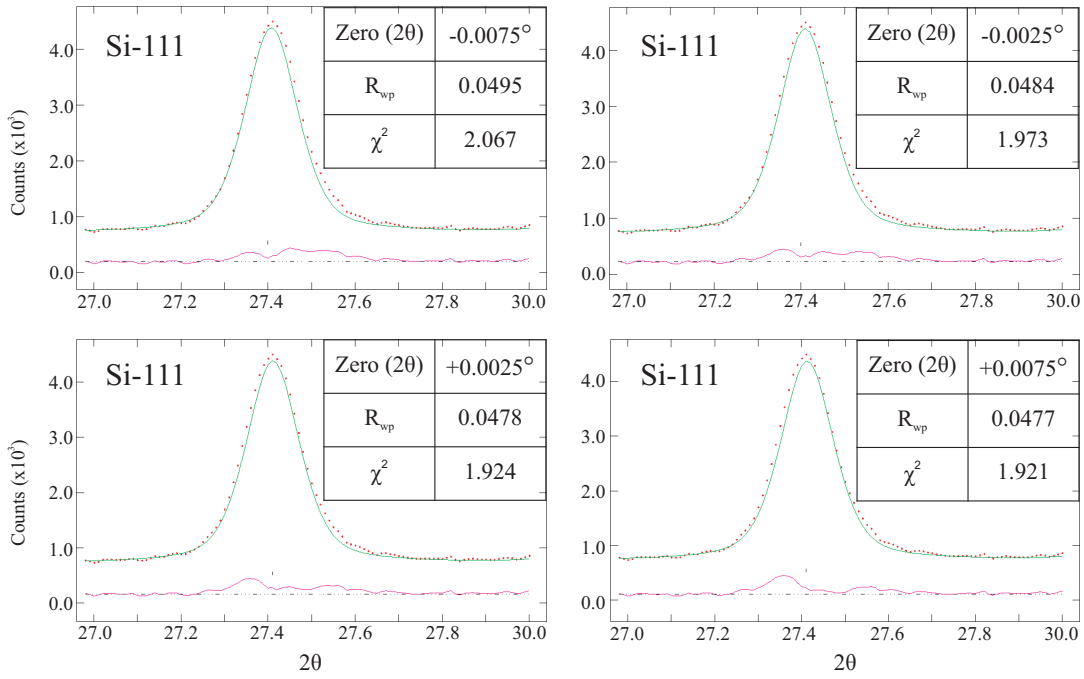


Figure 7.4: Effect of zero-point changes on the fit to the Si 111 peak.

negligible) differences in refinement quality correspond to significant variations in the values obtained for unit cell volume. It can be seen that the difference between the two extremes considered here ($\pm 0.0075°$) corresponds to a difference of 0.100 Å^3: this is approximately equal to the decrease in unit cell volume between $x_{Ni} = 0$ and $x_{Ni} = 0.025$, encompassing 6 samples. It is unlikely that the true uncertainty in zero point is as high as $\pm 0.0075°$, as the data appear to follow a reasonably well-behaved trend. A more modest uncertainty of $\pm 0.0012°$ would be enough to change the refined unit cell volume by approximately ± 0.01 Å^3, which is large enough to obscure the differences between adjacent samples in the low-doping region $0 \leq x_{Ni} \leq 0.025$.

Comparison of these results with the response of the c/a ratio is enlightening: figure 7.3 shows that the ratio of refined parameters c/a is far less sensitive to changes in $2\theta_0$. For this parameter, a significant change in $2\theta_0$ of ± 0.0050 would change c/a by ± 0.0001, which is comparable to the estimated standard deviation calculated by GSAS. Hence, the observation of a well-behaved trend in c/a ratio and a less smooth trend in unit cell volume can be explained by small differences in diffraction geometry (due to slightly differing sample heights).

Appendix C: Structural Parameters of Two Samples of $CeCu_{1-x}OS$ from NPD Experiments

Table 7.1: Refined lattice parameters and *R*-factors.

Sample	Sample 1 $CeCu_{0.987(2)}OS$	Sample 2 $CeCu_{0.862(2)}OS$
Instrument	POLARIS	
Temperature / K	295	
Space Group	*P4/nmm*	
a / Å	3.95828(2)	3.92759(9)
c / Å	8.45071(5)	8.3596(2)
V / Å^3	132.405(1)	128.955(5)
c/a	2.135	2.128
Z	2	
R_{wp} (145° bank)	0.0135	0.0172
R_{F^2} (145° bank)	0.0552	0.0554
R_{wp} (90° bank)	0.0224	0.0250
R_{F^2} (90° bank)	0.0793	0.0952
R_{wp} (35° bank)	0.0483	0.0496
R_{F^2} (35° bank)	0.0971	0.1303
χ^2	8.871	

Table 7.2: Refined atomic coordinates for $CeCu_{0.987(2)}OS$ (Sample 1).

Atom	Site	x	y	z	$(U_{eq}$ / Å$^2)\times 100$	Occupancy
Ce	2*c*	0.25	0.25	0.14725(5)	0.46	1[a]
Cu	2*b*	0.25	0.75	0.5	1.80	0.987(2)
S	2*c*	0.25	0.25	0.66608(8)	0.92	1[a]
O	2*a*	0.25	0.75	0	0.57	1[a]

[a] Not refined

Table 7.3: Refined atomic displacement factors for Sample 1 (/ Å$^2)\times 100$.

Atom	U_{11} $(= U_{22})$	U_{33}
Ce	0.435(9)	0.52(1)
Cu	1.88(1)	1.65(2)
S	0.89(2)	0.99(4)
O	0.469(7)	0.78(1)

Table 7.4: Refined atomic coordinates for $CeCu_{0.862(2)}OS$ (Sample 2).

Atom	Site	x	y	z	$(U_{eq}$ / Å$^2)\times 100$	Occupancy
Ce	2*c*	0.25	0.25	0.15159(9)	0.60	1[a]
Cu	2*b*	0.25	0.75	0.5	1.88	0.862(2)
S	2*c*	0.25	0.25	0.66903(1)	1.07	1[a]
O	2*a*	0.25	0.75	0	0.70	1[a]

[a] Not refined

Table 7.5: Refined atomic displacement factors for Sample 2 (/ Å^2)$\times$100.

Atom	U_{11} (= U_{22})	U_{33}
Ce	0.52(2)	0.78(2)
Cu	2.20(2)	1.24(3)
S	1.05(3)	1.12(6)
O	0.57(1)	0.95(3)

Appendix D: Structural Parameters of the Series $Li_{1-y}Fe_{1+y}As$ from joint XRPD-NPD Experiments

Table 7.6: Summary of joint NPD-XRPD Rietveld refinement for LiFeAs "Sample 2" at 295 K, and individual refinements against NPD data at 295 K and 6.5 K (HRPD diffractometer).

Instrument(s)	Joint HRPD + ID31	HRPD	HRPD
Temperature / K	295	295	6.5
Space Group	*P4/nmm*		
a / Å	3.776360(4)	3.77543(3)	3.76982(4)
c / Å	6.35679(1)	6.35345(6)	6.30693(7)
V / Å^3	90.6536(2)	90.561(1)	89.631(2)
R_{wp}	0.0521	0.0389	0.0304
χ^2	10.07	7.035	8.115

Table 7.7: Refined atomic parameters for LiFeAs (Sample 2) at 295 K, from joint refinement against NPD and synchrotron XRPD data.

Atom	Site	x	y	z	U_{equiv} / Å$^2 \times 100$	Occupancy
Fe	2*a*	0.75	0.25	0	0.68(1)	1[a]
Li	2*c*	0.25	0.25	0.6536(2)	1.78(5)	0.997(4)
As	2*c*	0.25	0.25	0.23715(3)	0.74(1)	0.995(1)

[a]Not refined

Table 7.8: Refined atomic parameters for LiFeAs (Sample 2) at 295 K (upper figures) and 6.5 K (lower figures) obtained by refinement against NPD data (HRPD diffractometer).

Atom	Site	x	y	z	U_{equiv} / Å$^2 \times 100$	Occupancy
Fe	2*a*	0.75	0.25	0	0.68(1)	1[a]
					0.18(1)	1[a]
Li	2*c*	0.25	0.25	0.6536(2)	1.78(5)	0.963(4)
				0.6554(2)	0.77(6)	0.950(4)
As	2*c*	0.25	0.25	0.23715(3)	0.74(1)	0.995(1)
				0.23646(5)	0.12(1)	0.976(1)

[a]Not refined

Table 7.9: Refined anisotropic displacement parameters for LiFeAs (Sample 2) at 295 K, from joint refinement against NPD and synchrotron XRPD data.

Atom	$U_{11}(=U_{22})$ / Å$^2 \times 100$	U_{33} / Å$^2 \times 100$
Fe	0.609(6)	0.835(8)
Li	2.03(4)	1.29(6)
As	0.769(5)	0.673(8)

Table 7.10: Refined anisotropic displacement parameters for LiFeAs (Sample 2) at 295 K (upper figures) and 6.5 K (lower figures) obtained by refinement against NPD data (HRPD diffractometer).

Atom	$U_{11}(=U_{22})$ / Å$^2 \times 100$	U_{33} / Å$^2 \times 100$
Fe	0.580(8) 0.184(7)	0.82(1) 0.177(9)
Li	1.95(4) 0.90(4)	0.94(6) 0.50(6)
As	0.535(9) 0.089(9)	0.80(2) 0.18(1)

Table 7.11: Summary of refinement for LiFeAs (Sample 1) against NPD data at 295 K (POLARIS diffractometer).

Instrument	POLARIS
Temperature / K	295
Space Group	*P4/nmm*
a / Å	3.7773(7)
c / Å	6.3565(1)
V / Å^3	90.696(5)
R_{wp}	0.0264
χ^2	0.7325

Table 7.12: Refined atomic parameters for LiFeAs (Sample 1) at 295 K from NPD data (POLARIS diffractometer).

Atom	Site	x	y	z	U_{equiv} / Å$^2 \times 100$	Occupancy
Fe	2*a*	0.75	0.25	0	0.65(2)	1[a]
Li	2*c*	0.25	0.25	0.6551(4)	1.77(9)	0.99(1)
As	2*c*	0.25	0.25	0.23654(9)	0.65(2)	0.977(3)

[a]Not refined

Table 7.13: Refined anisotropic displacement parameters for LiFeAs (Sample 1) at 295 K from NPD data (POLARIS diffractometer).

Atom	$U_{11}(=U_{22})$ / Å$^2 \times 100$	U_{33} / Å$^2 \times 100$
Fe	0.66(1)	0.64(2)
Li	2.13(8)	1.1(1)
As	0.63(2)	0.70(3)

Table 7.14: Refined bond lengths (Å) and angles (degrees) for LiFeAs Sample 1 and Sample 2. Table includes joint refinements against NPD and synchrotron XRPD data (Sample 2 only); and individual refinements against NPD data from HRPD (Sample 2) and POLARIS (Sample 1).

Distance or Angle	Sample 2			Sample 1
	Joint 295 K	HRPD 295 K	HRPD 6.5 K	POLARIS 295 K
Fe-As [4][a]	2.4162(1)	2.4141(2)	2.4035(2)	2.4141(3)
Li-As [4]	2.7592(3)	2.7585(3)	2.7515(3)	2.7584(6)
Li-As [1]	2.647(1)	2.6493(9)	2.642(1)	2.661(2)
Fe-Fe [4]	2.67029(1)	2.66963(2)	2.66566(3)	2.67098(5)
Li-Fe [4]	2.9008(8)	2.8984(7)	2.8767(8)	2.894(2)
Li-Li [4]	3.308(1)	3.309(1)	3.309(1)	3.320(3)
As-Fe-As [4]	112.910(3)	112.865(5)	112.643(6)	112.83(1)
As-Fe-As [2]	102.793(6)	102.88(1)	103.30(1)	102.95(2)
As-Li-As [4]	104.58(2)	104.58(2)	104.35(2)	104.46(5)
As-Li-As [4]	86.37(1)	86.37(1)	86.48(1)	86.43(3)

[a] The number in square brackets indicates the number of symmetry equivalent bond lengths/angles.

Table 7.15: Results of joint XRD-NPD refinements on the series $Li_{1-y}Fe_{1+y}As$.

y (nominal)	0.000	0.000	0.010	0.020	0.030	0.040	0.050
y (refined)	-0.001(1)	0.004(1)	-0.002(1)	0.010(1)	0.018(1)	0.007(1)	0.040(1)
Sample ID	MP127	MP98	MP142	MP143	MP144	MP145	MP129
Radiation	Combined Neutron - Synchrotron X-ray						
Instruments	POLARIS - I11	HRPD - I11	HRPD - I11	HRPD - I11	HRPD - I11	HRPD - I11	POLARIS - I11
T / K	295						
Space Group	*P4/nmm*						
a / Å	3.776840(2)	3.775280(2)	3.776047(2)	3.77377(5)	3.772561(5)	3.773962(3)	3.768861(2)
c / Å	6.35589(1)	6.351610(11)	6.35540(1)	6.34850(2)	6.34513(3)	6.34994(2)	6.333277(11)
V / Å	90.664(0)	90.528(0)	90.619(0)	90.411(1)	90.305(1)	90.441(0)	89.960(0)
Z	2						
R_{wp}	0.0453	0.0534	0.0386	0.0437	0.0401	0.0379	0.0563
R_{F^2}	0.0664	0.0455	0.0506	0.0499	0.0533	0.0420	0.0576
χ^2	4.035	4.929	5.686	4.244	7.169	5.441	3.127

Table 7.16: Refined atomic parameters for the series $Li_{1-y}Fe_{1+y}As$, derived from joint XRD-NPD experiments.

	y (nominal)	0.000	0.000	0.010	0.020	0.030	0.040	0.050
	y (refined)	-0.001(1)	0.004(1)	-0.002(1)	0.010(1)	0.018(1)	0.007(1)	0.040(1)
	Sample ID	MP127	MP98	MP142	MP143	MP144	MP145	MP129
	Instruments	POLARIS - I11	HRPD - I11	HRPD - I11	HRPD - I11	HRPD - I11	HRPD - I11	POLARIS - I11
Atom / Site	Parameter							
Li $(1/4, 1/4, z)$	z	0.6580(2)	0.6535(1)	0.6545(1)	0.6529(1)	0.6525(1)	0.6538(1)	0.6551(2)
	Occupancy[a]	1.001(1)	0.996(0)	1.002(1)	0.990(1)	0.982(1)	0.993(0)	0.960(1)
	$100 \times U_{11}$	1.61(2)	1.83(3)	2.22(4)	2.57(5)	2.35(5)	2.49(4)	1.68(4)
	$100 \times U_{33}$	2.72(6)	0.78(4)	1.25(6)	1.08(7)	0.82(7)	1.08(6)	1.60(7)
Fe1 $(1/4, 1/4, 0)$	$100 \times U_{11}$	0.633(5)	0.438(5)	0.531(8)	0.646(9)	0.553(8)	0.665(7)	0.567(5)
	$100 \times U_{33}$	1.248(7)	0.730(7)	0.591(9)	0.872(11)	0.899(11)	0.780(9)	0.955(8)
Fe2 $(1/4, 1/4, z)$	z	0.6578(2)	0.6535(1)	0.6545(1)	0.6529(1)	0.6525(1)	0.6538(1)	0.6551(2)
	Occupancy[a]	-0.001(1)	0.004(0)	-0.002(1)	0.010(1)	0.018(1)	0.007(0)	0.04(1)
	$100 \times U_{11}$	1.61(2)	1.83(3)	2.22(4)	2.57(5)	2.35(5)	2.49(4)	1.68(7)
	$100 \times U_{33}$	2.72(6)	0.78(4)	1.25(6)	1.08(7)	0.82(7)	1.08(6)	1.60(7)
As $(1/4, 1/4, x)$	x	0.23688(4)	0.23700(3)	0.23671(3)	0.23736(4)	0.23763(4)	0.23737(4)	0.23831(3)
	$100 \times U_{11}$	0.764(6)	0.622(6)	0.782(8)	0.842(10)	0.814(9)	0.914(8)	0.651(6)
	$100 \times U_{33}$	1.570(11)	0.810(9)	0.775(11)	1.208(14)	1.189(14)	1.028(12)	1.123(11)

[a] Total site occupancy of Li / Fe2 is restrained to 1

Table 7.17: Refined inter-atomic distances (Å) and angles (degrees) for the series $Li_{1-y}Fe_{1+y}As$, derived from joint XRD-NPD experiments.

y (nominal)	0.000	0.000	0.010	0.020	0.030	0.040	0.050
y (refined)	-0.001(1)	0.004(1)	-0.002(1)	0.010(1)	0.018(1)	0.007(1)	0.040(1)
Sample ID	MP127	MP98	MP142	MP143	MP144	MP145	MP129
Instruments	POLARIS - I11	HRPD - I11	HRPD - I11	HRPD - I11	HRPD - I11	HRPD - I11	POLARIS - I11
Fe-Fe [4]	2.67063(0)	2.66953(0)	2.67007(0)	2.66846(0)	2.66760(0)	2.66859(0)	2.66499(0)
Fe-As [4]	2.4151(2)	2.4144(1)	2.4141(1)	2.4147(2)	2.4149(2)	2.4151(1)	2.4143(1)
Li-As [1]	2.667(1)	2.646(1)	2.655(1)	2.638(1)	2.633(1)	2.645(1)	2.640(1)
Li-As [4]	2.7529(3)	2.7586(2)	2.7581(2)	2.7579(3)	2.7571(3)	2.7566(2)	2.7491(4)
Li-As (mean)	2.7377	2.7360	2.7376	2.7338	2.7320	2.7341	2.7273
As-Fe-As [2]	102.871(9)	102.858(7)	102.903(8)	102.779(10)	102.725(10)	102.766(8)	102.617(8)
As-Fe-As [4]	112.869(5)	112.876(4)	112.852(4)	112.918(5)	112.946(5)	112.924(4)	113.003(4)
As-Li-As [4]	86.62(1)	86.36(1)	86.39(1)	86.34(1)	86.34(1)	86.40(1)	86.55(1)
As-Li-As [4]	104.05(2)	104.60(2)	104.52(2)	104.64(2)	104.64(2)	104.52(2)	104.21(3)
As-Li-As [2]	151.91(5)	150.80(3)	150.96(3)	150.73(4)	150.72(4)	150.97(3)	151.58(6)

Appendix E: Structural Parameters of Three Series of $LiFe_{1-x}M_xAs$ from XRPD and NPD Experiments

Table 7.18: Lattice parameters from the series $LiFe_{1-x}Co_xAs$, derived from Rietveld refinement against synchrotron XRPD and joint XRPD-NPD data.

x (nominal)	0.000	0.025	0.050	0.75	0.100	0.150	0.200
Sample ID	MP127	MP151	MP152	MP171	WTT9	MP161	WTT19
Radiation	Combined Neutron-XRD	Synchrotron X-ray	Synchrotron X-ray	Synchrotron X-ray	Synchrotron X-ray	Combined Neutron-XRD	Combined Neutron-XRD
Instrument(s)	POLARIS - I11	I11	I11	I11	ID31	POLARIS - I11	POLARIS - ID31
T / K	295						
Space Group	*P4/nmm*						
a / Å	3.776840(2)	3.777858(4)	3.778905(4)	3.779206(4)	3.78105(1)	3.781453(1)	3.783230(7)
c / Å	6.35589(1)	6.35021(1)	6.34237(1)	6.33216(1)	6.32658(3)	6.30989(1)	6.29562(2)
V / Å	90.664(0)	90.632(0)	90.570(0)	90.438(0)	90.447(1)	90.228(0)	90.108(0)
Z	2						
R_{wp}	0.0453	0.0558	0.0763	0.0776	0.1055	0.0580	0.0479
R_{F^2}	0.0664	0.0647	0.0967	0.0544	0.0487	0.0608	0.0395
χ^2	4.035	6.844	6.922	5.630	1.790	6.407	1.867

Table 7.19: Atomic coordinates from the series $LiFe_{1-x}Co_xAs$, derived from Rietveld refinement against synchrotron XRPD and joint XRPD-NPD data.

	x (nominal)	0.000	0.025	0.050	0.75	0.100	0.150	0.200
	Sample ID	MP127	MP151	MP152	MP171	WTT9	MP161	WTT19
	Radiation	Combined Neutron-XRD	Synchrotron X-ray	Synchrotron X-ray	Synchrotron X-ray	Combined Neutron-XRD	Combined Neutron-XRD	Combined Neutron-XRD
	Instrument(s)	POLARIS - I11	I11	I11	I11	HRPD-ID31	POLARIS - I11	POLARIS - ID31
	λ_{XRD} (Å)	0.82720	0.60036	0.60036	0.60036	0.39940	0.60095	0.39940
Atom	Parameter							
Li ($1/4\ 1/4\ z$)	z-coordinate	0.6580(2)	0.6557(8)	0.6641(8)	0.6521(7)	0.6548(2)	0.6569(3)	0.6580(1)
	$100\times U_{iso}$	2.0(1)	1.8(1)	1.8(1)	2.1(1)	1.6(1)	1.6(1)	1.6(1)
	$100\times U_{11}$	1.61(2)	-	-	-	1.31(4)	1.67(4)	1.63(2)
	$100\times U_{33}$	2.72(6)	-	-	-	2.23(8)	1.41(7)	1.55(4)
Fe ($3/4\ 1/4\ 0$)	Occupancy[a]	1.000	0.975	0.950	0.925	0.917(2)	0.857(3)	0.812(1)
	$100\times U_{11}$	0.633(5)	0.193(9)	0.155(8)	0.435(1)	0.440(7)	0.474(7)	0.590(5)
	$100\times U_{33}$	1.248(7)	0.233(15)	0.112(15)	0.54(2)	1.14(1)	0.69(1)	0.834(7)
Co ($3/4\ 1/4\ 0$)	Occupancy[a]	0.000	0.025	0.050	0.075	0.083(2)	0.143(3)	0.188(1)
	$100\times U_{11}$	-	0.193(9)	0.155(8)	0.435(1)	0.440(7)	0.474(7)	0.590(5)
	$100\times U_{33}$	-	0.233(15)	0.112(15)	0.54(2)	1.14(1)	0.69(1)	0.834(7)
As ($1/4\ 1/4\ y$)	y-coordinate	0.23688(4)	0.23645(6)	0.23586(4)	0.23573(4)	0.23581(4)	0.23480(4)	0.23433(3)
	$100\times U_{11}$	0.764(6)	0.358(7)	0.287(6)	0.674(8)	0.471(6)	0.473(7)	0.639(4)
	$100\times U_{33}$	1.570(11)	0.323(13)	0.117(12)	0.69(1)	1.13(2)	0.692(10)	0.910(8)

[a] Fe/Co site occupancy refined only for combined PND-XRD experiments.

Table 7.20: Bond distances and angles from the series $LiFe_{1-x}Co_xAs$, derived from Rietveld refinement against synchrotron XRPD and joint XRPD-NPD data.

x (nominal)	0.000	0.025	0.050	0.75	0.100	0.150	0.200
Sample ID	MP127	MP151	MP152	MP171	WTT9	MP161	WTT19
Radiation	Combined Neutron-XRD	Synchrotron X-ray	Synchrotron X-ray	Synchrotron X-ray	Combined Neutron-XRD	Combined Neutron-XRD	Combined Neutron-XRD
Instrument(s)	POLARIS - I11	I11	I11	I11	HRPD-ID31	POLARIS - I11	POLARIS - ID31
λ_{XRD} (Å)	0.82720	0.60036	0.60036	0.60036	0.39940	0.60095	0.39940
Bond Distance / Å							
Fe-Fe [4]	2.67063(0)	2.67135(0)	2.67209(0)	2.67230(0)	2.67360(1)	2.67389(0)	2.67515(0)
Fe-As [4]	2.4151(2)	2.4130(2)	2.4099(2)	2.4081(2)	2.4100(2)	2.4021(2)	2.3989(1)
Li-As [1]	2.677(1)	2.662(5)	2.716(5)	2.637(5)	2.6504(15)	2.664(2)	2.6675(8)
Li-As [4]	2.7529(3)	2.758(1)	2.7463(12)	2.7651(12)	2.7619(4)	2.7598(4)	2.7597(2)
Li-As (mean)	2.738	2.739	2.740	2.739	2.740	2.7406	2.7512
Bond Angle / °							
As-Fe-As [2]	102.871(9)	103.038(10)	103.262(10)	103.386(9)	103.341(10)	103.835(9)	104.100(6)
As-Fe-As [4]	112.869(5)	112.781(5)	112.662(5)	112.597(5)	112.620(5)	112.361(5)	112.222(3)
As-Li-As [4]	86.62(1)	86.46(5)	86.94(5)	86.22(5)	86.405(16)	86.49(2)	86.543(9)
As-Li-As [4]	104.05(2)	104.38(10)	103.35(11)	104.88(9)	104.502(32)	104.33(3)	104.22(2)
As-Li-As [2]	151.91(5)	151.24(19)	153.30(21)	150.23(19)	151.00(6)	151.34(7)	151.57(4)

Table 7.21: Lattice parameters from the series $LiFe_{1-x}Ni_xAs$, derived from Rietveld refinement against synchrotron XRPD and joint XRPD-NPD data.

x (nominal)	0.000	0.005	0.010	0.015	0.020	0.025	0.050	0.100	0.200
Sample ID	MP127	MP159	MP156	MP157	MP158	MP155	MP160	WTT31	WTT42
Radiation	Combined Neutron-XRD	Neutron	Synchrotron X-ray	Neutron	Neutron	Neutron	Neutron	Neutron	Neutron
Instrument(s)	POLARIS-I11	POLARIS	I11	POLARIS	POLARIS	POLARIS	POLARIS	POLARIS	POLARIS
T / K	295								
Space Group	*P4/nmm*								
a / Å	3.776840(2)	3.77562(2)	3.77775(1)	3.77690(2)	3.77732(2)	3.7777(2)	3.77931(2)	3.78408(3)	3.78686(4)
c / Å	6.35589(1)	6.35269(4)	6.35460(2)	6.35051(4)	6.34849(5)	6.34710(4)	6.33938(4)	6.32770(5)	6.30122(7)
V / Å	90.664(0)	90.559(2)	90.689(1)	90.590(1)	90.581(2)	90.579(2)	90.547(1)	90.608(2)	90.361(2)
Z	2								
R_{wp}	0.0453	0.0223	0.0547	0.0218	0.0221	0.0250	0.0217	0.0234	0.0217
R_{F^2}	0.0664	0.0449	0.0765	0.0472	0.0474	0.0465	0.0494	0.0541	0.0688
χ^2	4.035	1.565	5.081	1.582	1.584	2.044	2.089	0.9778	0.8609

Table 7.22: Atomic coordinates from the series $LiFe_{1-x}Ni_xAs$, derived from Rietveld refinement against synchrotron XRPD and joint XRPD-NPD data.

	x (nominal)	0.000	0.005	0.010	0.015	0.020	0.025	0.050	0.100	0.200
	Sample ID	MP127	MP159	MP156	MP157	MP158	MP155	MP160	WTT31	WTT42
	Radiation	Combined Neutron-XRD	Neutron	X-ray	Neutron	Neutron	Neutron	Neutron	Neutron	Neutron
	Instrument(s)	POLARIS-I11	POLARIS	I11	POLARIS	POLARIS	POLARIS	POLARIS	POLARIS	POLARIS
	λ_{XRD} (Å)	0.82720	-	0.60036	-	-	-	-	-	-
Atom	Parameter									
Li ($1/4\ 1/4\ z$)	z-coordinate	0.6580(2)	0.6556(1)	0.665(1)	0.6560(1)	0.6560(1)	0.6560(1)	0.6564(1)	0.6572(2)	0.6596(3)
	$100\times U_{iso}$	2.0(1)	1.6(1)	1.8(2)	1.7(1)	1.6(1)	1.6(1)	1.7(1)	1.7(1)	1.9(1)
	$100\times U_{11}$	1.61(2)	1.75(2)	-	1.74(2)	1.75(2)	1.72(2)	1.72(2)	1.69(3)	1.69(4)
	$100\times U_{33}$	2.72(6)	1.38(4)	-	1.47(4)	1.43(4)	1.46(4)	1.59(4)	1.73(5)	2.45(9)
Fe ($3/4\ 1/4\ 0$)	Occupancy[a]	1.000	0.995	0.990	0.985	0.980	0.975	0.950	0.900	0.800
	$100\times U_{11}$	0.633(5)	0.585(5)	0.48(2)	0.589(5)	0.584(5)	0.575(5)	0.580(4)	0.598(6)	0.584(8)
	$100\times U_{33}$	1.248(7)	0.753(6)	0.51(3)	0.759(6)	0.770(6)	0.801(6)	0.809(6)	0.828(8)	1.11(1)
Ni ($3/4\ 1/4\ 0$)	Occupancy[a]	0.000	0.005	0.010	0.015	0.020	0.025	0.050	0.100	0.200
	$100\times U_{11}$	-	0.585(5)	0.48(2)	0.589(5)	0.584(5)	0.575(5)	0.580(4)	0.598(6)	0.584(8)
	$100\times U_{33}$	-	0.753(6)	0.51(3)	0.759(6)	0.770(6)	0.801(6)	0.809(6)	0.828(8)	1.11(1)
As ($1/4\ 1/4\ y$)	y-coordinate	0.23688(4)	0.23664(3)	0.23659(7)	0.23653(3)	0.23645(3)	0.23642(3)	0.23606(3)	0.23578(4)	0.23550(7)
	$100\times U_{11}$	0.764(6)	0.685(6)	0.644(15)	0.684(6)	0.677(6)	0.670(6)	0.642(5)	0.686(8)	0.614(10)
	$100\times U_{33}$	1.570(11)	0.84(1)	0.81(3)	0.84(1)	0.84(1)	0.87(1)	0.86(1)	0.87(1)	1.18(2)

Table 7.23: Bond distances and angles from the series $LiFe_{1-x}Ni_xAs$, derived from Rietveld refinement against synchrotron XRPD and joint XRPD-NPD data.

x (nominal)	0.000	0.005	0.010	0.015	0.020	0.025	0.050	0.100	0.200
Sample ID	MP127	MP159	MP156	MP157	MP158	MP155	MP160	WTT31	WTT42
Radiation	Combined Neutron-XRD	Neutron	X-ray	Neutron	Neutron	Neutron	Neutron	Neutron	Neutron
Instrument(s)	POLARIS - I11	POLARIS	I11	POLARIS	POLARIS	POLARIS	POLARIS	POLARIS	POLARIS
λ_{XRD} (Å)	0.82720	-	0.60036	-	-	-	-	-	-
Bond Distance / Å									
Fe-Fe [4]	2.67063(0)	2.66977(2)	2.67084(1)	2.67067(2)	2.67096(2)	2.67124(2)	2.67238(1)	2.67575(2)	2.67772(3)
Fe-As [4]	2.4151(2)	2.4133(1)	2.4138(3)	2.4130(1)	2.4125(1)	2.4124(1)	2.4104(1)	2.4095(2)	2.4056(3)
Li-As [1]	2.677(1)	2.6615(8)	2.721(6)	2.6639(8)	2.6638(2)	2.6631(9)	2.6648(9)	2.666(1)	2.673(2)
Li-As [4]	2.7529(3)	2.7561(2)	2.7432(14)	2.7565(2)	2.7568(2)	2.7572(2)	2.7580(2)	2.7602(3)	2.7580(5)
Li-As (mean)	2.738	2.737	2.739	2.738	2.738	2.738	2.739	2.741	2.741
Bond Angle / °									
As-Fe-As [2]	102.871(9)	102.938(7)	102.965(15)	103.001(7)	103.045(7)	103.071(7)	103.250(7)	103.49(1)	103.83(2)
As-Fe-As [4]	112.869(5)	112.869(5)	112.819(8)	112.800(4)	112.777(4)	112.763(4)	112.670(4)	112.544(5)	112.365(8)
As-Li-As [4]	86.62(1)	86.463(9)	87.02(6)	86.486(9)	86.486(9)	86.483(1)	86.497(9)	86.55(1)	86.71(2)
As-Li-As [4]	104.05(2)	104.382(2)	103.19(13)	104.33(2)	104.33(2)	104.34(2)	104.31(2)	104.21(3)	103.86(4)
As-Li-As [2]	151.91(5)	151.24(4)	153.62(26)	151.33(4)	151.33(4)	151.32(4)	151.38(4)	151.58(5)	152.28(8)

Table 7.24: Lattice parameters from synchrotron XRPD and Si-calibrated laboratory XRPD refinements on the series $LiFe_{1-x}Ni_xAs$.

x (nominal)	0.000	0.000	0.005	0.010	0.015	0.020	0.025	0.050	0.100	0.200
Sample ID	MP127	MP127	MP159	MP156	MP157	MP158	MP155	MP160	WTT31	WTT42
Radiation	X-ray									
Instrument(s)	I11	X'Pert	X'Pert	I11	I11	X'Pert	I11	X'Pert	X'Pert	X'Pert
λ	0.82720 Å	Cu $K_{\alpha 1}$	Cu $K_{\alpha 1}$	0.60036 Å	0.60036 Å	Cu $K_{\alpha 1}$	0.60036 Å	Cu $K_{\alpha 1}$	Cu $K_{\alpha 1}$	Cu $K_{\alpha 1}$
Space Group	*P4/nmm*									
a / Å	3.776840(2)	3.77514(5)	3.77550(5)	3.77714(1)	3.77719(1)	3.77640(4)	3.777716(9)	3.77719(5)	3.78012	3.78451(5)
c / Å	6.35589(1)	6.3572(1)	6.3558(2)	6.35368(2)	6.35220(3)	6.3498(1)	6.34818(2)	6.3412(1)	6.3244(1)	6.3007(1)
V / Å	90.664(0)	90.601(2)	90.598(3)	90.647(1)	90.628(1)	90.556(2)	90.596(1)	90.471(2)	90.371(2)	90.241(2)
a/a_0	1.00000	1.00000	1.00011[a]	1.00006[b]	1.00008[b]	1.00034[a]	1.00022[b]	1.00055[a]	1.00133[a]	1.00249[a]
c/c_0	1.00000	1.00000	0.99978[a]	0.99967[b]	0.99943[b]	0.99883[a]	0.99880[b]	0.99749[a]	0.99484[a]	0.99111[a]
V/V_0	1.00000	1.00000	0.99997[a]	0.99979[b]	0.99958[b]	0.99950[a]	0.99923[b]	0.99857[a]	0.99746[a]	0.99603[a]
R_{wp}	0.0453	0.0456	0.0697	0.0500	0.0802	0.0476	0.0463	0.0397	0.0434	0.0615
R_{F^2}	0.0664	0.3117	0.2515	0.1097	0.0943	0.2915	0.0795	0.2962	0.3562	0.5201
χ^2	4.035	3.129	0.9620	4.156	1.137	1.551	4.279	2.732	3.190	5.928

[a]Calculated using x_0 from X'Pert

[b]Calculated using x_0 from I11

Table 7.25: Lattice parameters from the series $LiFe_{1-x}Mn_xAs$, derived from Rietveld refinement against neutron powder diffraction data.

x (nominal)	0.000	0.01	0.02	0.05
Sample ID	MP127	MP169	MP164	MP146
Radiation	Combined Neutron-XRD	Neutron	Neutron	Neutron
λ	-	1.59432	1.59432	1.59432
Instrument(s)	POLARIS-I11	D2B	D2B	D2B
T / K	295			
Space Group	*P4/nmm*			
a / Å	3.776840(2)	3.78115(3)	3.77913(3)	3.77396(4)
c / Å	6.35589(1)	6.36658(8)	6.35524(9)	6.3444(1)
V / Å	90.664(0)	91.024(2)	90.765(2)	90.362(2)
Z	2			
R_{wp}	0.0453	0.0685	0.0702	0.0648
R_{F^2}	0.0664	0.0255	0.0408	0.0321
χ^2	4.035	2.576	2.588	3.534

Table 7.26: Atomic coordinates from the series $LiFe_{1-x}Mn_xAs$, derived from Rietveld refinement against neutron powder diffraction data.

	x (nominal)	0.000	0.01	0.02	0.05
	Sample ID	MP127	MP169	MP164	MP146
	Radiation	Combined Neutron-XRD	Neutron	Neutron	Neutron
	Instrument(s)	POLARIS - I11	1.59432	1.59432	1.59432
	λ_{XRD} (Å)	0.82720	D2B	D2B	D2B
Atom	Parameter				
Li ($1/4\ 1/4\ z$)	z-coordinate	0.6580(2)	0.6552(6)	0.6560(7)	0.6585(7)
	$100\times U_{11}$	1.61(2)	1.5(1)	1.4(1)	1.6(1)
	$100\times U_{33}$	2.72(6)	1.4(2)	1.3(2)	1.1(1)
Fe ($3/4\ 1/4\ 0$)	Occupancy[a]	1.000	0.99	0.98	0.95
	$100\times U_{11}$	0.633(5)	0.52(2)	0.19(2)	0.36(3)
	$100\times U_{33}$	1.248(7)	0.66(3)	0.69(4)	0.43(4)
Mn ($3/4\ 1/4\ 0$)	Occupancy[a]	0.000	0.01	0.02	0.05
	$100\times U_{11}$	-	0.52(2)	0.19(2)	0.36(3)
	$100\times U_{33}$	-	0.66(3)	0.69(4)	0.43(4)
As ($1/4\ 1/4\ y$)	y-coordinate	0.23688(4)	0.23719(18)	0.23869(21)	0.23875(22)
	$100\times U_{11}$	0.764(6)	0.74(3)	0.54(3)	0.86(4)
	$100\times U_{33}$	1.570(11)	0.90(6)	1.12(7)	0.94(7)

Table 7.27: Bond distances and angles from the series $LiFe_{1-x}Mn_xAs$, derived from Rietveld refinement against neutron powder diffraction data.

x (nominal)	0.000	0.01	0.02	0.05
Sample ID	MP127	MP169	MP164	MP146
Radiation	Combined Neutron-XRD	Neutron	Neutron	Neutron
Instrument(s)	POLARIS - I11	1.59432	1.59432	1.59432
λ_{XRD} (Å)	0.82720	D2B	D2B	D2B
Bond Distance / Å				
Fe-Fe [4]	2.67063(0)	2.67368(2)	2.67225(2)	2.66859(3)
Fe-As [4]	2.4151(2)	2.4196(7)	2.4231(8)	2.4197(9)
Li-As [1]	2.677(1)	2.661(4)	2.652(4)	2.663(4)
Li-As [4]	2.7529(3)	2.7600(11)	2.7547(12)	2.7471(13)
Li-As (mean)	2.738	2.740	2.734	2.730
Bond Angle / °				
As-Fe-As [2]	102.871(9)	102.77(4)	102.49(5)	102.49(5)
As-Fe-As [4]	112.869(5)	112.923(23)	113.073(26)	113.071(27)
As-Li-As [4]	86.62(1)	86.47(4)	86.62(5)	86.77(5)
As-Li-As [4]	104.05(2)	104.37(9)	104.05(10)	103.73(11)
As-Li-As [2]	151.91(5)	151.26(18)	151.89(20)	1521.53(21)

Appendix F: Structural Parameters of LiFeAs and NaFeAs Under High Pressures

Table 7.28: Lattice parameters obtained by Lebail fits to high-pressure synchrotron XRD data from LiFeAs (instrument ID28, with sample in He-filled diamond anvil cell), taken on increasing pressure. Pressure values were determined by ruby fluorescence and are considered to be accurate to within 0.025 GPa. .

Pressure / GPa	a / Å	c / Å	V / Å^3	c/a
0.037	3.7731(4)	6.3519(9)	90.24(2)	1.6830(1)
0.077	3.7720(3)	6.3478(9)	90.23(2)	1.6827(1)
0.092	3.7716(4)	6.348(1)	90.19(2)	1.6831(1)
0.136	3.7713(4)	6.346(1)	90.13(2)	1.6824(1)
0.231	3.7692(4)	6.342(1)	89.95(2)	1.6825(1)
0.346	3.7677(3)	6.337(1)	89.82(2)	1.6818(1)
0.358	3.7691(3)	6.3390(9)	89.81(2)	1.6816(1)
0.423	3.7674(3)	6.3354(8)	89.76(1)	1.6816(1)
0.835	3.7597(4)	6.317(1)	89.16(2)	1.6800(1)
1.165	3.7538(4)	6.304(1)	88.68(2)	1.6791(1)
1.661	3.7459(5)	6.282(1)	87.97(2)	1.6773(1)
2.272	3.7327(5)	6.259(1)	87.06(2)	1.6776(1)
2.611	3.7280(6)	6.249(1)	86.65(2)	1.6762(1)
3.138	3.7197(5)	6.228(1)	85.88(2)	1.6746(1)
4.340	3.7027(5)	6.188(1)	84.55(2)	1.6717(1)
4.773	3.6969(5)	6.174(1)	84.07(2)	1.6703(1)
5.562	3.6850(3)	6.1459(9)	83.33(2)	1.6680(1)
6.326	3.6784(5)	6.126(1)	82.73(2)	1.6656(1)
6.859	3.6607(5)	6.107(1)	82.04(2)	1.6640(1)
7.264	3.6664(5)	6.097(1)	81.65(2)	1.6626(1)
8.111	3.6561(5)	6.071(1)	80.96(2)	1.6606(1)
8.594	3.6498(5)	6.059(1)	80.44(2)	1.6595(1)
9.117	3.6440(5)	6.046(1)	79.97(2)	1.6591(1)
9.776	3.6363(5)	6.027(1)	79.40(2)	1.6574(1)
10.846	3.6224(2)	5.9956(8)	78.52(1)	1.6550(1)
11.376	3.6175(4)	5.985(1)	78.22(2)	1.6544(1)
13.251	3.5984(3)	5.943(1)	76.83(2)	1.6518(1)
15.767	3.5770(3)	5.896(1)	75.33(2)	1.6491(1)
17.102	3.5660(5)	5.871(1)	74.45(2)	1.6474(1)

Table 7.30: Structural parameters derived by Rietveld refinement against high-pressure NPD data for LiFeAs (sample contained in the Ti:Zr He gas pressure cell, data obtained from the POLARIS diffractometer). Pressure values were measured with a piezoelectric device located within the cell.

Pressure / GPa	a / Å	c / Å	V / Å^3	Fe-Fe / Å	Fe-As / Å	Li-As (1) / Å	Li-As (4) / Å
0.01	3.7787(1)	6.3582(2)	90.787(6)	2.6720(1)	2.4120(4)	2.6697(34)	2.7596(10)
0.02	3.7784(1)	6.3579(2)	90.767(7)	2.6717(1)	2.4119(5)	2.6700(40)	2.7591(11)
0.20	3.7748(1)	6.3491(2)	90.469(6)	2.6692(1)	2.4105(4)	2.6703(33)	2.7545(9)
0.40	3.7707(1)	6.3396(2)	90.139(5)	2.6663(1)	2.4094(4)	2.6592(32)	2.7517(9)
0.55	3.7686(1)	6.3341(2)	89.958(5)	2.6648(1)	2.4083(4)	2.6579(31)	2.7494(9)

Pressure /GPa	As-Fe-As [2] / deg	As-Fe-As [4] / deg	As-Li-As [2] / deg	As-Li-As [4] / deg
0.01	103.13(3)	112.73(1)	151.05(15)	86.42(4)
0.02	103.12(3)	112.74(2)	151.09(18)	86.43(4)
0.20	103.07(3)	112.76(1)	151.41(15)	86.50(4)
0.40	102.98(3)	112.81(1)	151.38(14)	86.497(4)
0.55	102.97(2)	112.82(1)	151.5(14)	86.526(3)

Table 7.31: Structural parameters derived by Rietveld refinement against high-pressure NPD data for LiFeAs (sample contained in the Paris-Edinburgh cell, data obtained from the POLARIS diffractometer). Pressure values were derived from the unit cell volumes (as described in the main text), using the equation of state determined in Chapter 6.

Pressure / GPa	a / Å	c / Å / Å	V / Å^3	Fe-Fe / Å / Å	Fe-As / Å / Å	Li-As (1) / Å / Å	Li-As (4) / Å / Å
0.09	3.7796(2)	6.3642(4)	90.917(8)	2.6726(1)	2.4186(16)	2.621(10)	2.7691(31)
0.66	3.7691(2)	6.3383(6)	90.044(11)	2.6652(2)	2.4156(18)	2.575(12)	2.766(4)
1.74	3.7507(3)	6.2922(7)	88.518(13)	2.6522(2)	2.4039(20)	2.553(11)	2.751(4)
2.29	3.7406(3)	6.2734(8)	87.780(14)	2.6450(2)	2.4050(22)	2.590(12)	2.726(4)
6.21	3.6851(4)	6.1385(10)	83.363(17)	2.6058(3)	2.3729(29)	2.534(10)	2.6772(33)
9.85	3.6433(5)	6.0358(14)	80.115(20)	2.5762(4)	2.3510(40)	2.462(11)	2.646(4)

Pressure / GPa	As-Fe-As (2) / deg	As-Fe-As (4) / deg	As-Li-As (a) / deg	As-Li-As (b) / deg
0.09	102.77(9)	112.92(5)	149.7(5)	86.07(12)
0.66	102.55(11)	113.04(6)	148.9(6)	85.88(14)
1.74	102.55(12)	113.04(6)	149.2(5)	85.94(14)
2.29	102.10(13)	113.28(7)	152.0(5)	86.65(15)
6.21	101.88(17)	113.39(9)	153.5(6)	86.98(13)
9.85	101.60(21)	113.54(11)	153.7(7)	87.03(16)

Table 7.32: Lattice parameters and bond distances obtained by Rietveld refinements against high-pressure XRD data for NaFeAs (sample contained in He-filled diamond anvil cell). Numbers in brackets indicate 1 ESD. Pressure values were determined by ruby fluorescence and are considered to be accurate to within 0.025 GPa. .

Pressure / GPa	a / Å	c / Å	V / Å^3	Fe-As [4] / Å	Na-As [1] / Å	Na-As [4] / Å
5.336	3.8520(0)	6.7991(6)	100.855(10)	2.4290(20)	2.668(14)	2.965(8)
5.387	3.8518(0)	6.7985(7)	100.465(8)	2.4281(27)	2.654(17)	2.971(6)
5.660	3.8472(0)	6.7883(6)	99.781(8)	2.4274(21)	2.667(14)	2.958(6)
6.135	3.8388(0)	6.7711(7)	99.183(10)	2.4228(22)	2.648(14)	2.954(8)
6.541	3.8316(0)	6.7557(7)	98.488(9)	2.4205(28)	2.630(18)	2.950(6)
7.061	3.8231(0)	6.7385(6)	98.349(10)	2.4187(23)	2.630(15)	2.932(7)
7.199	3.8212(0)	6.7355(7)	97.770(8)	2.4170(27)	2.631(17)	2.934(6)
7.646	3.8139(0)	6.7214(6)	97.314(8)	2.4139(22)	2.617(14)	2.930(6)
8.108	3.8085(0)	6.7092(6)	96.826(8)	2.4089(22)	2.596(14)	2.933(6)
8.585	3.8023(0)	6.6972(6)	96.372(9)	2.4081(22)	2.596(15)	2.922(6)
8.984	3.7966(0)	6.6859(6)	95.820(9)	2.4055(23)	2.586(15)	2.919(6)
9.511	3.7897(0)	6.6720(6)	95.370(9)	2.4028(23)	2.573(15)	2.914(6)
9.920	3.7839(0)	6.6609(6)	95.183(9)	2.3999(23)	2.564(15)	2.910(7)
10.084	3.7810(0)	6.6580(7)	94.923(8)	2.4013(27)	2.566(17)	2.903(6)
10.307	3.7779(0)	6.6508(6)	94.888(10)	2.3978(23)	2.555(15)	2.905(8)
10.372	3.7774(0)	6.650(7)	94.392(8)	2.3978(28)	2.547(18)	2.908(6)
10.834	3.7712(0)	6.6371(6)	94.221(8)	2.3931(23)	2.528(15)	2.909(6)
10.988	3.7690(0)	6.6329(6)	94.007(9)	2.3921(22)	2.528(14)	2.906(8)
11.200	3.7662(0)	6.6274(7)	93.244(9)	2.3907(27)	2.521(18)	2.905(7)
12.006	3.7562(0)	6.6088(7)	92.749(8)	2.3859(26)	2.506(17)	2.898(6)
12.567	3.7498(0)	6.5963(6)	92.729(7)	2.3838(21)	2.497(14)	2.892(6)
12.657	3.7495(0)	6.596(6)	92.974(8)	2.3823(20)	2.490(13)	2.896(6)
12.317	3.753(0)	6.6009(6)	92.638(7)	2.3823(21)	2.490(13)	2.903(6)
12.738	3.7486(0)	6.5926(6)	92.161(7)	2.3808(21)	2.490(13)	2.896(6)
13.311	3.7424(0)	6.5802(6)	91.744(8)	2.3772(21)	2.461(13)	2.900(7)
13.793	3.7370(0)	6.5696(6)	91.405(7)	2.3745(24)	2.441(16)	2.901(6)
14.141	3.7325(0)	6.561(6)	90.959(7)	2.3737(21)	2.442(14)	2.893(6)
14.619	3.7264(0)	6.5503(6)	90.563(7)	2.3720(20)	2.439(13)	2.885(6)
15.09	3.7212(0)	6.5402(6)	90.147(11)	2.3691(20)	2.432(13)	2.882(4)
15.604	3.7163(0)	6.5274(8)	89.845(11)	2.3803(25)	2.868(14)	2.715(4)

Continued overleaf...

Pressure / GPa	a / Å	c / Å	V / Å^3	Fe-As [4] / Å	Na-As [1] / Å	Na-As [4] / Å
16.009	3.7122(0)	6.5197(8)	89.557(12)	2.3773(29)	2.876(18)	2.710(6)
16.388	3.7085(0)	6.5118(9)	89.212(13)	2.3817(28)	2.882(18)	2.699(6)
16.835	3.7037(0)	6.5035(10)	88.416(13)	2.3778(29)	2.847(19)	2.704(6)
17.271	3.6926(0)	6.4845(10)	88.112(11)	2.3719(29)	2.834(17)	2.696(6)
17.701	3.6883(0)	6.4771(9)	87.785(11)	2.3707(29)	2.802(17)	2.699(6)
18.107	3.6839(0)	6.4686(9)	87.538(12)	2.3653(27)	2.783(17)	2.702(8)
18.475	3.6806(0)	6.4620(9)	87.286(12)	2.3713(25)	2.787(17)	2.691(7)
18.796	3.6769(0)	6.4561(9)	87.062(12)	2.3653(29)	2.764(19)	2.697(6)
19.122	3.6737(0)	6.4508(10)	86.840(12)	2.3681(31)	2.756(18)	2.692(6)
19.467	3.6703(0)	6.4465(10)	86.605(12)	2.3680(31)	2.754(19)	2.688(6)
19.799	3.6670(0)	6.4406(9)	86.417(12)	2.3637(30)	2.744(19)	2.689(9)
20.086	3.6643(0)	6.4359(9)	86.246(14)	2.3638(34)	2.728(19)	2.690(8)
20.373	3.6619(0)	6.4319(10)	86.079(13)	2.3650(33)	2.717(19)	2.688(8)
20.68	3.6593(0)	6.4283(10)	85.920(15)	2.3639(34)	2.701(20)	2.690(8)
20.992	3.6568(0)	6.4252(11)	85.786(15)	2.3630(35)	2.699(19)	2.688(8)
21.202	3.6553(0)	6.4206(11)	85.752(13)	2.3620(32)	2.695(21)	2.687(7)
21.238	3.6549(0)	6.4196(10)	85.639(13)	2.3635(31)	2.723(20)	2.677(7)
21.473	3.6530(0)	6.4175(10)	85.504(15)	2.3637(35)	2.697(20)	2.682(8)
21.748	3.6508(0)	6.4153(12)	85.466(13)	2.3610(31)	2.626(20)	2.701(8)
21.809	3.6503(0)	6.4142(10)	85.378(13)	2.3608(31)	2.640(20)	2.696(8)
22.031	3.6479(0)	6.4159(10)	85.340(15)	2.3610(31)	2.589(21)	2.710(9)
22.122	3.6470(0)	6.4162(12)	85.206(15)	2.3650(34)	2.532(21)	2.722(9)
22.319	3.6457(1)	6.4108(24)	85.207(31)	2.3730(61)	2.500(40)	2.722

Table 7.34: Bond angles derived by Rietveld refinement against high-pressure XRD data, with sample contained in He-filled diamond anvil cell (instrument: ID09a). Numbers in brackets indicate 1 ESD. Pressure values were determined by ruby fluorescence and are considered to be accurate to within 0.025 GPa.

Pressure / GPa	As-Fe-As (2) / deg	As-Fe-As [4] / deg	As-Na-As [2] / deg	As-Na-As [4] / deg
5.336	104.91(13)	111.80(7)	133.5(6)	113.26(26)
5.387	104.97(16)	111.77(9)	132.9(7)	113.55(33)
5.660	104.83(13)	111.84(7)	133.8(6)	113.10(27)
6.135	104.79(13)	111.86(7)	133.5(6)	113.25(28)
6.541	104.65(17)	111.93(9)	133.4(7)	113.30(35)
7.061	104.43(14)	112.05(7)	134.4(6)	112.79(28)
7.199	104.46(16)	112.03(9)	134.1(7)	112.94(34)
7.646	104.37(14)	112.08(7)	134.0(6)	112.99(28)
8.108	104.46(14)	112.03(7)	133.3(6)	113.34(28)
8.585	104.27(14)	112.13(7)	133.9(6)	113.07(28)
8.984	104.21(14)	112.16(7)	133.8(6)	113.10(29)
9.511	104.11(14)	112.22(7)	133.8(6)	113.12(29)
9.920	104.06(14)	112.24(7)	133.7(6)	113.14(29)
10.084	103.86(16)	112.35(9)	134.2(7)	112.92(34)
10.307	103.96(14)	112.30(7)	133.7(6)	113.14(29)
10.372	103.94(17)	112.30(9)	133.5(7)	113.27(29)
10.834	103.99(14)	112.28(7)	132.9(6)	113.55(35)
10.988	103.96(14)	112.30(7)	133.0(6)	113.48(29)
11.200	103.94(17)	112.31(9)	132.9(7)	113.55(28)
12.006	103.85(16)	112.36(8)	132.8(7)	113.6(34)
12.567	103.72(13)	112.42(7)	132.9(5)	113.54(33)
12.657	103.80(12)	112.38(6)	132.5(5)	113.74(27)
12.317	103.94(13)	112.31(7)	132.2(5)	113.90(26)
12.738	103.86(13)	112.35(7)	132.5(5)	113.76(26)
13.311	103.84(13)	112.36(7)	131.7(5)	114.15(26)
13.793	103.79(15)	112.38(8)	131.2(6)	114.39(26)
14.141	103.67(13)	112.45(7)	131.6(5)	114.18(31)
14.619	103.53(12)	112.52(7)	131.9(5)	114.04(27)
15.090	103.51(12)	112.53(7)	131.9(5)	114.06(26)
15.604	102.64(15)	112.99(8)	150.8(6)	104.60(26)

Continued overleaf...

Pressure / GPa	As-Fe-As [2] / deg	As-Fe-As [4] / deg	As-Na-As [2] / deg	As-Na-As [4] / deg
16.009	102.66(14)	112.98(7)	151.2(5)	104.39(31)
16.388	102.26(14)	113.20(7)	152.6(5)	103.71(30)
16.835	102.30(14)	113.17(7)	151.2(5)	104.40(26)
17.271	102.23(14)	113.21(7)	151.1(5)	104.40(26)
17.701	102.14(14)	113.26(7)	150.1(5)	104.94(26)
18.107	102.29(16)	113.18(8)	149.2(6)	105.41(28)
18.475	101.80(16)	113.44(8)	150.6(6)	104.72(27)
18.796	102.02(15)	113.32(8)	149.2(6)	105.39(28)
19.122	101.73(17)	113.48(9)	149.6(7)	105.20(30)
19.467	101.60(17)	113.54(9)	149.8(7)	105.08(30)
19.799	101.74(17)	113.47(9)	149.2(7)	105.38(30)
20.086	101.63(19)	113.53(9)	148.9(7)	105.55(30)
20.373	101.47(17)	113.62(9)	148.9(7)	105.60(30)
20.68	101.43(16)	113.64(8)	148.3(6)	105.83(28)
20.992	101.41(16)	113.64(8)	148.3(6)	105.80(28)
21.202	101.38(16)	113.66(8)	148.3(6)	105.80(28)
21.238	101.28(14)	113.71(7)	149.7(5)	105.13(26)
21.473	101.20(14)	113.76(7)	148.8(5)	105.60(26)
21.748	101.27(13)	113.72(7)	145.8(5)	107.10(26)
21.809	101.27(14)	113.72(7)	146.4(5)	106.80(26)
22.031	101.19(18)	113.77(8)	144.3(6)	107.80(28)
22.122	100.91(17)	113.92(8)	142.6(6)	108.70(27)
22.319	100.40(32)	114.20(16)	142.5(12)	108.70(53)